Mitigating Greenwater Damage through Design

by

Kuang-An Chang, Hamn-Ching Chen, Yonguk Ryu, and Kai Yu

Ocean Engineering Program
Department of Civil Engineering
Texas A&M University

OTRC Library Number: 11/05A156

For more information contact:

Offshore Technology Research Center
Texas A&M University
1200 Mariner Drive
College Station, Texas 77845-3400
(979) 845-6000

or

Offshore Technology Research Center
The University of Texas at Austin
1 University Station C3700
Austin, Texas 78712-0318
(512) 471-6989

A National Science Foundation Graduated Engineering Research Center

Table of Contents

List of Tables and Figures

Table

Figure

Abstract

Green water damage to floating structures results from high pressures and loads that occur when wave crests inundate the structure far above the waterline in areas not designed to withstand such pressures. A combined effort with both numerical and experimental approaches was made to study the kinematics of plunging waves impinging on a structure and the associated green water. A fixed and simplified 2D rectangular structure based on the dimensions of a typical TLP (1:168 scaled down) was tested in a laboratory 2D wave tank using extreme waves breaking and impinging on the structure with green water. A new non-intrusive image based technique called bubble image velocimetry (BIV) was developed and validated to measure the velocity field of the multiphase flow. BIV is capable of measuring the full-field velocity of a gas-liquid flow by correlating the "texture" of the gas bubbles and the gas-liquid interfaces in the images. Detailed velocity fields in the vicinity of the structure, including green water, were measured over the entire impinging process using the particle image velocimetry (PIV) technique and the BIV technique. A prediction equation for the greenwater velocity profile based on the measured velocity fields was developed. Comparisons among the measured green water velocity, the prediction equation, and the widely used linear dam break solution were made. In addition, an interface-preserving level set numerical method was incorporated into the Reynolds-Averaged Navier-Stokes (RANS) method for the simulation of green water effect numerically. In the method, free surface flows are modeled as immiscible air-water two-phase flows and the free surface itself is represented by the zero level set function. Calculations were performed for several two-dimensional green water problems including dam break flows, free jets, and the impingement of dam break flow on a fixed structure. The method has also been extended for the simulation of nonlinear waves generated by a numerical wavemaker.

Chapter 1

Introduction

1.1   Review of Green Water Incidents and Studies

The interaction between extreme waves and floating structures is of primary concern in the design of offshore structures.   Green water loads on offshore platform occur when an incoming wave significantly exceeds the free board and water runs on the deck. In the past extreme waves have caused significant damages to offshore structures due to the tremendous forces created by wave impingement (e.g., Buchner, 1995; Hamoudi and Varyani, 1998; Schoenberg and Rainey, 2002).   Frequently, green water washes out and damages equipment on the deck and in some cases causes injury or death to persons working on the deck.   Green water also could affect the stability of offshore structures.   Figure 1 shows the green water incident on the Selkirk Settler in mid Atlantic in 1987.

In 2004-2005, hurricanes Ivan, Katrina, and Rita damaged a number of offshore structures in the Gulf of Mexico.   These hurricanes were unusually intense and generated waves that were larger that the design criteria for many structures.   Large waves resulted in greenwater occurring in the decks of some structures causing damage that ranged from equipment on the deck being moved or damaged to the loss of older platforms designed to lower criteria.   Greenwater damage can in principle be mitigated by a variety of means including increasing deck elevation, reconfiguring deck layouts, strengthening decks and equipment supports, or installing shielding to protect equipment. Appropriate choices would depend on the type of structure and deck equipment and appurtenances.   The focus of this study is to develop a model to predict greenwater veloicities that can be used to provide design guidance to avoid or minimize greenwater damage to offshore structures.

Figure 1: Green water incident at the side of Selkirk Settler.   (Photographed by Captain G. A. Ianiev and courtesy of Prof. Douglas Faulkner).

The green water problem has been investigated experimentally and numerically.   Among the experimental studies, Buchner (1995a, b) presented experimental investigations based on model tests with a floating, production, storage, and offloading (FPSO) unit.   From various tests, he suggested that the green water occurrence and loading are strongly dependent on the conditions of the ocean such as wave period, wave height and current velocity.   In the studies, he showed the resemblance of green water to a dam break flow and commented that the application would be limited due to the shallow water assumption in the dam break flow.   Buchner (1996) later also investigated the effect of green water with different bow shapes.   In addition, Hamoudi and Varyani (1998) investigated the probability of green water occurrence for various Froude numbers and wave heights experimentally.   The study examined the number of deck wetness through laboratory tests to compute the probability of occurrence and compared it with the

study (1997) indicated that the front velocity of a real dam break flow is not constant and reduces as a function of time, which disagrees with Ritter's solution in which the front velocity is constant. Even though many green water studies used the dam break flow for velocity estimation, validation on the similarity between the dam break flow and green water flow has not yet been well studied or carefully proved.

The probability of green water incidents increases in a harsher ocean condition, meaning green water occurs and becomes a concern mainly due to extreme waves. Typically large breaking waves are used to represent the extreme waves. Since breaking waves impinging on a structure and the overtopping water on the structure generates significant loads on the structure, it is of importance to understand the breaking waves and associated overtopping water. The impinging patterns of breaking waves have been classified into four categories by researchers (e.g. Oumeraci et al., 1993; Hattori et al., 1994; Hull and Müller, 2002). Their studies found that the impact loads are strongly influenced by the shape of breaking wave as it impinges on a wall. Although there are many studies investigating the relation between wave impacts on a vertical wall and the breaking shape, the flow pattern after the impingement and overtopping green water have not been well understood. On the other hand, there have been other approaches mainly focusing on the forces of the waves on structures and simple flow field kinematics. Most of these studies were based on the potential flow theory therefore the nature of the multiphase highly turbulent flow in the problem is not realistically simulated. The results are therefore at most for the "engineering accuracy" for the prediction of global wave forces rather than looking into the physical insight of the phenomenon with a resolved accuracy in velocity, pressure, and force distributions. Recently, more advanced approaches, either based on the Reynolds averaged Navier-Stokes equations (RANS) or large eddy simulation (LES), that feature turbulent models and provide much more physical insight have started to be used in the study (e.g., Lin and Liu, 1998a, 1998b; Watanabe and Saeki, 1999; Christenson and Deigaard, 2001). However, only limited success has been achieved due to the lack of comprehensive treatments on the splashing water over the free surface and the high void fraction bubbly flow, and lack of experimental data to validate the calculations of models.

experimental works of other researchers. They also found that there is no direct relation between the velocity of waves and the velocity of green water on the deck.

Among the numerical studies, Maruo and Song (1994) studied the effect of the wave steepness on the green water effect in the bow region using the boundary element method. They simulated the case with a high speed vessel two-dimensionally. Nielsen and Mayer (2004) used a Navier-Stokes solver with a volume-of-fluid scheme to model the green water loads on a vessel with and without motions in both 2D and 3D. The model shows a good agreement in 2D comparison between the calculated water level on the deck and experimental data in Buchner's (1995a) study. In their extended study to 3D, they found that the 3D effect is insignificant.

Due to the possible similarity between green water and a dam break flow, there have been many studies that applied the dam break theory to green water studies. Fekken et al. (1999) simulated green water incidents using a Navier-Stokes solver with a volume-of-fluid method for free surface modeling. They modeled a dam break flow to mimic the green water flow on the deck without considering the ship-wave interaction and ship motion. Shoenberg and Rainey (2002) modeled the green water flow by simulating a moving shelf submerged in a pool using the potential flow theory and the boundary integral equation method. They compared their results with an analytical solution of dam break flow and found a reduction in damage if using the moving shelf model. Yilmaz et al. (2003) developed a semi-analytical solution for a dam break flow to simulate green water on a deck. They obtained the solution using the Fourier Series Analysis and Fourier Transformation technique to describe the nonlinear dam break problem.

In a typical design procedure for the green water load, the standard approach to estimate the velocity of a green water incident is to use the dam break solutions (Shoenberg and Rainey, 2002). The dam break flow is a class problem that has been investigated by numerous researchers. Many solutions were proposed for the dam break flow. Among the solutions, a classic analytical solution that has been widely used for a dry frictionless flat bed and considered as a simplest one is Ritter's solution (Lauber and Hager, 1997; Vischer and Hager, 1998; Zoppou and Roberts, 2003). That solution has been used frequently for green water predictions (Buchner, 1995a, b; Shoenberg and Rainey, 2002). However, Lauber and Hager's experimental

In experimental approach, very few non-intrusive quantitative velocity measurements of breaking waves impinging on structures exist. We thus review the measurement of breaking waves instead. Various measurement techniques, including laser Doppler velocimetry (LDV) and particle image velocimetry (PIV), have been employed for the velocity measurements of the wave breaking process in both of surf zone and deep water (e.g., Greated and Emarat, 2000; Ting and Kirby, 1994, 1995; Perlin et al., 1996). Among the efforts, PIV is a new comer and only about 10 years old. However, the technique is perhaps the most robust and state-of-the-art technique among all the methods. This is due to not only its full field nature but also its recent advances in the improvement of the spatial and temporal resolutions and time resolving capability, and its still-evolving foreseeable future. Among the recent advances in breaking wave measurement using PIV, Chang and Liu (1998) measured the maximum velocity and associated acceleration and vorticity of the overturning jet of a breaking wave. Unfortunately, as a wave breaks and entrains air bubbles, the technique is then restricted to the region outside the aerated area, in general under the trough level or away from the breaking point. Despite some success on the measurements of the breaking wave flow field and generated turbulence outside the aerated region (Chang and Liu, 1999, 2000; Melville et al., 2002), the advances in the understanding of the flow structure inside the highly aerated region have rarely been reported. Few exceptions are perhaps the early work of Jansen (1986) and the very recent work of Govender et al. (2002). Jansen measured particle trajectories in the aerated region of breaking waves using fluorescent tracers and ultraviolet light, but the measurements suffered from poor spatial resolution. More comprehensive measurements were obtained by Govender et al. (2002), who used a technique similar to PIV based on the digital image acquisition and cross-correlation algorithms with the use of a laser light sheet to illuminate the aerated region. Bubble structures in the images were used for correlation between consecutive images for velocity determination. Even though the measurements are promising, no detailed description on the technique itself was provided.

In addition to the direct measurement of bubbly flow under breaking waves, the measurement of gas-liquid flows has been investigated in various areas. Typically the bubble void fraction and the bubble size are much lower and smaller than that in a breaking wave. For such flows the scattering of laser light due to bubbles is much less and thus more controllable.

The PIV technique have been successfully used to measure bubble velocity by correlating bubbles or tracking each bubble in the recorded images that were taken by applying the "shadowgraphy" method (Hassan et al., 1998; Nishino et al., 2000; Lindken and Merzkirch, 2001). The method uses a light source behind the bubbles therefore the bubbles appear in the images as their shadows. Again, the density and size of bubbles have to be within a certain limit so the shadows are separated and identifiable. Typically the two methods above are used in low void fraction flow with small bubbles, and inapplicable in breaking wave measurements.

1.2   Objective and Approach of the Present Study

Green water damage to floating structures results from high pressures and loads that occur when wave crests inundate the structure far above the waterline in areas not designed to withstand such pressures. Green water damage is often associated with the use of floating structures in operations or locales for which they were not initially designed. Modification of existing floating structures to prevent greenwater damage is often difficult to achieve, and prevention is generally approached through localized reinforcements or barriers added to the structure and/or modified operating procedures. The *objective* of this research is to focus on the development of a prediction model of green water velocity on the deck. This prediction model could be subsequently applied in new designs, and used to develop design guidance. The goal is to allow designers to avoid or minimize green water on new floating structures through design. The applications may be to the ship-shaped FPSO's and other structure geometries such as spars or TLP's.

The *approach* is to form a combined effort with both numerical expertise and experimental expertise to investigate the kinematics of plunging waves impinging on a laboratory model structure and the associated green water. Since instruments capable of measuring the flow field of green water does not exist, development of a new measurement technique is the first step in the experimental approach. A new measurement technique called bubble image velocimetry (BIV) was developed to directly track the air bubbles and measure velocity in gas-liquid flows. The validation for the accuracy of BIV was conducted. A fixed 2D rectangular

structure based on the dimensions of a typical TLP (1:168 scaled down) was tested in the 2D laboratory wave tank using extreme waves breaking and impinging on the structure with greenwater.   Velocity fields in the vicinity of the structure, including greenwater, were measured over the entire impinging process using the particle image velocimetry (PIV) technique and the newly developed BIV technique.   A prediction equation for greenwater velocity distribution based on the measured velocity fields was developed and tested.   Comparisons among the measured greenwater velocity, the prediction equation, and the widely used linear dam break solution were made.

In addition to the experimental approach, an interface-preserving level set numerical method was incorporated into the Reynolds-Averaged Navier-Stokes (RANS) method for simulation of greenwater effect numerically.   In the level set method, free surface flows are modeled as immiscible air-water two-phase flows and the free surface itself is represented by the zero level set function.   In order to maintain a uniform interface thickness between the gas and liquid phases, a reinitialization (or redistancing) algorithm was implemented to ensure that mass conservation is satisfied throughout the entire simulation.   Calculations were performed for several two-dimensional greenwater problems including dam-breaking, free jets, and the impingement of dam-breaking flow on a fixed structure.   The method has also been extended for the simulation of nonlinear waves generated by a numerical wavemaker.   The ultimate goal is to develop a numerical model capable of simulating the green water flow, to validate the numerical model using the measured data in this study, and to apply the validated numerical model to simulate the real scale flow and complex geometry platforms with green water inundation.

Chapter 2

Experimental Condition and Setup

2.1 Experimental Condition

The experiments were performed in a glass-walled wave tank located at the Department of Civil Engineering, Texas A&M University. The wave tank is 36 m long, 0.9 m wide and 1.5 m high. The water depth was kept constant at $d = 0.80$ m throughout the experiments. The wavemaker is of dry-back flap type installed at one end of the wave tank and controlled by a computer. A 1:5.5 sloping beach with a layer of horsehair is at the other end of the tank to absorb the wave energy and reduce reflection. A rectangular model structure that has a length of 0.15 m, a height of 0.31 m and a width the same as that of the tank was installed in the wave tank. The draft of the model structure is 0.20 m. Figure 2.1 shows the side view and top view of the wave flume and the model structure. The model was constructed based on a simplified two-dimensional tension-leg platform (TLP) with a scale ratio of 1:168. The model structure was mounted on aluminum frames that were rigidly fixed to the bottom of the tank and suspended from the top of the tank. The aluminum frames were designed to minimize vibration of the model induced by breaking wave impingement.

Velocity field was measured using two optics-based image techniques: particle image velocimetry (PIV) and bubble image velocimetry (BIV). While PIV is a modern measurement technique and has become popular in many fluid mechanics laboratories since late 90's, BIV was developed by the investigators for this project. The details of PIV can be found in Raffel et al. (2001) while the description of BIV was given in Ryu et al. (2005).

The detailed sketch of the model structure is shown in Figure 2.2 with the coordinate system and the fields of view (FOV) used for the PIV and BIV measurements. Note that the origin $(x, z) = (0, 0)$ is at the intersection of the structure front wall and the stationary water level.

The structure was located at 21.7 m away from the wavemaker. All the control signals, including the signals controlling the wavemaker and triggering the PIV and BIV systems, and measured data were synchronized.
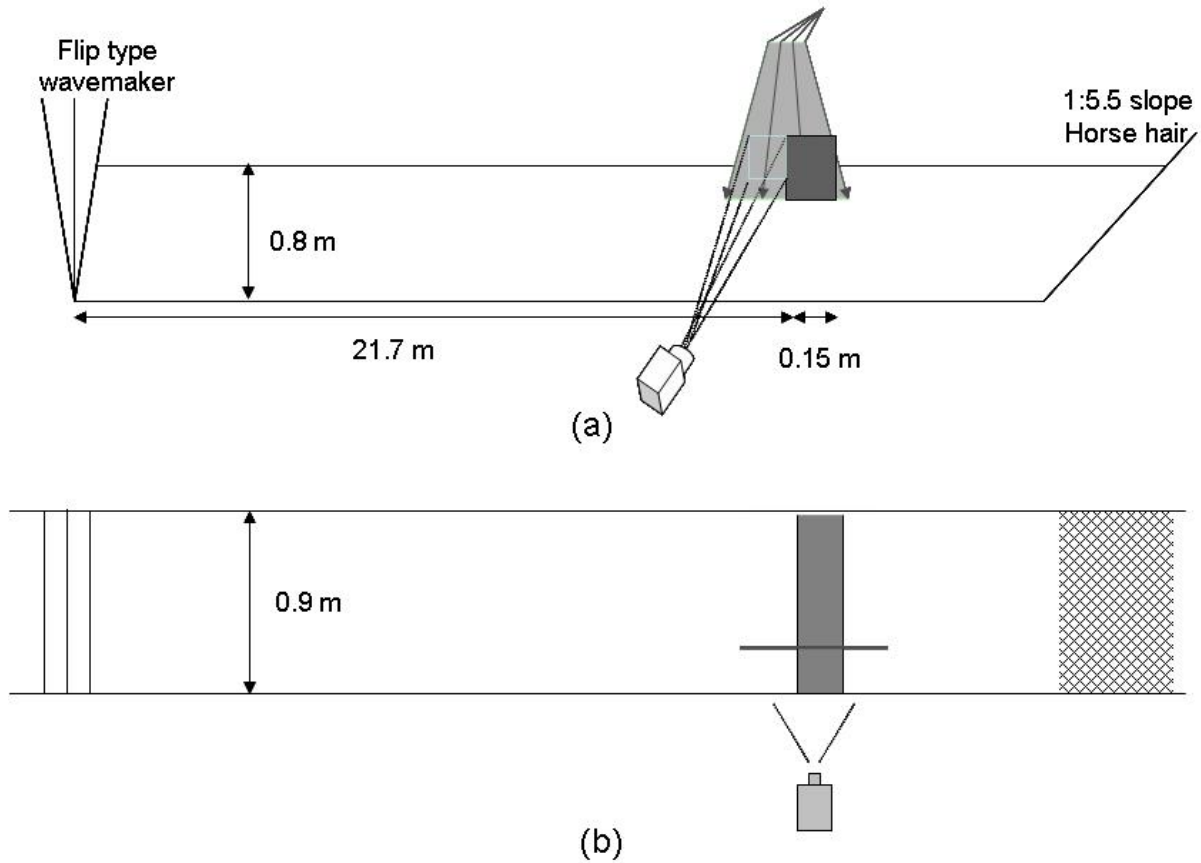
Figure 2.1: Wave flume: (a) side view, (b) top view.

Velocity measurements were performed with three different FOVs. First, the PIV technique was used to measure the flow field in front of the model structure in FOV 1. The focus of FOV 1 was on the instant when the breaking wave impinges on the structure. FOV 2 was for the BIV measurements in the vicinity of the structure that covers the front and the top of the structure. Since the waves have broken in the region, the flow is bubbly and the region is aerated. In order to investigate the green water effect without the end-of-the-deck problem (water falls off the short deck immediately after rushing up to the deck), a longer deck of 0.22 m

in length was later added to the original model structure. This is for the easier analysis (so the length of the deck is no longer a variable), and for later comparisons with the dam-breaking model widely used for green water prediction. With the extended deck, the total length of the deck of the structure becomes 0.37 m. Even though the deck length is more than doubled, it is still much shorter than the wavelength of the breaking waves used in the study. To measure the flow fields on the extended deck using BIV, the large FOV 3 was used. The setup condition is shown in Table 2.1.

The breaking wave tested here is a plunging breaker that was generated using a wave focusing method similar to that in Skyner et al. (1990). The wave train consists of waves with various frequencies ranging from 0.7 Hz to 1.3 Hz. The water depth was kept constant at $d = 80$ cm. With the superposition of different wave frequencies and some trials and errors, a plunging breaker breaks at a desired location right in front of the model structure was obtained. The generated breaking wave is highly repeatable so the tests can be repeated multiple times for a better accuracy and later calculation of mean and turbulence velocities. The free surface elevation was measured using two wave gauges located at 5.1 m and 21.7 m from the wavemaker (i.e., $x = -16.6$ m and $x = 0.0$ m in front of the structure) to measure the incoming waves and the water elevation at the front edge of the structure, respectively. The measured wave profiles by the gauges are shown in Figure 2.3. In Figure 2.3(a), the primary frequency, wavelength, wave height, and phase speed of the target breaking wave in the deep water are 0.77 Hz, 2.54 m, 17.1 cm, and 1.95 m/s, respectively. On the other hand, in Figure 2.3(b) the height of the wave became about 24 cm right at the frontal edge of the structure, and about 1 cm below the deck (freeboard 11 cm). However, video images show the water level is much higher (approximately 5 cm higher) than the deck (to be showed later). This is due to the high void fraction when the wave was broken at the leading edge of the deck.
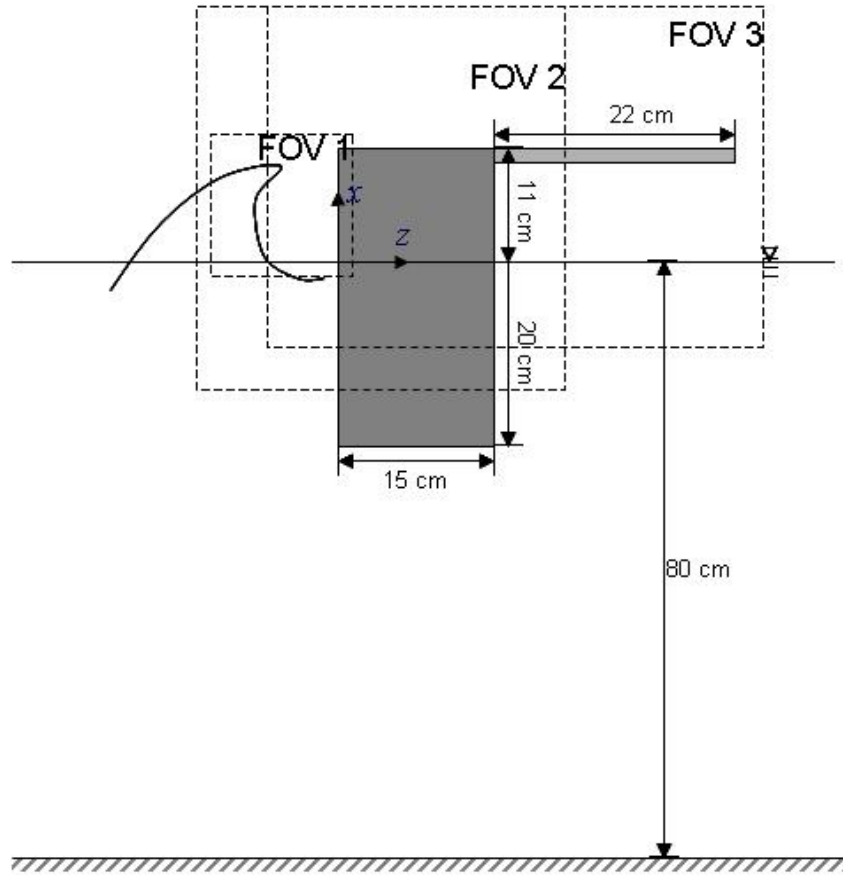
Figure 2.2: Model structure and fields of view (FOVs)

Table 2.1: FOVs and setup conditions

FOV	Condition	Method	FOV size (mm^2)	Spatial resolution (mm^2)
FOV 1	Model	PIV	150×120	1.8×1.8
FOV 2	Model	BIV	378×378	5.5×5.5
FOV 3	Model with extended deck	BIV	410×275	7.0×7.0
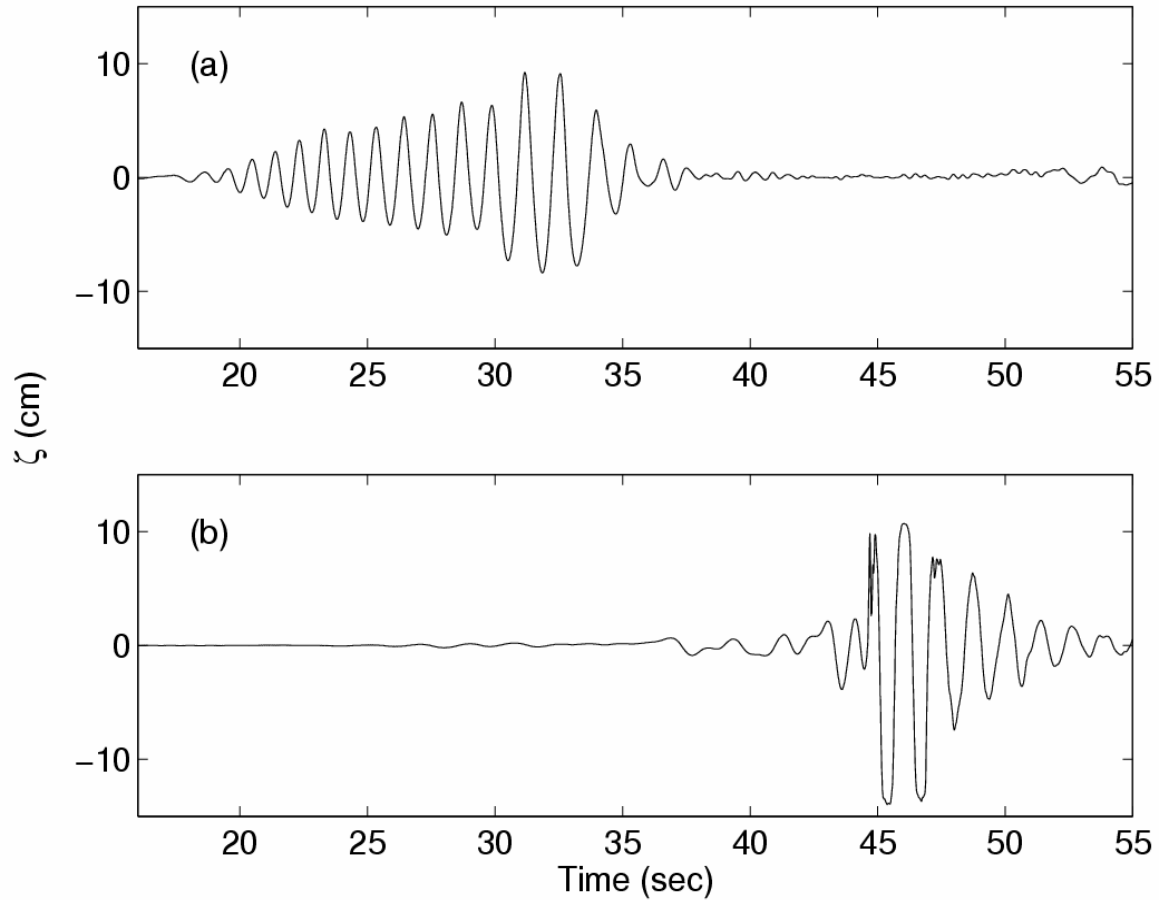
Figure 2.3:   Wave elevations measured at (a) 5.1 m (x = -16.6 m), and (b) 21.7 m (x = 0.0 m) from the wavemaker.

2.2 Principle and Setup of PIV System

The PIV technique in the present study was first used to measure the velocity field near the front wall of the model structure.   The PIV technique is a non-intrusive, indirect, and whole field method.   The tested flow had no intrusive probes in it but was seeded with neutrally buoyant tiny particles as tracers.   The sketch of PIV is shown in Figure 2.4.   The basic principle of the PIV technique is that the tiny seeding particles in the fluid are illuminated by a thin sheet of pulsing laser light twice within a short time interval with images captured using a camera.   As a result, there is one image for each particle on a single frame and two consecutive

frames are used to trace the particle motion.   Figure 2.5 shows the double-frame/single-pulsed method for the image recording.
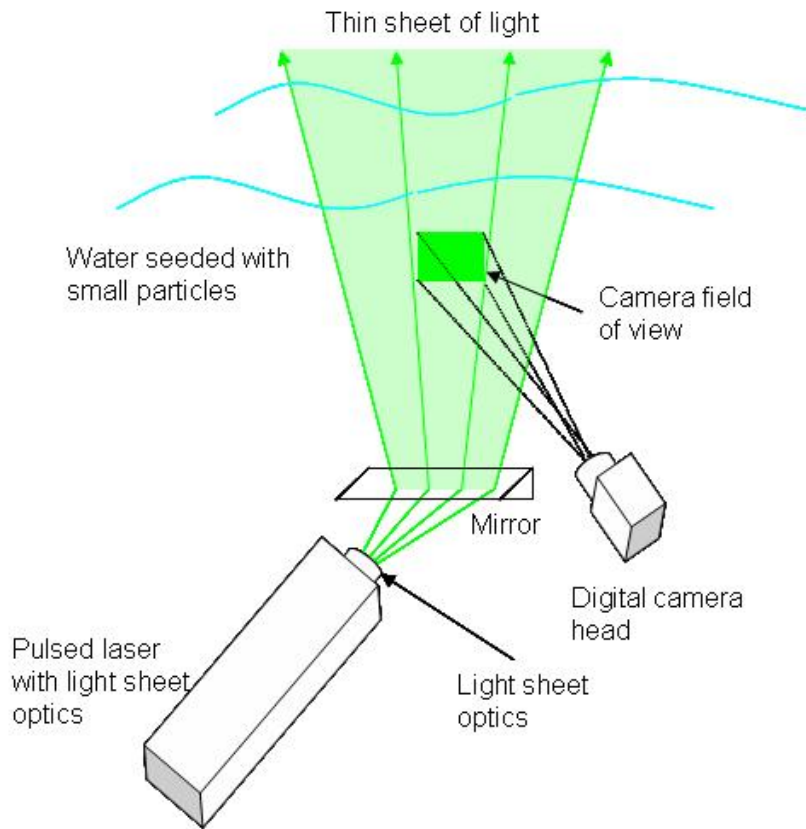
Figure 2.4: Sketch of PIV technique
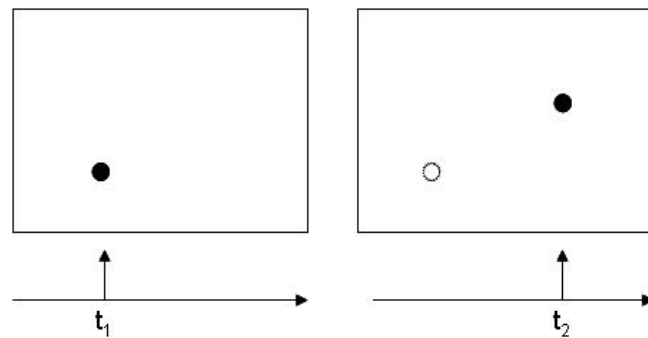
Figure 2.5: Image recording technique: Double-frame/single-pulsed method.   The black dots represent the exposed images of a particle by a pulsing laser light at time t_1 and t_2.

After the images containing particles are acquired, cross correlation is employed to obtain the displacement of particles over the short time separation, Δt. Small areas (called subwindow or interrogation area) in the images are used to find the particle displacement in the areas. The cross correlation can be written as

$$R(\mathbf{s}) = \int_{subwindow} f(\mathbf{x})g(\mathbf{x}+\mathbf{s})d\mathbf{x} \qquad (2.1)$$

in which R, a 2D function, is the result from the correlation, f and g are the 2D mathematical representation of the two images (call an image pair), and $\mathbf{x}$ and $\mathbf{s}$ are the position vector and the displacement vector, respectively. With the finding the maximum value in the 2D function R and curve fitting technique for subpixel accuracy, the *mean* particle displacement ($\Delta x, \Delta z$) over the small area occurs at the highest correction can be obtain. The velocity can be subsequently calculated from the displacement as $u = \Delta x / \Delta t$, $w = \Delta z / \Delta t$. In general, Fast Fourier Transform (FFT) is used to speed up the processing for correlation computation. The details of the PIV techniques can be found in Raffel et al. (2001).

The light source of the PIV system in the present study is a dual-head frequency-doubled Spectra-Physics Nd:YAG laser that has a 532 nm wavelength (green light), 400 mJ per pulse maximum output energy, 6 ns pulse duration, and 10 Hz repetition rate for each head. A set of optics consisting of cylindrical and spherical lenses was used to generate the light sheet with a thickness of approximately 1 mm. The image recording system is a CCD camera from LaVision Inc., a frame grabber housed in a computer, and the controlling computer. The camera has an 8 frames per second (fps) maximum framing rate, a 1024×1280 pixels resolution, and a 12-bit dynamic range. A 105 mm Nikon micro lens was mounted on the camera with the aperture set at f/5.6. The seeding particles, Vestosint 2157, have a mean diameter of 56 µm and a specific weight of 1.02. The FOV for the PIV measurements is from $x = $ -14 cm and to $x = 0.7$ cm and from $z = 1$ cm to $z = 13$ cm with $x = 0$ being the leading edge of the structure and $z = 0$ being the calm water level as shown Figure 2.2 (denoted as FOV1). The time interval between two successive laser pulses is 0.6 ms. The frame rate of the camera was set at 7.27 Hz throughout the experiments. The measurements were repeated 11 times with a small delay between each set of measurements to form continuous velocity fields with a time separation of

0.025 second.   The interrogation area for velocity determination was 32×32 pixels with a 50 % overlap.   Commercial software from LaVision Inc. was used for the velocity computation.

2.3 Principle and Setup of BIV system

The BIV technique was developed and used to obtain the velocity field in the highly aerated region.   The technique correlates the bubble images and "texture" in the images created by the bubbles and the air-water interfaces.   No small seeding particles used in the traditional PIV technique are needed.   The idea of the BIV method came from combining the shadowgraphy technique that illuminates the fluid from behind to reveal the flow pattern, and the PIV technique that correlates the consecutive images to determine the velocity.   Since the velocity is calculated through cross-correlating the images obtained by the shadowgraphy technique with the bubble structure in the images as tracers, the BIV technique requires only two light projectors to illuminate the air bubbles in the aerated region.   Unlike the traditional PIV technique, no laser and light sheet are needed.   In the experiments, regular 600 W light bulbs with reflecting mounts were used to illuminate the flow.   The images were captured by two Phantom high speed cameras mounted with a Nikon 105 mm micro focal lens.   One of the cameras used for the measurements of the model without the extended deck (FOV 2) has a resolution of 512×512 pixels, an 8-bit dynamic range, and a maximum framing rate of 1000 fps. The other one, borrowed from National Chung Hsing University in Taiwan, is a newer version of the first camera.   This newer one has a resolution of 1024×1024 pixels, the same dynamic range, and a maximum framing rate of 1200 fps, and was used for the model test with the extended deck (FOV 3).   In this study, the resolution used for the newer camera was set at 1024×768 pixels and the camera is capable of measuring up to 1680 fps with that resolution. The aperture of the focal lens mounted on both cameras was set at f/1.8.

The illumination of the flow in BIV is the modification of the traditional shadowgraphy method with lights being placed at both sides of the wave tank.   One light placed at the back side of the tank was used to illuminate the flow from behind (the high speed camera was located at the other side).   A thin sheet of translucent white plastic glass was attached on the back-side

glass wall of the tank. This way the light bulb illuminates the flow more uniformly without the use of a costly large high intensity light emitting diode (LED) plate typically used in the shadowgraphy technique. However, for the region with a high concentration of bubbles the captured images are filled with shadows and appear to be all dark in that region. The images do not provide the needed differences in intensity to reveal the bubble structure or bubble "texture" for later correlation for velocity determination. To resolve this problem, a light was placed on the other side of tank (at the same side with the high-speed camera but with an angle) in order to produce the desired intensity differences in the images. The light illuminating behind the tank was located with an angle of 0° (normal to the FOV) while the other at the other side had an angle of about 60°. Subsequently, images captured using the modified shadowgraphy technique were inverted so the high intensity (bright) represents the bubbles. The flow velocity was calculated by cross-correlating the flow texture from the inverted consecutive images.

Since the BIV technique does not use a light sheet to illuminate a specific plane of interest like the traditional PIV method, it is necessary to know where the measured bubbles are in the cross-tank direction (i.e. the y direction). The problem is solved by limiting the depth of field (DOF) in the experiment, achieved by carefully setting up the camera. The DOF is defined as a distance within which objects captured by the camera are well focused and appear to be sharp and clear. The camera focal point and the DOF can be considered as the light sheet plane and light sheet thickness, respectively, in the PIV technique. This way the FOV of the captured images can be defined. Assuming that a lens focuses on a point at a distance L from the forward nodal point of the lens (which is sufficiently close to the distance between the lens front and the point), the DOF can be calculated using the formulae below. Following Ray (2002), the formulae for the nearest limit, R, and the farthest limit, S, of the DOF can be expressed as

$$R = Lf^2 / \left(f^2 + NLC \right) \tag{2.2}$$

$$S = Lf^2 / \left(f^2 - NLC \right) \tag{2.3}$$

in which f is the focal length of the camera focal lens, C the value for the circle of confusion that depends on the property of the camera, and N the f-number of the camera aperture. The DOF is thus $D = S - R$.
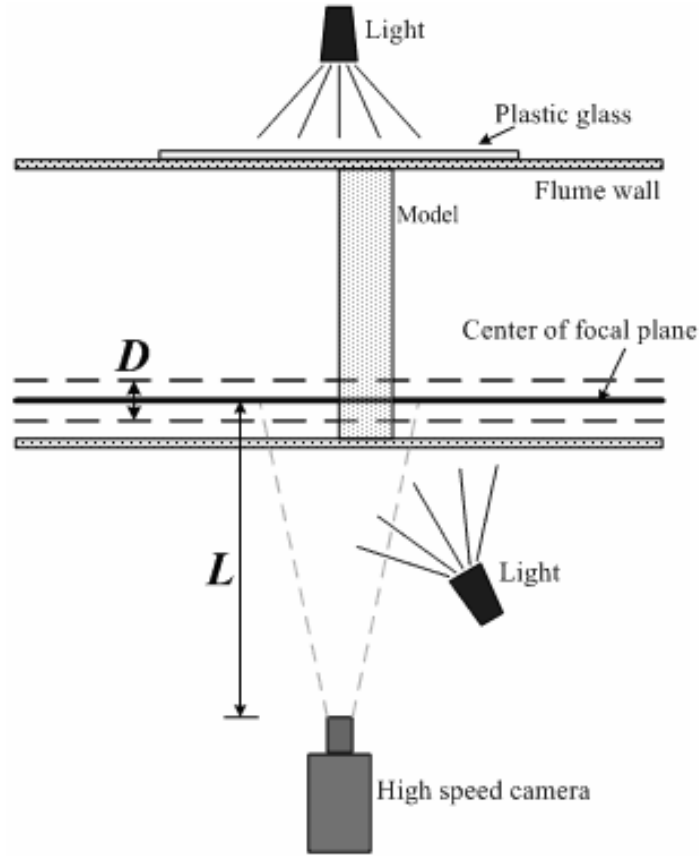
Figure 2.6: Sketch of BIV technique

Objects located in front of and behind the DOF will appear to be blurry without a clear texture in the captured image and therefore have little effect on the later correlation process for velocity determination. On the other hand, objects located within the DOF will be sharp in the image with a featured pattern due to the flow. This means that the obtained velocity from cross-correlating the captured images is indeed mainly contributed from the image of fluid within the DOF. The uncertainty on the position of the images in the cross tank direction is therefore one-half of the thickness of the DOF from the center of the DOF. As a result, the error due to the thickness of DOF in the obtained velocity can be estimated approximately as $\varepsilon = D/2L$. If the depth of view D is thin and the distance between the camera and the focal plane L is long, the error can be minimized. In the present study, $L = 4.0$ m, $f = 105$ mm, $N = 1.8$, and $C = 0.03$ mm. The calculated R is about 3.92 m and S is about 4.07 m, therefore the corresponding DOF in the

present study is $D = 0.15$ m.   The error due to the thickness of the DOF is thus estimated as 2%.
The arrangement of the BIV system is sketched in Figure 2.6.   An example of the BIV method
and the validation of the method will be discussed later.

The FOV of the BIV measurement for the model without the extended deck is 37.8 cm ×
37.8 cm and centered at $x = 5.2$ cm and $z = $ -5.3 cm as shown Figure 2.2 (denoted as FOV 2).
The first high speed camera (the older version) was used to capture the images.   The time
interval between the consecutive recorded images was 1.75 ms that is equal to the time
separation between the consecutive frames captured by the camera.   The images were processed
using the LaVision PIV software and the velocity field was calculated using an adaptive multi-
pass algorithm with an initial interrogation window size of 32×32 pixels and a final window size
of 16×16 pixels with a 50% overlap between the adjacent windows.   In addition, FOV 3 for the
model with the extended deck is 41.0 cm × 27.5 cm.   The images were captured using the
newer version camera with a framing rate set at 1000 fps, i.e., a time interval of 1 ms between
images.   Velocities were obtained using the same software and the same algorithm but with an
initial interrogation window size of 64×64 pixels and a final window size of 32×32 pixels with a
50% overlap.   A median filter was subsequently applied to eliminate the spurious vectors in the
calculated velocity maps.   The mean velocity was calculated from ensemble averaging 10
instantaneous velocity fields for the measurements of FOV 2 and 20 for FOV 3 from repeated
runs with the same test condition.

2.4 Example and Validation of BIV Technique

The BIV technique uses the bubbles as tracers and correlates the bubble texture in the
aerated region.   This means that the BIV technique works in the region where the PIV technique
does not work.   Figure 2.7 shows a sample of inverted BIV images captured for the present
study.   The flow pattern of the bubble in front of the structure and the splashing jet above the
structure are clearly identified in the image.   Figure 2.8(a) shows the image and texture in the
aerated region that is the close-up of Figure 2.7 (see the marked area in the figure) without image
inversion.   Since the air bubbles appeared to be dark, the image was inverted, as shown in

Figure 2.8(b), before performing correlation for velocity determination. Figure 2.8(c) shows the obtained BIV velocity vectors through cross-correlating the inverted images. As a result, it has shown that as long as there exist a certain amount of air bubbles or air-water interfaces that form a distinct flow pattern or texture in the images, velocities can be obtained by cross correlating the images.
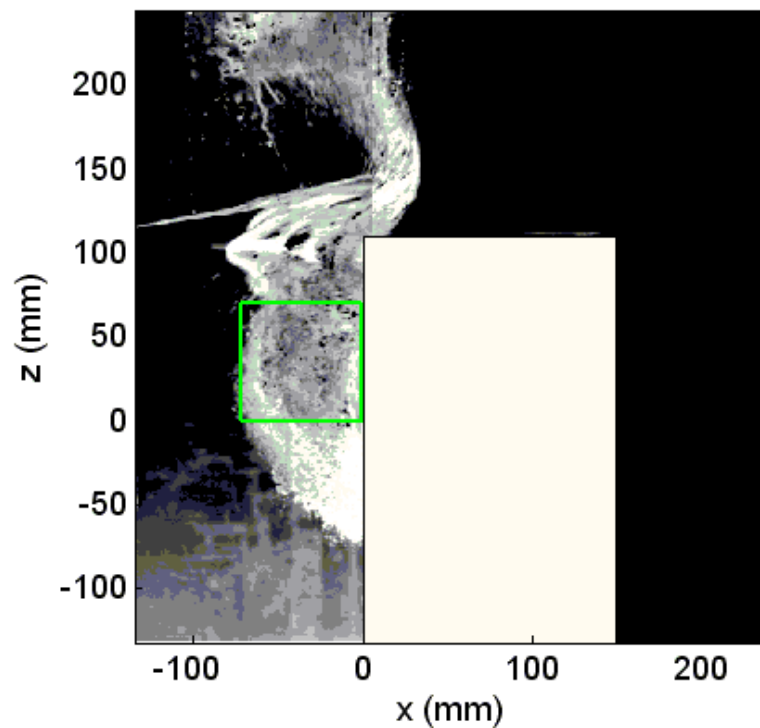

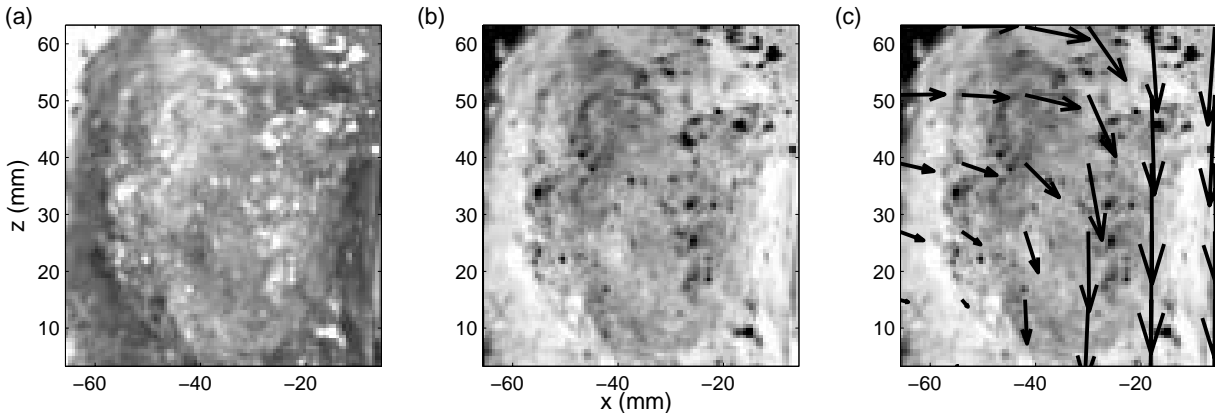Figure 2.7: Sample BIV image of wave impinging on structure

Figure 2.8: Close-up of the bubbly flow in Figure 2.7 and associated velocity vectors obtained using BIV. (a) Raw image, (b) inverted image, (c) instantaneous velocity field.

The validation of BIV was performed in two ways: (1) to compare the velocity measured using the BIV technique with that measured using the fiber optic reflectometer (FOR) technique (Chang et al., 2003); (2) to check the effect of the out-of-focus blurry images (outside of the DOF) in the BIV velocity measurements. A bubble plume in a water tank was used in the validation. A two-phase quasi-steady bubbly flow in a vertically standing narrow tank was measured using both the BIV technique and the FOR technique. The objective is to validate the BIV method by comparing the results obtained from these two methods. The FOR technique is capable of measuring the velocity time history of both water (seeded with small particles) and air bubbles at a given point in a multi-phase flow. Details of FOR are given in Chang et al. (2003).

The narrow tank used in the validation has a length of 0.4 m, a width of 0.4 m, and a height of 0.8 m. Water was filled to a depth of 0.7 m in the tank. An air diffuser generating air bubbles was located at the bottom of the tank. A bubble plume was formed in the tank with a diameter approximately 0.11 m at the measurement section. The BIV method was used to measure the velocity of the bubble plume with a FOV of 12.6 cm × 12.6 cm. Subsequently, the FOR technique was employed to measure the velocity at $x_b = 0$ and $z_b = 45$ cm, located in the region of the BIV FOV with $x_b = 0$ and $z_b = 0$ being the center of the air diffuser. The experiment setup is sketched in Figure 2.9.
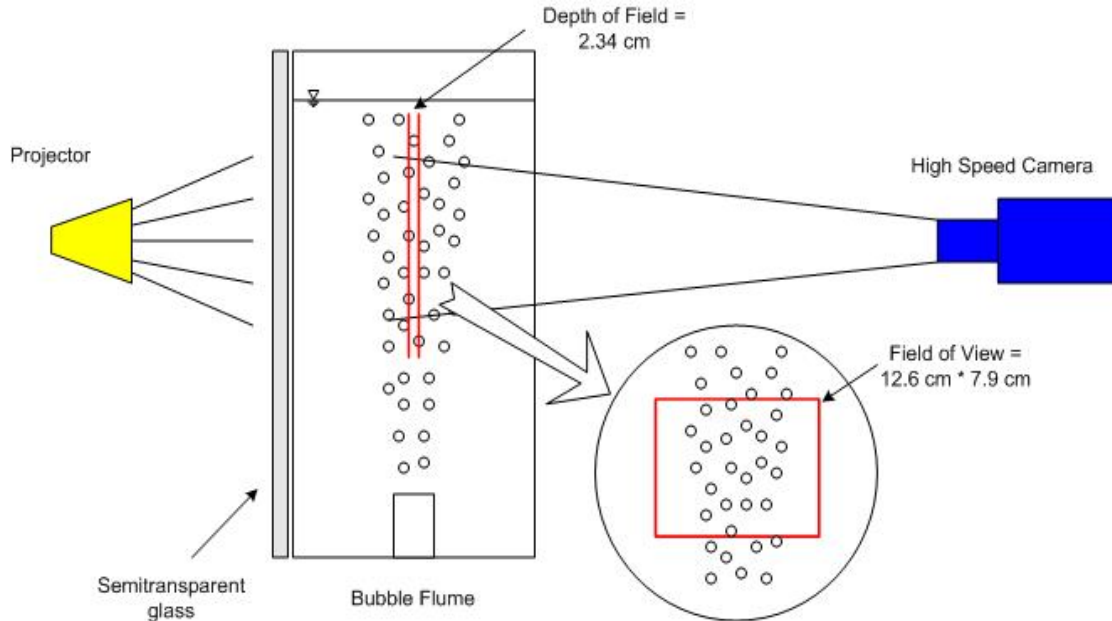
Figure 2.9: Schematic of the BIV validation experiment

Figure 2.10 shows the mean velocity field of the bubble plume measured by the BIV method. The mean velocities were obtained by ensemble average using 20 instantaneous velocities. Figure 2.10(b) is the distribution of the cross-sectional vertical velocity at the level of $z = 45$ cm, the same as that of the FOR probe. The mean velocity distribution measured in the present study is not identical to the known cross sectional mean velocity profile because the number of instantaneous velocities used for averaging is not big enough. Figure 2.11 shows the measured bubble velocities using both the BIV and FOR methods at the point where the FOR probe was located. The void fraction is 4 % with the average size of the bubble equal to 3 mm at the FOR measurement point, obtained by FOR. The mean velocities were obtained using 20 and 10 instantaneous velocities in the BIV and the FOR measurements, respectively. The comparison between the mean velocities shows very good agreement with a small discrepancy of about 1% (approximately 4 mm/s). The scattering of the instantaneous velocities may be due to the turbulent nature of the flow.
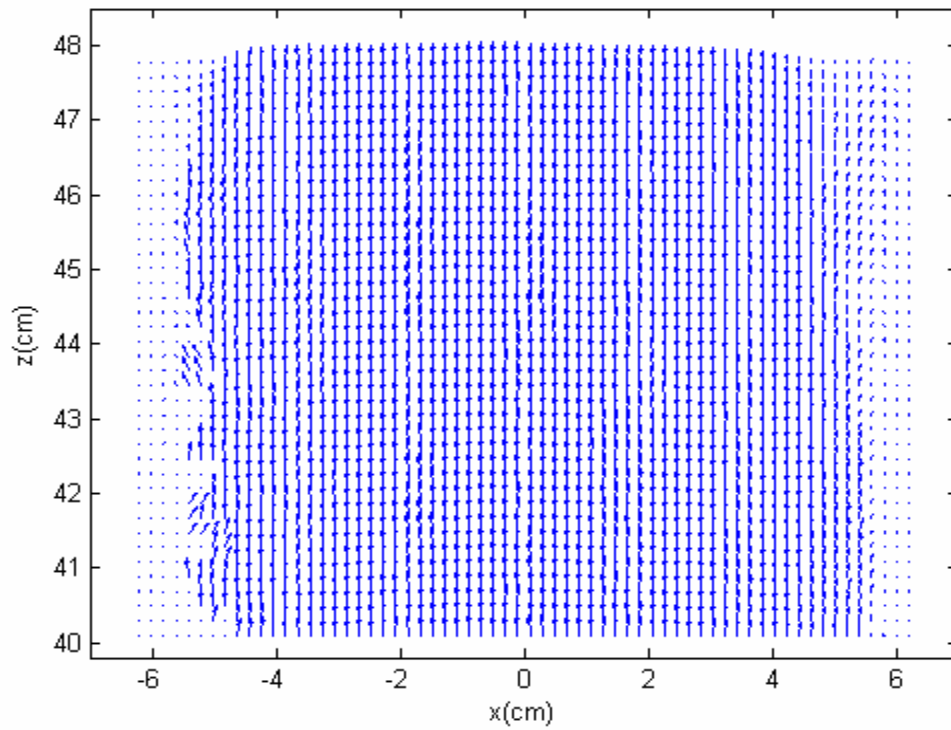
(a)
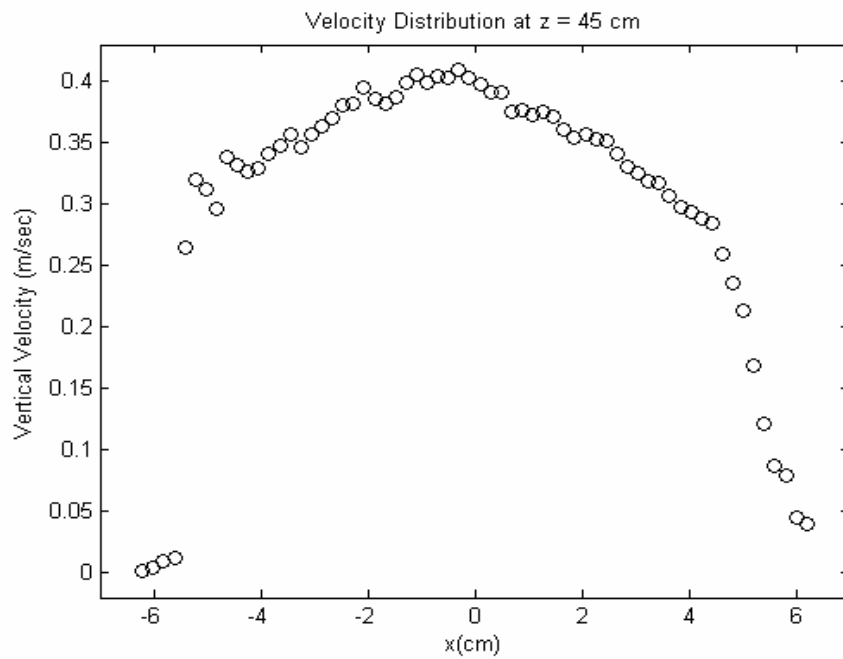
(b)

Figure 2.10: Bubble plume measurement using BIV: (a) mean velocity field, (b) cross-sectional vertical velocity at $z = 45$ cm.
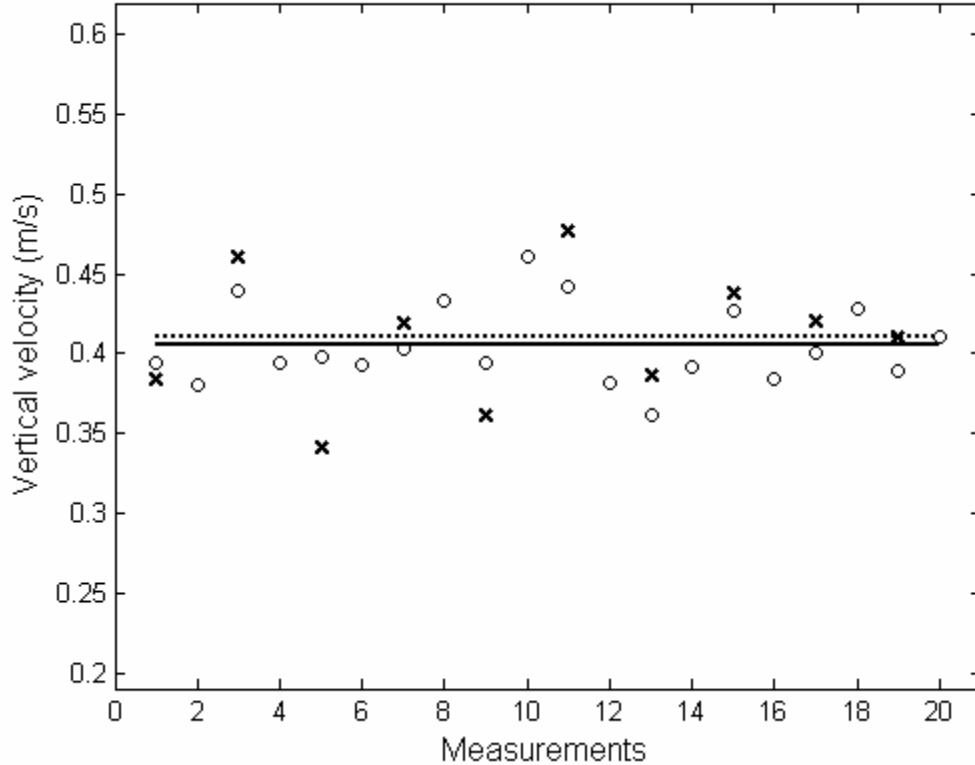
Figure 2.11: Comparison of velocities measured using BIV and FOR. o, BIV instantaneous velocity; ×, FOR instantaneous velocity; solid line, BIV mean velocity; dotted line, FOR mean velocity.

In theory the blurring images contributed from the bubbles outside the DOF are expected to have insignificant influence in the correlation for velocity determination because the intensity of the bubbles is much weaker (and spreads much wider) than that of the well-focused bubbles inside the DOF. Since the BIV measurements are in general performed in highly aerated bubbly flows, the captured images are indeed the sharp images inside the DOF superimposed with the blurry images outside the DOF. In order to investigate the blurry image effect to the BIV accuracy, the velocity obtained from the well-focused clear bubble images was compared with that obtained from artificially superimposed out-of-focus blurry bubble images. The process to examine the blurry image effect is presented in Figure 2.12. Two sets of images were taken from similar flow fields but with different bubble velocities due to different bubble sizes. One

set focused at the center of the bubble plume so the bubble images are sharp and clear while another set focused 15 cm behind the center of the plume therefore the bubble images are blurry and out of focus. Figures 2.12(a) and (b) represent the former and the later set, respectively. Clear and blurry images were then artificially added in two ways. Firstly, the blurry images were added to the clear images directly, shown in Figure 2.12 (d). Secondly, the blurry images were vertically flipped (Figure 2.12 (c)) and then added to the clear images (Figure 2.12(e)). Figure 2.13 shows five sets of images corresponding to the scheme of Figure 2.12 and the instantaneous velocity fields.
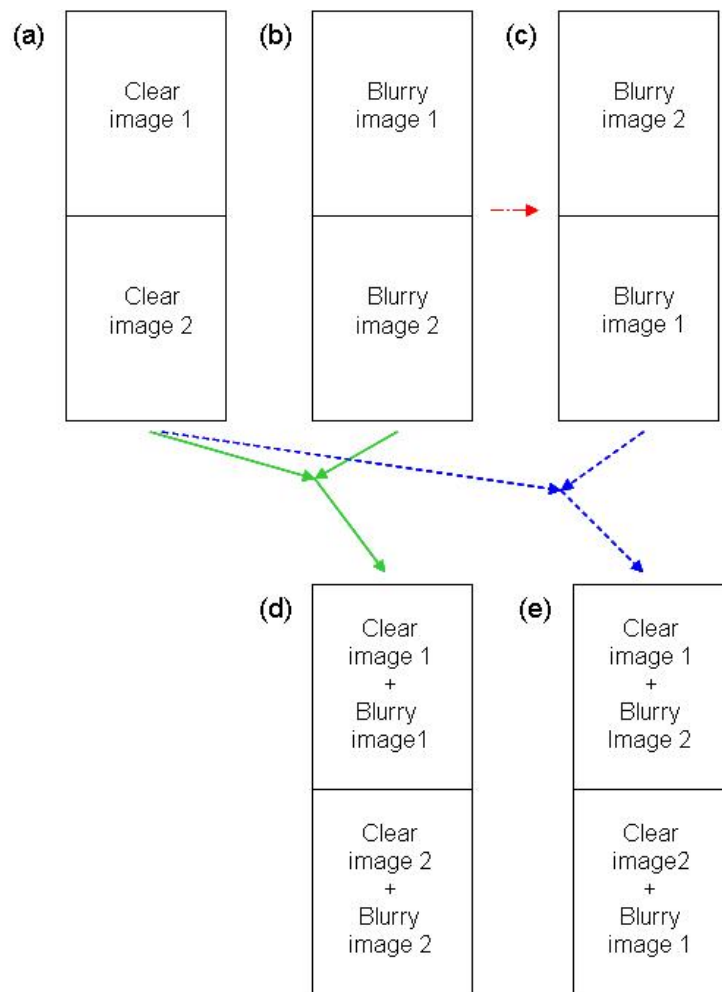
Figure 2.12: Scheme of superimposition of clear and blurry images using two set of clear and blurry images: (a) clear images, (b) blurry images, (c) vertically flipped blurry images, (d) superimposed clear and blurry images, and (e) superimposed clear and flipped blurry images.
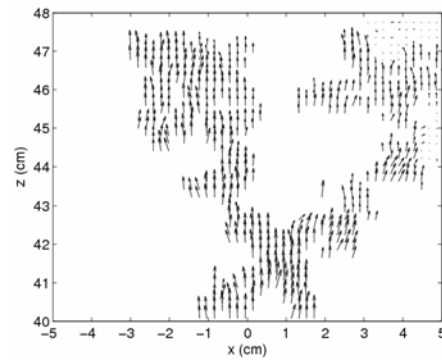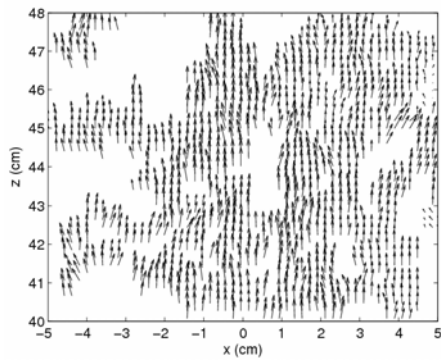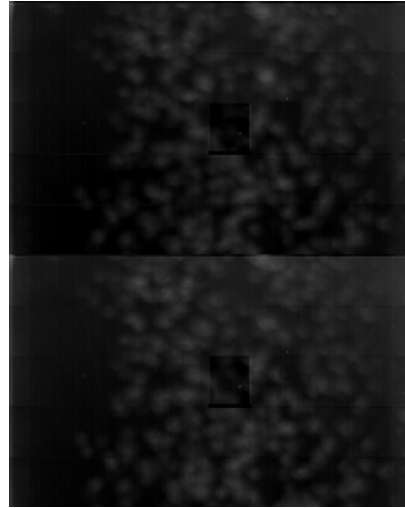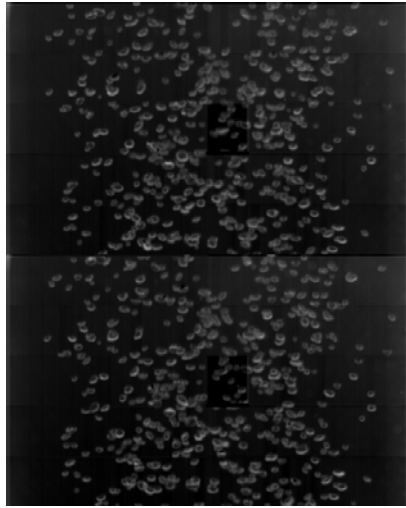
(a)   (b)

Figure 2.13: Image sets and instantaneous flow fields corresponding to Figure 2.12.
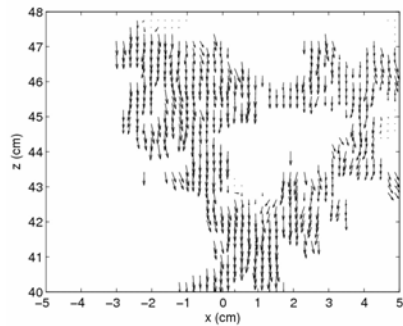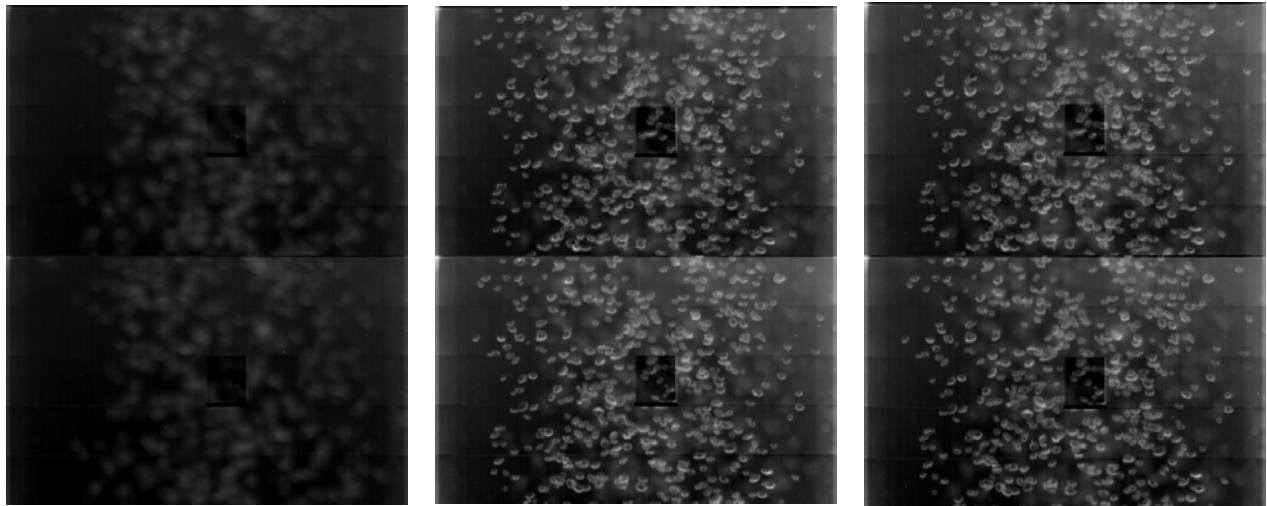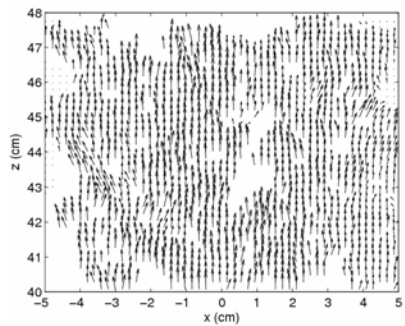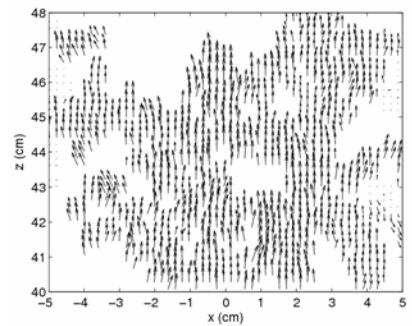
(c)   (d)   (e)

Figure 2.13: (continued)

Figure 2.14 shows the instantaneous vertical velocity distribution obtained along the centerline of the bubble plume from the clear images (Figure 2.13(a)), blurry images (Figure 2.13(b)), vertically flipped burry images (Figure 2.13(c)), superposition of the clear images and burry images (Figure 2.13(d)), and superposition of the clear images and the vertically flipped

burry images (Figure 2.13(e)). The Figure shows that both the velocities obtained from the clear-blurry superimposed images are very close to that from the clear images. Therefore the blurry and out of focus bubble images have little effect on the accuracy of the BIV velocity measurements.
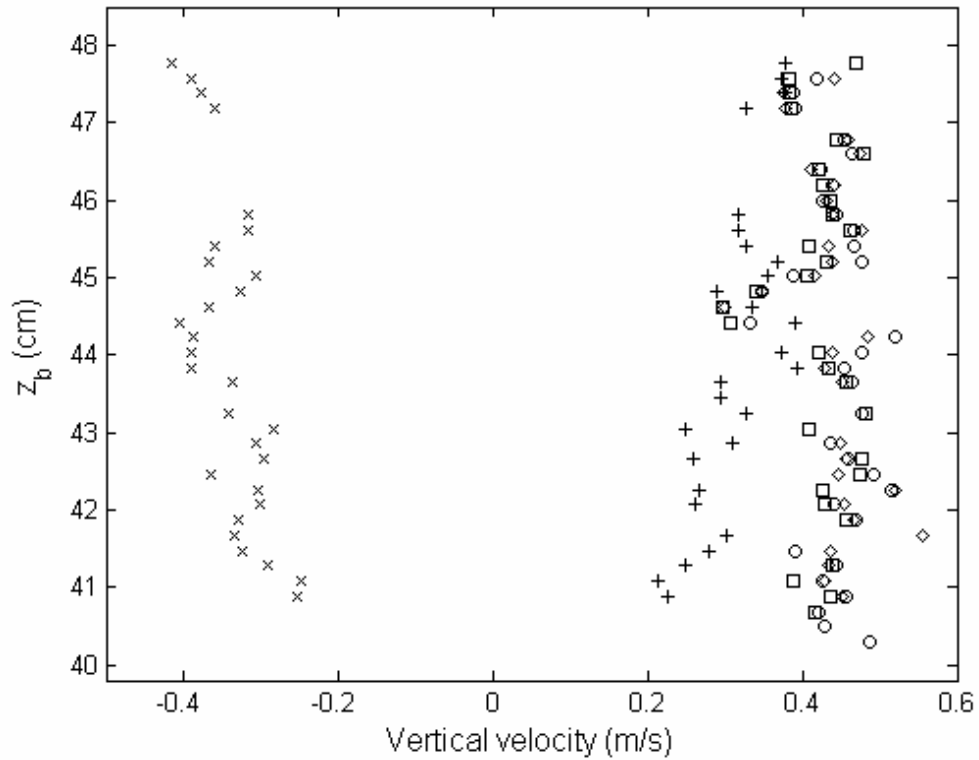
Figure 2.14: Velocity distribution along the centerline of the bubble plume obtained from: clear images (o), blurry images (+), vertically flipped blurry images (×), superimposed clear and blurry images (□), superimposed clear and flipped blurry images (◊).

Chapter 3

Experimental Results and Discussion

3.1 Velocity Measurement Using PIV

The velocity measurement in the vicinity of the model structure was first carried out using the PIV technique. If a spilling type of breaking wave impinges on the structure, the air pocket between the wave front face and the structure is relatively small. In such a condition the majority of the region in front the leading edge of the structure is not highly aerated and is suitable for PIV. The measurement taken at FOV 1 (shown in Figure 2.2) is shown in Figures 3.1(i) to 3.1(iv). However, even for the cases with only a small air pocket, green water on the deck of the structure due to overtopping is highly aerated and not ideal for PIV. If the impinging wave is of plunging type, a large air pocket in front of the structure will form immediately and cause severe laser light scattering and result in saturated and not useful images for PIV correlation in the image processing. The problem continues, if not gets worse, to green water on top of the structure. Figures 3.1(a) to 3.1(d) show the PIV measurement of the plunging breaking wave. Clearly there exists a large region where no velocity vectors were obtained due to the large amount and size of air bubbles. A similar problem was also observed in Chang and Liu (1999, 2000). One interesting thing worth of pointing out is that the maximum horizontal velocity in Figure 3.1 reached 1.5 times the phase speed of the wave, C. This result is consistent with that reported in Chang and Liu (1998). Figure 3.2 shows the cross sectional horizontal velocities along the x axis corresponding to Figures 3.1(a) to 3.1(d). Cross sectional velocity, denoted as U_C, is the maximum horizontal velocity of a vertical column at a location along the deck. As shown Figure 3.2, the largest magnitude around $1.5C$ persisted for a certain period of time, corresponding to the instants in Figures 3.1(b) to 3.1(d).
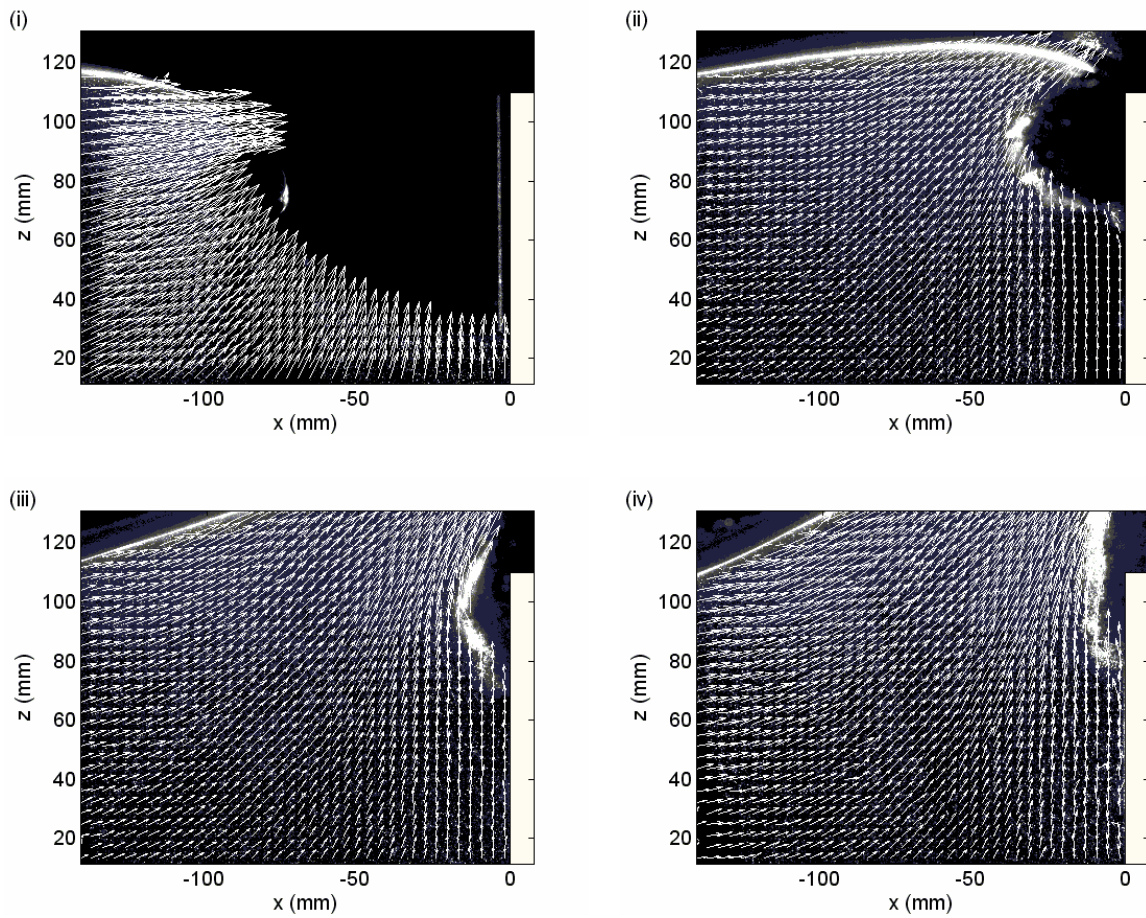
Figure 3.1: PIV measurement of breaking waves impinging on structure: (i-iv), spilling breaker with a small air pocket; (a-d), plunging breaker with a large air pocket.   The time separation between the consecutive frames is 25 ms.

(a)

(b)

(c)

(d)
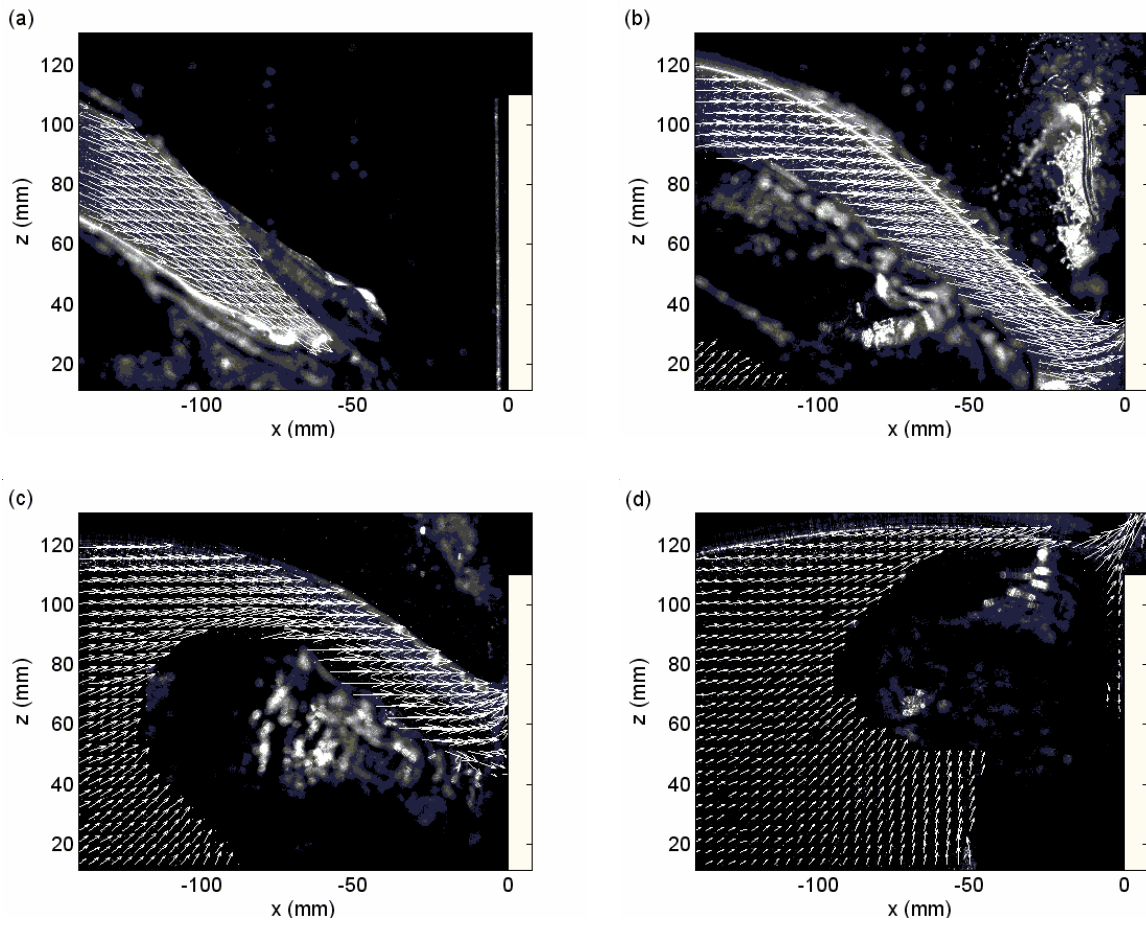
Figure 3.1 (Continued)
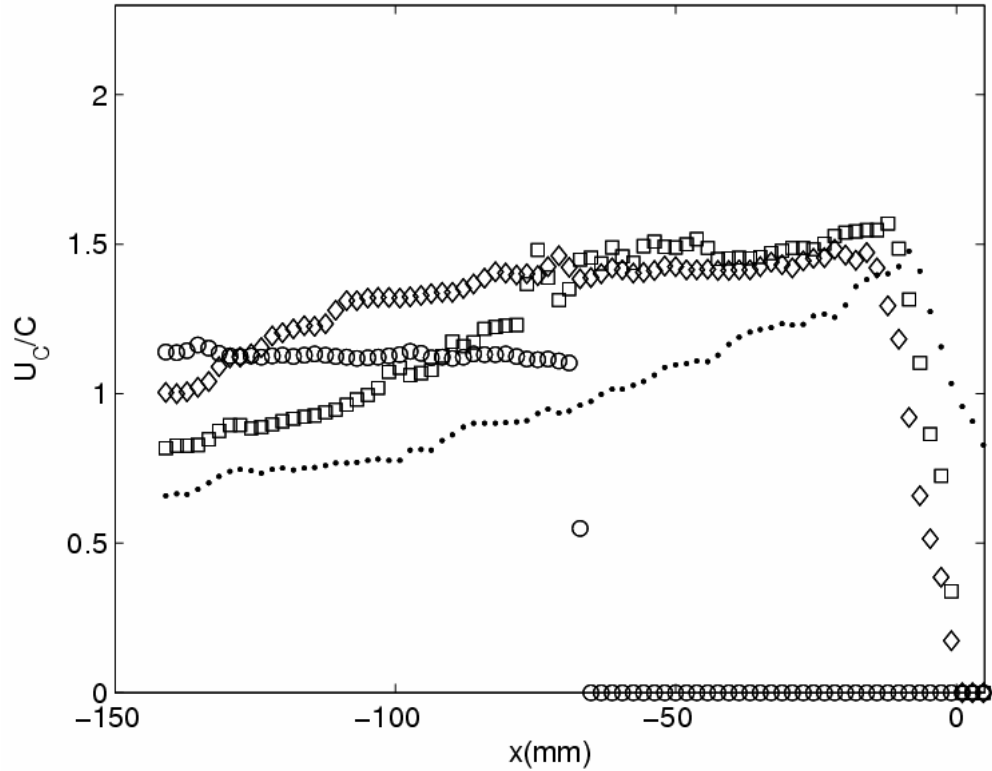
Figure 3.2: Cross sectional horizontal velocities along the *x* axis corresponding to Figures 3.1(a) to 3.1(d). "o", velocity in Figure 3.1(a); "◊", Figure 3.1(b); "□", Figure 3.1(c); "•", Figure 3.1(d).

3.2 Velocity Measurement Using BIV: Short Deck

Figure 3.3 shows the velocity fields measured using the BIV method. The length of the deck is 0.15 m long without the 0.22 m long extension section added (see Figure 2.2). The tested wave is the same as the one used for the PIV measurements. The field of view is shown in Figure 2.2 and denoted as FOV 2. The entire sequence of velocity field during the impinging and green water processes is demonstrated in the figure. Note that the velocity field is the mean velocity obtained from ensemble averaging 10 repeated instantaneous velocity measurements while the images were picked from one of the 10 realizations (i.e., the images are instantaneous).

Since the wave breaking process is highly turbulent, the instantaneous images do not match the mean velocities perfectly in some instants. Note that $t = 0$ in the figure represents the instant when the free surface of the wave was crossing the leading edge of the structure and overtopping the structure. All the 10 sets of the instantaneous velocity fields were matched at this moment so that errors in the ensemble average due to mismatch of the cases are minimized, if not eliminated. In addition, this determination of $t = 0$ is for the future comparisons with the dam break flow that has been widely applied to describe the green water effect without careful validation. Thus, the moments before $t = 0$ are denoted as negative time.

Figure 3.3(a) shows the moment right after the overturning jet touched its front water surface and before it touched the front wall of the structure. The jet velocity is moving downstream and mainly downward. After a short duration of 35 ms to Figure 3.3(b), the overturning wave impinged the structure front wall and splashed upward. At this moment a large part of wave was still moving horizontally towards the structure while the splashing jet was moving vertically upward. The process continued through Figure 3.3(c) until the wave momentum pushed the wave front to move forward onto the deck, as shown in Figure 3.3(d). At the same time right in front of the structure, when the wave momentum pushed part of the water to move upward, it also pushed part of the water to move downward and created a large vortex at around $z = 0$, started in Figure 3.3(c). The upward water did not touch the deck surface until the instant in Figure 3.3(e). The horizontal velocity on the deck was small initially until the water started to touch the deck. In Figures 3.3(f - g) the green water lost its vertical momentum and the velocity became completely horizontal. This motion could create a large horizontal force exerting on any objects located on the deck due to the large horizontal momentum of water. Since the deck is not long (and this is typically the case for an offshore platform), the green water on top of the deck passed the deck and moved downward back to the "ocean" quickly at the rear edge of the deck. The velocity of green water continued to move downstream but started to change to downward motion as seen in Figures 3.3(h - i). After that the green water quickly recessed and lost its momentum with the velocity being significantly reduced, as seen in Figures 3.3(j - l).
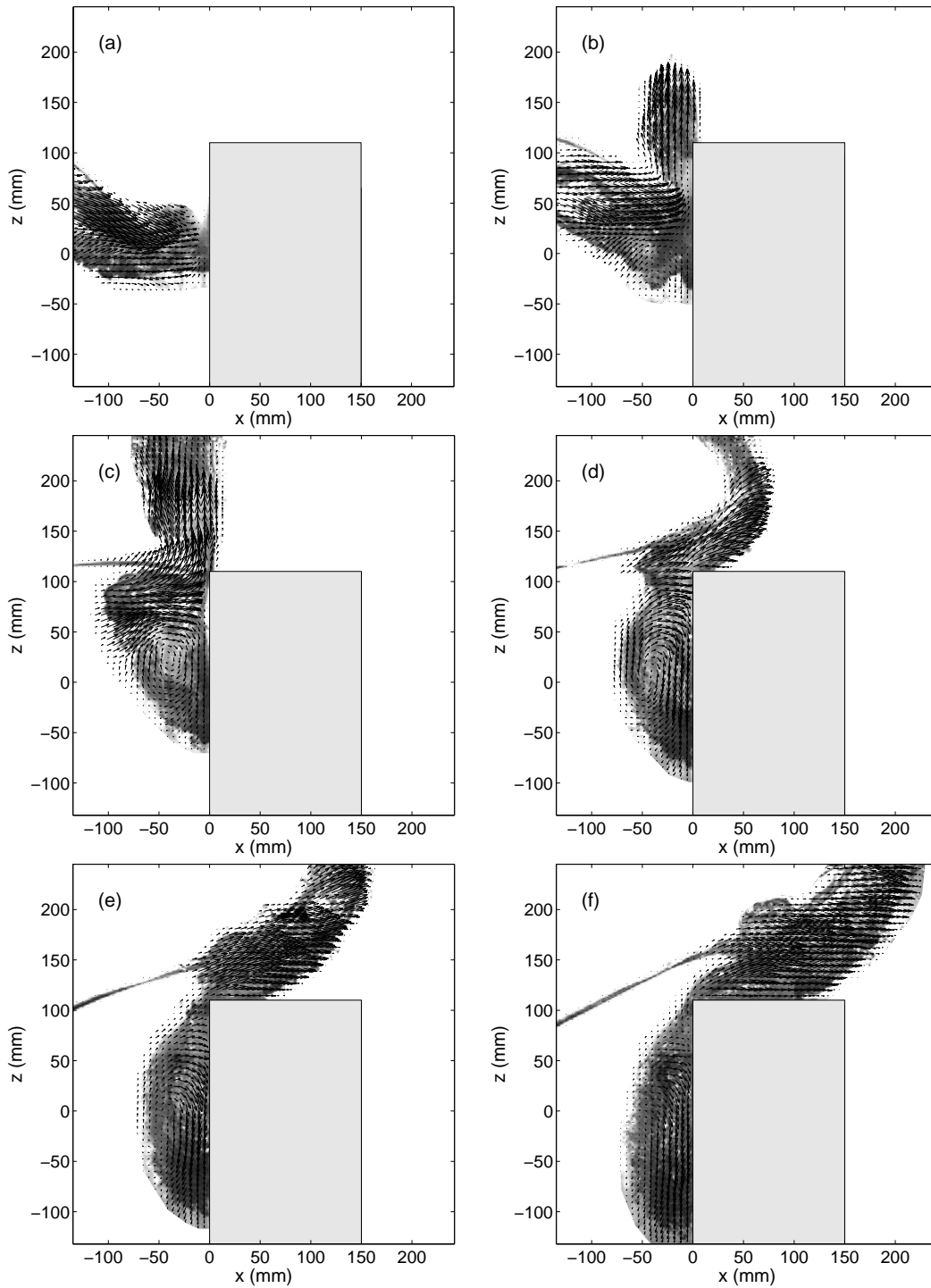
Figure 3.3: Mean velocity fields obtained by BIV at t = (a) -0.07 s, (b) -0.035 s, (c) 0.000 s, (d) 0.035 s, (e) 0.070 s, (f) 0.105 s, (g) 0.140 s, (h) 0.175 s, (i) 0.210 s, (j) 0.245 s, (k) 0.280 s, and (l) 0.315 s.
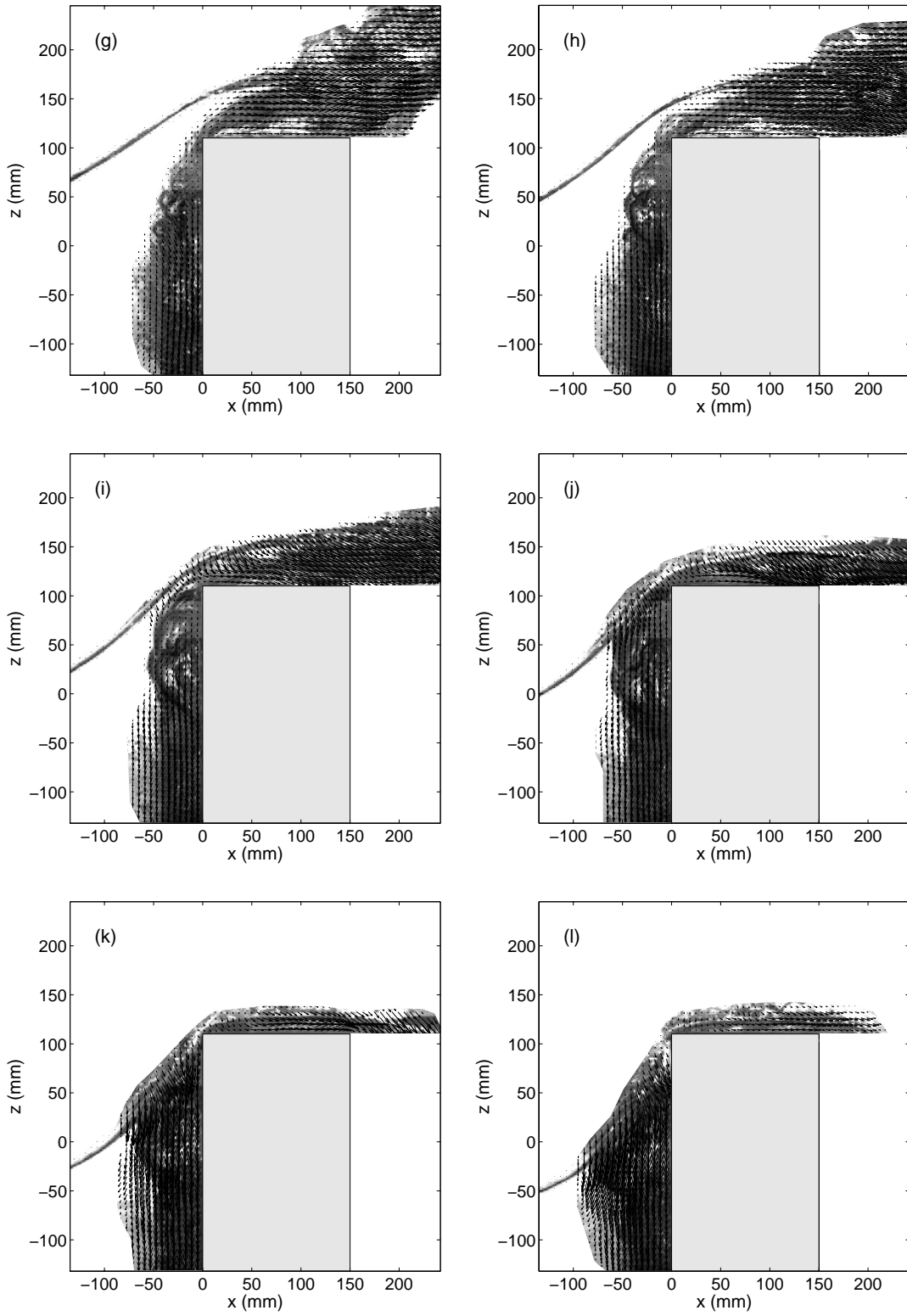
Figure 3.3 (Continued)

Figure 3.4 shows the profiles of cross sectional maximum horizontal velocity, U_C, of the green water with its velocity fields shown in Figure 3.3. The plot starts at $t = 0.035$ s because the horizontal momentum of the green water becomes dominant after this instant, as shown in Figure 3.3(d). Figure 3.4 displays the profile of U_C at five different instants with a time separation of 70 ms. The velocity along the deck has a non-linear behavior, different from the linear solution of a dam break flow (will be discussed later). Interestingly, the locations where the maximum cross-sectional velocity occurred is not at the front of the green water (but close) except at $t = 0.035$ s. One possible reason for such a trend is that the green water moved downward at the end of the deck and the momentum becomes vertical as shown in the velocity field in Figure 3.3. Note that $t = 0.035$ s is the instant before the green water reached the end of the deck. The maximum magnitude of U_C was about $1.05C$, indicating the maximum water speed of green water on the deck is approximately the phase speed or slightly higher than the phase speed. Since the green water passed the deck very fast (within 10 ms), it is very difficult to find a full flow pattern of the green water with the model structure. Thus, it may be necessary to conduct tests using a structure with a longer deck in order to better understand the behavior of green water.
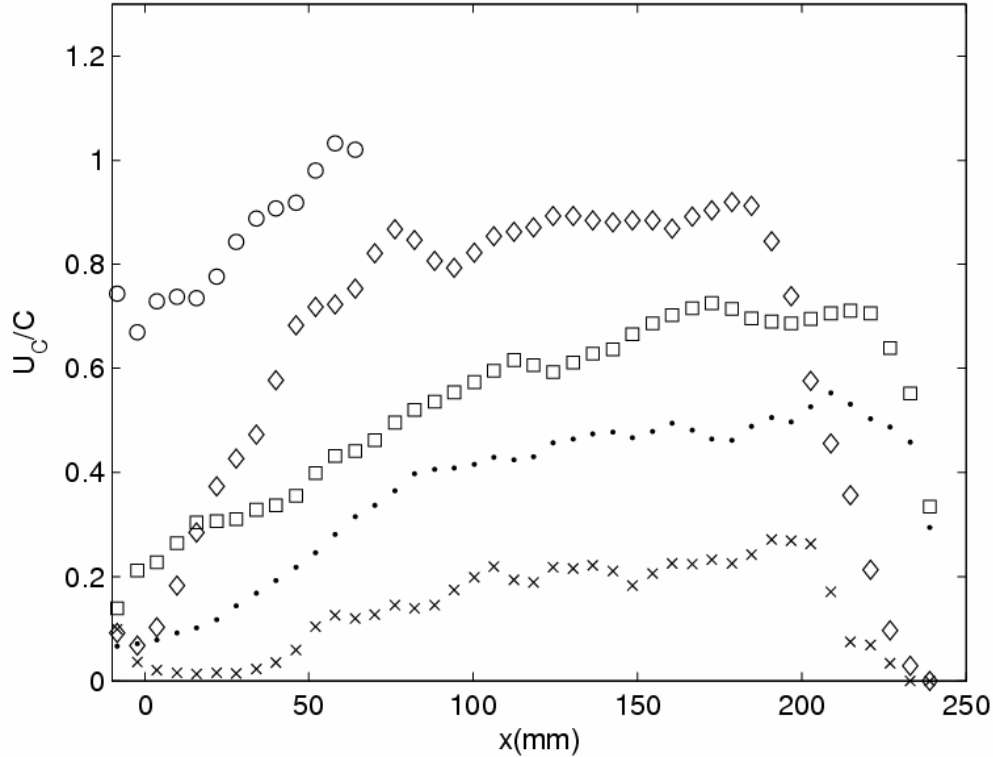
Figure 3.4: Cross-sectional horizontal velocity profiles of green water on the model with a short deck at time at t = 0.035 s (o), 0.105 s (◊), 0.175 s (□), 0.245 s (.), and 0.315 s (x).

3.3 Velocity Measurement Using BIV: Extended Deck

Figure 3.5 shows the velocity field of the same breaking wave as in Figure 3.1 impinging on the structure with the extended deck. Again, the BIV technique was used in the measurement and the newer high speed camera was employed in the image acquisition. The field of view is shown in Figure 2-2 and denoted as FOV 3. The case with the extended deck shows a similar velocity pattern as in the previous case without the extended deck until the moment when the wave is on the top of the deck. This means the velocities are very similar between and long deck and short deck cases before reaching the instant corresponding to Figure 3.3(h). The instant of Figure 3.3(h) corresponds to that between Figures 3.5 (k) and 3.5(l). Note that the time separation between the adjacent frames in Figure 3.5 is 20 ms while that in Figure 3.3 is 35 ms. Since the deck is long in this case, green water on top of the deck initially moved

downstream horizontally.   After the moment in Figure 3.5(k), the front of green water passed the end of the deck but continued to have dominant horizontal momentum, as shown in Figures 3.5(l - m).   Subsequently in Figures 3.5(n - p), the green water continued to move along the deck but started to move downward and back to the "ocean" at the rear edge of the deck.   After the moment in Figure 3.5(p), the green water recessed and lost its momentum, and showed a flow pattern similar to that in the case without the extended deck in Figures 3.3 (j - l).   The pattern of the velocity fields between the short and long deck cases looks very similar except that green water on the long deck stayed a longer period on the deck and the water on the deck moves with a dominant horizontal momentum.

We would like to point out that the measured velocity using BIV in Figure 3.5 is indeed mainly the bubble velocity for the highly aerated region in front of the structure, and the fluid (air-water mixture) velocity above the structure deck.   While we are more confident on the measured green water velocity above the deck due to its relatively minor effect of the buoyant force to the inertial force in that region, we are not sure whether the fluid velocity followed the air bubble velocity in the aerated region in front of the structure is correct.   The buoyant force may be significant in that region due to the relative low fluid velocity and the large bubble size.   This is especially true when large air bubbles were generated at certain phases.   From the images captured by the fast speed cameras, the bubble size reached nearly 5 cm in diameter during the period between Figures 3.5(m - n).
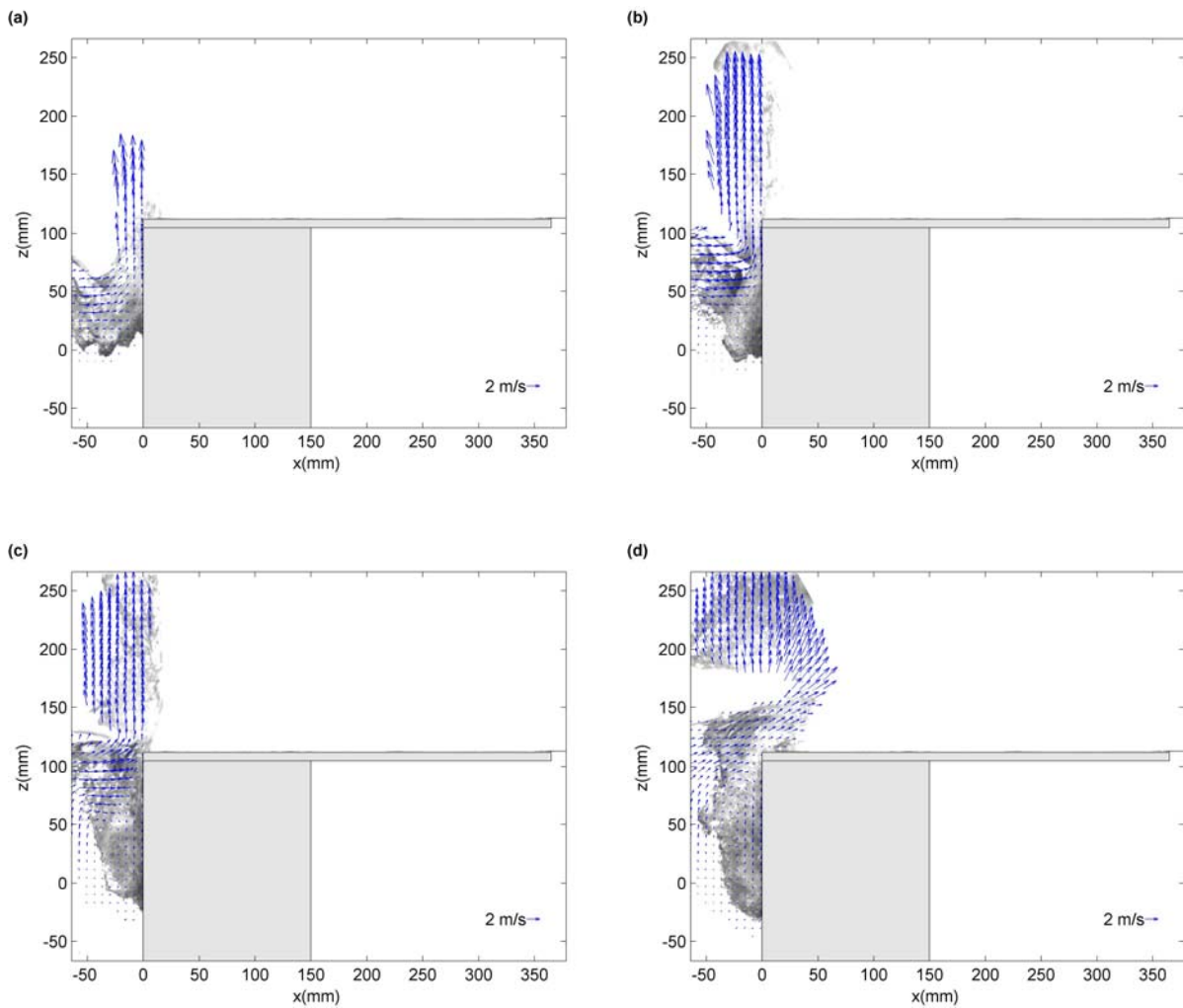
Figure 3.5: BIV measured mean velocity fields of a plunging breaking wave impinging on the model structure with the extended deck at t = (a) -0.04 s, (b) -0.02 s, (c) 0.00 s, (d) 0.02 s, (e) 0.04 s, (f) 0.06 s, (g) 0.08 s, (h) 0.10 s, (i) 0.12 s, (j) 0.14 s, (k) 0.16 s, (l) 0.18 s, (m) 0.20 s, (n) 0.22 s, (o) 0.24 s, and (p) 0.26 s.
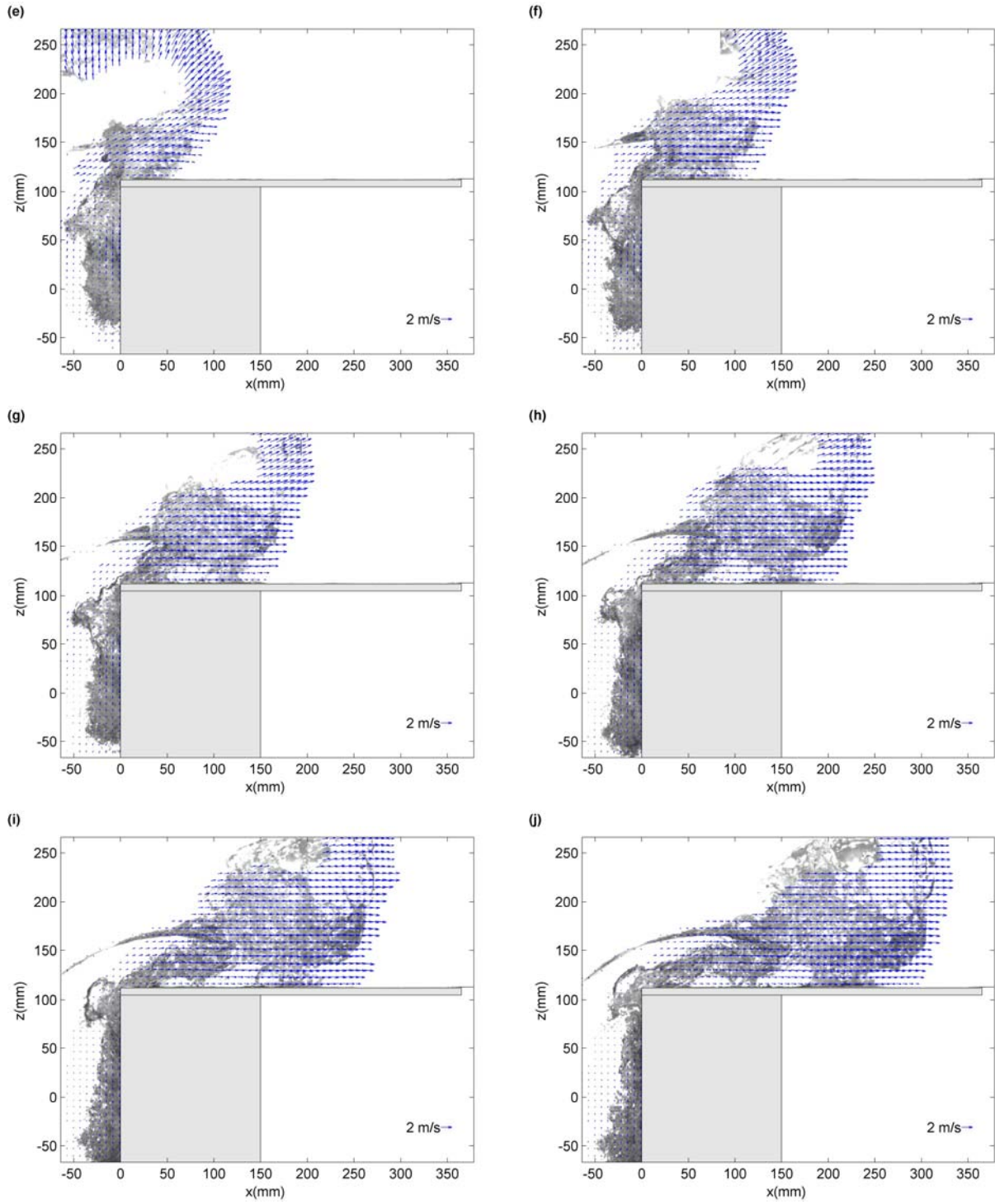
Figure 3.5 (Continued)
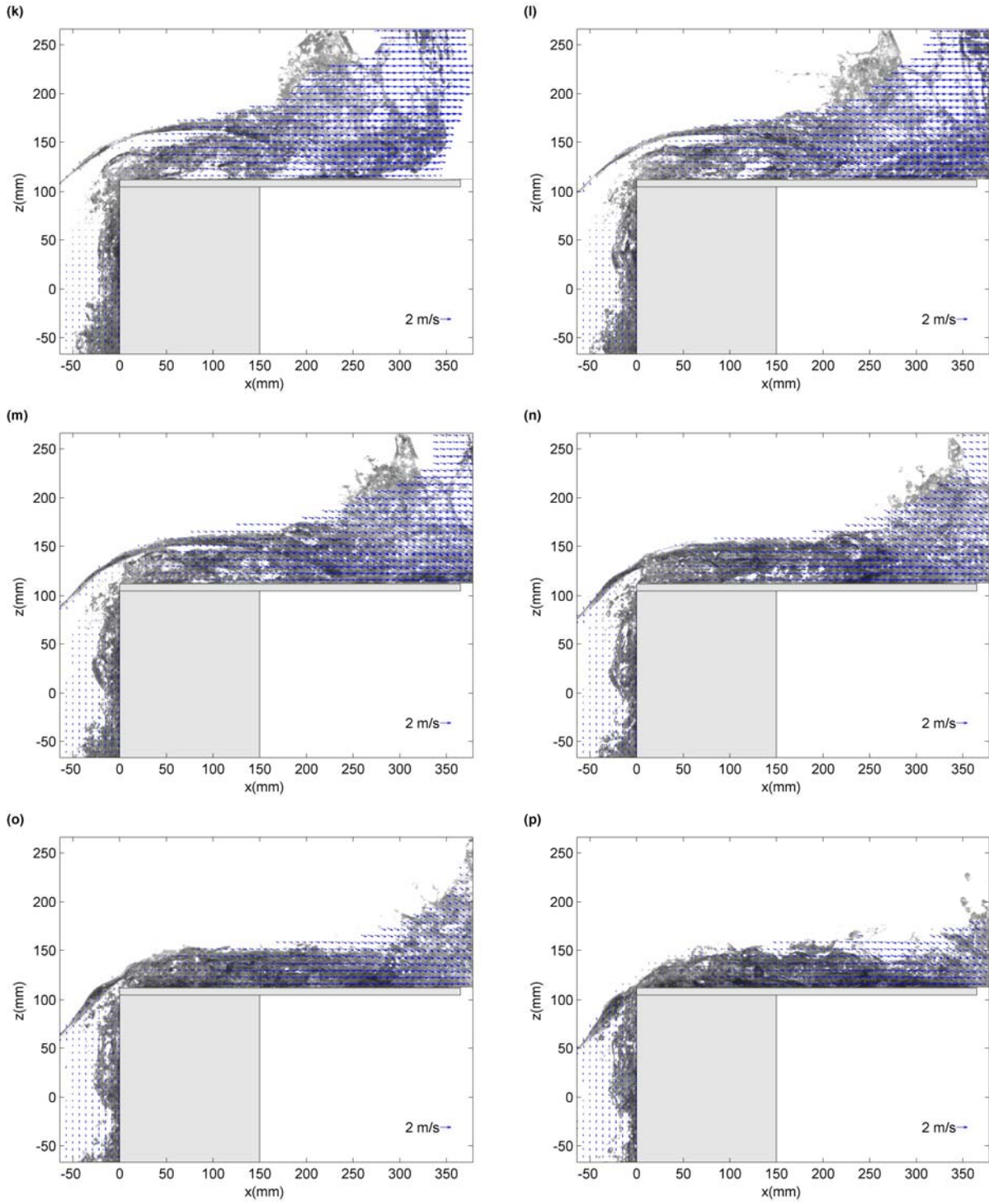
Figure 3.5 (Continued)

3.4 Green Water Turbulence Intensity

Figure 3.6 shows the turbulence intensity, I, corresponding to the flow field in Figure 3.5. The solid gray line indicates the mean free surface (by averaging the 20 instantaneous images). The instantaneous velocity can be decomposed into the mean quantity and turbulent fluctuations as

$$u_i = U_i + u_i'$$
(3.1)

where U_i is the mean velocity and u_i' the turbulent fluctuations. Since only two velocity components were measured, the turbulent intensity is defined as

$$I = \left\langle u'u' + w'w' \right\rangle^{1/2}$$
(3.2)

where u' and w' are the velocity fluctuations in the x and z directions, respectively. Every panel in Figure 3.6 has the maximum turbulence intensity, I_{max}, indicated in the panel. The largest I_{max} occurred at $t = -0.02$ sec in Figure 3.6(b) and the largest relative values of I_{max} (normalized by the maximum velocity in that panel) occurred during the period in Figures 3.6(a-d). During this short period when the splashing water moving upward after hitting the structure, the maximum vertical velocities reached more than 5.0 m/s in the measurements, or more than 2.5C (to be discussed later). By examining Figures 3.5 and 3.6, we found that the region with high turbulence intensity is near the front of the moving green water and coincident with the region with a high mean velocity.
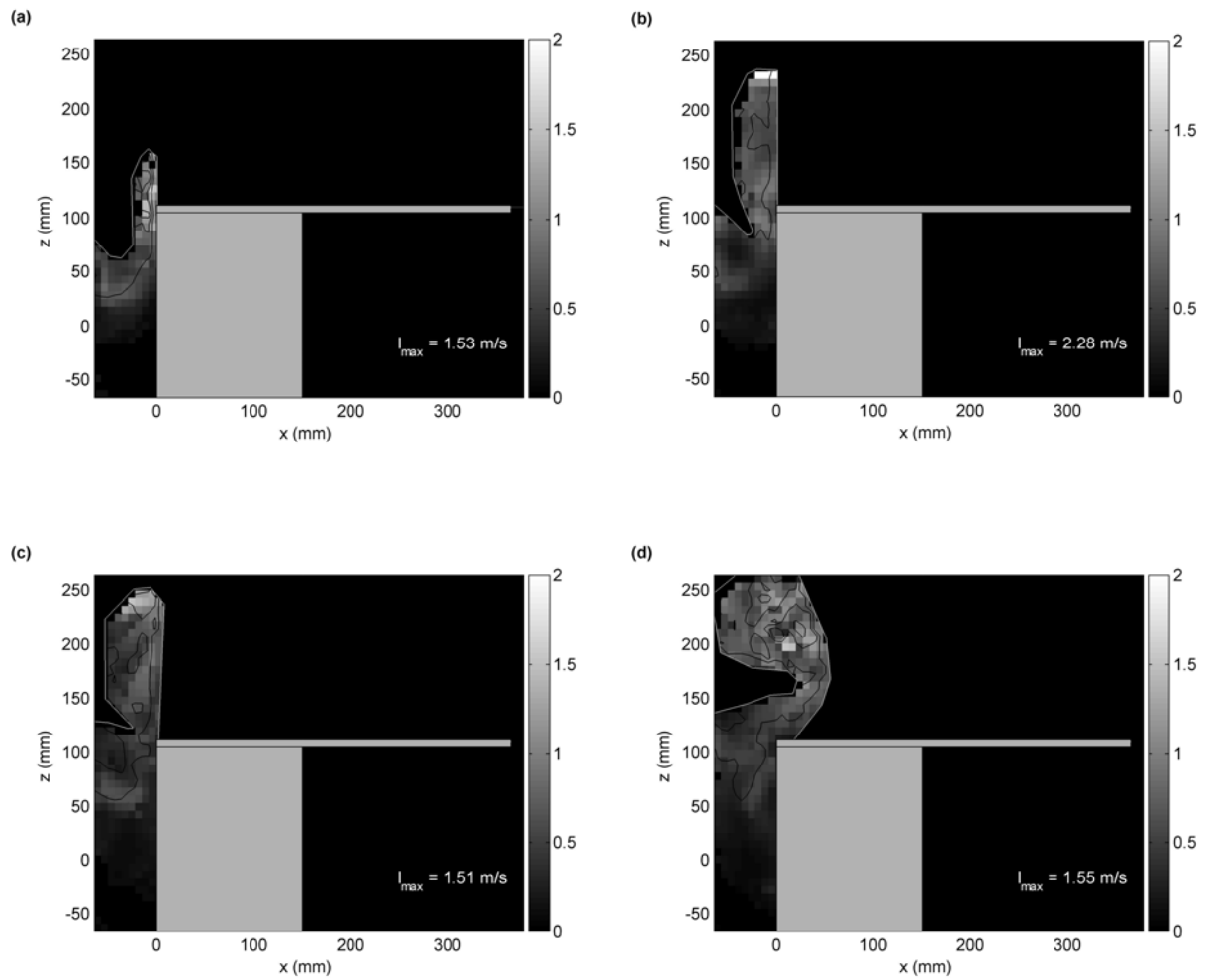
Figure 3.6: Turbulent intensity I (m/s) corresponding to the flow field in Figure 3.5. $t =$ (a) -0.04 s, (b) -0.02 s, (c) 0.00 s, (d) 0.02 s, (e) 0.04 s, (f) 0.06 s, (g) 0.08 s, (h) 0.10 s, (i) 0.12 s, (j) 0.14 s, (k) 0.16 s, (l) 0.18 s, (m) 0.20 s, (n) 0.22 s, (o) 0.24 s, and (p) 0.26 s.
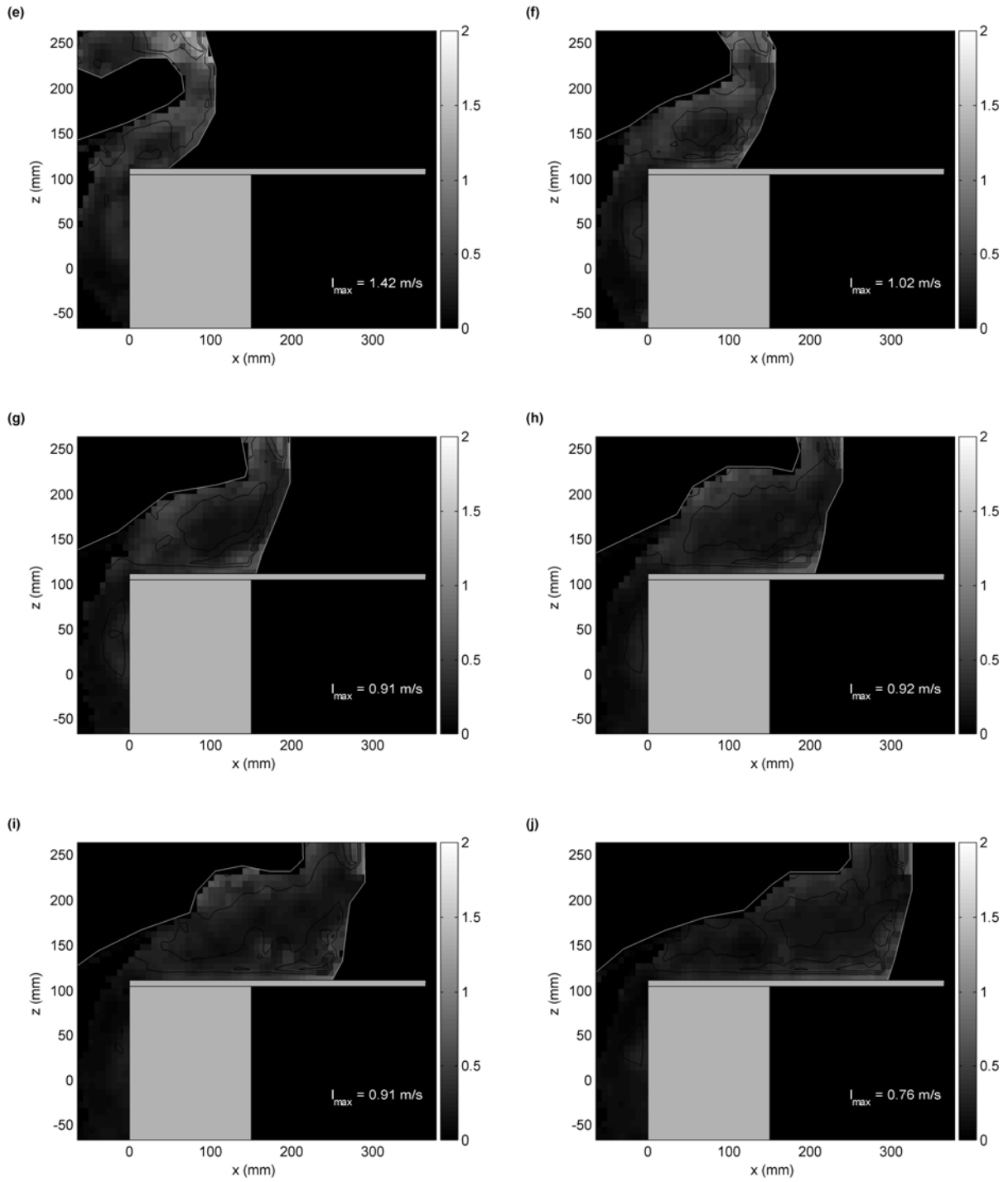
Figure 3.6 (continued)
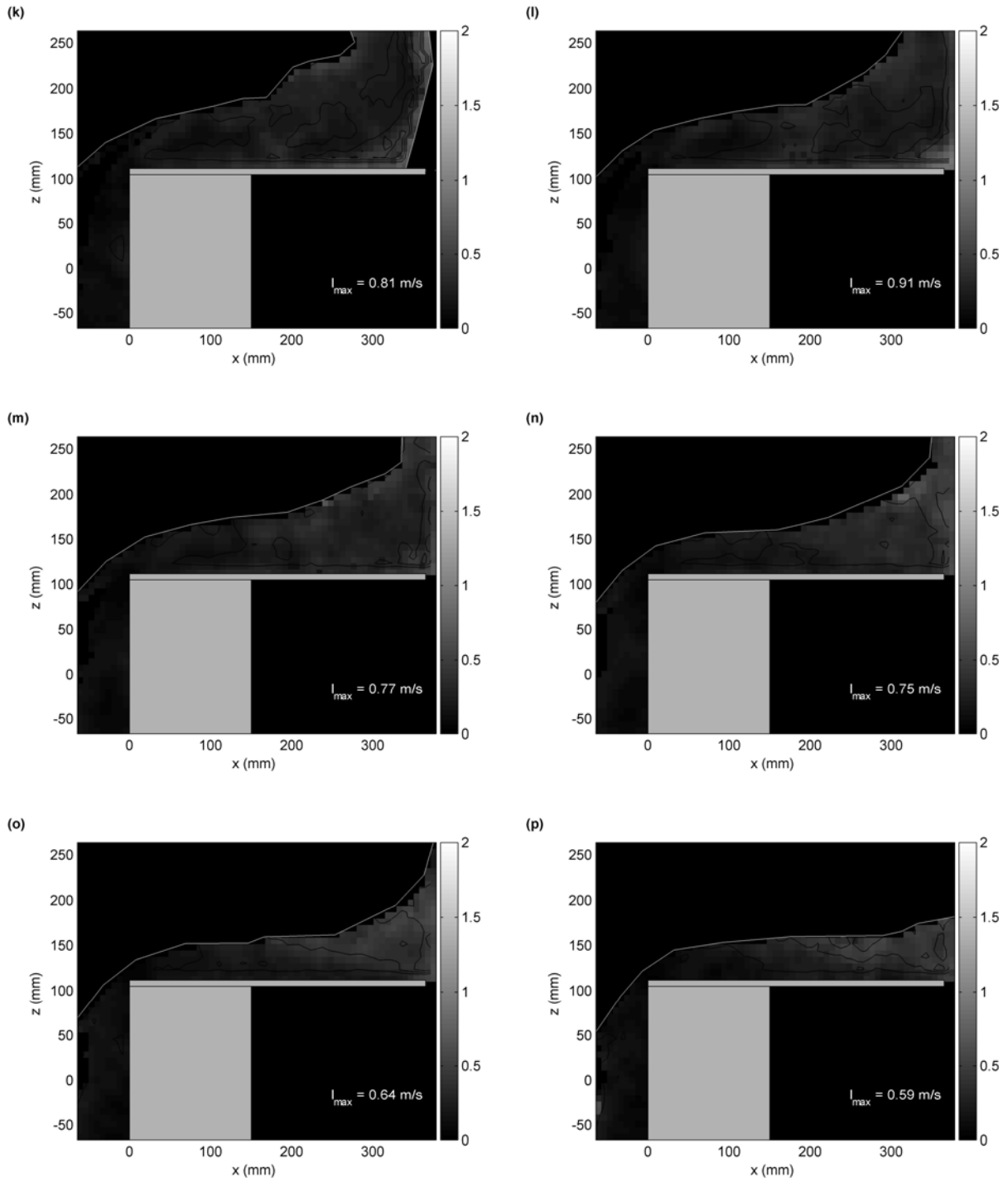
Figure 3.6 (continued)

Figure 3.7 shows the time history of I_{max} and the relative turbulence level obtained by normalizing with the maximum mean velocity, $\langle UU + WW \rangle^{1/2}_{max}$ at the same instant. The relative turbulence levels are somewhat uniform and between 40% and 50 % over entire measurement period except at the very beginning stages. A smaller relative turbulent level was resulted in near $t = -0.02$ s and $t = 0$ s due to the large mean velocity, even though the maximum turbulence intensity occurred at the same moments of about $t = -0.02$ s in Figure 3.6(b).
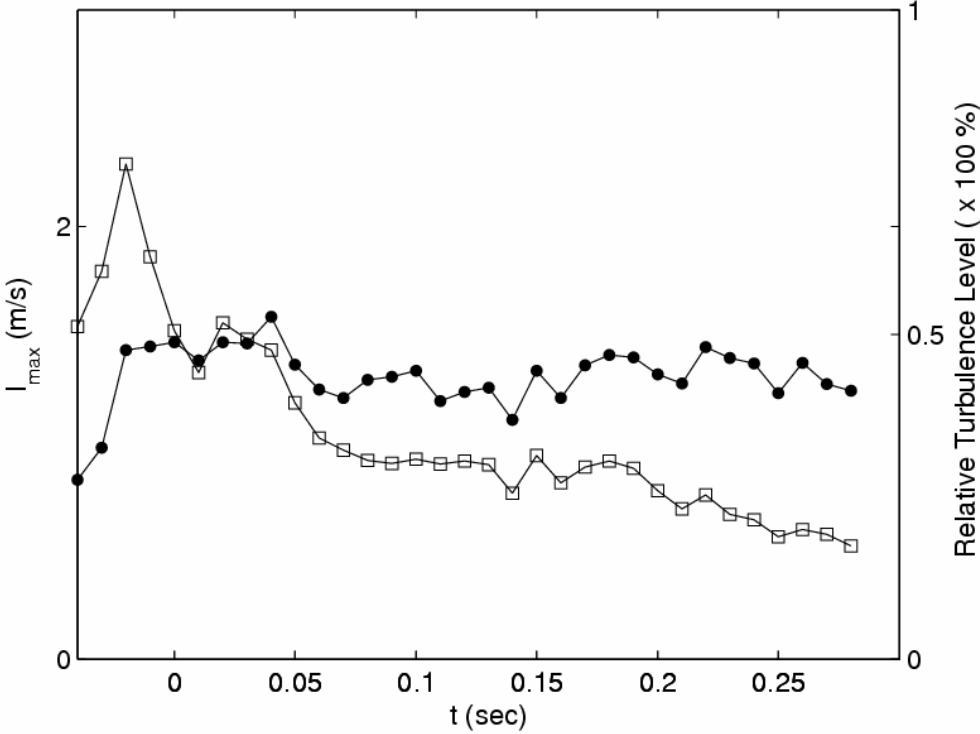
Figure 3.7: Maximum turbulence intensity and relative turbulence level (normalized by the mean velocity). -□-, I_{max} (m/s);   -•-, $\dfrac{I_{max}}{\langle UU + WW \rangle^{1/2}_{max}}$.

3.5 Green Water Velocity Profile and Dimensional Analysis
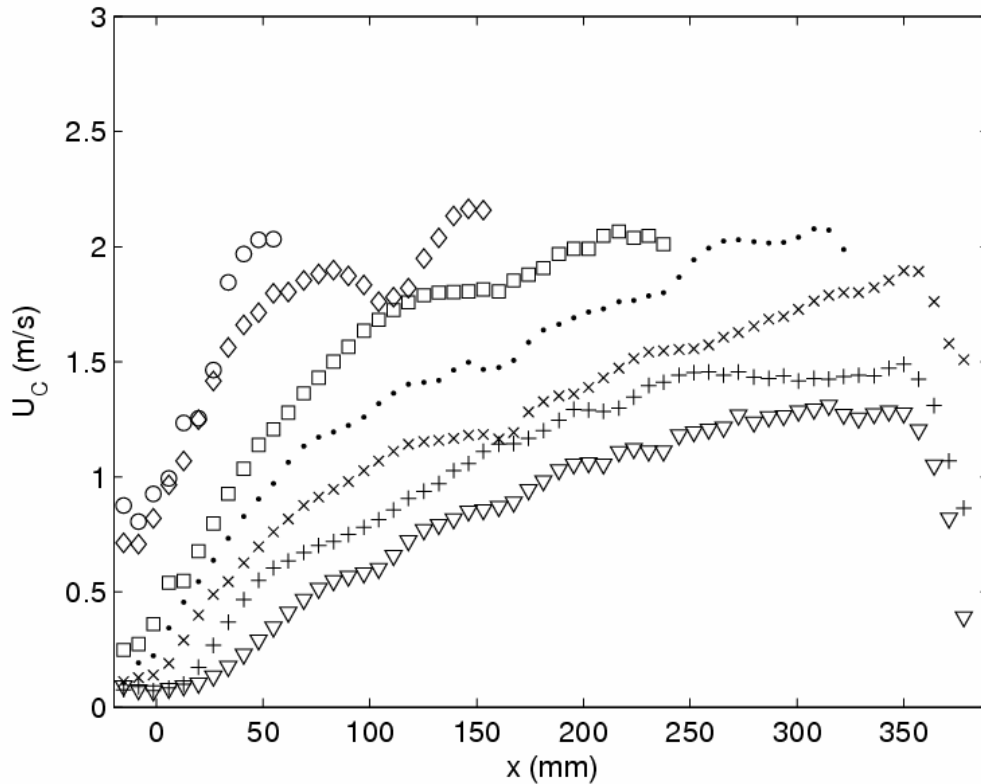
Figure 3.8: Cross-sectional velocity at time. $t = 0.02$ s (o), 0.06 s (◊), 0.10 s (□), 0.14 s (●), 0.18 s (×), 0.22 s (+), and 0.26 s (∇).

The profiles of cross sectional velocity of green water corresponding to Figure 3.5 are shown in Figure 3.8. Velocity profile after $t = 0.02$ s is plotted since horizontal momentum of green water became dominant after this instant, whereas the horizontal velocity before this moment was relatively small. Cross sectional velocity, U_C, is defined as the maximum horizontal velocity at a cross section (a vertical column) on the deck. The figure includes seven velocity profiles with a time separation of 40 ms between the adjacent lines. The velocity profiles along the deck show a non-linear distribution. It also gives the speed of the front of the

green water. As time increases, an asymptotic pattern started to show. At each time step, the largest velocity typically occurred near the front of the green wave while the smallest velocity at the leading edge of the deck, as shown in Figure 3.8. Therefore, the front of the rushing green water is expected to exert a significant impact force to any facility and equipment on the deck as it slams on them.

The maximum horizontal velocity at each time step in Figure 3.8 was almost constant until the wave front passed the end of the deck at $t = 0.16$ s. This indicates the front speed of green water is nearly constant.   After the front of green water passed the end of the deck (i.e., at $t = 0.16$ s), the maximum horizontal velocity decreased at a rapid rate while the maximum velocity on the deck occurred at almost a fixed located about 2 cm to 3 cm from the end of the deck (the length of the deck is 37 cm). This is because when the front of green water moved downward after passing the end of the deck the momentum becomes vertical, as shown in the velocity fields in Figure 3.5. However, as pointed out earlier in the case with a short deck, it is difficult to extract physical meanings of green water after $t = 0.16$ s when the front moved out of the deck. An extended deck length as the case studied here is therefore needed to analyze the green water effect.

In order to understand the physical process in the proposed problem using the measurements, dimensional analysis is performed.   The variables of interest are

$$U_C = f(x,t,h,U_M,C,g,T) \tag{3.3}$$

where x is the downstream distance from the deck leading edge, t time, h the water level on the deck, U_C the cross-sectional horizontal velocity, U_M the maximum horizontal velocity at a given time t, C the phase speed, g the gravitational acceleration, and T the wave period.   By dimensional analysis, the obtained non-dimensional parameters are

$$\frac{U_C}{U_M} = \phi\left(\frac{x}{Ct}, \frac{t}{T}, \frac{U_M}{C}, \frac{U_C}{\sqrt{gh}}\right) \tag{3.4}$$

Note that the fluid viscosity is neglected because of a large Reynolds number in the experiments.
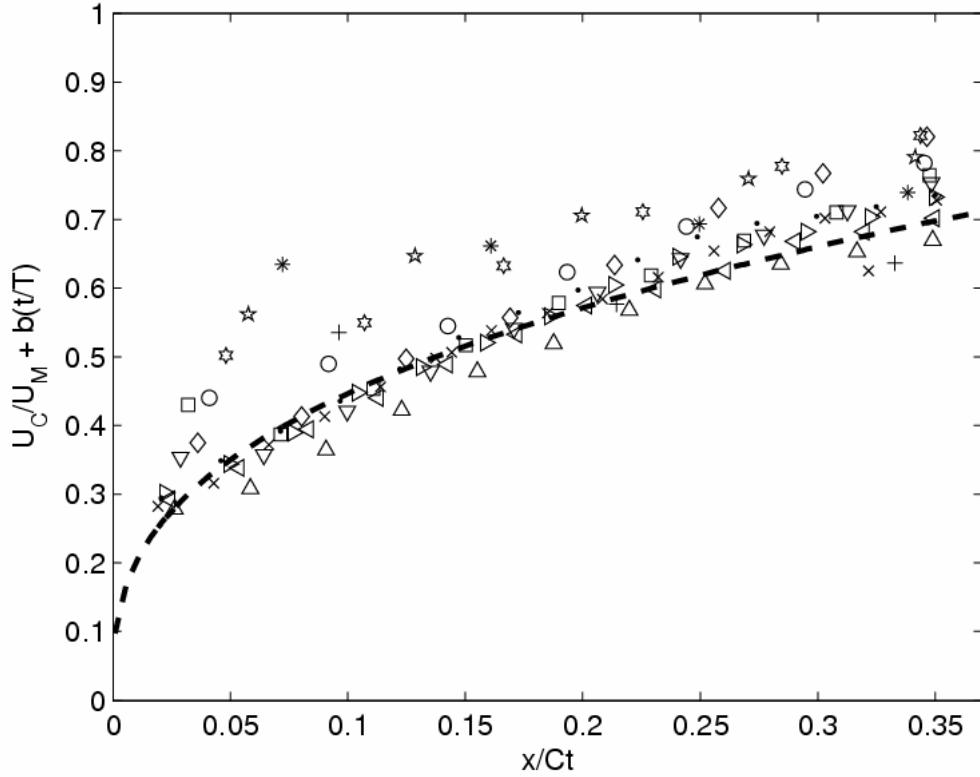
Figure 3.9: Similarity profile obtained using the non-dimensional velocity, time and distance. $t =$ 0.02(o), 0.03($\Diamond$), 0.04($\square$), 0.05(*), 0.06($\star$), 0.07($\maltese$), 0.08(∇), 0.09($\triangle$), 0.10($\triangleleft$), 0.11($\triangleright$), 0.12($\bullet$), 0.13($\times$), 0.14(*), and 0.15(+) s.   Dashed line is the fitting curve using least square regression.

Figure 3.9 shows the relation among the three non-dimensional parameters, $\dfrac{U_C}{U_M}$, $\dfrac{x}{Ct}$, and

$\dfrac{t}{T}$, that are the cross sectional velocity, downstream distance on the deck, and time.   If directly

plotting $\dfrac{U_C}{U_M}$ versus $\dfrac{x}{Ct}$, the normalized velocity profile against the non-dimensional distance

decayed at a fast rate.   Based on the fact that the relationship depends on time, the non-

dimensional time $\dfrac{t}{T}$ with a constant b, was added to $\dfrac{U_C}{U_M}$ to seek similarity profiles.   The

constant b is to adjust the change rate of $\frac{t}{T}$. The velocity profiles along the deck from the instant the wave rushed onto the deck with a significant horizontal momentum to the instant the front of green water reached the end of the deck, i.e., from $t = 0.02$ s to 0.15 s, are plotted in Figure 3.9. Since the non-dimensional cross-sectional velocity $\frac{U_C}{U_M}$ is normalized by the largest velocity measured at each time step, the profiles after $t = 0.15$ s might be normalized by the largest velocity above the deck, but not the largest velocity at the instance (which could be behind the deck and out of the FOV).

In Figure 3.10 we plot the maximum velocity U_M against time t, it is obvious that U_M decreased rapidly after $t = 0.15$ s, supporting the point we made above. However, it is very interesting to see the U_M is nearly constant during the entire period when the front of greenwater is on the deck (from $t = 0.02$ s to 0.15 s). The maximum velocity indeed fluctuates and tend to decreases slightly as time increases before $t = 0.15$ s. After that moment, the maximum velocity decreases rapidly. The value of U_M, with a unit of m/s, can be fitted linearly as

$$U_M = -0.23t + 2.20 \qquad\qquad \text{for } t < 0.15 \text{ s} \qquad\qquad (3.5)$$

in which the unit of t is in second. Since the dependence of the maximum horizontal velocity on time is insignificant, we can treat it as constant. The value of U_M is close to 2.20 m/s that is approximately $1.13C$. This maximum value is close to that in the short deck case of $1.05C$. In Figure 3.9, the results display good similarity over that period. Using curve fitting to fit a curve as $\frac{U_C}{U_M} + b\frac{t}{T} = a\left(\frac{x}{Ct}\right)^n + c$, we obtained the following coefficients: $a = 1.00$, $b = 1.20$, $c = 0.02$, $n = 0.37$. The similarity curve can therefore be expressed as:

$$\frac{U_C}{U_M} + 1.2\frac{t}{T} = \left(\frac{x}{Ct}\right)^{0.37} + 0.02 \qquad\qquad (3.6)$$
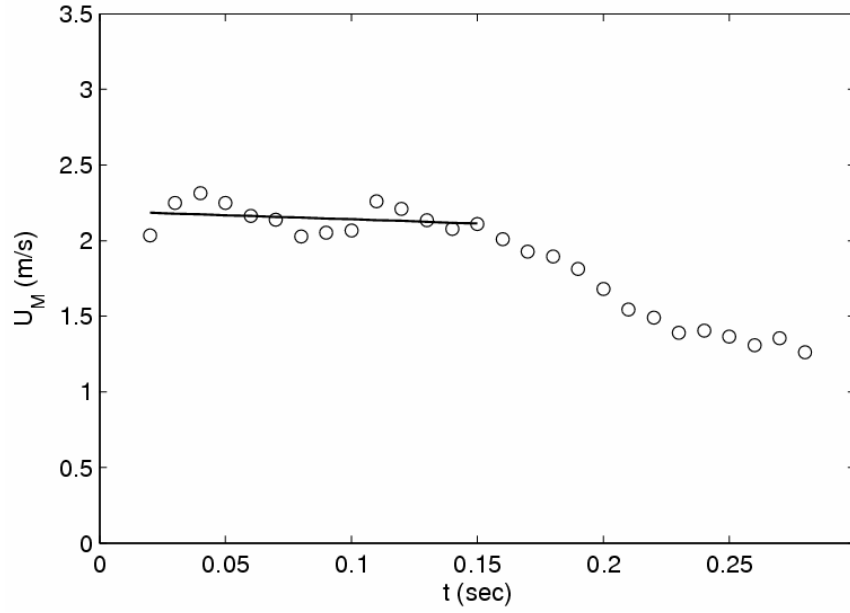
Figure 3.10: Maximum horizontal velocity U_M against time t.   Solid line: regression fit.
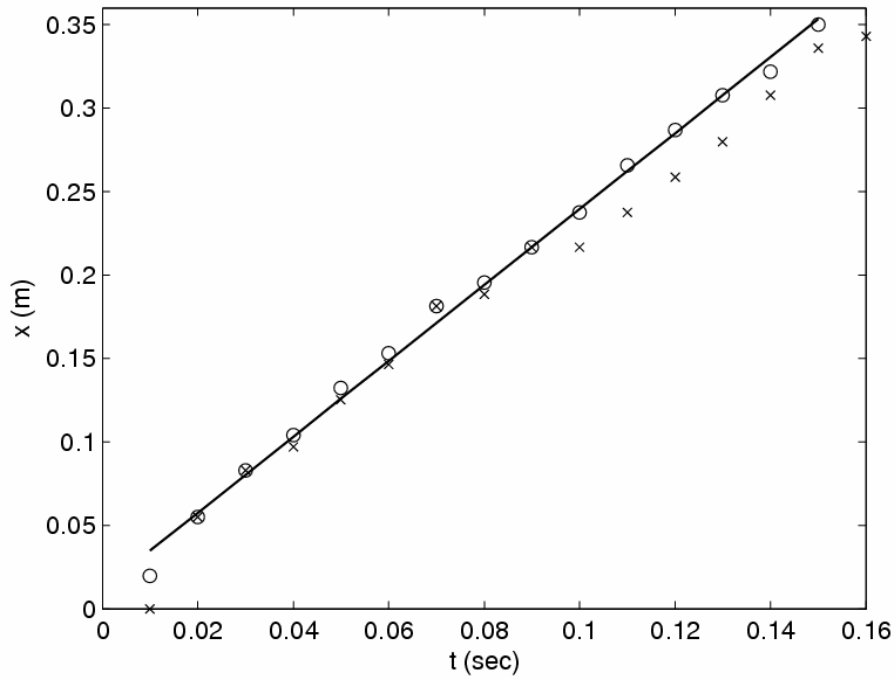
Figure 3.11: Locations of wave front and maximum horizontal velocity (U_M).   "o", wave front; "×", U_M; solid line, curve fitting of wave front.

Figure 3.11 shows the location of the front of green water and the location of the maximum horizontal velocity, U_M. The figure shows U_M occurred near the front of green water and the locations of U_M and the front of green water are almost identical except that U_M was slightly lag behind the front when the front was approaching the end of the deck and the horizontal momentum was about to change to vertical. The location of the wave front as a function of time shows linear behavior. Using linear regression a slope of 2.27 (unit m/s) was obtained. That means the front velocity of green water is constant as 2.27 m/s ($\approx 1.16C$), which is in agreement with the value of $U_M = 2.20$ m/s ($\approx 1.13C$) before $t = 0.15$ s.

From Figure 3.5 we can see the velocity on the deck varied as a function of the location and time. A prediction equation is thus proposed to model the velocity profile on top of the deck as a function of time and space. From equation 3.5 and Figure 3.10, the maximum velocity U_M at each time step is approximately constant and close to the front velocity of green water. We hereafter use the front velocity to replace U_M to simplify the prediction model. Based on a constant U_M and following equation 3.6, an equation for cross-sectional velocity U_c can be obtained as

$$U_C = 1.1C \left[\left(\frac{x}{Ct} \right)^{0.37} - 1.2\frac{t}{T} + 0.02 \right] \tag{3.7}$$

Equation 3.7 is the prediction equation for green water on the deck. Note that this equation based on the similarity profile found from the experimental data (shown in Figure 3.9). The equation is valid from the moment when water rushes onto the deck and momentum changes from primarily vertical to primarily horizontal to the moment the front of green water falls back to the ocean at the end of the deck. The period is the period covered by the fitted lines in Figures 3.10 and 3.11. After that period, U_c decreases rapidly, as implied in Figure 3.10 ($U_c \leq U_M$).

Although the front velocity used for the maximum velocity U_M in the equation is obtained from the moments between $t = 0.02$ and 0.15 s, the same velocity was used for the prediction after $t = 0.15$ s. Since the measurements did not cover the region behind the end of the deck while the sudden decrease in the horizontal velocity is expected to occur due to the fall of the wave after

reaching the end of the deck, it is not appropriate to decide the maximum velocity from the measurements. Since the maximum velocity is approximately constant when the front was on of the deck, we guess the maximum velocity would continue to be constant if the deck is longer. Therefore, after $t = 0.15$ s, we keep the same maximum velocity as that at $t < 0.15$ s.

3.6 Prediction of Green Water and Comparison with Dam Break Flow

The green water prediction equation (equation 3.7), obtained through dimensional analysis and based on a similarity profile and curve fitting to the experimental data, will be tested using the experimental data. The experimental is the velocity measured using BIV and shown in Figure 3.5. Since the dam break flow has been used by industry to predict green water, the result of dam break flow will also be tested against the experimental data. A dam break flow is typically governed by the Saint Venant equations with the assumptions of the flow being one-dimensional with a uniform velocity distraction over the depth and hydraulic static pressure. The classic and widely used analytical solution of dam break flow is Ritter's solution. Ritter's solution for velocity profile can be expressed as

$$u = \frac{2}{3}\left(\sqrt{gh_0} + \frac{x}{t}\right) \tag{3.8}$$

where u is the horizontal velocity, g the gravitational acceleration, and h_0 the initial water depth of the reservoir. By examining equation 3.8, the velocity is obviously strongly depends on the initial depth h_0, and the velocity is singular at $t \to 0$ (except at $x = 0$).

Since the green water problem does not have a well-defined h_0 in equation 3.8, we need to estimate this crucial value. Two different approaches were used in the estimations. Firstly, we assume perfect wave reflection at the deck to estimate the height of water above the free board of the deck. Under linear wave assumption, the wave elevation of a perfectly reflected as the structure equals to the wave height of the incoming waves. The initial water depth can therefore be express as

$$h_0 = H - z_{deck} \tag{3.9}$$

in which H is the incoming wave height in deep water and z_{deck} is the free board elevation from the still water surface. The tested wave has a wave height of about 17.0 cm in deep water, as shown in Figure 2-3, and a free board of 11.0 cm. We therefore estimate the first initial depth h_0 = 6.0 cm.

Secondly, we assume the front velocity of the dam break flow matches the front velocity of green water. With this assumption we can back calculate h_0 using the measured front velocity of green water. The front velocity of green water is nearly constant and approximately equal to $1.16C$, obtained from Figure 3.11 and discussed previously. Since the front velocity of dam break flow in Ritter's solution is $2\sqrt{gh_o}$, we let $V_{FG} = 2\sqrt{gh_0}$ with V_{FG} being the front velocity of green water. The initial depth can thus be easily calculated as $h_0 = \dfrac{V_{FG}^2}{4g}$. Since $V_{FG} \approx 1.2C$ from the laboratory measurement, The initial depth can be rewritten as

$$h_0 = 0.36\frac{C^2}{g} \tag{3.10}$$

in which C is the wave phase speed. Using equation 3.10 and the wave phase speed of 1.95 m/s, h_0 is calculated as 14.0 cm. Note that this value is more than twice that obtained using equation 3.9.

The comparison of cross-sectional velocities among the experimental data, the prediction model (equation 3.7), and Ritter's solution (equation 3.8) is shown in Figure 3.12. Note that the end of the data and lines in the figure indicates the location of the front of green water. Both h_0 values from Equations 3.9 and 3.10 are plotted for Ritter's solution in the figure. In addition to the determination of the initial water depth h_0 in Ritter's solution, it is also necessary to determine at what instant the green water process starts corresponds to the instant of dam removal for the dam break flow (i.e. $t = 0$). As explained earlier, $t = 0$ for green water process represents the instant when the free surface of the wave overtopping the structure and across the leading edge of the structure (Figure 3.3(c) and Figure 3.5(c)). After $t = 0$, the wave momentum pushed the wave front to move forward onto the deck and momentum started to change to horizontal as shown in Figures 3.3(d) and 3.5(d).

From the comparison, we found that the result from the prediction model (equation 3.7) agrees with the measured green water velocities fairly well at all the instants expect near the end of the deck where water falling back into the ocean. On the other hand, Ritter's solution gives a linear line for the velocity predict while the measurement data show otherwise. It seems that Ritter's solution under predicts the green water velocity from the beginning until around $t = 0.14$ s (corresponding to Figures 3.12(a) to (g)), regardless which method was used for h_0. However, it does predict the front velocity of the green water reasonably well, especially the one using equation 3.10 for h_0. Note that $t = 0.15$ s was the instant when the front of green water reached the end of the deck. This means the Ritter's solution under predict the green water velocity until the moment the front of the water reached to the end of the deck. The comparison also shows that using equation 3.10 for h_0 estimation may give a better prediction of green water velocity if Ritter's solution is to be used. After the front of green water passed the end of the deck (corresponding to Figures 3.12(h) to (l)), the result from the prediction model (equation 3.7) again agrees very well with the measured data. Ritter's solution, however, either over predicts the velocity, if equation 3.10 is used for h_0, or under predicts if equation 3.10 is used.

Overall, all three predictions result in a reasonable "engineering accuracy" in practical application, while the present prediction model gives the best agreement, followed by Ritter's solution with equation 3.10 for h_0. Although there is some discrepancies at some times and regions and weakness in describing the non linear behavior of the green water velocity, the prediction by Ritter's solution can be considered to be competitive giving the advantage of its simple form and universal recognition. Interestingly, Ritter's solution does not agree well with the experimental measurement of a real dam break flow in velocity prediction (Lauber, 1997). The main reason is that while the solution has a constant front velocity, the real flow does not. The measured front velocity in Lauber's study reached the same constant front velocity in the Ritter's solution at an instant after the dam was removed and velocity decreased. On the contrary, the green water experiments did show that the front velocity is nearly constant with only an insignificant variation along the deck. This would be the reason for the agreement between Ritter's solution and the green water measurements.
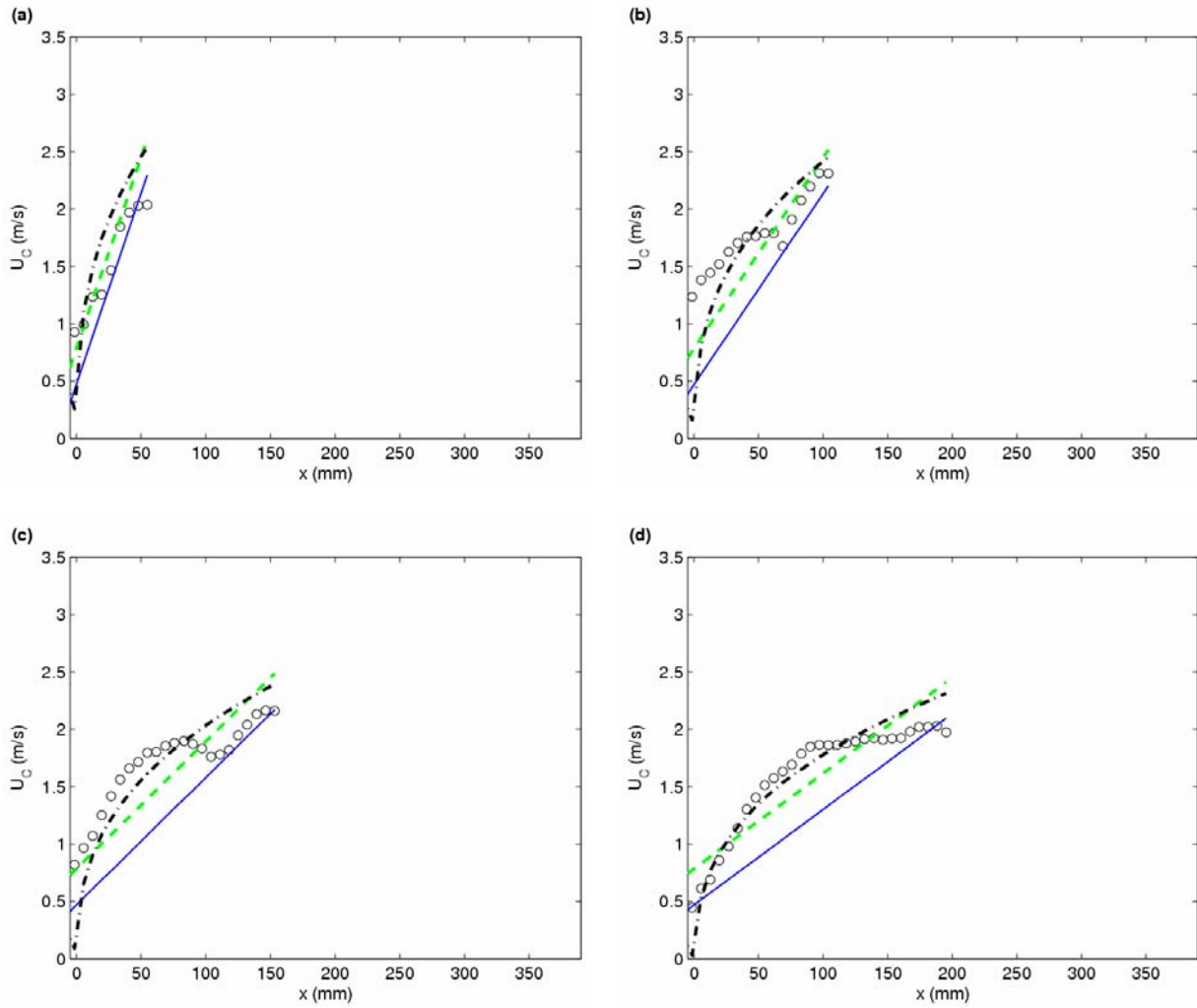
Figure 3.12. Comparisons of cross sectional horizontal velocity U_c along the deck among the experimental data (velocity measured using BIV and shown in Figure 3.5), the prediction equation (equation 3.7), and the analytical solution of dam break flow (Ritter's solution in equation 3.8). Time $t =$ (a) 0.02 s, (b) 0.04 s, (c) 0.06 s, (d) 0.08 s, (e) 0.10 s, (f) 0.12 s, (g) 0.14 s, (h) 0.16 s, (i) 0.18 s, (j) 0.20 s, (k) 0.22 s, and (l) 0.24 s. Solid line, Ritter's solution with $h_0 =$ 6.0 cm (obtained using equation 3.9); dashed line, Ritter's solution with $h_0 =$ 14.0 cm (obtained using equation 3.10); dashed-dotted line, prediction equation.
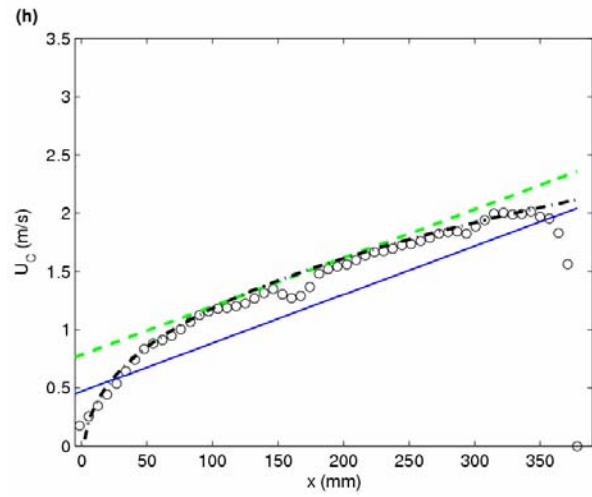
Figure 3.12: (Continued)
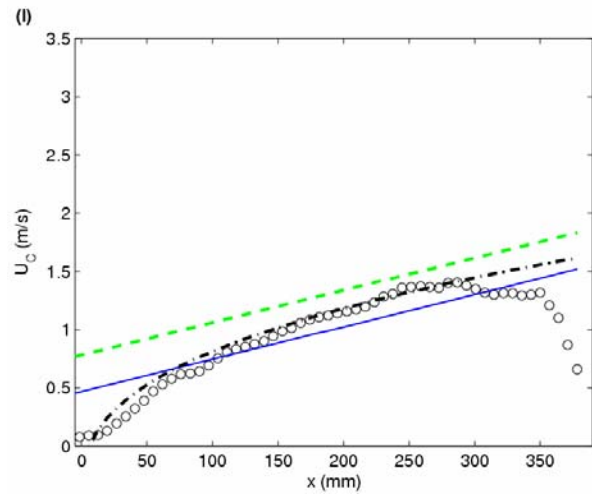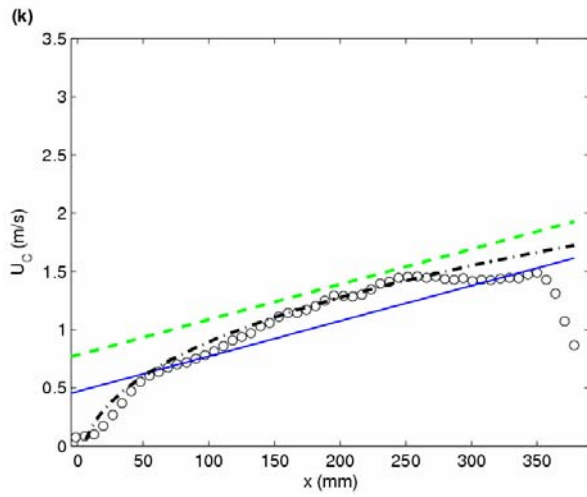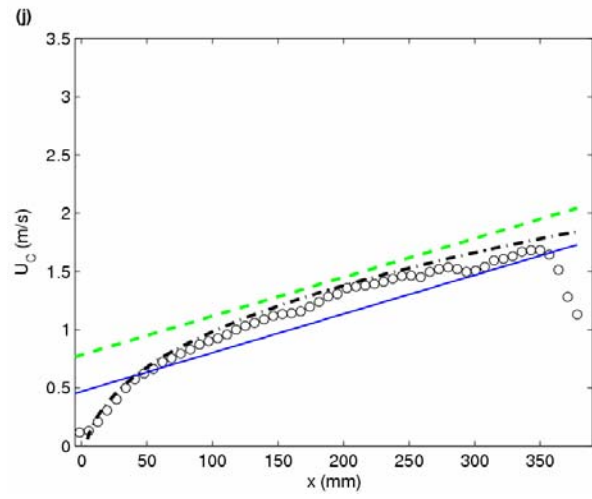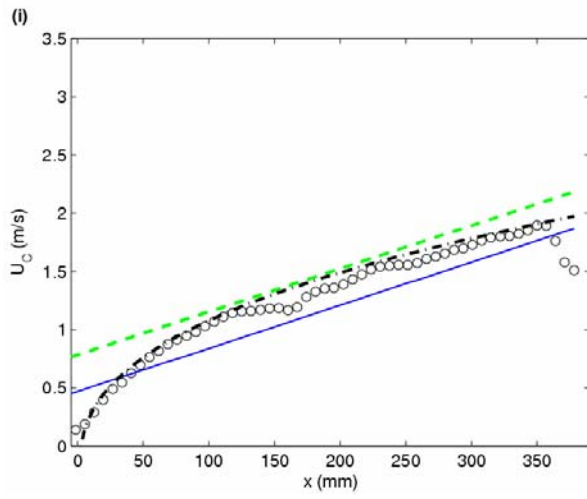
Figure 3.12: (Continued)

Figure 3.13 shows the time history of the green water velocity at different locations along the deck. All the results in Figure 3.12 are presented in Figure 3.13, including the BIV measurements, results from the prediction model (equation 3.7), and results from Ritter's solution (equations 3.8 to 3.10). Note that first panel (Figure 3.13(a)) represents the location close to the leading edge of the deck while the last one (Figures 3.13(l)) locates right outside of the deck (the deck length is 370 mm). Therefore Figure 3.13(k) represents the last point on the deck. Similar to the results in Figure 3.12, the prediction model shows very good agreements for all locations except at the locations very close to the end of the deck (Figures 3.13(j) and (k)) and outside of the deck (Figure 3.13(l)). On the other hand, Ritter's solution does a poor job in the prediction at the locations close to the leading edge of the deck, and gradually improves downstream, and becomes reasonable at locations closer to the end of the deck. It is perhaps due to the nature of the solution. Ritter's solution gives a distinct shape from the measurements in Figures 3.13, especially when the location is close to the leading edge of the deck. As the location away from the leading edge, Ritter's solution with h_0 obtained from equation 3.10 over predicts the velocity, while solution with h_0 obtained from equation 3.9 under predicts. However, the magnitude of the front velocity of green water is quite close to the measurement. Since the front velocity may cause most damage, this again implies Ritter solution does provide "engineering accuracy" with a acceptable prediction. The same conclusion was only founds when analyzing Figure 3.12.
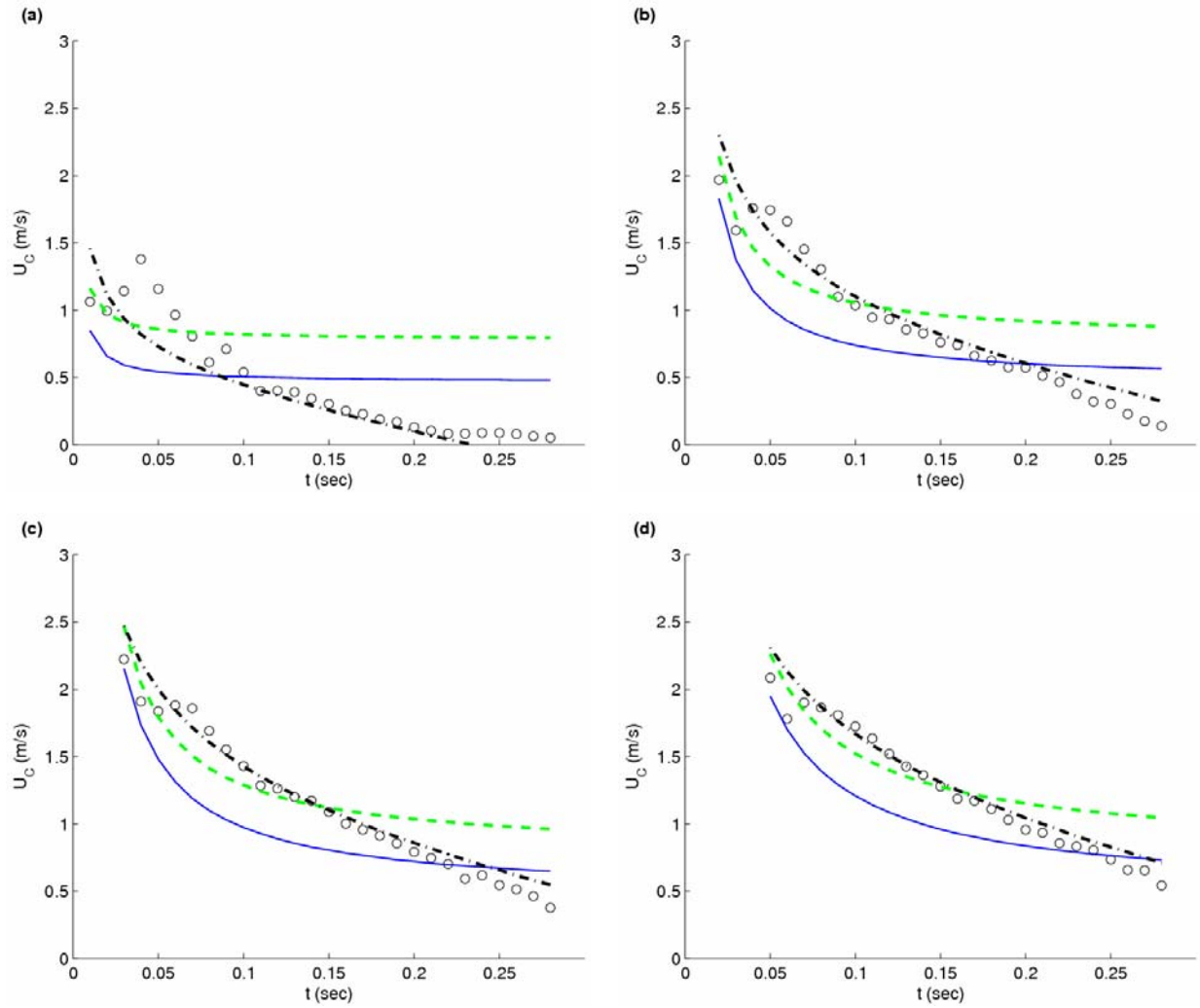
Figure 3.13. Time history of horizontal velocity of green water at x = (a) 5.7 mm, (b) 40.8 mm, (c) 75.9 mm, (d) 111.1 mm, (e) 146.2 mm, (f) 181.3 mm, (g) 216.5 mm, (h) 251.6 mm, (i) 286.7 mm, (j) 321.8 mm, (k) 356.9 mm, and (l) 378.0 mm. "o", BIV measurements, solid line, Ritter's solution with h_0 = 6.0 cm (obtained using equation 3.9); dashed line, Ritter's solution with h_0 = 14.0 cm (obtained using equation 3.10); dashed-dotted line, prediction model (equation 3.7).
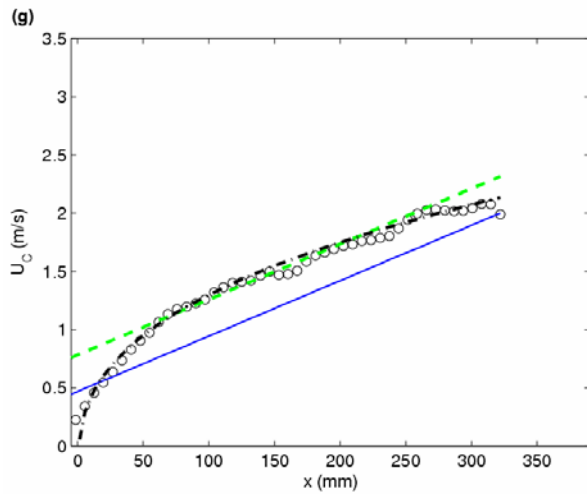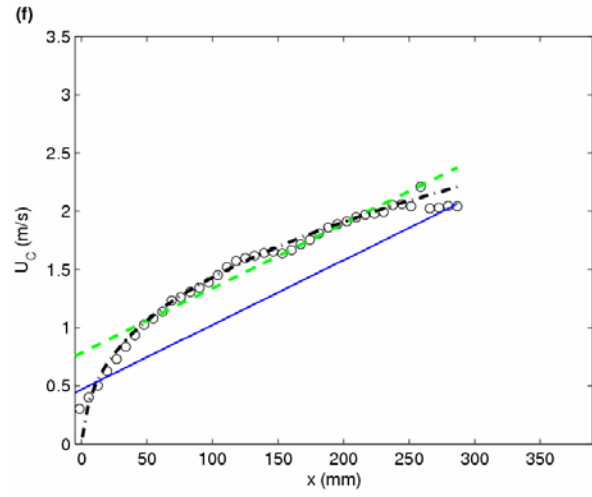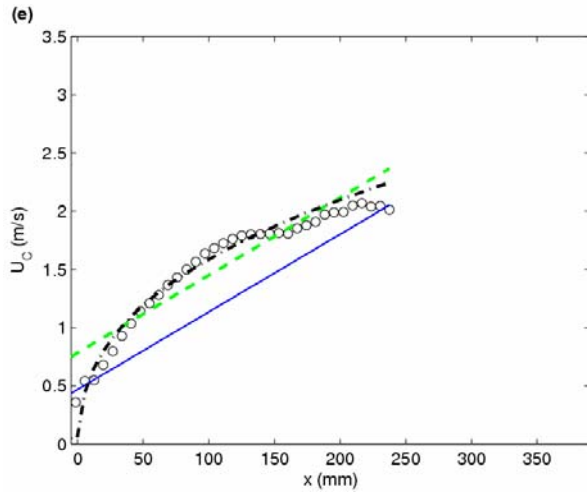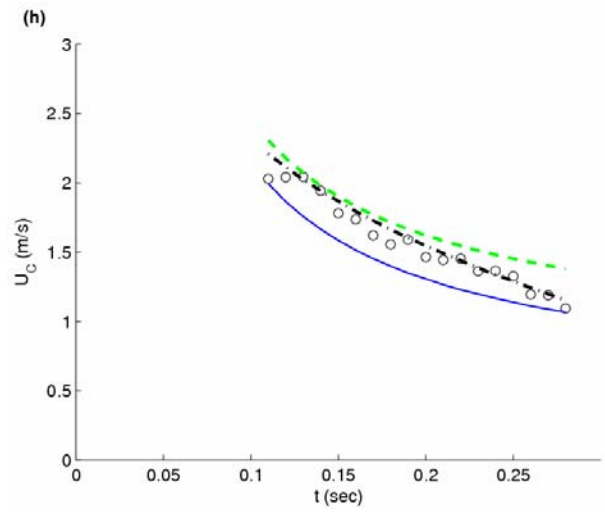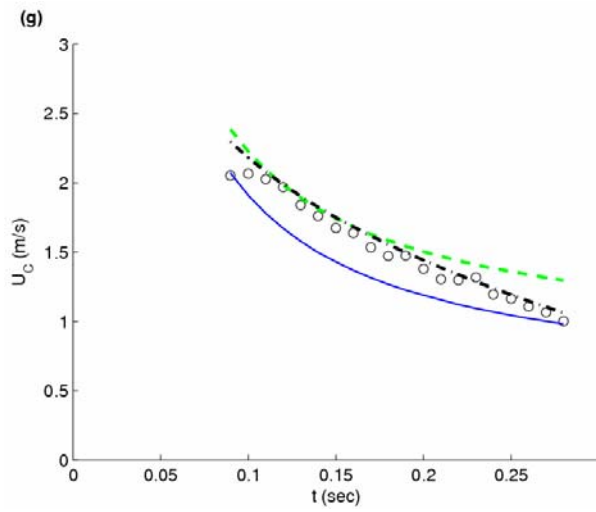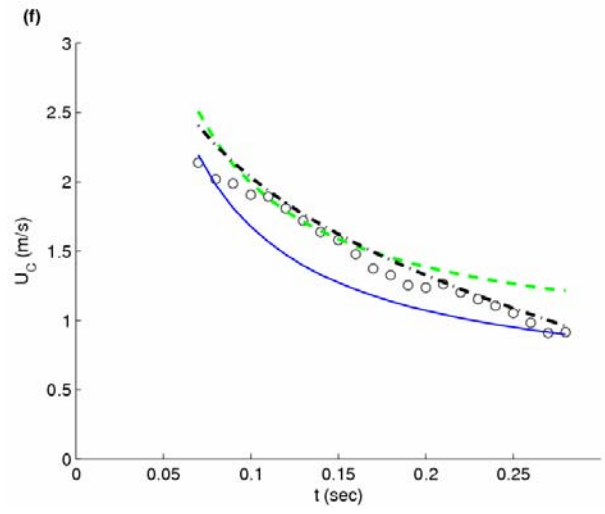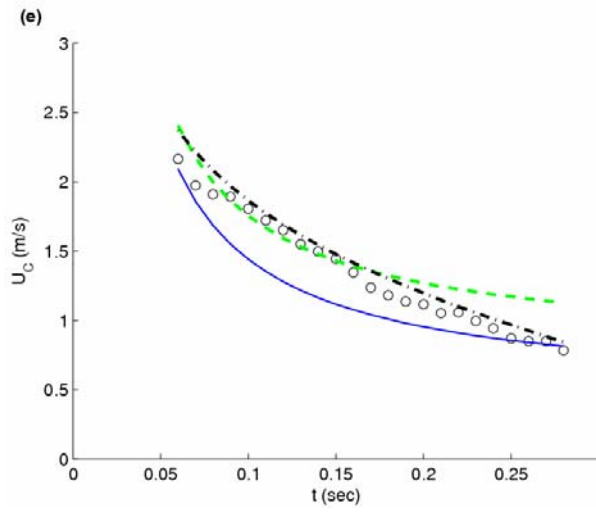
Figure 3.13: (Continued)
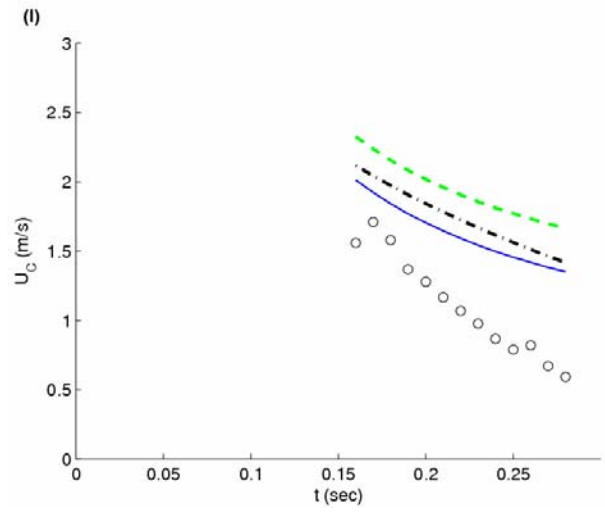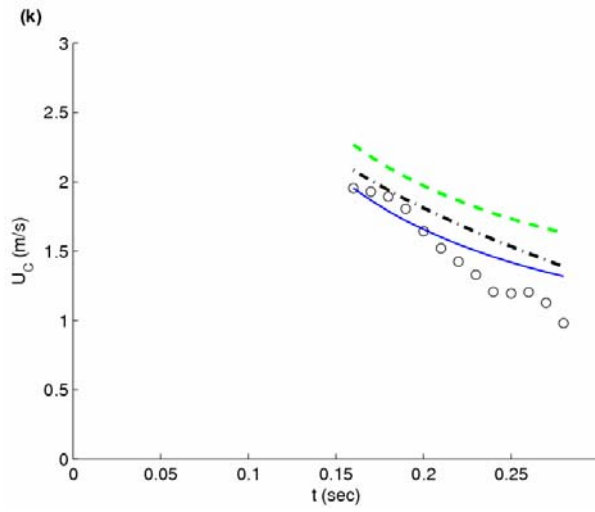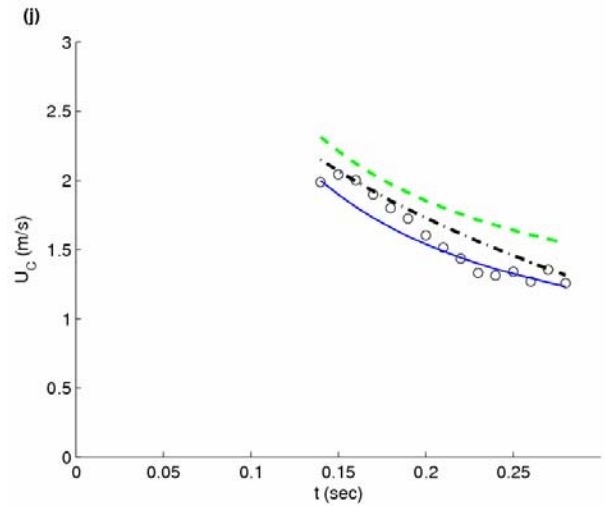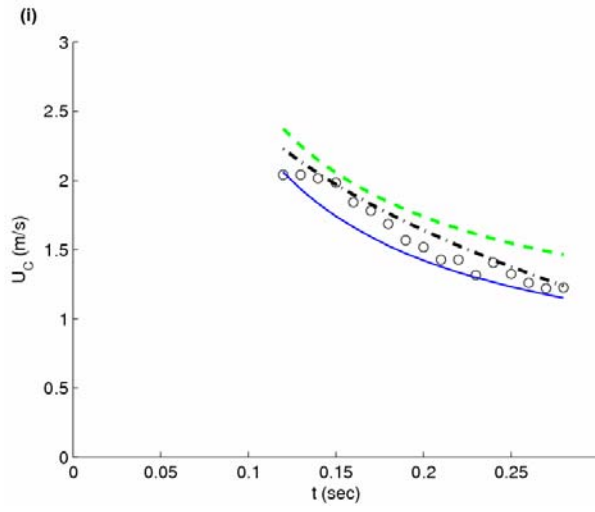
Figure 3.13: (Continued)

3.7 Vertical Velocity Distribution

The distributions of the maximum vertical velocities and the locations where the velocity occur are presented in Figure 3.14. Splashing water occurred when a large wave slams on the front wall of the structure and moves upward, creating significant vertical momentum. Since offshore structures such as TLP and SPAR have deck and deck facilities installed above the floating column and intruding outward from the column, it may be important to estimate the vertical momentum of splashing water impacting vertically normal to the deck. Similarly to the concept of cross-sectional horizontal velocity, maximum vertical velocity at every level is plotted. Note that the deck is at z = 110 mm in the figure. The measured maximum vertical velocity is surprisingly large. It reached 5.65 m/s, occurred at t = -0.04 s (corresponding to Figure 3.5(a)). That is the instant after the wave impinged on the structure and moved upward but not yet reached the top of the deck and developed a visible horizontal velocity. This maximum vertical velocity is about 2.90C, and comparing with the maximum horizontal velocity of 1.13C, is about 2.6 times the maximum horizontal velocity occurred over entire green water process. This velocity could develop into a huge vertical load to a structure if the deck or a portion of the structure stretches out from the vertical front wall.

The magnitude of the largest vertical velocity was reduced the moment shown in Figure 3.5(a), found by examining the velocities in Figure 3.5(b) and subsequent velocity fields. Even though after Figure 3.5(b) the front of the upward splashing water is out of the FOV, we expect the maximum vertical velocity to continue to drop due to gravity and the development of the horizontal momentum. Since we did not measure the entire flow field covering the vertically splashing water due to the limit of the FOV, the maximum velocity at a given moment would not be possible to obtain. However, what we are interested is the maximum velocity near the elevation of the deck because this is more related to the stability of the deck and its structure. As shown in the consecutive plots in Figure 3.14, the maximum vertical velocities occurred in front of the deck at x < 0 before the moment of t = 0.00 s (corresponding to Figure 3.14(c)). After the instant of t = 0.00 s, the location of the maximum vertical velocity move onto the deck. The

magnitude reached almost 3 m/s ($\approx 1.5C$) at the very beginning of the green water process in Figure 3.14(d). The magnitude reduced while the location shifted downstream as the green water was on the deck and moving downstream. However, the vertical velocity can not be ignored because it posts a large upward vertical load to equipment and facility on the deck and close to the frontal edge of the deck. The corresponding velocity field in Figure 3.5 will help visualizing the effect.
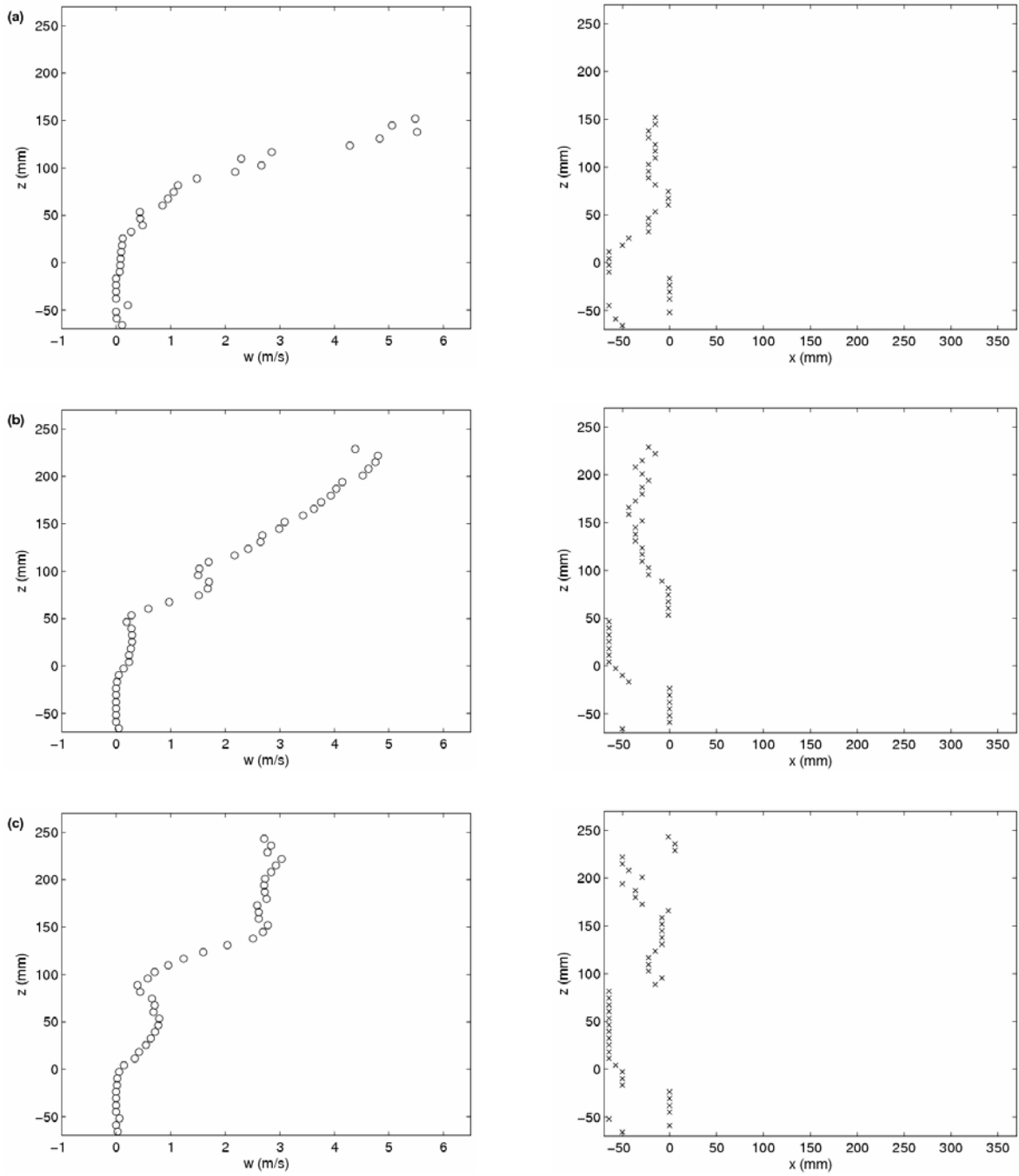
Figure 3.14: Measured maximum vertical velocities and locations along the *z* axis at *t* = (a) -0.04 s, (b) -0.02 s, (c) 0.00 s, (d) 0.02 s, (e) 0.04 s, (f) 0.06 s, (g) 0.08 s, (h) 0.10 s, and (i) 0.12s.
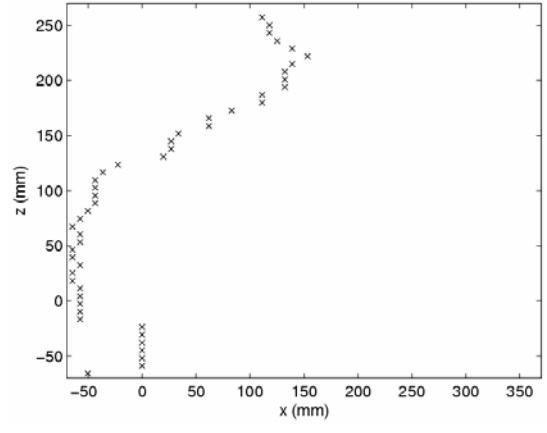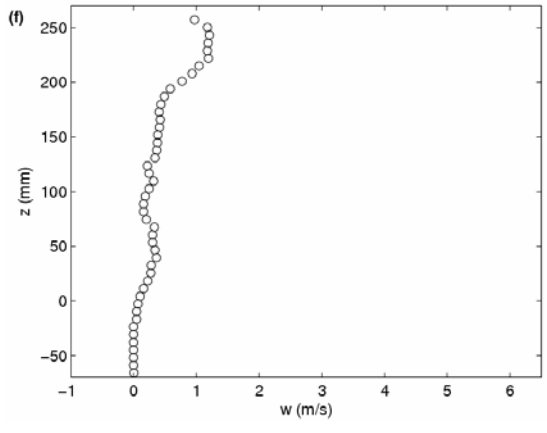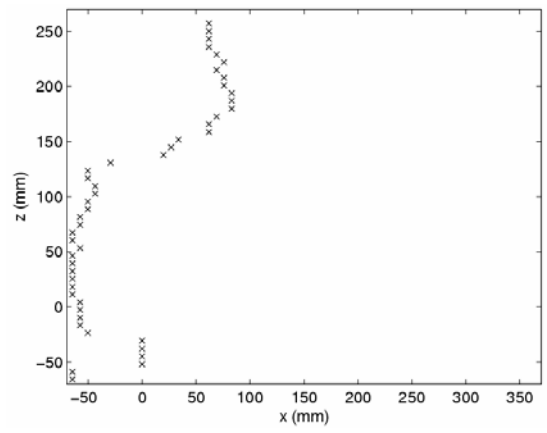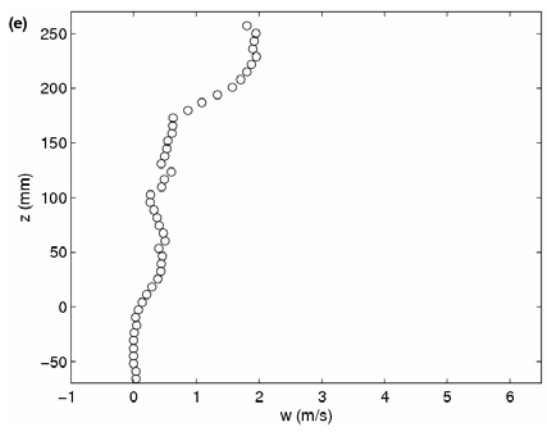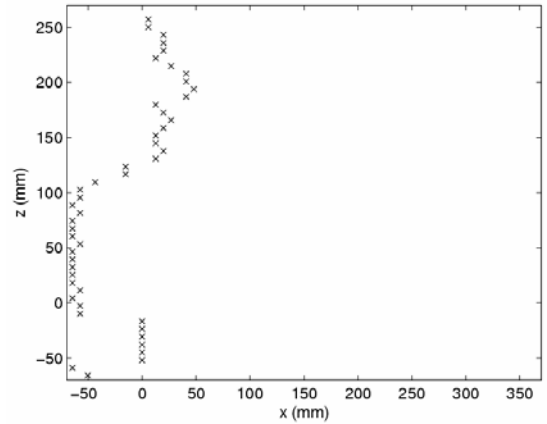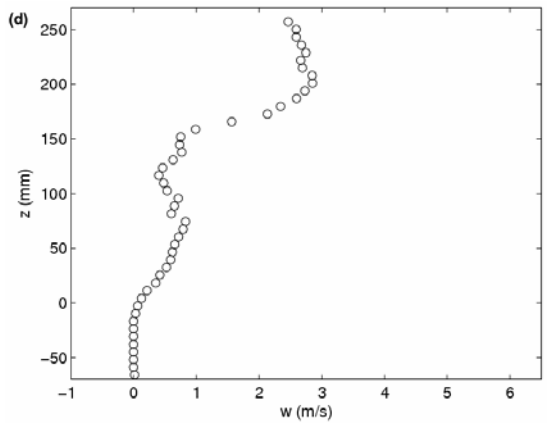
Figure 3.14: (Continued)
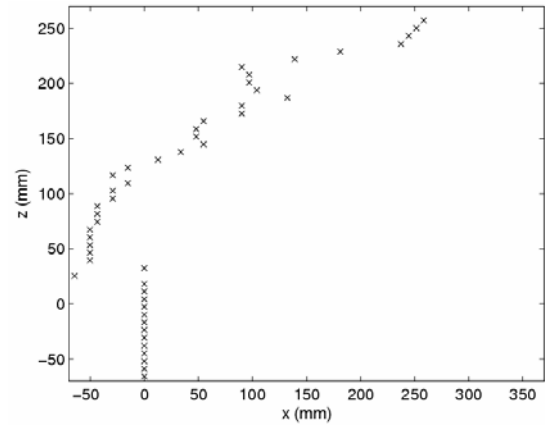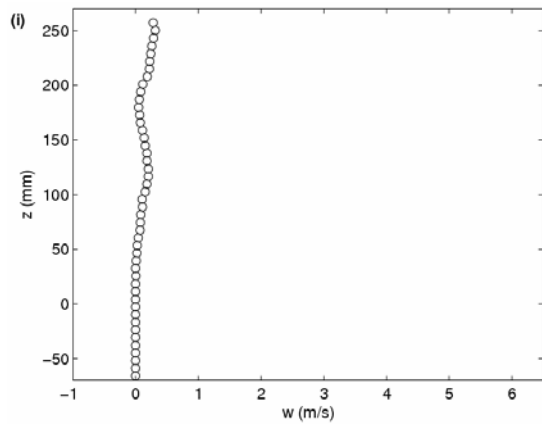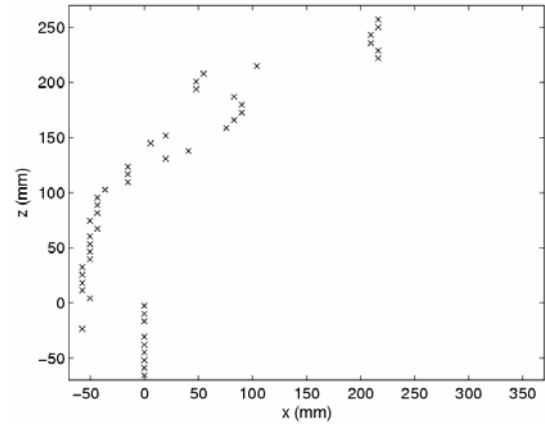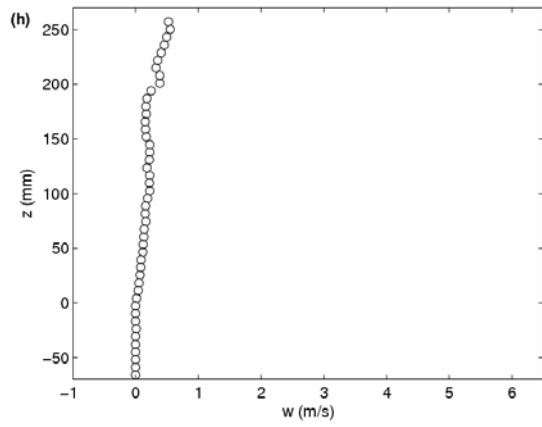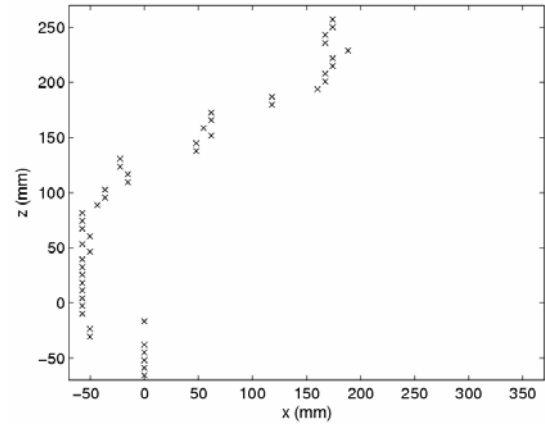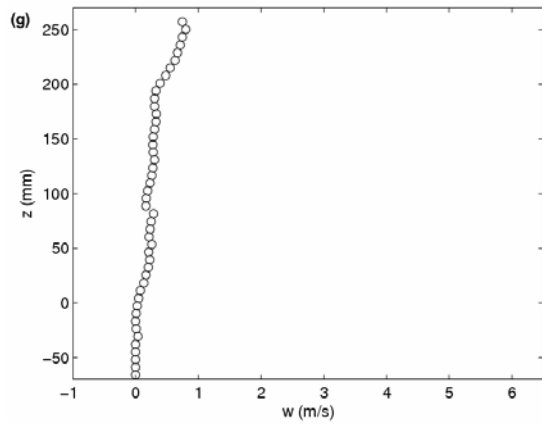
Figure 3.14: (Continued)

Chapter 4
Theoretical Formulation and Numerical Method

4.1 Interface-Capturing Methods

The interaction between the extreme waves and floating structures is of primary concern in the design of offshore structures. Most of the earlier work employed potential flow theory without considering the viscous effects. In the past several years, however, the viscous-flow methods have been used by, among others, Ananthakrishnan (1998), Dong and Huang (1999), Park et al. (2001), and Chen et al. (2001, 2002) for the study of fully nonlinear free surface flow around coastal and offshore structures. In order to provide accurate resolution of viscous, nonlinear free surface flow around offshore structures, it is necessary to employ more sophisticated numerical methods and turbulence models which are capable of dealing with complex three-dimensional flow separation and fully nonlinear free surface waves.

Green water loads on offshore platform occur when an incoming wave significantly exceeds the free board and water runs on the deck. The primary difficulty in the simulation of the green water phenomena lies in the tracking of the air-water interface. Many methods have been proposed to predict the interface between two different fluids. They could be classified into two different approaches: the interface-tracking methods and the interface-capturing methods (Ferziger and Peric, 1999). The interface-tracking methods follow the free surface motions and use boundary-fitted grids which are re-adjusted in each time step whenever the free surface moves. In contrast, the interface-capturing methods do not define a sharp free surface boundary. The computation is performed on a fixed grid, which is extended beyond the free surface and the shape of this free surface is determined by cells that are partially filled. A variety of numerical methods in this interface-capturing approach have been developed over the past several decades. Here, three typical methods, Marker and Cell (MAC) scheme (Harlow and Welch, 1965), volume of fluid (VOF) scheme (Nichols et al., 1980; Hirt and Nichols, 1981) and level set method (Osher and Sethian, 1988) are summarized in the following section.

The MAC scheme is attractive because it can treat complex free surface phenomena including wave breaking. However, intensive computational effort is needed especially for three-dimensional problems with violent free surface motions. In addition to solving the equations governing the fluid flow, one has to follow the motion of a large number of particles. In VOF, in addition to the conservation equations for mass and momentum, one has to introduce and solve an auxiliary function, namely the volume fraction or color function. There are several different surface reconstruction procedures available for VOF schemes. However, most of them cannot build an accurate and smooth free surface for complex three-dimensional free surface problems.

In the present study, we used both the interface-tracking and interface-capturing methods in conjunction with a chimera Reynolds-Averaged Navier-Stokes (RANS) method for time-domain simulation of nonlinear waves around offshore structures. For the interface-tracking method, it is convenient to use separate body-fitted numerical grids for the structures and the ambient wave field. In the present chimera domain decomposition approach, the numerical grids around the offshore structures remain fixed while the free surface grids are adjusted every time step to conform to the exact free surface. Since the submerged portion of the structures change continuously at different time instants, the interpolation between different chimera grid blocks were updated every time step to enforce conservation of mass and momentum across block boundaries over the entire simulation. In addition, an effective damping beach approach proposed by Chen and Huang (2004) was implemented on the wavemaker boundary to prevent the reflected waves from reaching the wavemaker boundary. This enables us to perform long-duration simulations without significantly increase the size of the computational domain. In the present study, the chimera RANS method of Chen et al. (2000, 2001, 2002) has been generalized for time-domain simulation of fully nonlinear wave runup around two- and three-dimensional offshore structures.

The present interface-tracking method was used with considerable success by Chen et al. (2002) for time-domain simulation of barge capsizing. However, the interface-tracking method is not suitable for the simulation of more complex green water problems with the presence of water spray and air bubbles. In view of these limitations, we have also developed an interface-capturing method based on the level set method of Osher and Sethian (1988). In the level set formulation, the level set function ϕ is typically defined as the signed distance from the interface; $\phi < 0$ in air

region, $\phi > 0$ in water region, and $\phi = 0$ on the air-water interface. In the beginning of the calculation, the value of ϕ is the physical distance from the interface. It varies smoothly across the interface and is advected by the local velocity field using the advection equation

$$\frac{\partial \phi}{\partial t} + \vec{V} \cdot \nabla \phi = 0 \tag{4.1}$$

The interface can be captured at any time by locating the zero level set. In general, the computed ϕ may not remain the signed distance from the interface and needs to be reinitialized for every time step. Sussman et al. (1994) proposed that this be done by solving the following equation until the steady state is reached.

$$\frac{\partial \phi}{\partial \tau} = sign(\phi_0) \cdot (1 - |\nabla \phi|) \tag{4.2}$$

This guarantees that ϕ has the same sign and zero level as ϕ_0 and satisfies the condition that $|\nabla \phi| = 1$. The level set method was shown to lower the difficulties in handling topological merging, breaking and even self-intersecting of interfaces problems. More details of the level set methods can be found in Sethian (1996).

In the present study, the level set method has been incorporated into the chimera RANS method of Chen and Chen (1998) for the prediction of green water on offshore platforms. The governing equations are formulated in curvilinear coordinate system and discretized using the finite-analytic method of Chen et al. (1990) on a non-staggered grid. For the additional level set equations of evolution and re-initialization, we use the 3rd-order TVD (total variation diminishing) Runge-Kutta scheme (Yu et al, 2003b) for time derivative, and the 3rd-order ENO (essentially non-oscillatory) scheme for spatial derivatives. The present interface-capturing method was validated first for several benchmark cases including a stationary circle, the Zalesak's problem, and the stretching of a circular fluid element under prescribed free motion. The level set method was then incorporated into the chimera RANS method of Chen and Chen (1998) for complex free surface flow simulations. Calculations were performed first for dam breaking and free jet problems in single-block rectangular grids. The feasibility of using the chimera domain decomposition approach in level set method was also evaluated for the dam breaking problem using two different embedding grid systems. Finally, the new chimera RANS method was used for the simulation of a traveling solitary wave, and green water on offshore platforms. These test cases clearly

demonstrated that the level set method is capable of simulating violent free surface flows encountered in the wave runup on offshore platforms.

4.2 Theoretical Formulation

We formulate the Navier-Stokes equations in the level set formulation. Both the density and viscosity at air-water interfaces depend on the level set function being a distance function. The fluid properties are assumed to vary smoothly across a narrow transition zone around the free surface. This enables us to obtain accurate and stable numerical results for violent free surface motions encountered in the simulations of green water on offshore platforms.

In the present algorithm, the interface is the zero level set of ϕ:

$$\Gamma = \{\vec{x} \mid \phi(\vec{x},t) = 0\} \tag{4.3}$$

By defining $\phi < 0$ for air region and $\phi > 0$ for water region, we have

$$\phi(\vec{x},t) \begin{cases} > 0 & if \quad \vec{x} \in water \\ = 0 & if \quad \vec{x} \in \Gamma \\ < 0 & if \quad \vec{x} \in air \end{cases} \tag{4.4}$$

The evolution of ϕ is given by the advection equation (4.1) in the transition zone defined by $|\phi| \le \varepsilon$, where ε is the half thickness of the interface. In the transition zone, the fluid properties are smoothed by Heaviside function $H(\phi)$:

$$H(\phi) = \begin{cases} 0 & if \, \phi < -\varepsilon \\ \frac{1}{2}\left(1 + \frac{\phi}{\varepsilon} + \frac{1}{\pi}\sin(\frac{\pi\phi}{\varepsilon})\right) & if - \varepsilon \le \phi \le \varepsilon \\ 1 & if \, \phi > \varepsilon \end{cases} \tag{4.5}$$

More specifically, the density and viscosity are calculated in the following way:

$$\begin{aligned} \rho(\phi) &= \rho_a + (\rho_w - \rho_a) \cdot H(\phi) \\ \mu(\phi) &= \mu_a + (\mu_w - \mu_a) \cdot H(\phi) \end{aligned} \tag{4.6}$$

where the subscripts 'a' and 'w' represent air and water, respectively.

After a new level set value ϕ_0 is obtained in each time step, it is necessary to solve the re-distancing equation (4.2) in order to ensure that the level set value remains as a real distance. However, it is well known that numerical errors may accumulate due to repeated re-distance operations on a level set function. In order to prevent the straying of the zero level set from initial position even after many iterations, a mass constraint term proposed by Sussman and Fatemi (1999) is added to equation (4.2) as follows:

$$\frac{\partial \phi}{\partial \tau} = L(\phi_0, \phi) + \lambda_{ij} f(\phi) \tag{4.7}$$

where

$$L(\phi_0, \phi) = sign(\phi_0)(1 - |\nabla \phi|) ; \quad f(\phi) \equiv H'(\phi)|\nabla \phi| \tag{4.8}$$

The coefficient λ is determined by

$$\lambda_{ij} = \frac{- \int\limits_{\Omega_{ij}} H'(\phi) L(\phi_0, \phi)}{\int\limits_{\Omega_{ij}} H'(\phi) f(\phi)} \tag{4.9}$$

for every grid cell $\Omega_{ij} = \{(x, y) | x_{i-1/2} < x < x_{i+1/2} \;\; and \;\; y_{j-1/2} < y < y_{j+1/2}\}$.   A more detailed description of the mass constraint term is given in Sussman and Fatemi (1999).

We assume that both water and air are governed by the incompressible Navier-Stokes equations:

$$\rho_w \left(\frac{\partial \overrightarrow{V'}}{\partial t'} + \overrightarrow{V'} \cdot \nabla \overrightarrow{V} \right) = \rho_w \overrightarrow{g} + \mu_w \nabla^2 \overrightarrow{V'} - \nabla p' \tag{4.10}$$

$$\rho_a \left(\frac{\partial \overrightarrow{V'}}{\partial t'} + \overrightarrow{V'} \cdot \nabla \overrightarrow{V} \right) = \rho_a \overrightarrow{g} + \mu_a \nabla^2 \overrightarrow{V'} - \nabla p' \tag{4.11}$$

The above equations are normalized using the following three dimensionless variables

$$\overrightarrow{V} = \frac{\overrightarrow{V'}}{U_0}, \qquad t = \frac{t'}{t_0} = \frac{U_0}{L} t' , \qquad p = \frac{p'}{\rho_w U_0^2}$$

After dividing by $\frac{\rho_w U_0^2}{L}$, we obtain

$$\frac{\partial \vec{V}}{\partial t} + \vec{V} \cdot \nabla \vec{V} = \frac{\vec{g}L}{U_0^2} + \frac{\mu_w}{\rho_w U_0 L} \nabla^2 \vec{V} - \nabla p \tag{4.12}$$

$$\frac{\partial \vec{V}}{\partial t} + \vec{V} \cdot \nabla \vec{V} = \frac{\vec{g}L}{U_0^2} + \frac{\mu_a}{\mu_w} \frac{\rho_w}{\rho_a} \frac{\mu_w}{\rho_w U_0 L} \nabla^2 \vec{V} - \frac{\rho_w}{\rho_a} \nabla p \tag{4.13}$$

The above two equations can be combined together using the level set terms $\rho(\phi)$ and $\nu(\phi) = \mu(\phi)/\rho(\phi)$ as defined earlier in equation (4.6):

$$\frac{\partial \vec{V}}{\partial t} + \vec{V} \cdot \nabla \vec{V} = -\frac{\delta_{i,3}}{Fr^2} + \frac{\nu(\phi)}{\mathrm{Re}} \nabla^2 \vec{V} - \frac{1}{\rho(\phi)} \nabla p \tag{4.14}$$

Now we can transform the continuity and momentum equations into curvilinear coordinate system

$$\sum_{i=1}^{3} \frac{\partial U_i}{\partial x^i} = 0 \tag{4.15}$$

$$\frac{\partial U_i}{\partial t} + \sum_{j=1}^{3} \left(U_j \frac{\partial U_i}{\partial x^j} + \frac{\partial \overline{u_i u_j}}{\partial x^j} \right) + \frac{1}{\rho(\phi)} \frac{\partial p}{\partial x^i} - \frac{\nu(\phi)}{\mathrm{Re}} \nabla^2 U_i + \frac{\delta_{i,3}}{Fr^2} = 0 \tag{4.16}$$

with $\nabla^2 = \sum_{j=1}^{3} \frac{\partial^2}{\partial x^j \partial x^j}$

The Reynolds stresses $\overline{u_i u_j}$ are related to the corresponding mean rate of strain through an isotropic eddy viscosity ν_t

$$-\overline{u_i u_j} = \nu_t \left(\frac{\partial U_i}{\partial x^j} + \frac{\partial U_j}{\partial x^i} \right) - \frac{2}{3} \delta_{ij} k \tag{4.17}$$

where $k = (\overline{uu} + \overline{vv} + \overline{ww})/2$ is the turbulent kinetic energy. The substitution of Reynolds stresses into the momentum equations yields:

$$\frac{\partial U_i}{\partial t} + \sum_{j=1}^{3} \left[\left(U_i - \frac{\partial \nu_t}{\partial x^j} \right) \frac{\partial U_i}{\partial x^j} - \frac{\partial \nu_t}{\partial x^j} \frac{\partial U_j}{\partial x^i} \right] = -\frac{\delta_{i,3}}{Fr^2} + \left(\frac{\nu(\phi)}{\mathrm{Re}} + \nu_t \right) \nabla^2 U_i - \left(\frac{1}{\rho(\phi)} \frac{\partial p}{\partial x^i} + \frac{\partial (\frac{2}{3}k)}{\partial x^i} \right) \tag{4.18}$$

Let $\varphi = U_i$ and rearrange the momentum equations as follows:

$$\nabla^2 \varphi = R_\varphi \cdot \left[\sum_{j=1}^{3} \left(U_j - \frac{\partial v_t}{\partial x^j} \right) \frac{\partial \varphi}{\partial x^j} + \frac{\partial \varphi}{\partial t} \right] + s_\varphi \qquad (4.19)$$

where the effective viscosity is $R_\varphi = \left(\dfrac{v(\phi)}{\text{Re}} + v_t \right)^{-1}$ and the source terms are given by:

$$s_\varphi = R_\varphi \left[\frac{1}{\rho(\phi)} \frac{\partial p}{\partial x^i} + \frac{\partial (\frac{2}{3}k)}{\partial x^i} - \sum_{j=1}^{3} \frac{\partial v_t}{\partial x^j} \frac{\partial U_j}{\partial x^i} + \frac{\delta_{i,3}}{Fr^2} \right] \qquad (4.20)$$

In curvilinear coordinate system, the above equations can be converted to:

$$\nabla^2 \varphi = \sum_i \sum_j g^{ij} \frac{\partial^2 \varphi}{\partial \xi^i \partial \xi^j} + \sum_j f^j \frac{\partial \varphi}{\partial \xi^j} \qquad (4.21)$$

$$\frac{\partial \varphi}{\partial t} = \frac{\partial \varphi}{\partial \tau} - \frac{1}{J} \sum_i \sum_j b_i^j \frac{\partial x^i}{\partial \tau} \frac{\partial \varphi}{\partial \xi^j} \qquad (4.22)$$

$$\sum_j U_j \frac{\partial \varphi}{\partial x^j} = \sum_i U_i \left(\frac{1}{J} \sum_j b_i^j \frac{\partial \varphi}{\partial \xi^j} \right) \qquad (4.23)$$

$$-\frac{\partial v_t}{\partial x^j} \frac{\partial \varphi}{\partial x^j} = -\sum_n \left[\frac{1}{J} \sum_m b_n^m \frac{\partial v_t}{\partial \xi^m} \cdot \frac{1}{J} \sum_j b_n^j \frac{\partial \varphi}{\partial \xi^j} \right] \qquad (4.24)$$

Substituting equations (4.21) – (4.24) into equation (4.19), we obtain the momentum equations in the transformed plane:

$$\sum_j \left(g^{ij} \frac{\partial^2 \varphi}{\partial \xi^j \partial \xi^j} - 2a_\varphi^j \frac{\partial \varphi}{\partial \xi^j} \right) = R_\varphi \frac{\partial \varphi}{\partial \tau} + S_\varphi \qquad (4.25)$$

with

$$2a_\varphi^j = \frac{R_\varphi}{J} \sum_n b_n^j \left[U_n - \frac{\partial x_i}{\partial \tau} - \sum_m \frac{1}{J} b_n^m \frac{\partial v_t}{\partial \xi^m} \right] - f^j \qquad (4.26)$$

$$S_\varphi = s_\varphi - 2 \left(g^{12} \frac{\partial^2 \varphi}{\partial \xi^1 \partial \xi^2} + g^{23} \frac{\partial^2 \varphi}{\partial \xi^2 \partial \xi^3} + g^{13} \frac{\partial^2 \varphi}{\partial \xi^1 \partial \xi^3} \right) \qquad (4.27)$$

4.3 Numerical Method

We further introduce the contravariant velocity components (Chen and Patel, 1989)

$$U^i = JV^i = \sum_{j=1}^{3} b_j^i U_j \tag{4.28}$$

The level set evolution equation is written in the transformed coordinates (ξ^i, t)

$$\frac{\partial \phi}{\partial t} + \sum_{i=1}^{3} \frac{\partial (U^i \phi)}{\partial \xi^i} = 0 \tag{4.29}$$

In the present study, equation (4.29) is advanced using the 3rd-order TVD Runge-Kutta scheme which is total variation stable (Yue et al., 2003)

$$\begin{cases} \phi^{(1)} = \phi^n - \Delta t \cdot R(\phi^n) \\[2ex] \phi^{(2)} = \frac{3}{4} \phi^{(n)} + \frac{1}{4} \phi^{(1)} - \frac{\Delta t}{4} R(\phi^{(1)}) \\[2ex] \phi^{(n+1)} = \frac{1}{3} \phi^{(n)} + \frac{2}{3} \phi^{(2)} - \frac{2\Delta t}{3} R(\phi^{(2)}) \end{cases} \tag{4.30}$$

where $R(\phi) = \dfrac{\partial (U^i \phi)}{\partial \xi^i}$ and the spatial operator R is discretized in transformed plane (ξ, η, ζ) in a conservative manner.

$$\frac{\partial (U^i \phi)}{\partial \xi^i} = (U^1 \phi)_{i+1/2,j,k} - (U^1 \phi)_{i-1/2,j,k} + (U^2 \phi)_{i,j+1/2,k} - (U^2 \phi)_{i,j-1/2,k} + (U^3 \phi)_{i,j,k+1/2} - (U^3 \phi)_{i,j,k-1/2} \tag{4.31}$$

The cell-face values of ϕ are constructed using the 3rd-order ENO interpolation scheme of Shu and Osher (1989). Denoting:

$$\delta \phi_i^{-1} = \phi_i - \phi_{i-1}, \quad \delta \phi_i^0 = \phi_{i+1} - \phi_i, \quad \delta \phi_i^1 = \phi_{i+2} - \phi_{i+1}$$

and use the same definitions for subscripts (j, k) in the (y, z) directions, we can express $\phi_{i+1/2}$ based on the left-shift parameter $r3$:

$$\phi_{i+1/2} = \begin{cases} \dfrac{11}{6}\phi_{i+1} - \dfrac{7}{6}\phi_{i+2} + \dfrac{1}{3}\phi_{i+3} & \text{if } r3 = -1 \\[4mm] \dfrac{1}{3}\phi_i + \dfrac{5}{6}\phi_{i+1} - \dfrac{1}{6}\phi_{i+2} & \text{if } r3 = 0 \\[4mm] -\dfrac{1}{6}\phi_{i-1} + \dfrac{5}{6}\phi_i + \dfrac{1}{3}\phi_{i+1} & \text{if } r3 = 1 \\[4mm] \dfrac{1}{3}\phi_{i-2} - \dfrac{7}{6}\phi_{i-1} + \dfrac{11}{6}\phi_i & \text{if } r3 = 2 \end{cases} \tag{4.32}$$

with $r3$ defined in terms of $r2$ and $r1$ as follows:

$$r1 = \begin{cases} 1 & \text{if } U_{i+1/2} \geq 0 \\ 0 & \text{if } U_{i+1/2} < 0 \end{cases}$$

$$r2 = \begin{cases} r1 & \text{if } \left|\delta\phi_i^{-r1+1}\right| \geq \left|\delta\phi_i^{-r1}\right| \\ r1-1 & \text{if } \left|\delta\phi_i^{-r1+1}\right| < \left|\delta\phi_i^{-r1}\right| \end{cases} \tag{4.33}$$

$$r3 = \begin{cases} r2 & \text{if } \left|\delta\phi_i^{-r2+1}\right| < \left|\delta\phi_i^{-r2}\right| \\ r2+1 & \text{if } \left|\delta\phi_i^{-r2+1}\right| \geq \left|\delta\phi_i^{-r2}\right| \end{cases}$$

In order to avoid the logical structures to distinguish whether a given stencil is completely inside the computational domain, one could set all the ghost values outside the computational domain to be very large with large variations. This way the ENO choosing procedure will automatically avoid choosing any stencil containing ghost points.

The transport equations for (U_i, k, ε) are solved by the finite-analytic scheme of Chen et al. (1990).

$$U_{i,P} = \hat{U}_i - \frac{\dfrac{1}{J}C_P R}{1 + C_P\left(C_U + C_D + \dfrac{R}{\Delta\tau}\right)} \frac{1}{\rho(\phi)} \sum_j b_i^j \frac{\partial p}{\partial \xi^j} \tag{4.34}$$

where the pseudo-velocities are defined by:

$$\hat{U}_i = \frac{1}{1 + C_P\left(C_U + C_D + \dfrac{R}{\Delta\tau}\right)}\left[\sum_1^8 C_{nb}U_{i,nb} + C_P\left(C_U U_{i,U} + C_D U_{i,D} + \frac{R}{\Delta\tau}U_{i,P}^{n-1}\right) - C_P R\left(S_{U_i} + \frac{1}{Fr^2}\right)\right] \tag{4.35}$$

The subscripts 'U' and 'D' represent points in the stencil, upstream and downstream of P.

Chapter 5

Numerical Simulations and Results

5.1 Wave Runup on Offshore Platforms

In this section, we shall present numerical simulation results obtained from the interface-tracking method of Chen et al. (2004) for wave runup on the two-dimensional tension leg platform (TLP) considered in our experimental investigations. As noted earlier, the length and height of the model platform are 0.15 m and 0.30 m, respectively. The still water level is 0.105 m below the platform deck. Velocity fields in the vicinity of the structure were measured using the particle image velocimetry (PIV) technique for 8 phases per each wave period. Both instantaneous and phase-averaged quantities were obtained and analyzed. These PIV data provide an excellent database for the validation of the present numerical method.

In the present chimera domain decomposition approach for platform wave runup simulation, the solution domain is divided into several computational blocks as shown in Figure 5.1 to provide appropriate resolution of the platform boundary layers, wakes, as well as the nonlinear free surface waves. Figures 5.1(a) and 5.1(c) shows the chimera grid block structures around the platform at t/T = 20.375 and 20.875, respectively. For completeness, the wave tank grids at the same time instants are also shown in Figures 5.1(b) and 5.1(d). These wave tank grids are not linked to the other grid blocks and are used solely for the implementation of absorbing beach in front of the wavemaker. For long-duration simulations over many wave periods, it is well known that the wave reflected by the platform will propagate back to the wavemaker boundary and interfere with the incident wave field. In the present study, a new absorbing beach approach developed recently by Chen and Huang (2004) has been implemented to prevent the reflected wave from returning to the wavemaker. In this absorbing beach approach, the wave tank grids shown in Figures 1(b) and 1(d) were used to allow concurrent computation of the incident wave field without the presence of the offshore structure. This enables us to determine the exact pattern of the reflected wave since both wave fields with and without the structure were computed simultaneously at every time step. A

damping function was then used to absorb the reflected waves so that the time-domain simulation can be continued for many wave periods without unphysical wave reflection from the wavemaker.

In the present wave runup simulations, the incident wave field was generated using the higher order nonlinear wave theory of Cokelet (1977). The free surface grid blocks are updated at every time step to follow the instantaneous free surface wave elevation. Furthermore, nonlinear dynamic free surface boundary condition is imposed on the exact free surface for accurate prediction of the fully nonlinear wave field. It should also be noted that the platform grid covers the entire platform surface including the dry deck area. Moreover, the platform grid remains fixed during the entire simulation even though the submerged section changes with instantaneous wave elevation. This not only simplifies the grid-generation process, but also eliminates undesirable grid distortion which typically occurs in the simulation of large amplitude wave motions.

(a) Chimera grid with structure; t/T = 20.375

(b) Wave tank grid without the structure; t/T = 20.375

(c) Chimera grid with structure; t/T = 20.875

(d) Wave tank grid without the structure; t/T = 20.875

Figure 5.1: Chimera grid structure for wave runup simulation

Simulations were performed for wave runup on the two-dimensional platform with two different incident wave heights of H = 0.0575 m and 0.0875 m, respectively. Figure 5.2 shows the computed free surface wave elevation and pressure contours at t/T = 20.375, 20.625, and 20.875, respectively, for the H = 0.0575 m case. The superposition and cancellation of the incident and reflected waves at different time instants can be clearly seen from this figure. The present simulation results also clearly demonstrated the effectiveness of the new absorbing beach approach as the simulation was continued for more than 20 wave periods without any distortion in incident wave field.

Wave Height = 0.0575 m; Time Step=4075 ; Time t/T=20.375

(a) *t/T* = **20.375**

Wave Height = 0.0575 m; Time Step=4125 ; Time t/T=20.625

(b) *t/T* = **20.625**
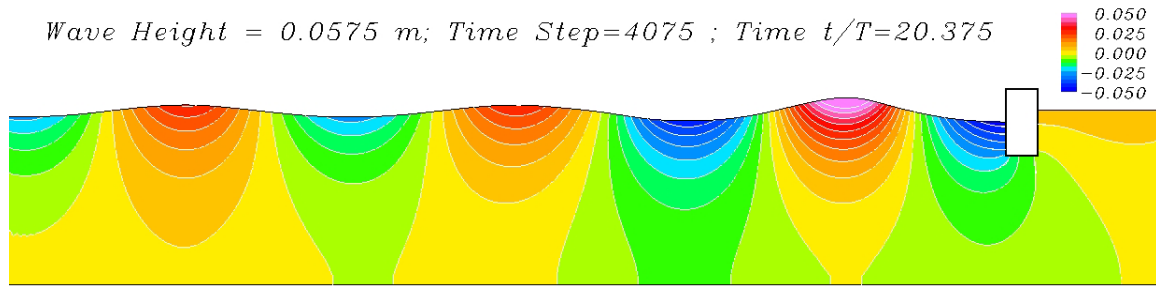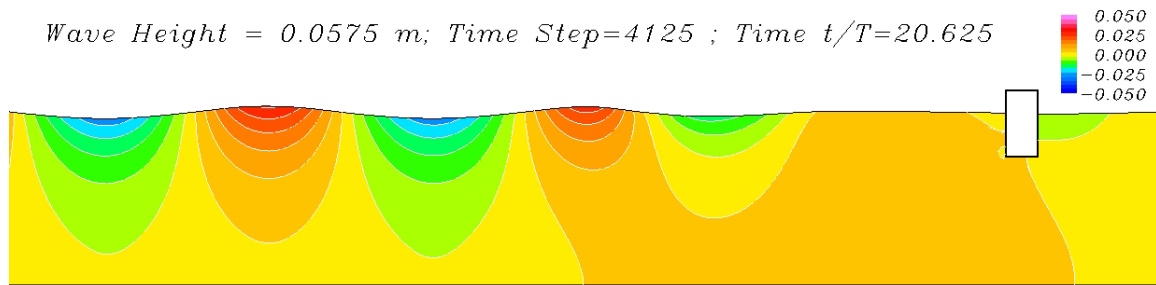
Wave Height = 0.0575 m; Time Step=4175 ; Time t/T=20.875
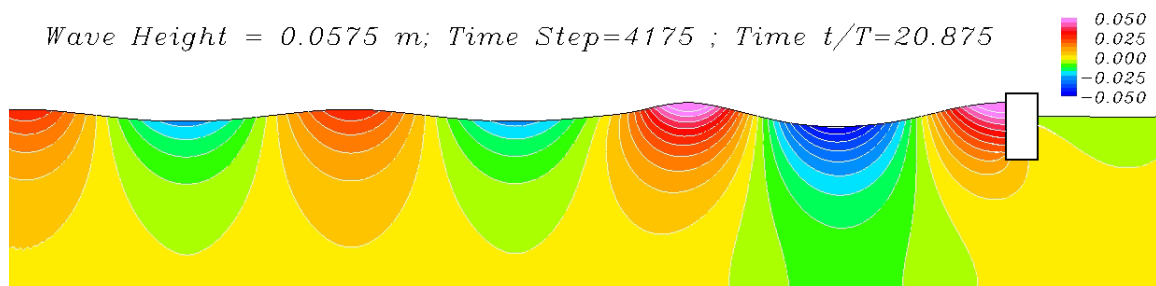
(c) *t/T* = **20.875**

Figure 5.2: Wave elevation and pressure contours; incident wave height H = 0.0575m

Figure 5.3 shows the time history of the wave elevation in front of the structure. It is seen that the first wave reaches the structure after three wave periods since the wavemaker is located about three wavelengths upstream of the model TLP. Note that the relatively large waves occurred around the 12th-13th wave periods followed by a transition period with significant fluctuation in wave height. The flow attained a nearly periodic pattern after about 20 wave periods. It is quite clear that the absorbing beach in front of the wavemaker successfully absorbed all the waves reflected from the structure so that the same incident wave can be maintained for long duration simulation with a rather small solution domain.

Figure 5.3: Time history of wave elevation in front of the model TLP; $H = 0.0575$m

Figure 5.4 shows the predicted velocity vectors and the corresponding vorticity contours at $t/T = 20.125$, 20.375, 20.625 and 20.875, respectively. At $t/T = 20.125$, the wave-induced current is moving downward and produces a strong counterclockwise vortex on the platform bottom surface adjacent to the weather side corner. Another weaker counterclockwise vortex was also observed on the lee side. The wave reaches its lowest elevation and begins to move upward around $t/T = 20.375$. At $t/T = 20.625$, the upward current velocity reaches a maximum value and a pair of clockwise vortices were induced around the sharp platform corners. The wave in front of the platform continue to move upward until the maximum runup is reached at $t/T = 20.875$. It is also worthwhile to note that the water elevation on the lee side of the platform changes only slightly since the platform draft is relatively deep with negligible wave transmission. The predicted velocity vector plots are in very good agreement with the corresponding PIV measurement at the same phases.
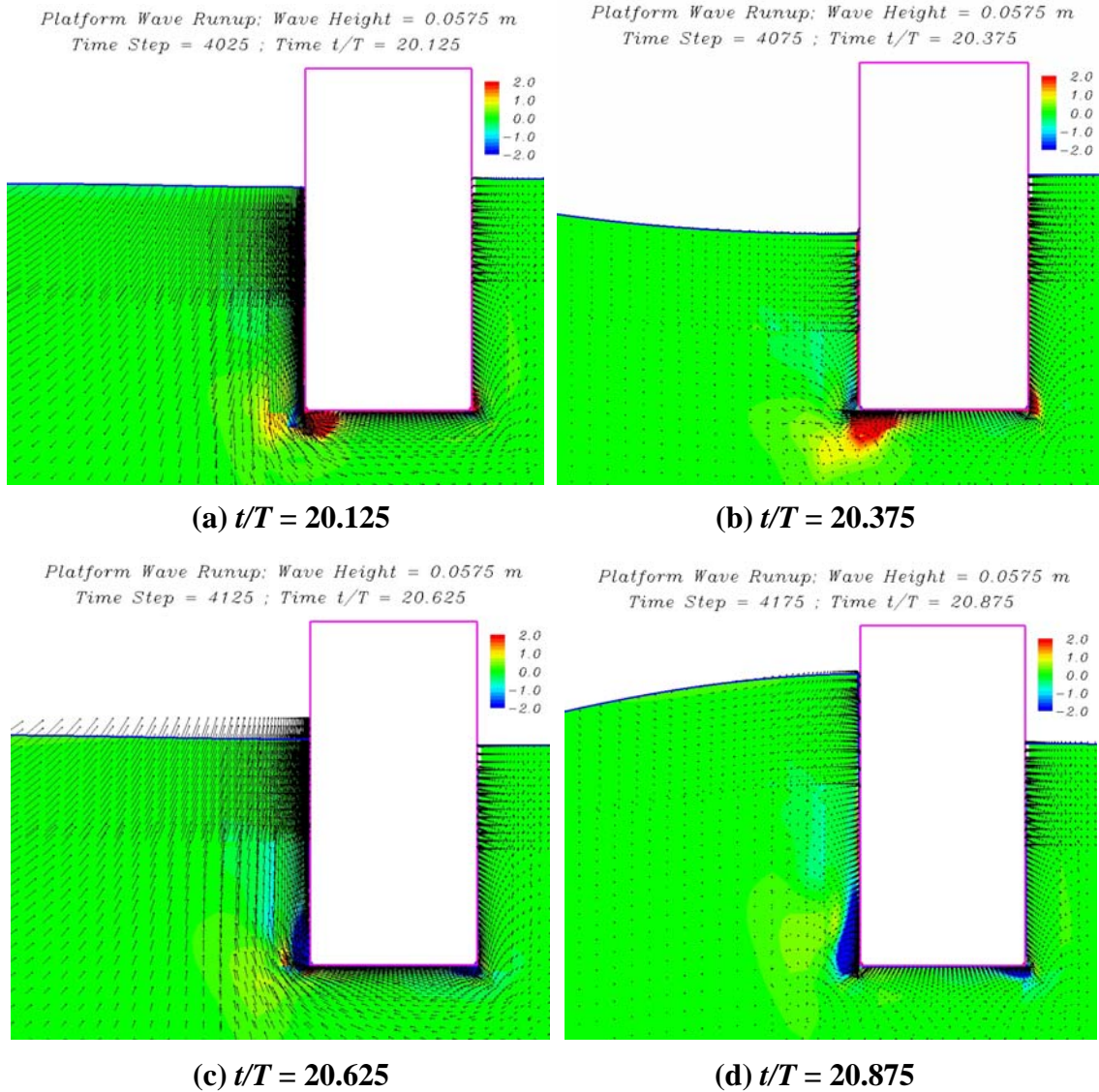
Figure 5.4: Velocity vectors and vorticity contours around the platform; $H = 0.0575$ m

Calculations were also performed for the higher wave case with an incident wave height $H = 0.0875$ m for a more critical evaluation on the capability of the chimera RANS method for large amplitude wave runup. In this simulation, the wavemaker is located at about five wavelengths in front of the structure. An absorbing beach is again implemented in front of the wavemaker to prevent the waves reflected by the model TLP from returning the wavemaker. Figure 5.5 shows the predicted free surface elevation and pressure contours for the higher incident wave case at $t/T = 21.27$, 21.52, and 21.77, respectively. More detailed vorticity contours and velocity vector plots

are also shown in Figure 5.6 at eight different time instants to provide a better understanding of the wave-induced flow field around the platform. At $t/T = 29.00$, the wave runup is very close to the platform deck. However, no green water was observed either in the experiment or the simulation. In general, the wave-induced vorticity field is considerably stronger than that observed earlier for the $H = 0.0875$ m case.
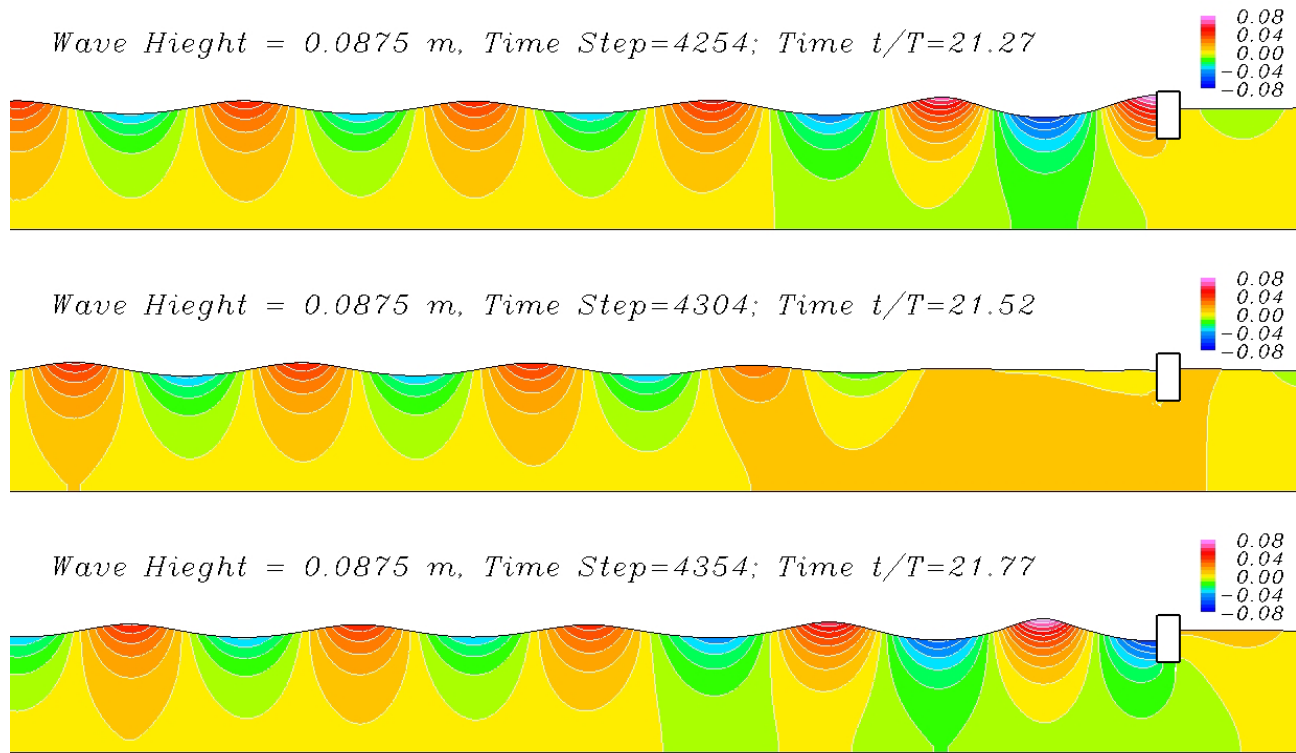
Figure 5.5: Wave elevation and pressure contours; incident wave height $H = 0.0875$m
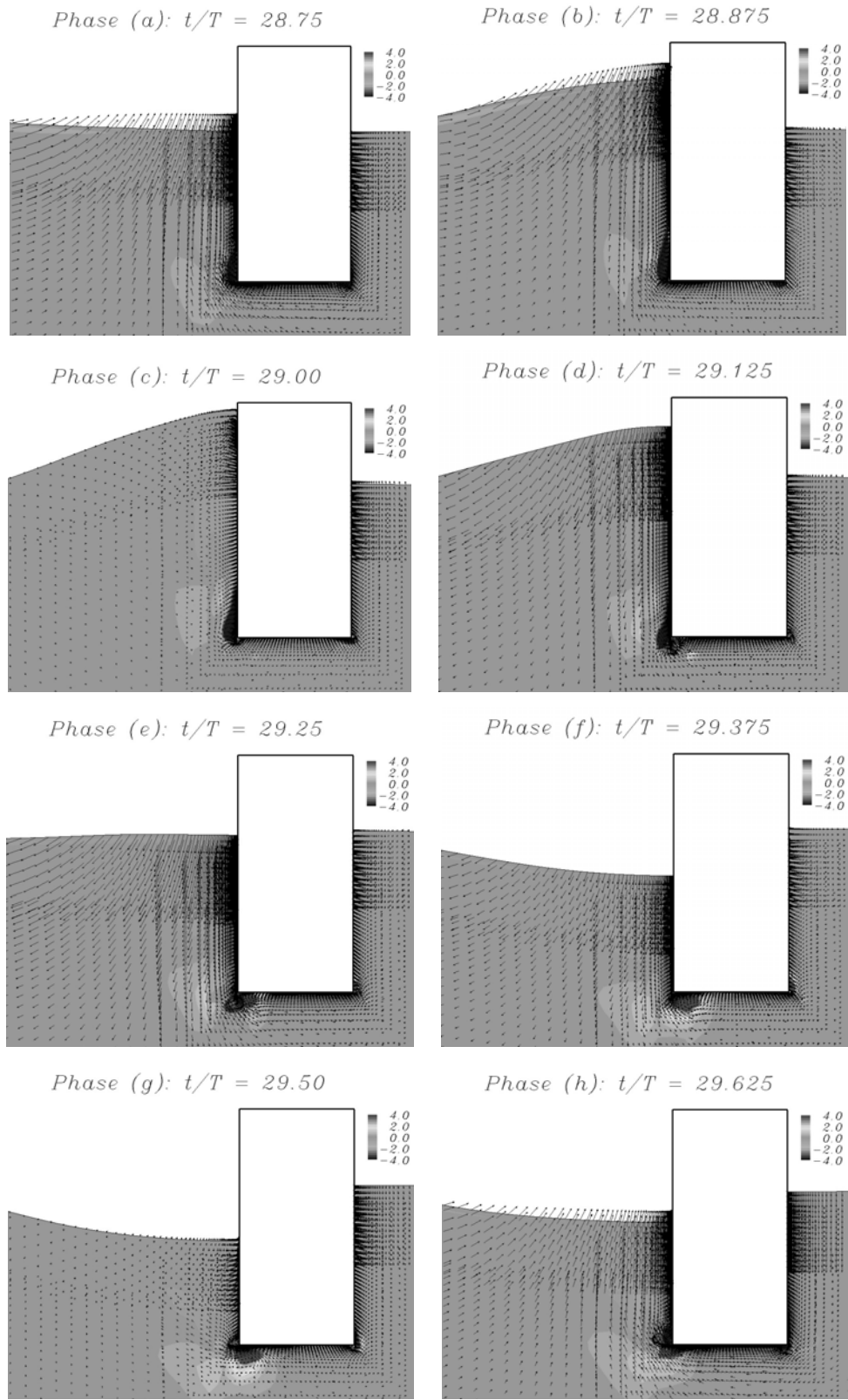
Figure 5.6: Vorticity contours and velocity vectors at eight different phases; $H = 0.0875$m.

For completeness, comparisons were made between the numerical results and the corresponding PIV measurement data to provide a detailed assessment on the predictive capability of the present chimera RANS method. Figure 5.7 shows the predicted and measured velocity field at eight different time instants over one wave period. It is clearly seen that the numerical results are in close agreement with the corresponding experimental data for the $H = 0.0875$ m case. Similar level of agreement was also observed for the $H = 0.0575$ m case. These results clearly demonstrate the capability of the present chimera RANS method for accurate prediction of the wave runup around offshore platforms.
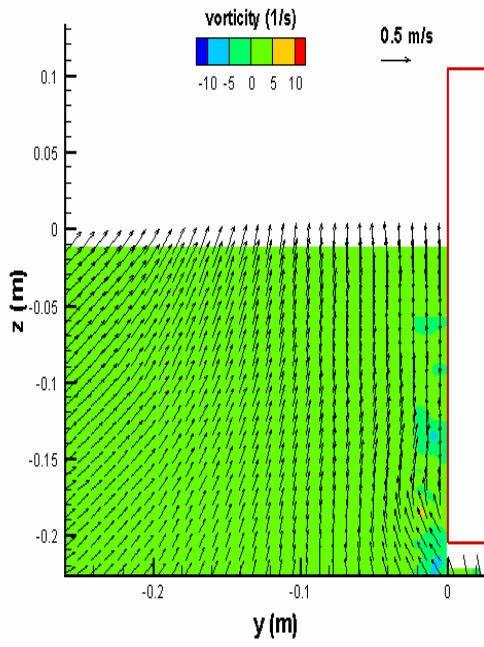
Phase (a)
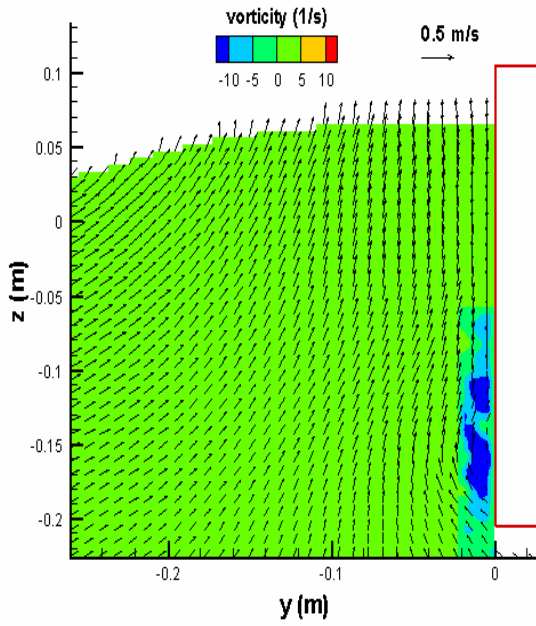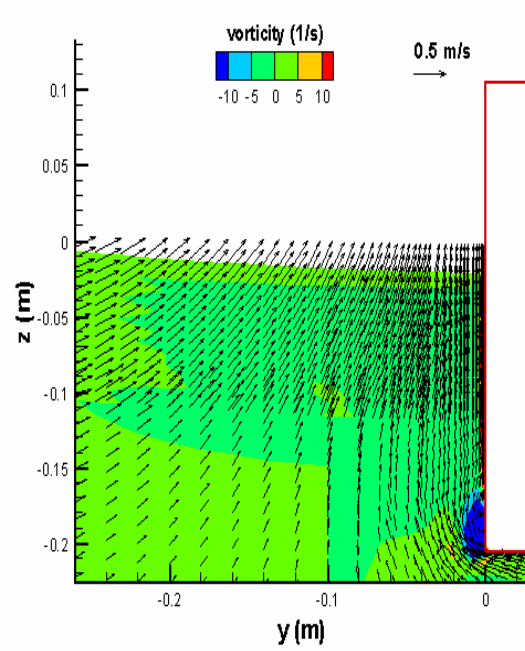
Phase (b)
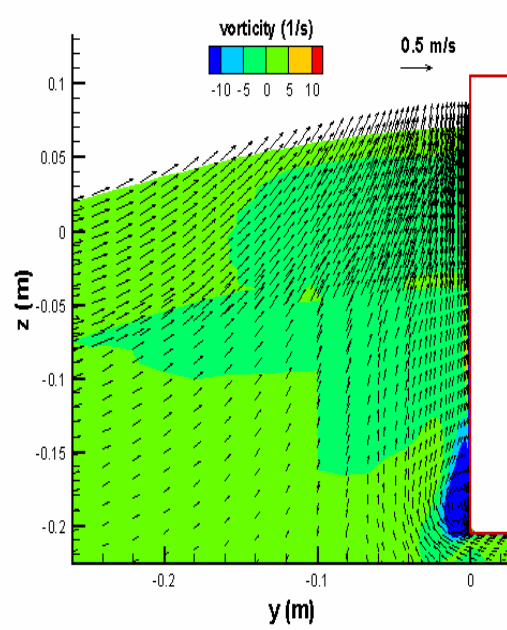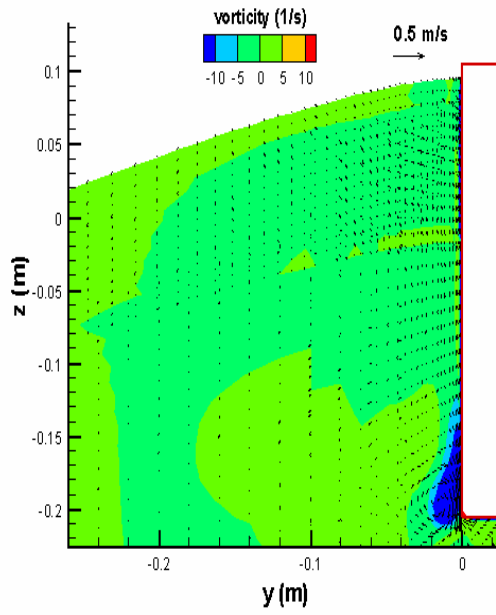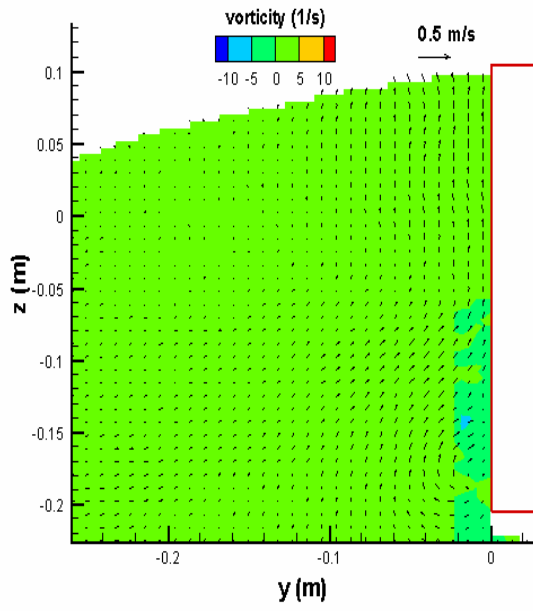
Phase (c)
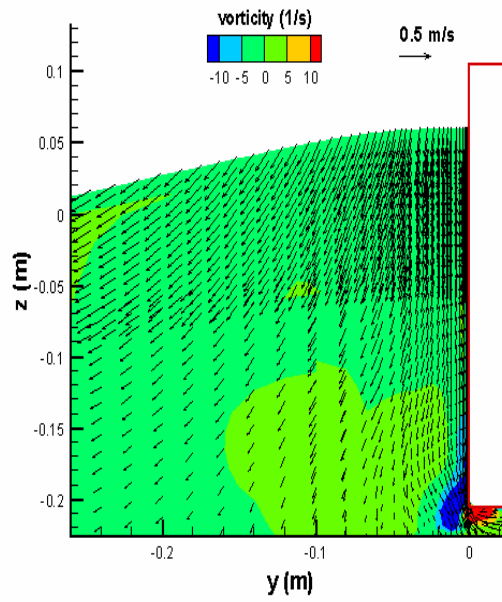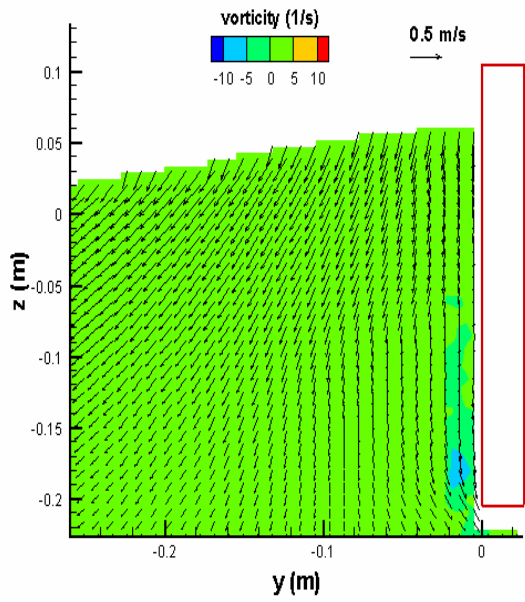
Phase (d)
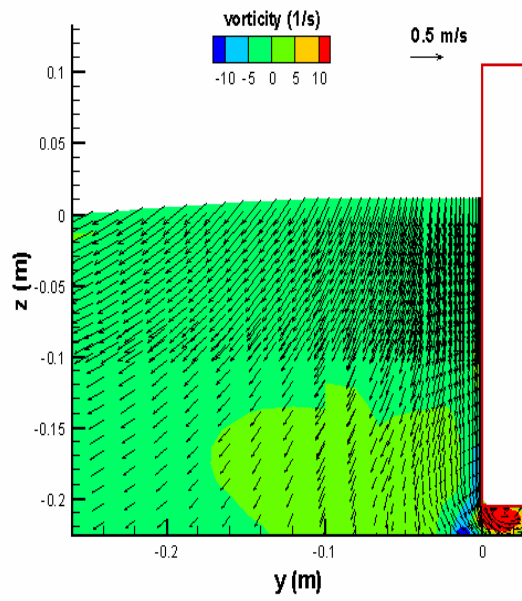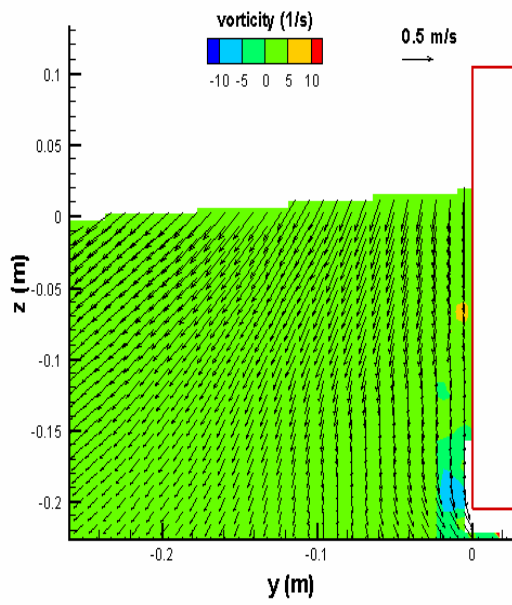
Phase (e)
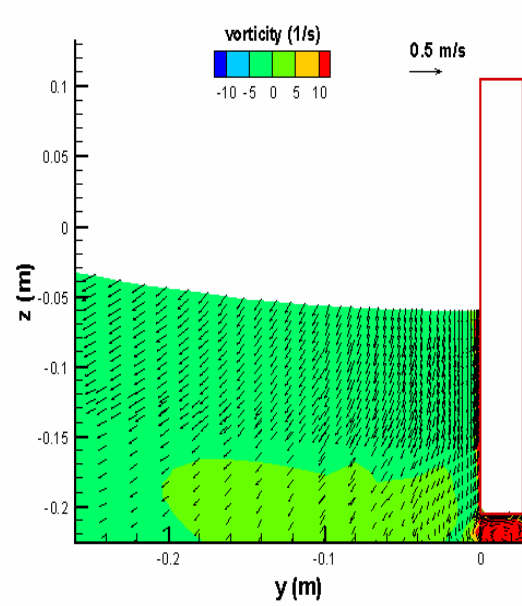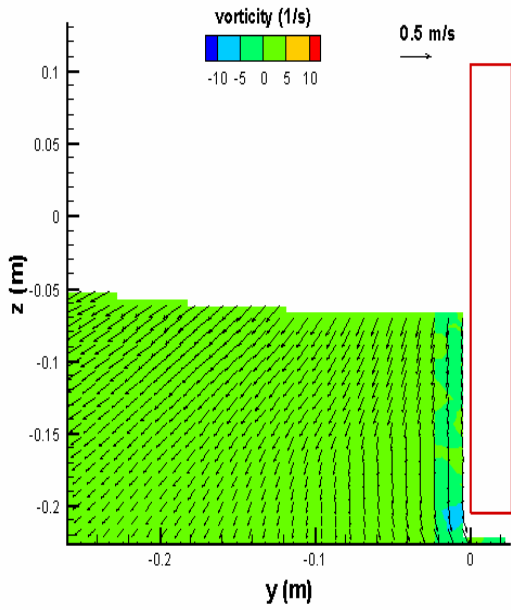
Phase (f)
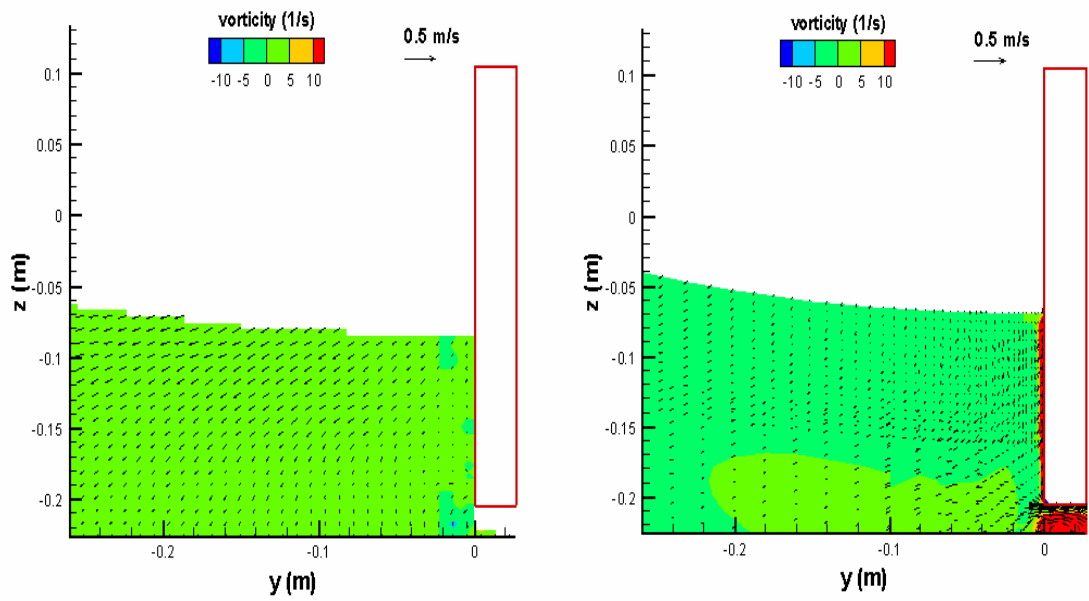
Phase (g)
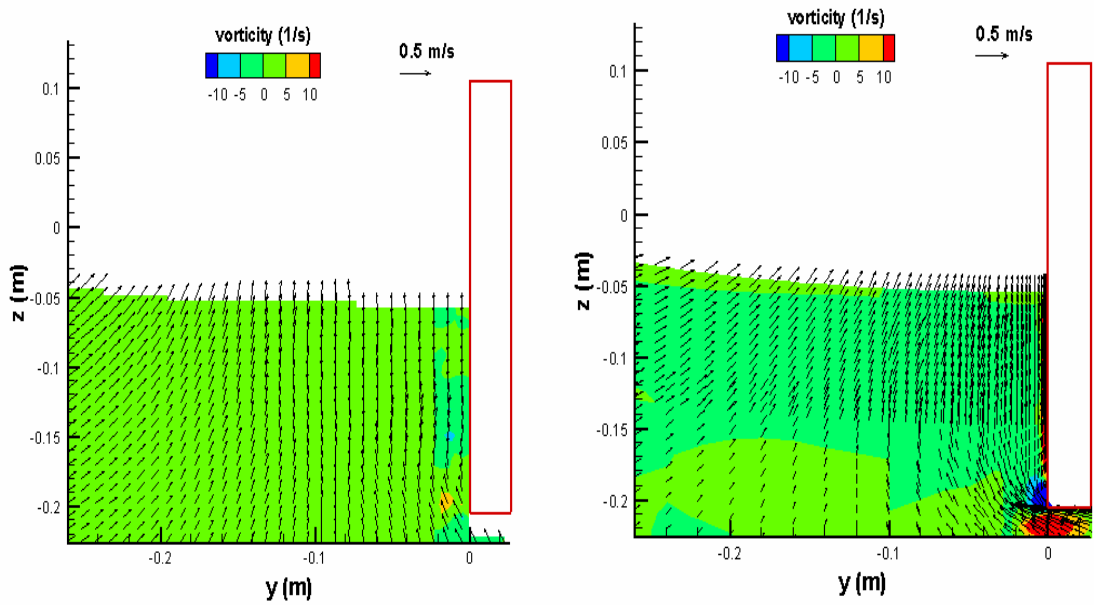
Phase (h)

Figure 5.7: Comparison of measured (left) and calculated (right) vorticity contours and velocity vectors at eight different phases within one wave period; $H = 0.0875$m.

After successful validations of the chimera RANS method for two-dimensional platform configurations, the method was further generalized for time-domain simulation of wave runup around single and multiple vertical cylinders which are common structural elements of TLP and other types of offshore structures. Figure 5.8 shows the numerical grids around three vertical cylinders. In the chimera domain decomposition approach, it is convenient to use overset grid system with body-fitted cylindrical grids embedded in the background rectangular grids. For the fully nonlinear waves considered here, the numerical grids are updated every time step to conform with the exact free surface.
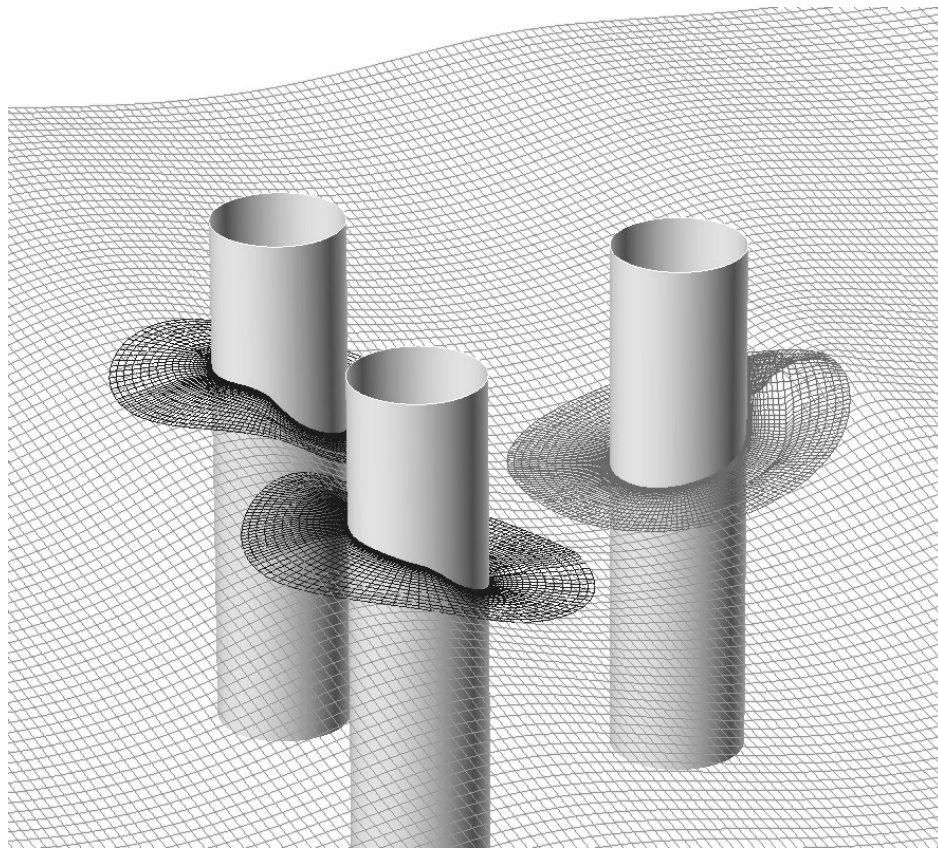
Figure 5.8: Chimera grids around vertical cylinders

Figure 5.9 shows the computed wave elevation and pressure contours around a single vertical cylinder. The incident wave height is $H/D = 0.1$ and the incident wavelength is $\lambda/D = 6.28$, where D is the diameter of the cylinder. The absorbing beaches were placed on all outgoing flow boundaries including the downstream boundary and the side walls. In addition, the wavemaker absorbing beach described earlier was used in front of the wavemaker boundary to absorb the reflected and deflected waves. The maximum wave height is nearly two times of the incident wave height as seen at $t/T = 0.45$. It is clearly seen that interaction of incident and diffracted waves produces a distinct ring wave diffraction pattern similar to those observed in Chen and Huang (2004) for wave diffraction around breakwaters and other coastal structures.

(a) $t/T = 2.0$

(b) $t/T = 3.0$

(c) $t/T = 3.75$

(d) $t/T = 4.0$

(e) *t/T* = **4.25**   **(f)** *t/T* = **4.5**

Figure 5.9: Free surface pressure contours around a single vertical cylinder

Time-domain simulations were also performed for wave diffraction around three vertical cylinders. The center-to-center spacing between the two front cylinders is 2.96 *D*, where *D* is the diameter of the cylinder. The third cylinder is placed at 2.56 *D* (center-to-center) downstream of the two front cylinders. Figure 5.10 shows the predicted wave patterns at *t/T* = 0.55, 0.60, 0.64, 0.66, 0.68 and 0.70. The incident wavelength specified in the present simulation is λ/D = 5.62 and the incident wave height is *H/D* = 0.30. The simulation results clearly indicated the presence of strong interactions between the two front cylinders in side-by-side arrangement. It is also seen that the wave runup on the downstream cylinder is almost completely out-of-phase in comparison with the front cylinders since the wavelength is about twice of the cylinder spacing. Moreover, the wave diffraction pattern on the downstream cylinder is significantly different from that of the single cylinder case. This is clearly due to the strong interactions among the three vertical cylinders.

(a) *t/T* = **5.5**

(b) *t/T* = **6.0**

(c) *t/T* = **6.4**

(d) *t/T* = **6.6**
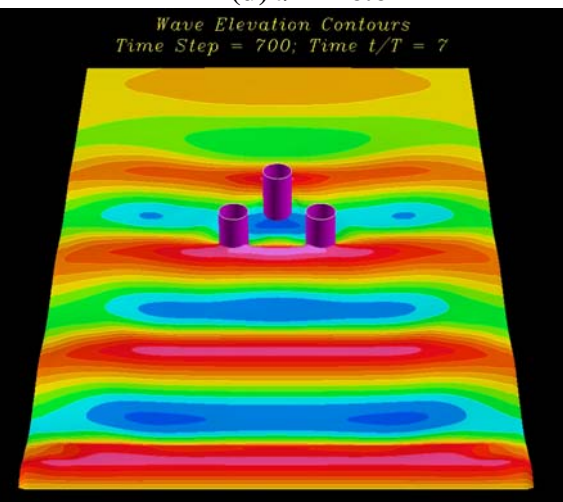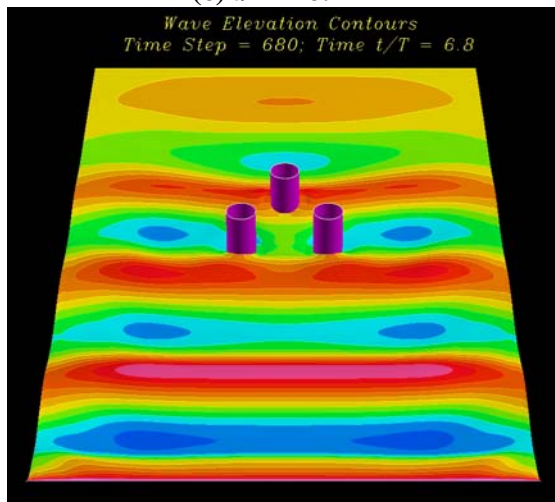
(e) *t/T* = **6.8**

(f) *t/T* = **7.0**

Figure 5.10: Free surface pressure contours around three vertical cylinders

5.2 Validation of Interface-Capturing Method

5.2.1 Re-distancing Test

In order to test the re-distancing procedure in level set method, we initialize a discontinuous level set function in a non-uniform rectangular grid with 101×101 grid points. The domain size is 1.0 $\times 1.0$ and the interface is a circle centered at (0.5, 0.5) with a radius of 0.25. The level set function is initially assigned a value of -0.1 outside the circle and $+0.1$ inside the circle as shown in Figure 5.11. We choose the artificial time increment to be the smallest grid size, i.e., $\Delta t = 0.005$. It can be shown in this test case that we need only to recalculate the level set ϕ for $L/\Delta t$ time steps to obtain the correct distance up to L.
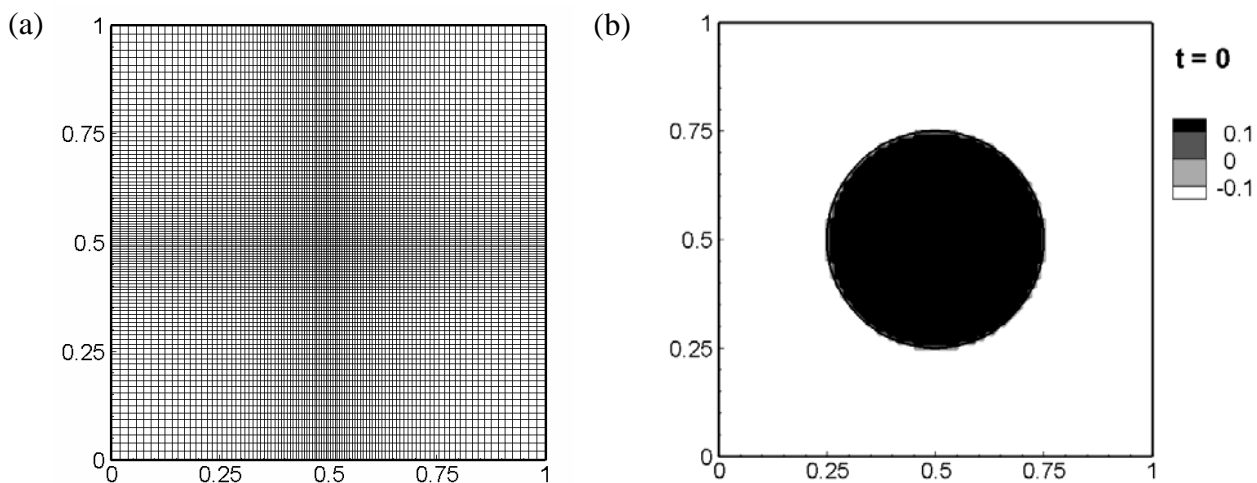
Figure 5.11: Re-distance of a circle: (a) numerical grid and (b) initial level set contours

Figure 5.12 shows the contours of ϕ at different artificial time t = 0.1, 0.2, 0.3, 0.4. It is seen that the devolution of ϕ starts from the interface where the zero level set is, and propagate on both sides of the interface. Theoretically, ϕ is the physical distance (i.e., $|\nabla \phi| = 1$) from the zero level set in the circle whose radius is equal to the artificial time t. It is clearly seen from Figure 2 that the zero level set does not change during the calculation. If we continue the calculations for more time steps until the steady state is reached, then ϕ will represent the physical distance from the interface over

the entire domain as shown in the last image at $t = 0.4$. We also repeated the same calculation with uniform grid spacing and obtained exactly the same result. This test case provided a good indication on the number of time steps needed for the re-distance procedure. In our numerical simulations, the initial level set is typically very close to the physical distance. Therefore, very few time steps are needed to obtain the steady state solution in the re-distance procedure. More specifically, we have chosen a transition zone width of two times of grid size and a time increment of one grid size. Therefore, only two iterations are needed in the present simulations for re-distancing of the level set function.
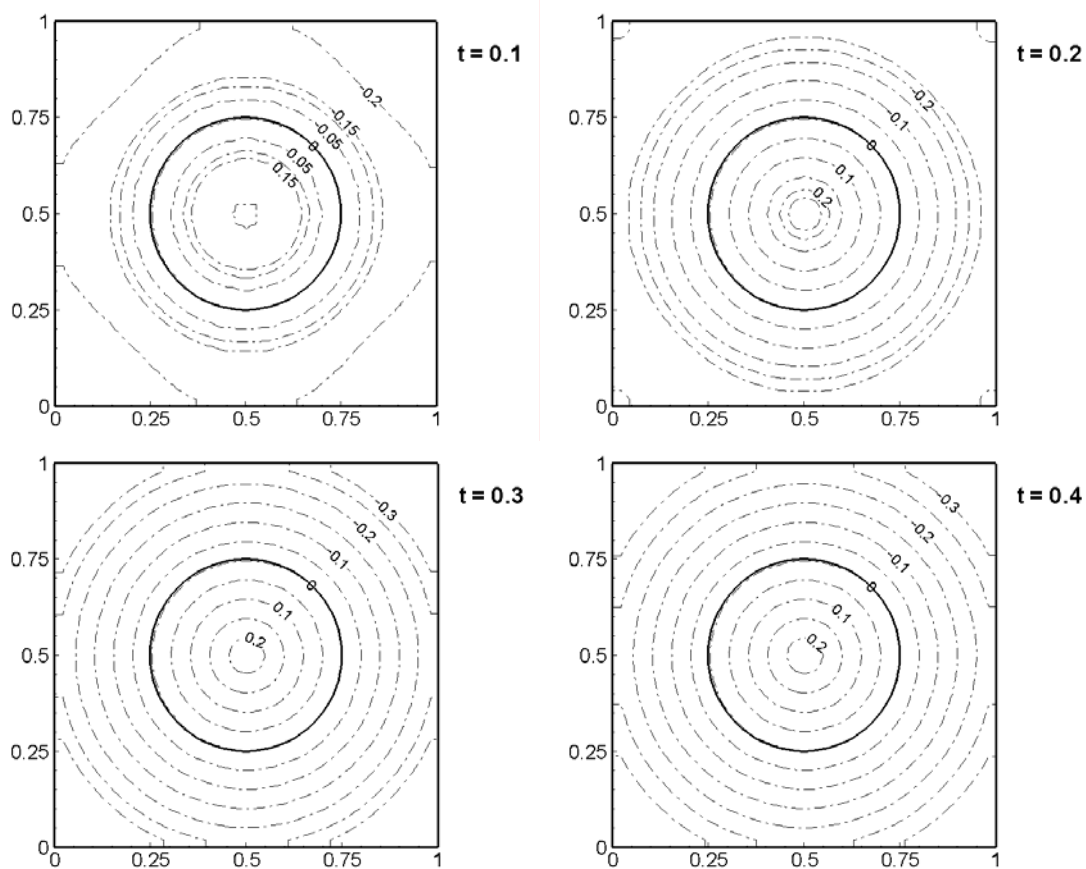
Figure 5.12: Evolution of level set contours at $t = 0.1, 0.2, 0.3, 0.4$

5.2.2 Zalesak's Problem

The Zalesak's problem of a rotating slotted disk is a benchmark case for testing an advection scheme. It consists of a slotted solid disk rotates around a center with a constant angular velocity. The slotted disk has a radius of 15 and a lot width of 6. It is initially located at (50, 75) in the domain of size (100, 100). The angular velocity Ω is set to 0.01 so that the disk returns to its original position at every 200π (≈ 628) time units. Figure 5.13 shows the numerical grids and the computed slotted disk edges (solid lines) at t = 0, 157, 314, 471 and 628. The dotted line in Figure 3(b) denotes the initial geometry of disk, while the dashed line represents the predicted disk geometry without imposing the mass constraint in the re-distancing procedure. It is seen that the slotted disk matches its original shape very well after one complete cycle of rotation except for some minor rounding of the sharp corners. This clearly demonstrated that the mass constraint term in Equation (4.7) is very effective in maintaining the overall mass conservation during the disk rotation.
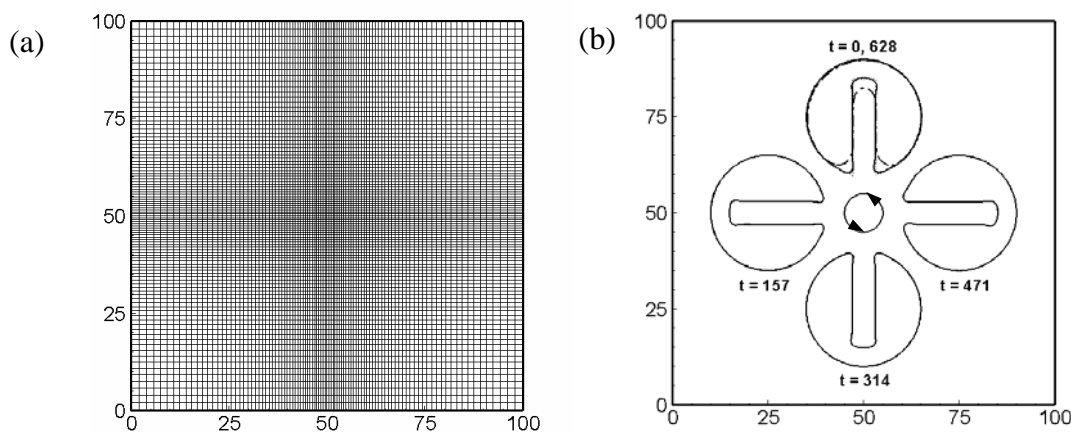
Figure 5.13:   Zalesk's problem: (a) numerical grid and (b) predicted interfaces

5.2.3 Stretching of a Circular Fluid Element

In the third test case, a circular fluid element is placed in a swirling shear flow field within a unit square. The flow field is prescribed in term of a two-dimensional stream function φ:

$$\varphi = \frac{1}{\pi}\sin^2(\pi y)\sin^2(\pi z)$$

This corresponds to a solenoidal velocity field with the following velocity components:

$$v = -\sin^2(\frac{\pi y}{100})\sin(\frac{\pi z}{50})$$

$$w = \sin^2(\frac{\pi z}{100})\sin(\frac{\pi y}{50})$$

The circular fluid element is stretched into a thin filament by the shearing velocity field as shown in Figure 5.14. This case provides a challenging test for surface-tracking and surface-capturing methods. The circle is initially centered at (50, 75) with a radius of 15. The total mass $M(t) = \int_{\Omega} H(\phi)d\Omega$ is evaluated at every time step to monitor the performance of the mass constraint term. As shown in Figure 5.15, the total mass decreases slightly from 706.858 to 704.694 (i.e., 0.3%). Therefore, the mass constraint term is very effective in maintaining global mass conservation during the advection of interfaces.
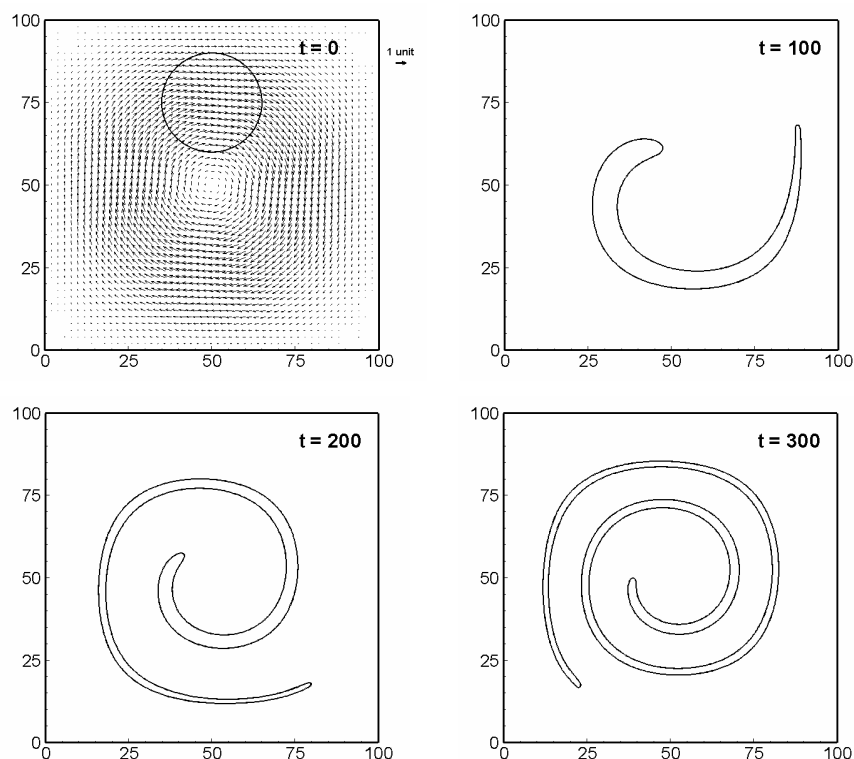
Figure 5.14: Stretching of a circular fluid element in swirling flow
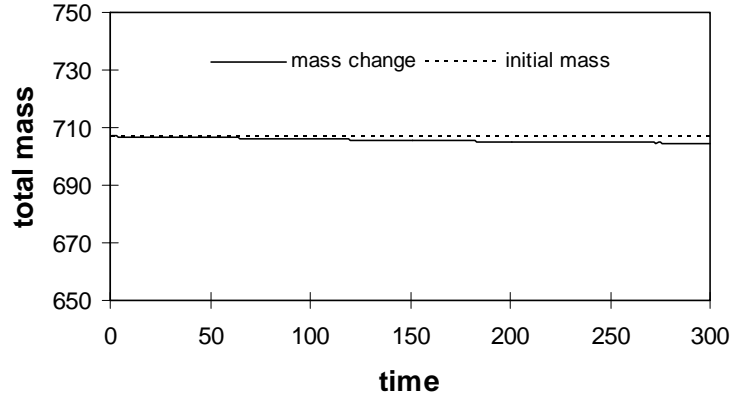
Figure 5.15: Time history of mass change in the stretching of a circular fluid element

5.2.4 Stretching and Restoration of a Circular Fluid Element

The last test case of the interface-capturing and re-distancing procedures involves the stretching and restoration (shrinking) of a circular fluid element. In this case, the circular fluid element is subjected to a swirling flow with oscillatory velocity components given by:

$$v = -\sin^2(\frac{\pi y}{100})\sin(\frac{\pi z}{50})\cos(\frac{\pi t}{T})$$

$$w = \sin^2(\frac{\pi z}{100})\sin(\frac{\pi y}{50})\cos(\frac{\pi t}{T})$$

It is worthwhile to note that the initial velocity field for the present swirling flow is identical to that considered in the previous test case. However, the swirling velocity decreases gradually as the circular fluid element is stretched out during $0 < t < T/2$. At $T/2$, the flow came to a complete stop and begins to reverse its direction. During $T/2 < t < T$, the stretched fluid element shrinks back gradually due to the reversal of the swirling flow direction. The fluid element is expected to recover its initial circular shape at $t = T$ for a perfect interface-capturing scheme. It is seen from Figure 5.16 that the present interface-capturing technique successfully restored the original shape of the circular fluid element. As noted in Figure 5.17 there is a very slight reduction of the total mass $M(t) = \int_\Omega H(\phi)d\Omega$ from 706.858 to 701.845 (i.e., 0.7%) after one complete cycle.
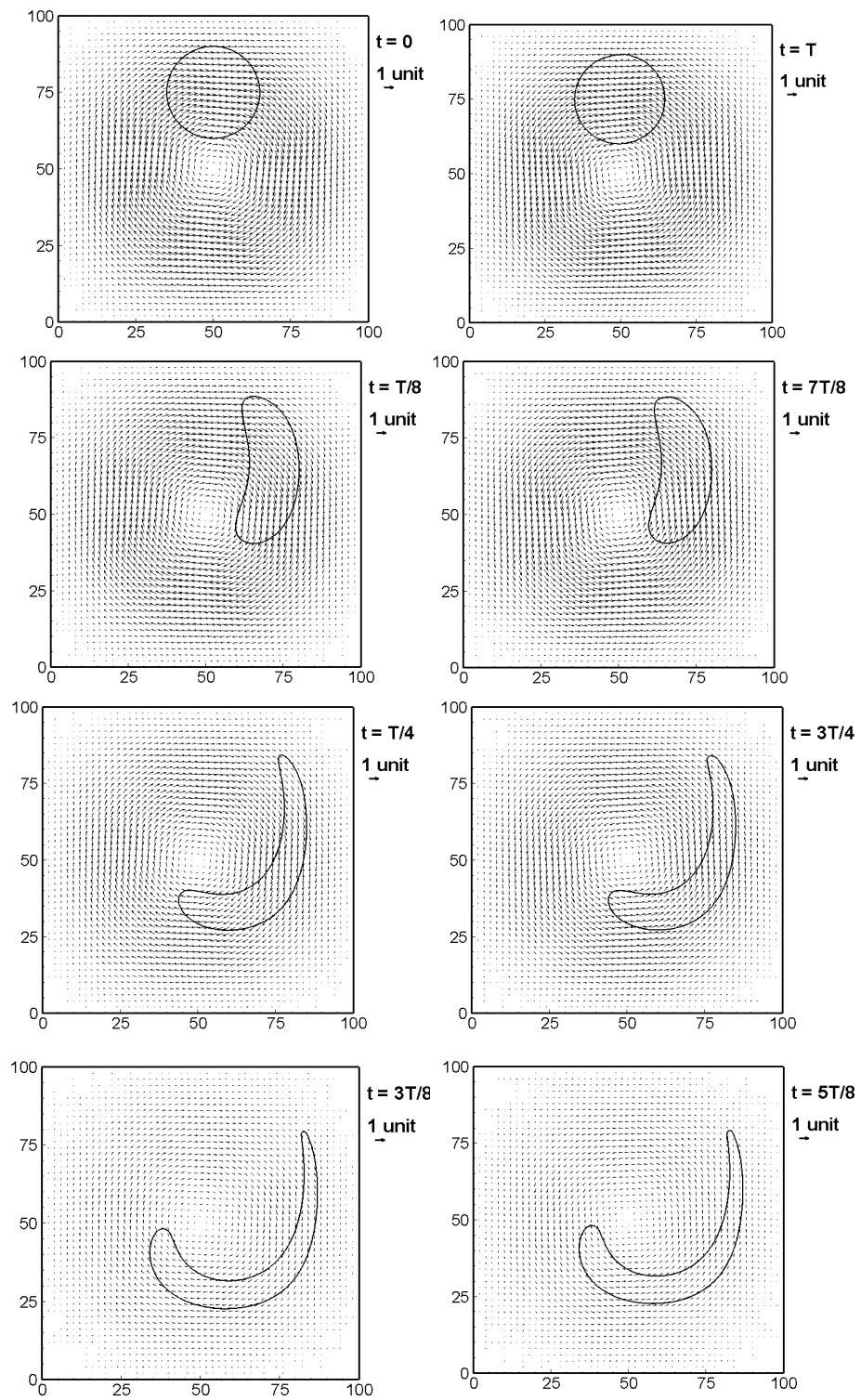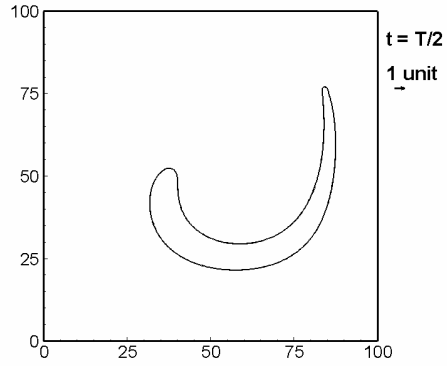
Figure 5.16: The evolution of level set during stretching /shrinking of a circular fluid element
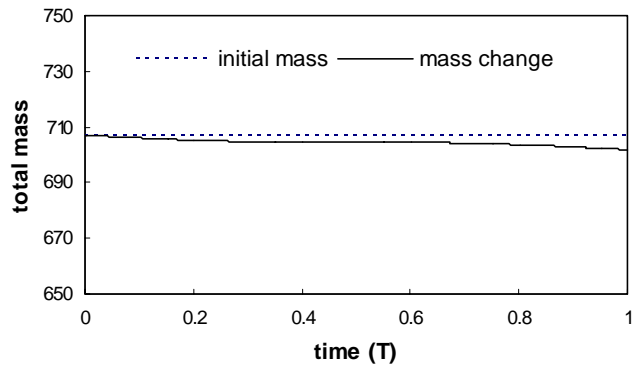
Figure 5.17: Time history of mass change in the stretching/shrinking of a circular fluid element

5.3 Green water on Offshore Platform

5.3.1 Traveling Solitary Wave

  Propagation of a solitary wave is a simple and practical free surface problem that has been studied experimentally and numerically. To generate a solitary wave, one can make use of the Laitone's analytical approximation. Here we release an initially still water surface with a Boussinesq profile from the left vertical wall which is in hydrostatic balance.

$$A(y,0) = A_0 \Big/ \cosh^2(\frac{\sqrt{3A_0} \cdot y}{2})$$

  Figure 5.18 shows the wave profile at different time for the $A_0 = 0.4$ case. The corresponding velocity profile at t = 10 s is shown in Figure 5.19. It is seen that the wave amplitude decay slightly during propagation as a result of the viscous effects.
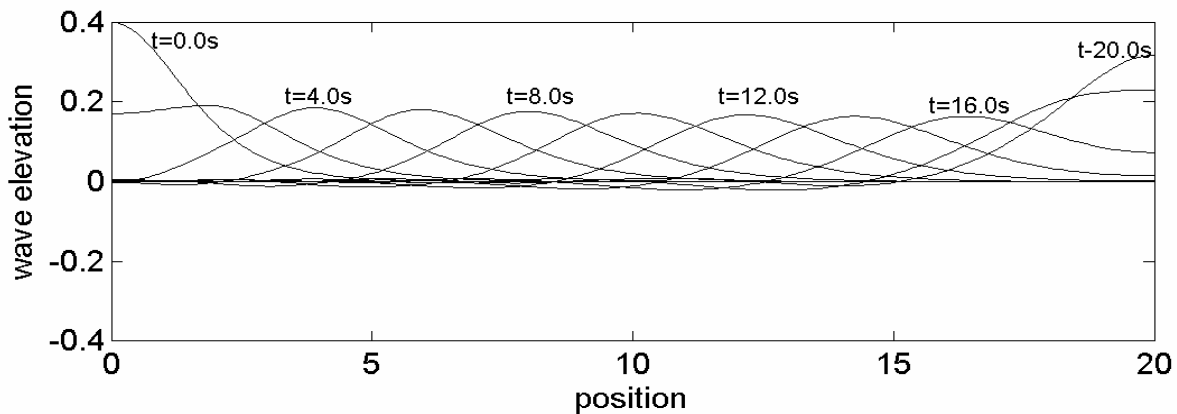
Figure 5.18: Propagation of solitary wave; $A_0 = 0.4$
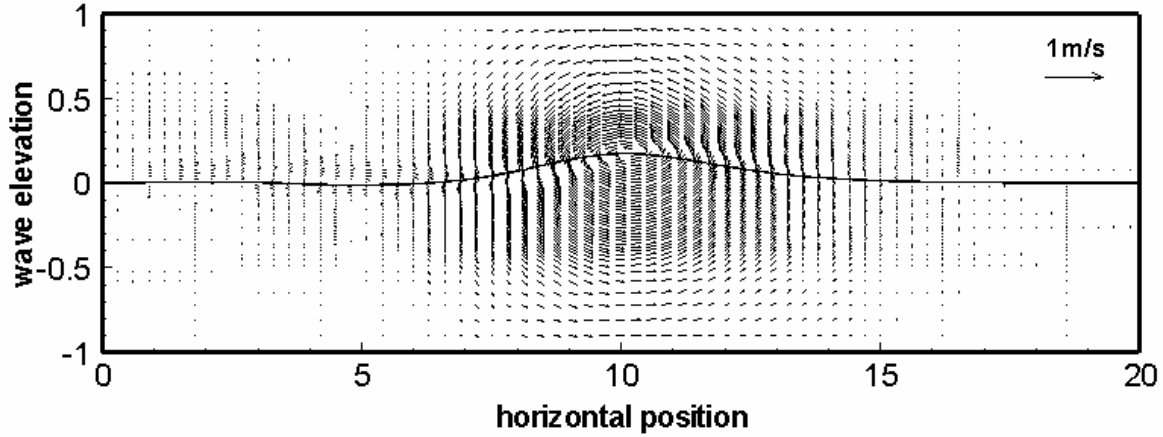
Figure 5.19: Typical velocity field of a solitary wave

To quantify the viscous damping characteristics of the wave, we compute three waves with different initial amplitude, and compare the results with those predicted by the perturbation theory of Mei (1989):

$$A^{-1/4} = A_0^{-1/4} + 0.08356 \left(\frac{\nu}{(gh)^{1/2} h^{3/2}} \right)^{1/2} \frac{Ct}{h}$$

where Ct is essentially the distance traveled by the solitary wave. This formula has been verified against the measurements of Russell. In this study, we set the theoretical wave velocity $C = \sqrt{gh}$ = 1 m/s and the water dynamic viscosity $\nu = 2.0 \times 10^{-6} m^2/s$. This gives a Reynolds number $Re = \frac{Ch}{\nu} = 5 \times 10^4$. It is seen from Figure 5.20 that the present simulation result is in close agreement with the perturbation theory in the middle section of the tank. The discrepancies on the right hand side of the tank are due to the reflection of the solitary wave by the tank wall.
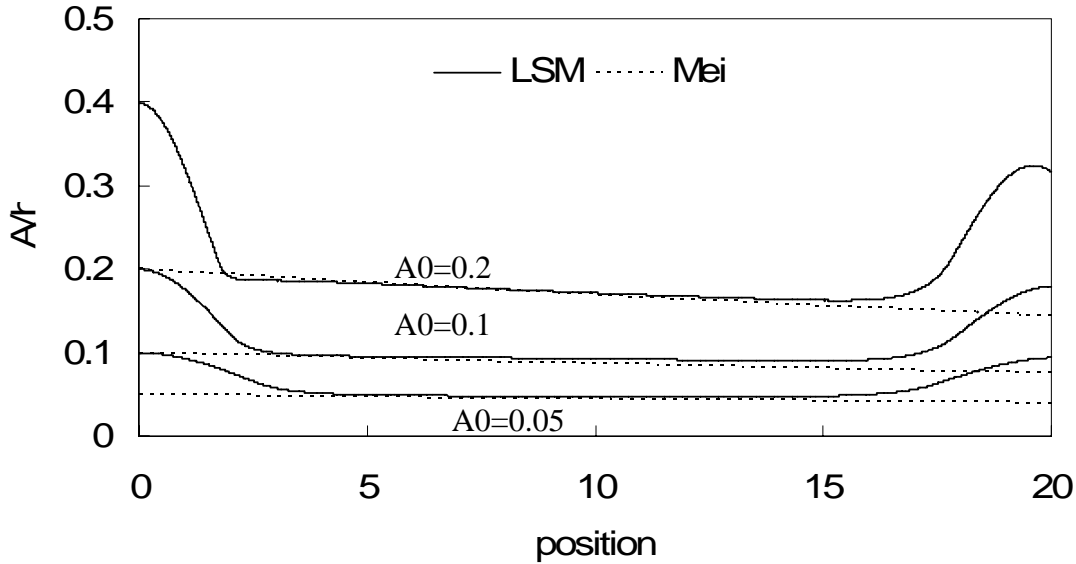
Figure 5.20: Comparison of the calculated and theoretical solitary wave amplitude

5.3.2 Dam-Breaking Problem

The collapse of a water column on a rigid horizontal plane is also called a broken-dam problem. It is used to simulate the abrupt failure of a dam, in which an initially blocked still water column starts to spread out after the barrier is removed. The dam-breaking problem has been the subject of many previous numerical and experimental investigations. In our simulation, the computational domain size is 2.0×5.0, and the parameters used in this study are the same as those used earlier in solitary wave simulation. The half-thickness of the air-water interface ε is fixed at two times of grid spacing, and the time step size used in the re-distancing procedure is equal to one grid spacing. Figure 5.21 shows snapshots of water surface profiles and the associated velocity fields for air and water in the entire computational domain at selected time instants. Initially, the water column is in hydrostatic balance with pressure linearly proportional to the water depth. When the vertical barrier is removed at t = 0, the water column collapses and flushes to the right due to the large pressure difference between the water and air at the interface. When the front of the water column hits the tank wall, it was pushed upward against the wall by the momentum of the water flow. As the water climbs up the tank wall, the front velocity decreases gradually as the fluid momentum is being converted to potential energy. After the water front comes to a complete stop on the tank wall, it begins to fall back into the bottom water pool due to the gravitational force. The collision

of falling water mass with the water in the pool produces a splash wave traveling to the left with a thin and elongated surge front. Several air pockets were observed when the simulation was terminated at t = 8.0 s. It is also clearly seen from the velocity vector plots that the violent free surface motions also induce very strong vortices at the surge front.

It has been demonstrated in previous studies by Chen (2005) that the chimera domain decomposition approach provides an effective means to deal with complex geometry and flow conditions by allowing the judicial use of grid overlapping or embedding techniques to simplify the grid generation process. The chimera grid system also allows for selective refinement of the numerical grids in areas of high gradient without significant increase on the overall computing cost. In the present study, the feasibility of using chimera domain decomposition approach in conjunction with level set function was demonstrated for the dam-breaking problem using two composite grid systems shown in Figure 5.22. In both cases, we made a hole in our computational domain first, and then patched the hole with two different grids, a rectangular grid and a semi-circular grid. In the chimera domain decomposition approach, the PEGSUS program of Suhs and Tramel (1991) was employed to identify the hole points and provide interpolation information for the hole fringe points as well as the outer boundary points for the embedded grid blocks.

Figure 5.23 shows the simulation results for two different grid embedding systems. It is clearly seen that the air-water interface remains smooth across the overlap region between different computational blocks. This indicates that the interpolation of velocity, pressure, turbulence quantities, and level-set function, is robust and accurate for arbitrary grid systems. A detailed comparison of the water surfaces and velocity vector plots in Figures 5.22 and 5.23, however, indicates that the air-water interface is somewhat affected by different implementation of the grid-capturing technique in different computational blocks. More specifically, the half thickness of the interface was chosen to be equal to two grid spacing in all three cases. Since the grid sizes are significantly different for two different grid patches, the predicted water surface profiles and air bubble sizes was found to change slightly at later stages of the simulation beyond t > 6 s. There is a slight phase lag of the surge front for the semi-circular grid case. Nevertheless, the velocity fields induced by the violent free surface motion are quite similar for all three test grids as seen in Figure 5.24.

The figure shows a two-column series of panels at times t = 0.0s, t = 1.2s, t = 2.6s, t = 4.2s, t = 5.6s, t = 6.6s, and t = 7.2s. Each panel spans 0 to 5 horizontally and 0 to 1.5 vertically. The left column shows colored contour plots (red and blue) of the fluid distribution; the right column shows the corresponding velocity vector fields with a 1 m/s scale arrow.
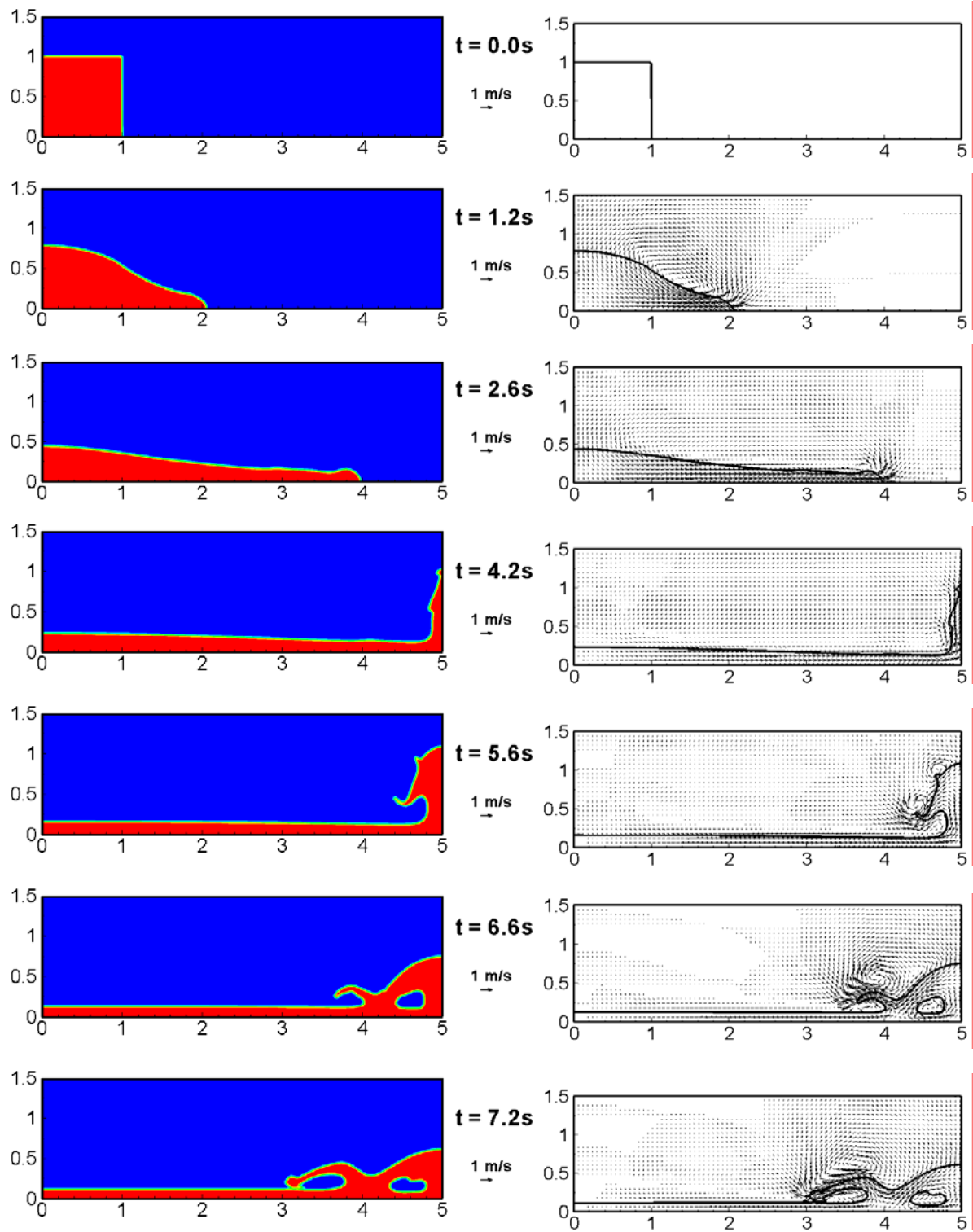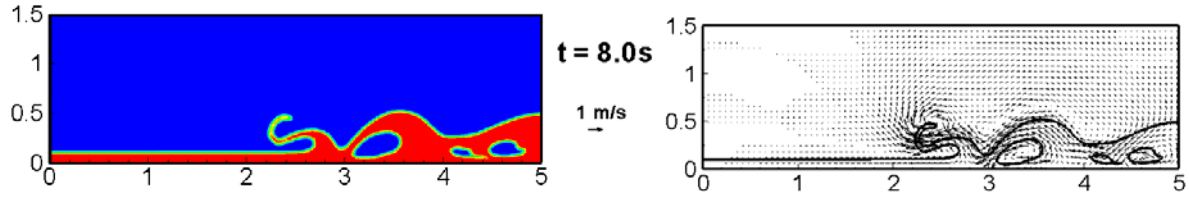
Figure 5.21: Free Surface profiles and velocity vectors for dam-breaking problem at selected time instants
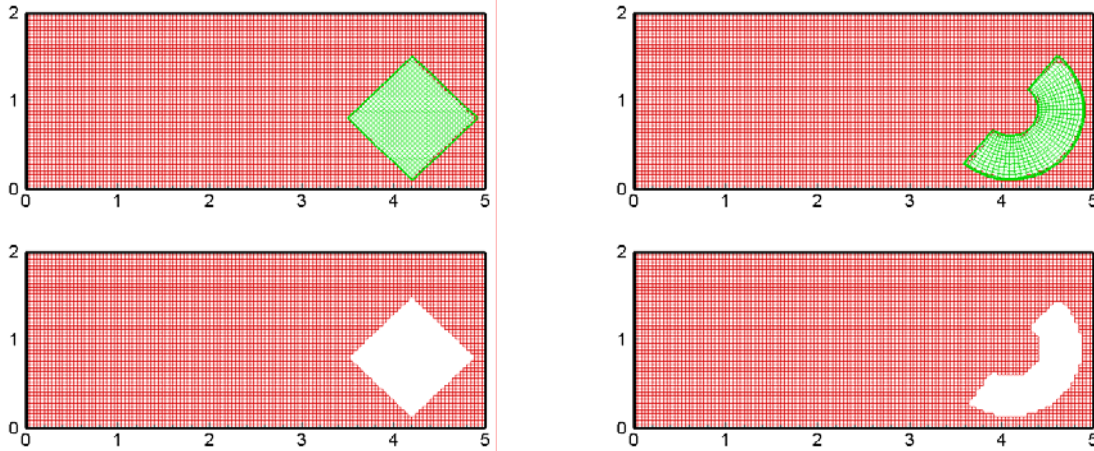
Figure 5.22: Chimera grids for dam-breaking problems
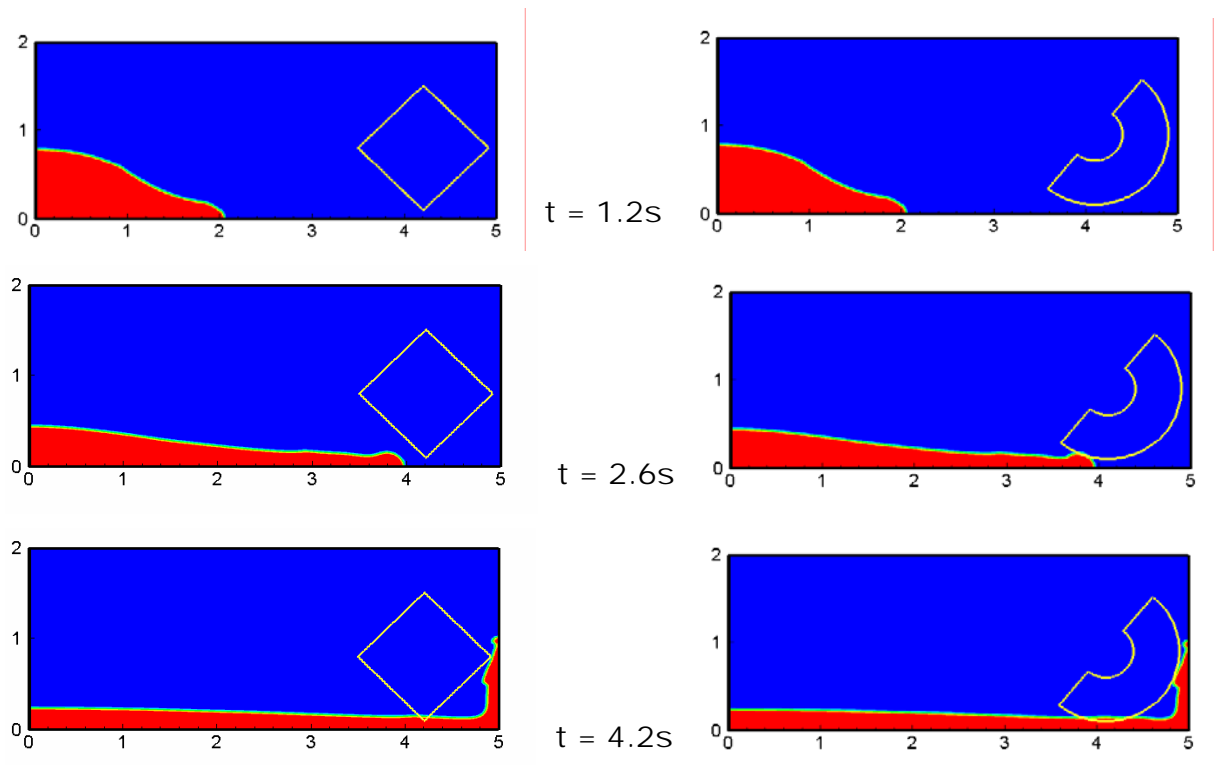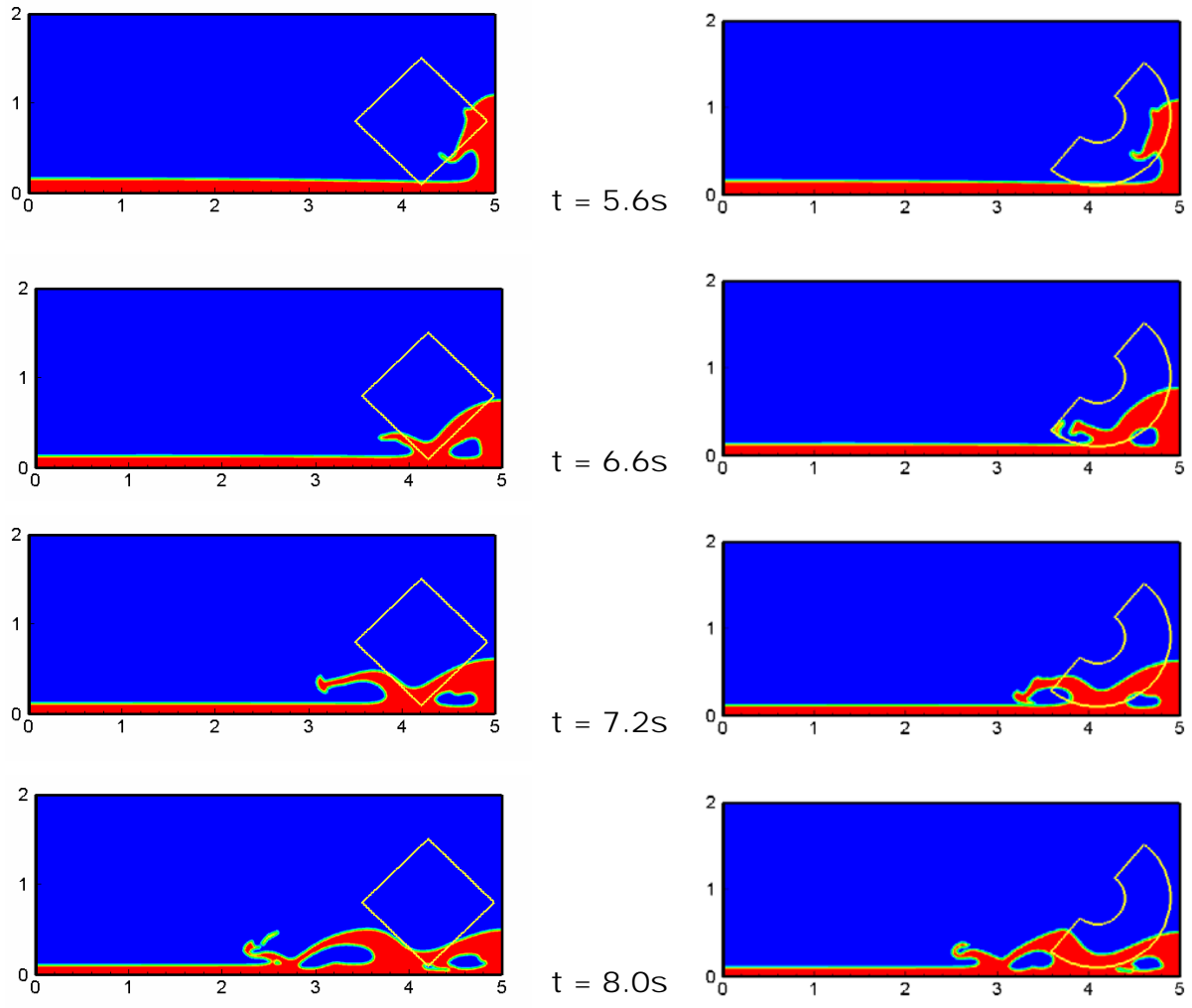
Figure 5.23: Simulation of dam-breaking problems with two different embedding grids
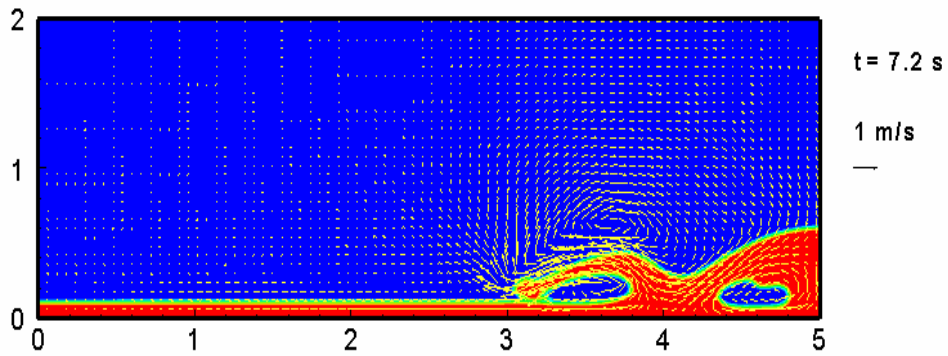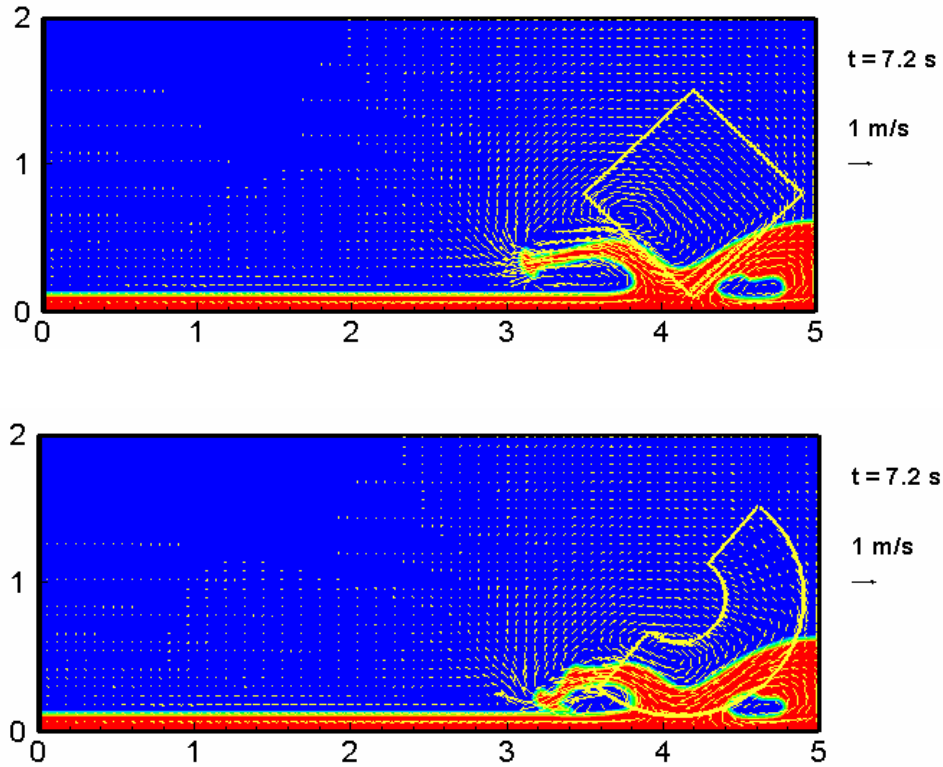
Figure 5.24: Comparison of velocity fields for dam-breaking problem with three different grids

5.3.3 Dam Breaking with an Obstacle

A more interesting test case of collapsing water column occurs when a small obstacle is placed downstream of the propagating water front. The test geometry used in the experimental investigation of Koshizuka et al. (1995) is illustrated in Figure 5.25. The height and width of the still water column are 2a and a (i.e., 0.292m × 0.146 m), respectively. The width of the tank is 4a (= 0.584 m) and the obstacle is located on the bottom wall at a distance of 2a (= 0.292 m) from the left wall. The size of the obstacle is 2d × d (0.048 m × 0.024 m). In the present study, we choose a = 0.146 m as the characteristic length. The computational domain after normalization is shown in Figure 5.26.
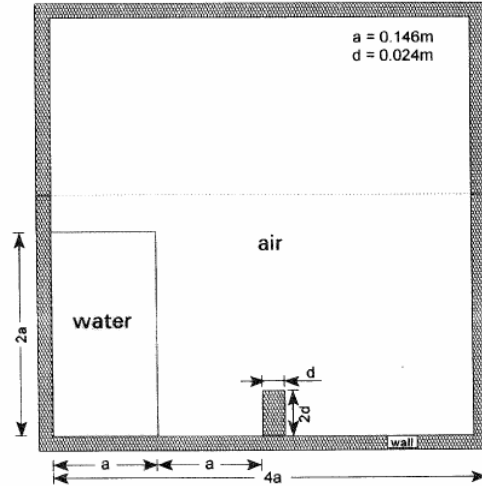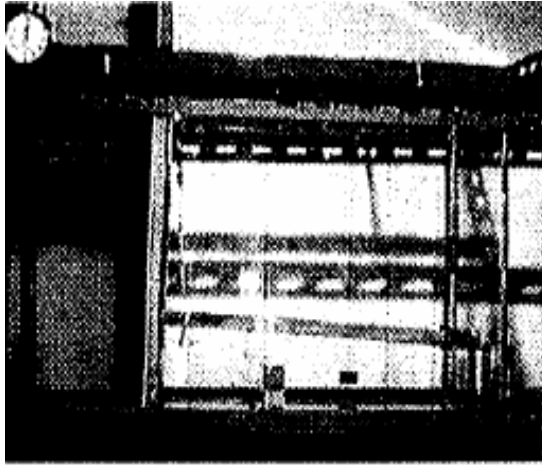
Figure 5.25: Experiment setup of dam-breaking with an obstacle
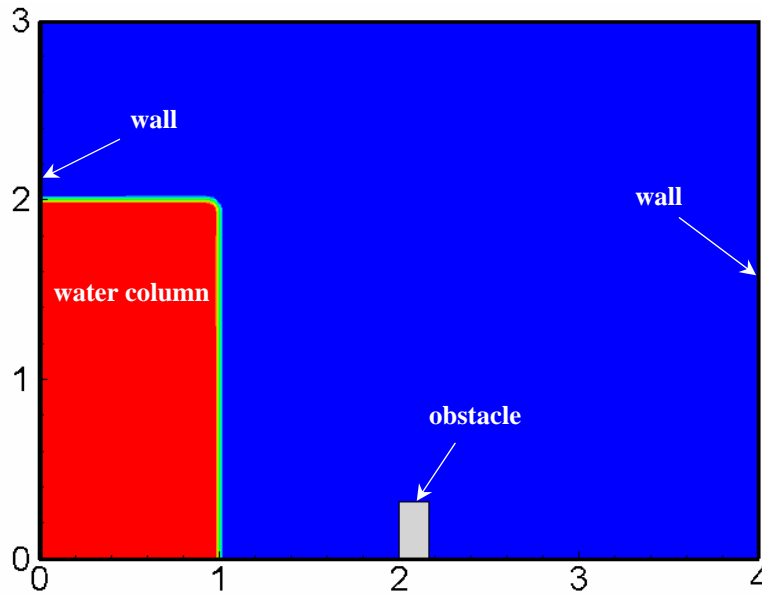
Figure 5.26: Computational domain for dam-breaking with an obstacle

Figure 5.27 shows a comparison between the experimental data and simulation results. At $t = 0$, the barrier holding the still water column was suddenly removed. The collapsed water column crashes upon the obstacle and produced a free jet with strong upward flow velocity. The jet continues to move to the right and eventually impinges on the vertical wall on the right hand side of

the tank. As the water moves towards the right side of the tank, the jet trajectory becomes considerably flatter due to the gradual decrease of the upward jet velocity under its own weight. After impingement against the vertical wall, the jet is split into two streams moving vertically upward and downward along the tank wall.   As the water level drops on the left hand side of the tank, the fluid momentum reduces gradually and the jet trajectory was deflated further downward under the gravitational force. In general, the numerical results are in close agreement with the corresponding experimental data of Koshizuka et al. (1995). This test case clearly illustrated the capability of the level set method in capturing violent free surface motions encountered in dam breaking problems. The same method can also be used for the simulation of vigorous sloshing in tanks and slamming of bodies onto liquid surface.
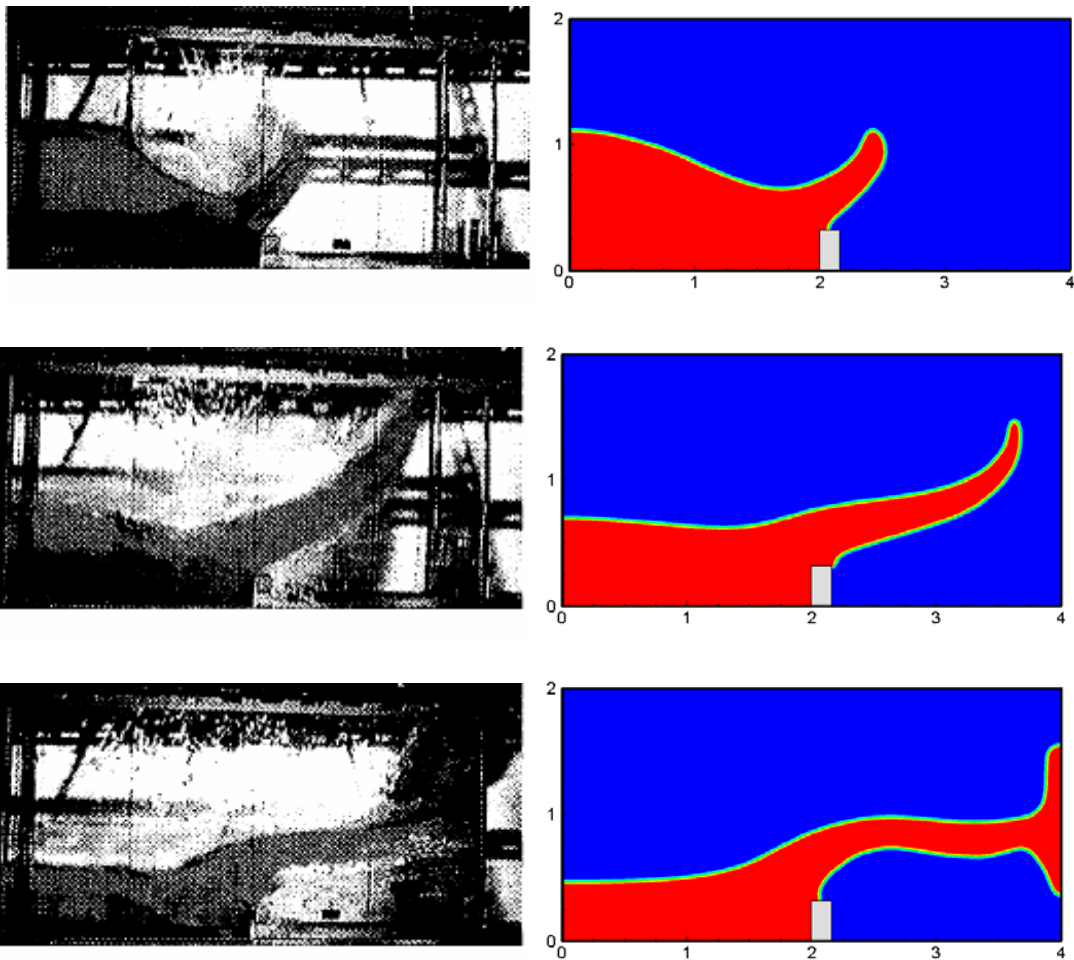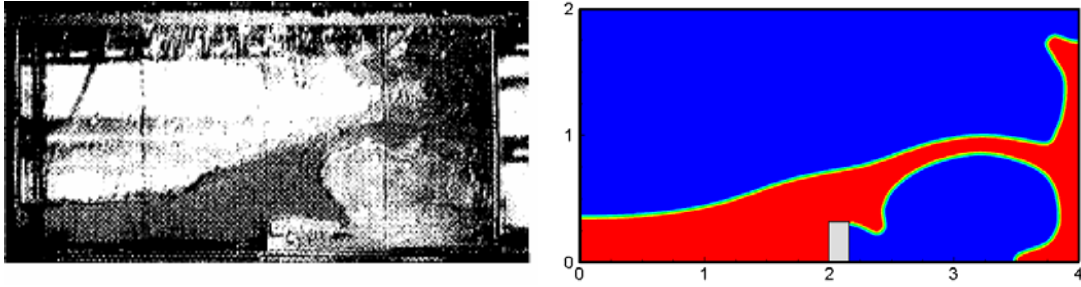
Figure 5.27: Comparison of measured and predicted free surface profiles for dam-breaking problem with an obstacle

5.3.4 Free Jet Simulation

In this test case, we consider a water jet enters horizontally from the left hand side of the computational domain on top of the platform at a constant velocity of 1.0. The dimension of the platform is 2.0×1.0, and the height of the water jet is 0.5 as shown in Figure 5.28. This is similar to a water fall caused by a sudden drop of the streambed elevation in a river. During the initial stage of the simulation, the water jet experiences a free fall under the action of the gravitational force. As the jet impinges on the tank bottom, it spreads across the tank in both directions and induces strong vortices along the front of the air-water interface. It should be noted that the horizontal velocity of the surge front is faster than the inlet velocity of the jet due to the conversion of potential energy into kinetic energy as the water flows into the tank. After the split water jets reach the tank walls, they continue to climb up against the vertical wall by converting the fluid kinetic energy back into potential energy. It is interesting to note that the water runup on the right tank wall is considerably higher than the water level at the jet inlet during the initial stage of the simulation. This is clearly due to the combined effects of the horizontal and vertical momentums and energy while the jet was deflected upward against the vertical tank wall. As the water level continues to rise inside the tank, however, the water level on the right tank wall begins to drop since a significant part of the energy is dissipated due to strong turbulent eddy motions resulted from water splash in the pool.
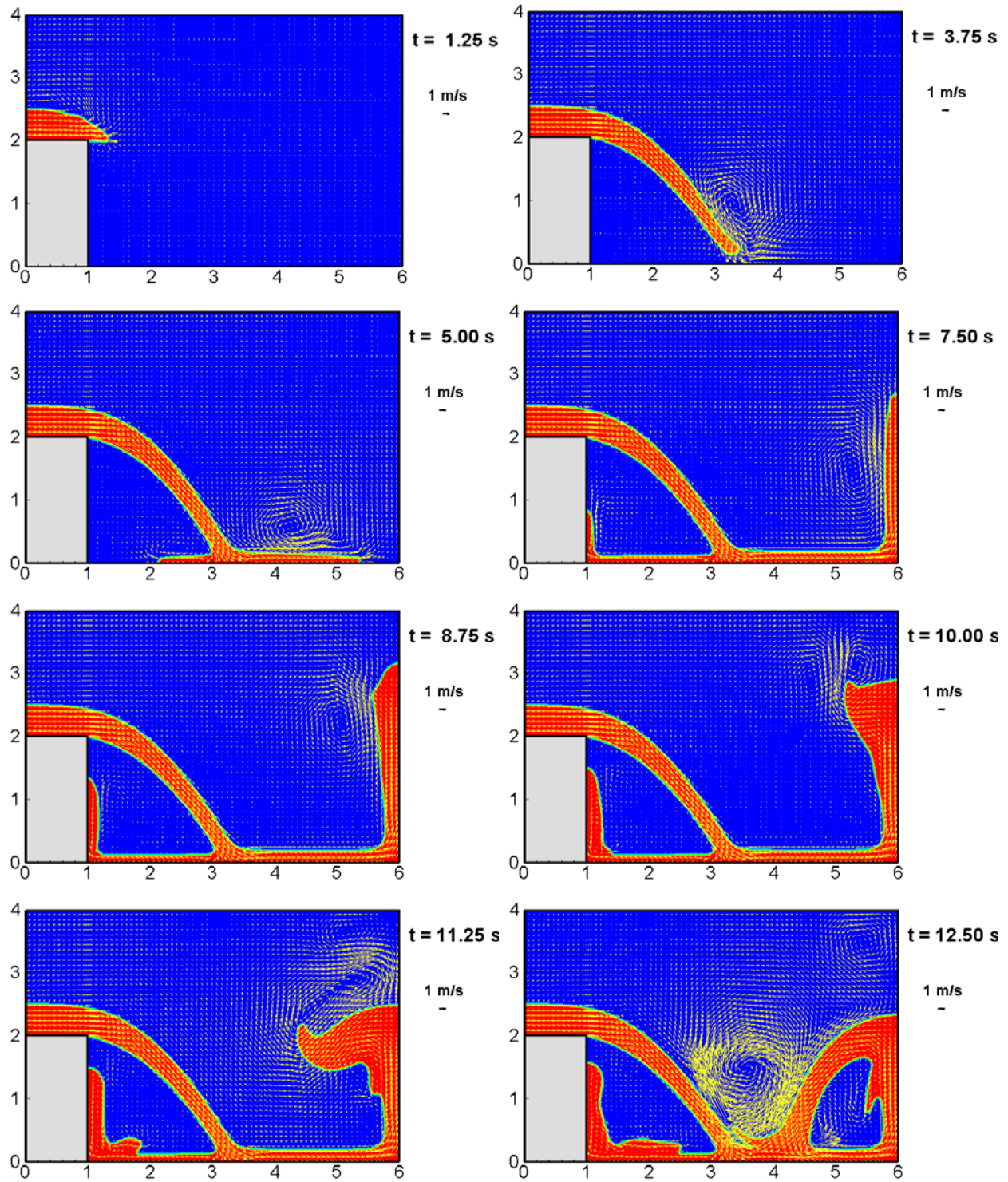
Figure 5.28: Free surface profiles and velocity field for free jet problem

5.3.5 Numerical Wave Tank

In order to simulate the effects of green water resulted from wave runup on a platform, it is necessary to develop a numerical wavemaker which is capable of generating large amplitude nonlinear waves at the wavemaker boundary. In this test case, we consider a two-dimensional wave tank with non-uniform rectangular grids as shown in Figure 5.29. The fine grids were used near the still water level to provide accurate resolution of the incoming waves. A damping beach was placed on the downstream boundary to eliminate undesirable wave reflection from the computational domain boundary. For convenience, we use the water depth as the characteristic length in the normalization of the tank dimension. A sinusoidal input wave was specified at the wavemaker boundary located on the left boundary of the wave tank. The wavelength is 1.5 and the wave amplitude is 0.114 (i.e., wave height 0.228). A wave gage was placed at a distance twice of the wavelength from the wavemaker. Figure 5.29(c) shows a comparison of the wave profiles between the wave gage location and the wavemaker. It is clearly seen that the predicted free surface elevation at the wave gage location displays a typical nonlinear wave characteristics with sharp peaks and flatter troughs. The predicted wave height, however, is somewhat lower than the incident wave height. This is probably caused by the linear wave input and the use of fixed grid distribution on the wavemaker boundary.
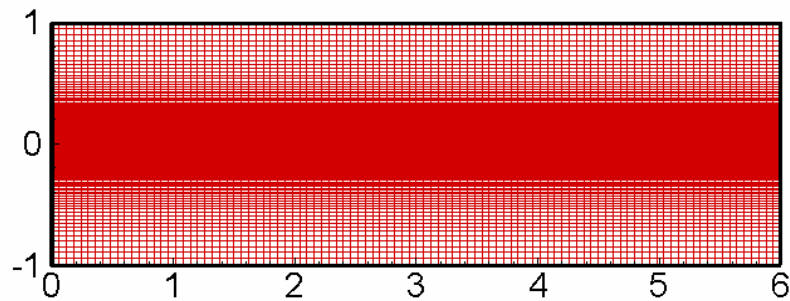
(a) Numerical Grid
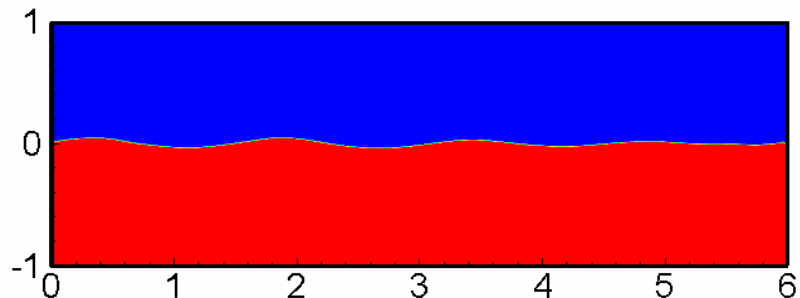
(b) Wave Profiles
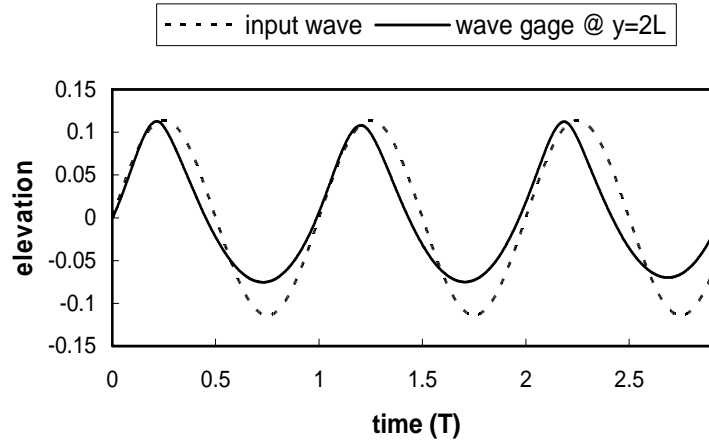
(c) Comparison of wave elevations between the wave gage station and the wavemaker

Figure 5.29: Numerical wave tank simulation

If we continue to increase the amplitude of the incident wave, then the generated wave will break in the wave tank as illustrated in Figure 5.30. In this test case, the numerical grid and the wavelength are the same as that used in the previous case, but a steeper wave with wave amplitude of 0.15 is used. It is clearly seen that the wave front steepened quickly as the wave propagated into the tank.
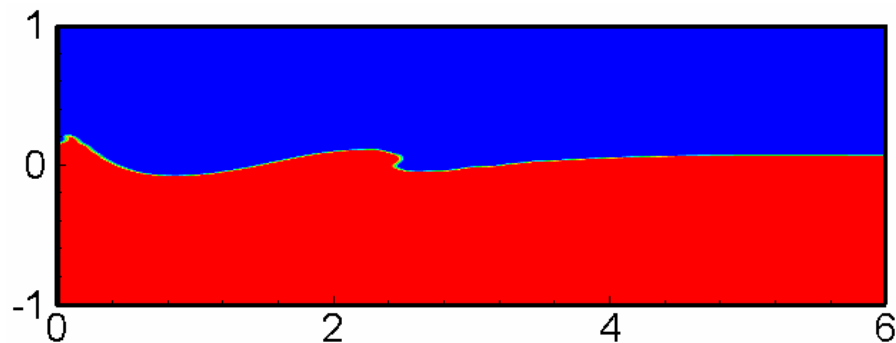
Figure 5.30: Wave breaking in a numerical wave tank

5.3.6 Green water on Offshore Platforms

In this test case, we consider a platform located in the middle of the wave tank. The wavemaker is placed on the left boundary of the computational domain. The wave tank and platform are made dimensionless using the water depth as the characteristic length. The dimension of the platform is

0.15×0.31 and the platform deck is located at 0.11 above the still water level. The coordinate of the bottom left corner of the platform is (4.0, -0.2). A sinusoidal input wave with wavelength 3.0 and wave height 0.30 is specified at the wavemaker boundary located on the left hand side of the wave tank as shown in Figure 5.31. Since the wave amplitude is significantly higher than the free board of the platform, it is anticipated that the platform deck will be inudated as the wave peak reaches the platform. Figure 5.32 shows the green water flowing over the platform deck at selected time instants. It is also worthwhile to note that there is a significant wave transmission across the platform since the platform height is considerably shorter the wavelength. This leads to a significant rise of water level downstream of the platform as the wave peak moves across the platform. It is quite clear that the level set method provides an effective approach to handle the partial and full submergence of the platform deck under extreme wave conditions.
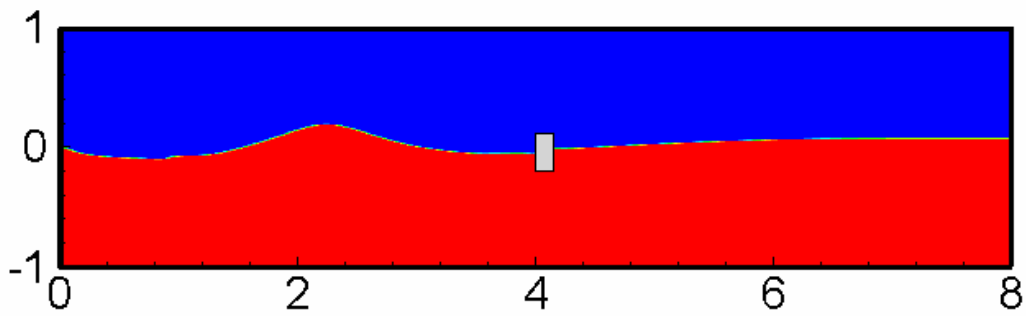
Figure 5.31: Large amplitude wave approaches a platform
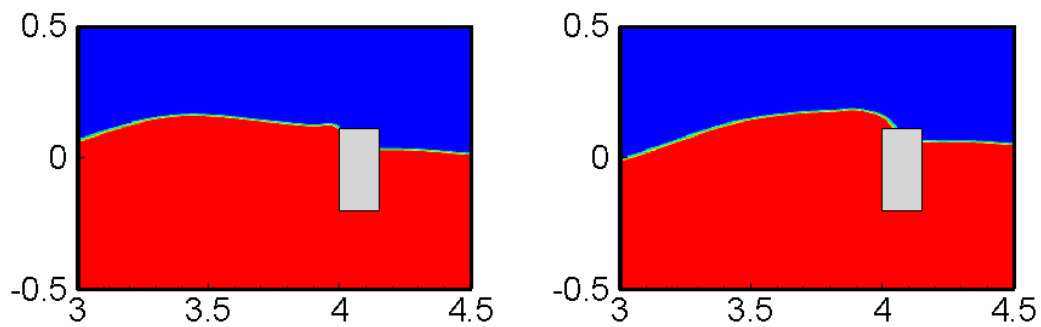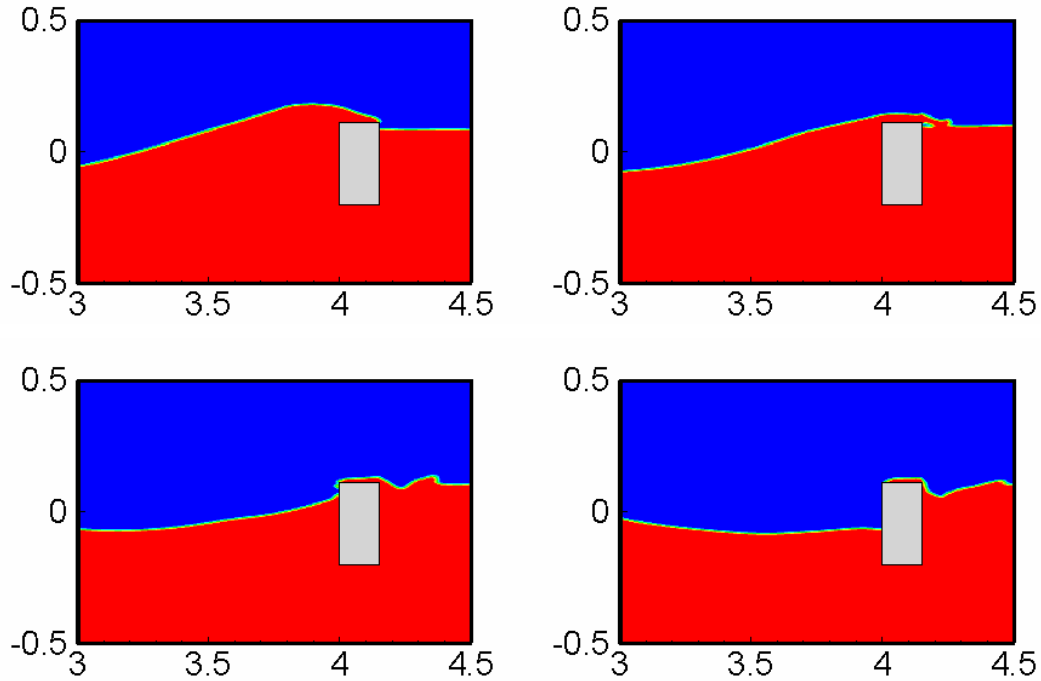
Figure 5.32: Green water on a platform

The last test case considered is the simulation of wave impact on the deck of a large platform as shown in Figure 5.33. The center of the platform is located at (4, 0.08), and the dimension of the platform deck is 1.0×0.03. The incident wave height is 0.15 and the wave length is 2.0. It can be seen from Figure 5.34 that the wave was about to break before hitting the platform deck. In addition to the water overtopping on the platform deck, the wave crest was also found to slam on the bottom of the platform at certain time instants. The wave slamming is expected to produce large uplift force which may damage the platform deck structure. It is also clearly seen that the green water on top of the platform rushes through the deck and falls back into the ocean on the lee side of the platform. The present simulation results clearly demonstrated the capability of the level set method in dealing with violent free surface motions including both the green water and wave slamming effects. In the next phase of research, the level set method will be generalized to provide accurate resolution of air-water interface around three-dimensional offshore platforms. In addition, a more robust numerical wavemaker will be implemented to enable the generation of highly nonlinear waves as observed in the present experimental investigations.
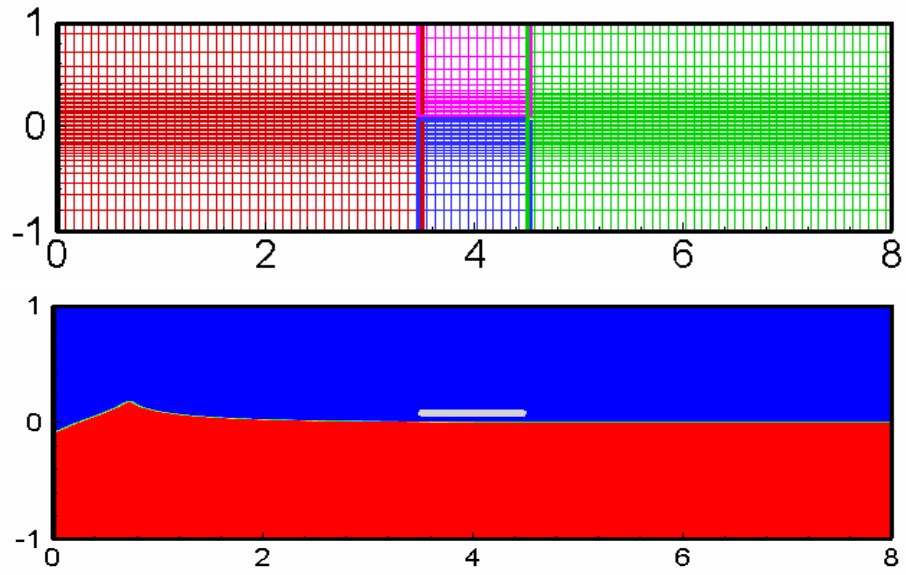
Figure 5.33: Wave slamming on a platform deck
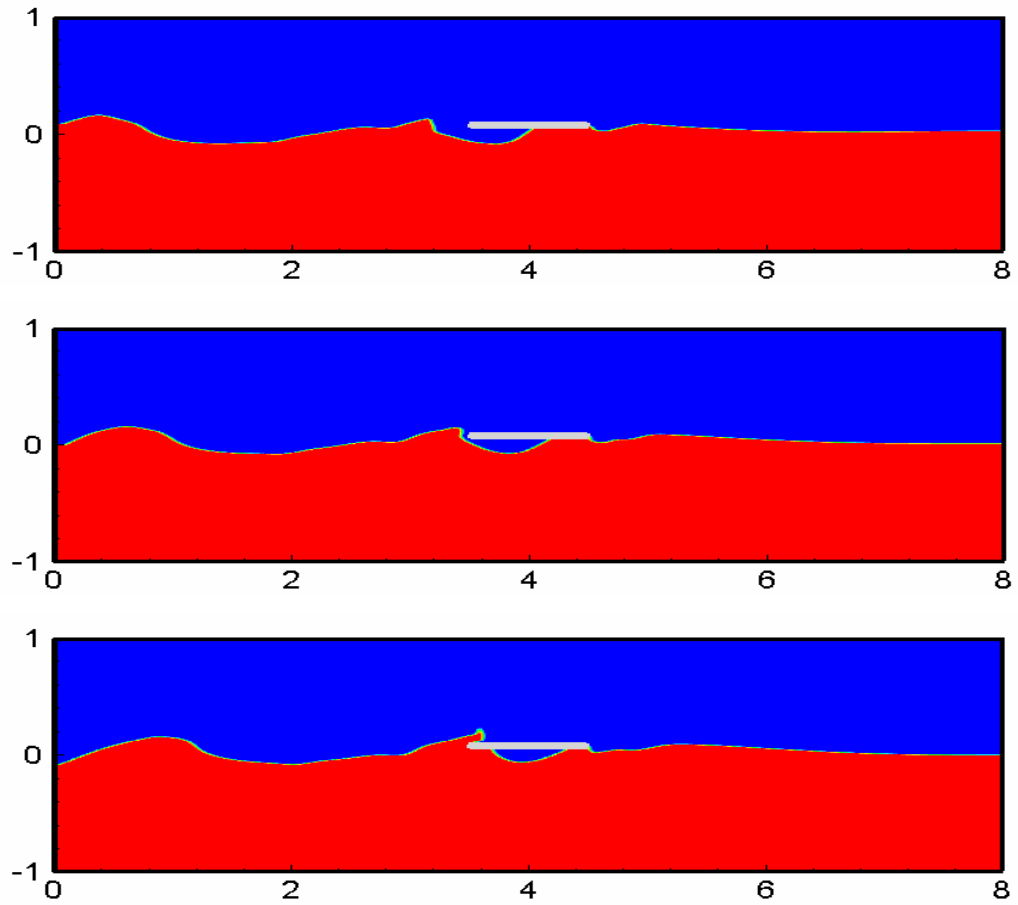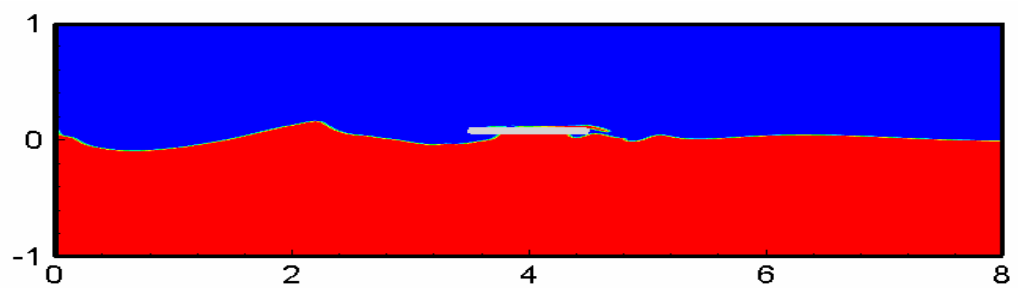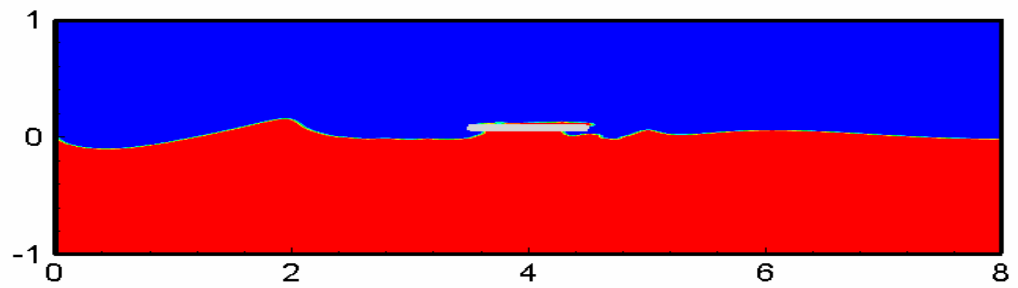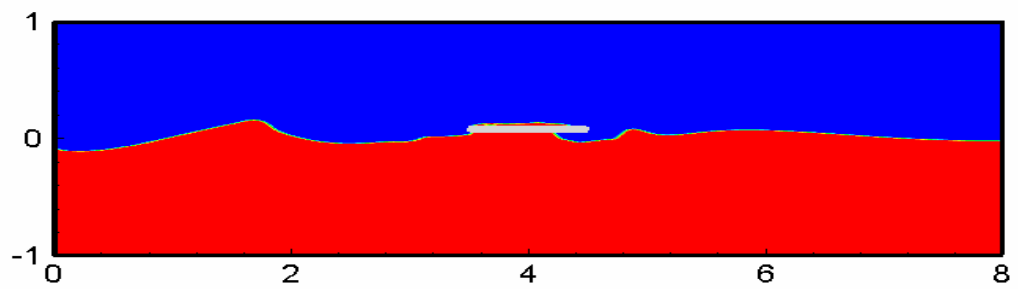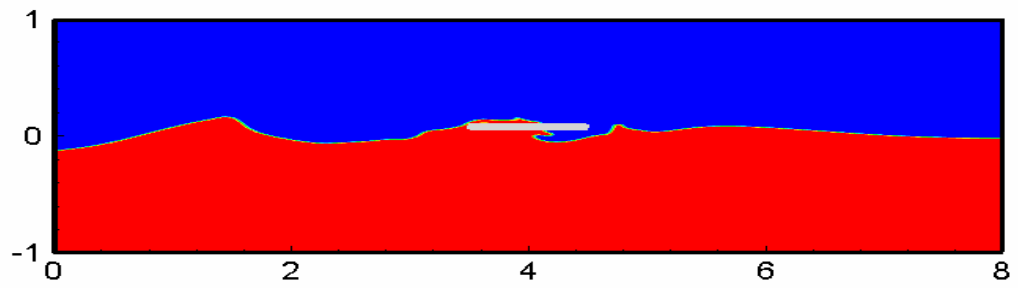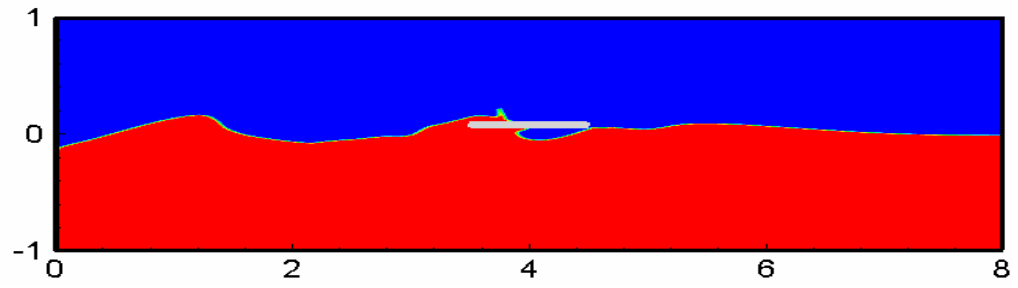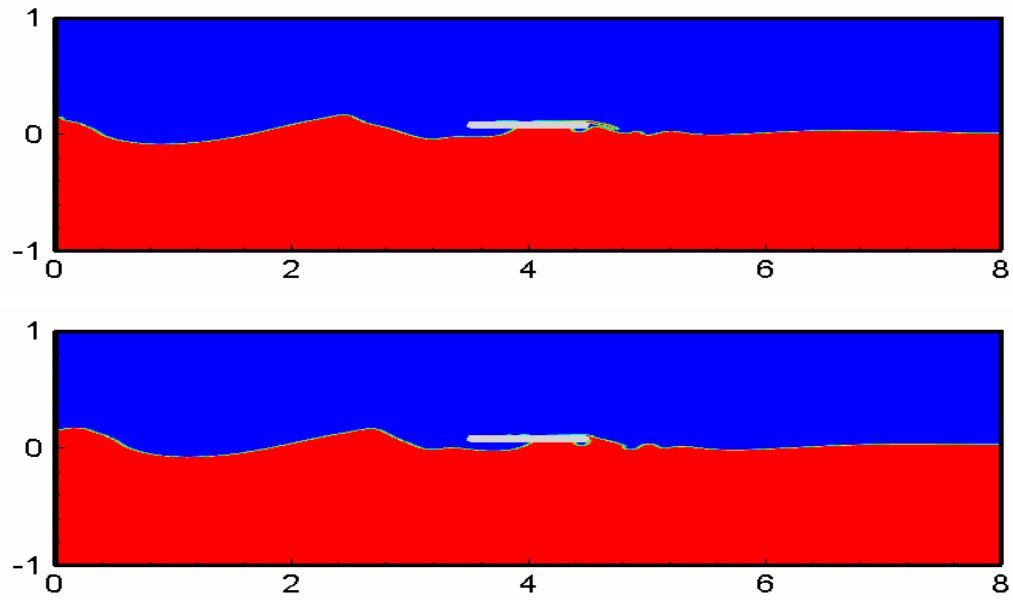
Figure 5.34: Green water around a platform deck

Chapter 6
Conclusions

For experimental approach, the measurements of velocity field of a plunging breaking wave impinging on a model structure and associated green water on top of the structure were successfully performed using two modern image based techniques – particle image velocimetry (PIV) and bubble image velocimetry (BIV). The latter technique was developed primarily for the velocity measurements in multiphase bubbly flows. By analyzing the measurements, a prediction equation was resulted in for the horizontal green water velocity distribution along the deck. The prediction equation was compared, along with the measured data, with the widely used dam break solution for green water prediction. The important findings are as follows:

The maximum horizontal velocity reached $1.5C$ with C being the wave phase speed before the overturning jet of the breaking wave impinging on the structure. This velocity is consistent with that measured in many other studies on breaking waves (without interactions with structures).

The front velocity of green water on the deck was approximately constant and equal to $1.1C$ to $1.2C$ along the deck. The maximum horizontal velocity during the period when the front of green water was on the deck is consistent with the front velocity of the green water. The location of the maximum horizontal velocity was also close to that of the front of green water during that period. The maximum horizontal velocity gradually decreased after the front of green water fallen back into the "ocean" after it passed the end of the deck.

The turbulence level of green water was between 40% and 50% of the maximum velocity at the particular given moment during the entire period when the front of green water was on the deck.

A prediction equation for the horizontal velocity distribution of green water along the deck was obtained applying dimensional analysis and the measurement data. The equation was present in Equation 3.7 and repeated here as

$$U_C = 1.1C \left[\left(\frac{x}{Ct} \right)^{0.37} - 1.2\frac{t}{T} + 0.02 \right]$$

in which U_c is the horizontal velocity of green water on the deck, C the phase speed of the breaking wave, T the wave period, x the horizontal coordinate axis with $x = 0$ at the leading edge of the deck, t the time. Note that this equation is valid during the entire period when the front of the green water was on the deck, and after the front fallen back into the ocean – meaning it is valid during the entire green water process. Comparisons show this prediction equation performs better if compared with the solution of dam break flow.

The widely used dam break solution for green water prediction also works reasonable well, if the initial water depth h_0 is carefully selected. Although, it fails to predict the shape of the velocity distribution of the green water flow, it gives a reasonable prediction on the maximum velocity of the flow. The Ritter's solution for a dam break flow was written in Equation 3.8 and repeated here as

$$u = \frac{2}{3} \left(\sqrt{gh_0} + \frac{x}{t} \right)$$

in which u is the horizontal velocity of the dam break flow, g the gravitational acceleration, x and t the coordinate system and the time (the same as that in the prediction equation above), and h_0 the initial upstream water depth. This study suggests the following two equations for the determine of h_0 (details are in Equations 3.9 and 3.10)

$$h_0 = H - z_{deck} \qquad \text{and} \qquad h_0 = \frac{(0.6C)^2}{g}$$

in which H is the breaking water height in deep water (before influenced by the structure) and z_{deck} is the height of the free board above the still water surface. This study also suggests that $h_0 = \dfrac{(0.6C)^2}{g}$ may give a better prediction if the dam break flow is to be used for green water prediction.

The vertical velocity of the upward moving splashing water right after the impinging of the breaking wave on the structure but before the wave become horizontal and moves onto the deck is huge – reached a maximum value of 2.8C. This velocity occurred on the front wall of the structure. It could result in significant damages to a deck or structure and equipment protruding from the wall when they are hit by this fast moving water from below.

These maximum greenwater velocities are summarized schematically in Figure 6.1 below by the vectors that have been added to Figure 2.7 (sample BIV image of wave impinging on structure). These velocities occur at different times.
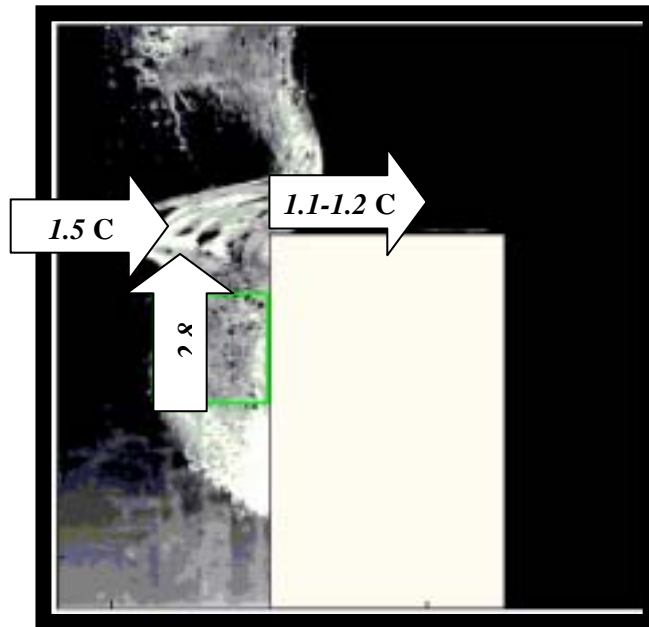
Figure 6.1Summary of maximum velocities

For numerical approach, time-domain simulations of wave runup and green water around offshore structures were performed using a Reynolds-Averaged Navier-Stokes (RANS)numerical method in conjunction with a chimera domain decomposition approach. The wave runup simulations were performed using the interface-tracking method, while the green water on offshore platforms were performed using the interface-capturing method based on level set formulation. The simulation results for wave runup on a two-dimensional TLP configuration are

in close agreement with the corresponding PIV measurements. Calculations were also performed for single and multiple vertical cylinders which are common structural elements of TLP and other offshore structures using the interface-tracking method to illustrate its capability for wave runup predictions including both the viscous and nonlinear wave effects.

The level set method was validated first for several benchmark test cases including the Zalesak's problem and stretching/shrinking of circular fluid elements. The new interface-capturing method was then employed in conjunction with the chimera RANS method for time-domain simulation of complex free surface problems including dam break, free jet, and green water on offshore platforms. The simulation results clearly demonstrate the flexibility and accuracy of the level set method for accurate prediction of violent free surface motions including wave breaking, slamming, and green water effects.

6.1 Suggestions for Continuation and Future Study

The followings are our suggestions for continuation and future study:

- To perform laboratory experiments using 3D model to investigate the 3D effect in the green water process. The present study used a 2D model in a 2D wave tank therefore the 3D effect is not covered. However, offshore structures in general have a width typically the same order of magnitude as the length so the 3D effect should be carefully examined.
- To validate the 2D numerical model with the laboratory measurements obtained in the present study. The validation will be performed by comparing both the geometry and velocity in the green water process.
- To use the validated numerical model to perform parametric study on a full scale structure with a complex and realistic geometry.
- To extend the present numerical model to 3D, validate the model with the proposed laboratory measurements, and perform parametric study on a full scale structure with a 3D complex geometry.

References

Ananthakrishnan, P. (1998) "Nonlinear Diffraction of Waves Over a Submerged Body in a Real Fluid," *Proceedings, 8th International Offshore and Polar Engineering Conference*, Vol. III, pp. 288-293, Montreal, Canada.

Buchner, B. (1995a) "The impact of green water on FPSO design." *Offshore Technology Conference*, Houston, OTC 7698, pp. 45–57.

Buchner, B. (1995b) "On the impact of green water loading on ship and offshore unit design." *The 6th International Symposium on Practical Design of Ships and Mobile Units (PRADS '95)*, pp. 1430-1443.

Buchner, B. (1996) "The influence of the bow shape of FPSOs on drift forces and Green Water." *Offshore Technology Conference*, Houston; OTC 8073, pp. 389-400.

Chang, K.-A., Lim, H.-J. and Su, C.B. (2003) "Fiber optic reflectometer for velocity and fraction ratio measurements in multiphase flows." *Review of Scientific Instruments,* Vol. 74, pp. 3559-3565.

Chang, K.-A. and Liu, P.L.-F. (1998) "Velocity, acceleration and vorticity under a breaking wave." *Physics of Fluids,* Vol. 10, pp. 327-329.

Chang, K.-A. and Liu, P.L.-F. (1999) "Experimental investigation of turbulence generated by breaking waves in water of intermediate depth." *Physics of Fluids,* Vol. 11, pp. 3390-3400.

Chang, K.-A. and Liu, P.L.-F. (2000) "Pseudo turbulence in PIV breaking-wave measurements." *Experiments in Fluids*, Vol. 29, pp. 331-338.

Chen, H.C. (2005) "Numerical Simulation of Flow and Heat Transfer around Complex Configurations by a Chimera RANS Method," (Keynote Paper), *12th National Computational Fluid Dynamics Conference*, August 19-21, Kaohsiung, Taiwan.

Chen, H.C. and Chen, M. (1988) "Chimera RANS Simulation of a Berthing DDG-51 Ship in Translational and Rotational Motions," *Int. J. of Offshore and Polar Eng*. Vol.8, No.3, pp. 182-191.

Chen, H.C. and Huang, E.T. (2004) "Time-Domain Simulation of Floating Pier/Ship Interactions and Harbor Resonance," Vol. III, pp. 772-779, *Proceedings of 14th International Offshore and Polar Engineering Conference*, Toulon, France.

Chen, H.C., Liu, T., Chang, K.A., and Huang, E.T. (2002) "Time-Domain Simulation of Barge Capsizing by a Chimera Domain Decomposition Approach," *12th International Offshore and Polar Engineering Conference*, Vol. III, pp. 494-501, KitaKyushu, Japan.

Chen, H.C., Liu, T., and Huang, E.T. (2001) "Time-Domain Simulation of Large Amplitude Ship Roll Motions by a Chimera RANS Method," *11th International Offshore and Polar Engineering Conference*, Vol. III, pp. 299-306, Stavanger, Norway.

Chen, H.C., Liu, T., Huang, E.T. and Davis, D.A. (2000) "Chimera RANS Simulation of Ship and Fender Coupling for Berthing Operations," *International Journal of Offshore and Polar Engineering*, Vol. 10, No. 2, pp. 112-122.

Chen, H.C. and Patel, V.C. (1988) "Near-Wall Turbulence Models for Complex Flows Including Separation," *AIAA Journal*, Vol. 26, No. 6, pp. 641-648.

Chen, H.C. and Patel, V.C. (1989) "The Flow around Wing-Body Junctions." *Proc. 4th Symp. on Numerical & Physical Aspects of Aerodynamic Flows*, Long Beach, CA, January 13-15, 15 pages.

Chen, H.C., Patel, V.C. and Ju, S. (1990) "Solutions of Reynolds-averaged Navier-Stokes Equations for Three-Dimensional Incompressible Flows," *Journal of Computational Physics*, Vol. 88, pp. 305–335.

Chen, H.C., Yu, Kai and Chen, S.Y. (2004) "Simulation of Wave Runup Around Offshore Structures by a Chimera Domain Decomposition Approach," Civil Engineering in the Oceans VI Conference, October 20-22, Baltimore, Maryland.

Christensen, E.D. and Deigaard, R. (2001) "Large eddy simulation of breaking waves." *Coastal Engineering,* Vol. 42, pp. 53-86.

Cokelet, E.D. (1977) "Steep Gravity Waves in Water of Arbitrary Uniform Depth," *Philosophical Transactions of Royal Society of London*, Vol, 286, pp. 183-230.

Dong, C.M. and Huang, C.J. (1999) "Vortex Generation in Water Waves Propagating Over a Submerged Rectangular Dike," Proceedings, *9th International Offshore and Polar Engineering Conference*, Vol. III, pp. 388-395, Brest, France.

Fekken, G., Veldman, A.E.P. and Buchner, B. (1999) "Simulation of green water loadings using the Navier-Stokes equations." 7*th International Conference on Numerical Ship Hydrodynamics*, Nantes. pp. 6.3.1-12.

Ferziger, J.H. and Peric, M. (1999) *Computational Methods for Fluid Dynamics*, 2nd Edition, Springer- Verlag.

Govender, K., Mocke, G.P. and Alport, M.J. (2002) "Video-imaged surf zone wave and roller structures and flow fields." *Journal of Geophysical Research,* Vol. 107, 3072.

Greated, C.A. and Emarat, N. (2000) "Optical studies of wave kinematics." *Advances in Coastal and Ocean Engineering vol. 6,* ed P L -F Liu (Singapore; World Scientific) pp. 185-223.

Harlow, F.H. and Welch, J.E. (1965) "Numerical Study of Large-Amplitude Free Surface Motions," *Physics of Fluids*, Vol. 8, pp. 2182-2189.

Hassan, Y.A, Schmidl, W.D. and Ortiz-Villafuerte, J. (1998) "Investigation of three-dimensional two-phase flow structure in a bubbly pipe." *Measurement Science and Technology,* Vol.9, pp. 309-326.

Hamoudi, B. and Varyani, K.S. (1998) "Significant load and green water on deck of offshore units/vessels." *Ocean Engineering,* Vol.25, pp.715–731.

Hattori, M., Arami, A. and Yui, T. (1994) "Wave impact pressure on vertical walls under breaking waves of various types." *Coastal Engineering,* Vol.22, pp. 79–114.

Hirt, C.W. and Nichols, B.D. (1981) "Volume of Fluid (VOF) Method for the Dynamics of Free Boundaries," *Journal of Computational Physics*, Vol. 39, pp. 201–225.

Hull, P. and Müller, G. (2002) "An investigation of breaker heights, shapes and pressures." *Ocean Engineering,* Vol. 29, pp. 59-79.

Jansen, P.C.M. (1986) "Laboratory observations of the kinematics in the aerated region of breaking waves." *Coastal Engineering,* Vol. 9, pp. 453–477.

Koshizuka, S., Tamako, H. and Oka, Y. (1995) "A Particle Method for Incompressible Viscous Flow with Fluid Fragmentation," *Computational Fluid Dynamics Journal*, Vol. 4, No. 1, pp. 29-46.

Lauber, G. and Hager, W.H. (1997) "Experiments to dambreak wave: Horizontal channel." *Journal of Hydraulic Research,* Vol.36, pp. 291-307.

Lin, P. and Liu, P.-F. (1998a) "A numerical study of breaking waves in the surf zone." *Journal of Fluid Mechanics,* Vol. 359, pp. 239-264.

Lin, P. and Liu, P.-F. (1998b) "Turbulence transport, vorticity dynamics, and solute mixing under plunging breaking waves in surf zone." *Journal of Geophysical Research,* Vol. 103 pp. 15677-15694.

Lindken, R. and Merzkirch, W. (2001) "A novel PIV technique for measurements in multi-phase flows and its application to two-phase bubbly flows." *4th International Symposium on Particle Image Velocimetry,* paper A231.

Maruo, H..and Song, W. (1994) "Nonlinear analysis of bow wave breaking and deck wetness of a high speedship by the parabolic approximation." *Proceedings of the 20th Symposium on Naval Hydrodynamics,* National Academic Press, pp. 59–73.

Mei, C.C. (1989) *The Applied Dynamics of Ocean Surface Waves*, World Scientific: Singapore.

Melville, W.K., Veron, F. and White, C.J. (2002) "The Velocity field under breaking waves: coherent structures and turbulence." *Journal of Fluid Mechanics,* Vol. 454, pp. 203-233.

Nielsen, K.B. and Mayer, S. (2004) "Numerical prediction of green water incidents." *Ocean Engineering,* Vol. 31, pp. 363-399.

Nichols, B.D., Hirt, C.W. and Hotchkiss, R.S (1980) *SOLA-VOF: A Solution Algorithm for Transient Fluid Flow with Multiple Free Boundaries*, Technical Report LA-8355, Los Alamos National Laboratory.

Nishino, K., Kato, H. and Torii, K. (2000) "Stereo imaging for simultaneous measurement of size and velocity of particles in dispersed two-phase flow." *Measurement Science and Technology,* Vol. 11, pp. 633-645.

Osher, S., and Sethian, J.A. (1988) "Fronts propagating with curvature-dependent speed: algorithms based on Hamilton-Jacobi formulations," *Journal of Computational Physics*, Vol. 79, No. 1, pp. 12-49.

Oumeraci, H., Klammer, P. and Partenscky, H.W. (1993) "Classification of breaking wave loads on vertical structures." *Journal of Waterway, Port, Coastal Ocean Engingeering,* Vol. 119(4), pp. 381–397.

Park, J.C., Uno, Y., Matsuo, H., Sato, T. and Miyata, H. (2001) "Reproduction of Fully-Nonlinear Multi-Directional Waves by a 3D Viscous Numerical Wave Tank," *Proceedings, 11th International Offshore and Polar Engineering Conference*, Vol. III, pp. 140-147, Stavanger, Norway.

Perlin, M., He, J. and Bernal, L.P. (1996) "An experimental study of deep water plunging breakers." *Physics of Fluids,* Vol.8, pp. 2365-2374.

Raffel, M., Willert, C. and Kompenbans, J. (2001) *Particle Image Velocimetry; A practical guide,* (Göttingen, Germany; Spring-Verlag).

Ray, S.D. (2002) *Applied photographic optics,* (Oxford, U.K; Focal press) pp. 215-233.

Ryu, Y., Chang, K.–A. and Lim, H.–J. (2005) "Use of bubble image velocimetry for measurement of plunging wave impinging on structure and associated greenwater." *Measurement Science and Technology,* Vol. 16, pp. 1945-1953.

Schoenberg, T. and Rainey, R.C.T. (2004) "A hydrodynamic model of Green Water incidents." *Applied Ocean Research* Vol.24, pp. 299–307.

Sethian, J.A.   (1996) *Level Set Methods*, Cambridge Univ. Press.

Shu, C.W.   and Osher, S. (1989) "Efficient Implementation of Essentially Nonoscillatory Shock Capturing Schemes II," *Journal of Computational Physics*, Vol. 83, pp. 32–78.

Skyner, D.J., Gray, C. and Greated, C.A. (1990) "A comparison of the time-stepping numerical predictions with whole-field flow measurement in breaking waves." *Water Wave Kinematics,* ed Torum A and Gudmestad O T (Boston; Kluwer Academic Publishers) pp. 491-508.

Sussman, M., Smereka, P. and Osher, S. (1994) "A Level Set Approach for Computing Solutions to Incompressible Two-Phase Flow," *Journal of Computational Physics*, Vol. 114, pp. 146–159.

Sussman, M. and Fatemi, E. (1999) "An Efficient, Interface-Preserving Level Set Redistancing Algorithm and Its Application to Interfacial Incompressible Fluid Flow," *SIAM J. of Scientific Comput.*, Vol. 20, pp. 1165–1191.

Suhs, N.E. and Tramel, RW (1991) *PEGSUS 4.0 Users Manual*, Arnold Eng Dev Center Rep AEDC-TR-91-8, Arnold Air Force Station, TN.

Ting, F.C.K. and Kirby, J.T. (1994) "Observation of undertow and turbulence in a laboratory surf zone." *Coastal Engineering,* Vol. 24, pp. 51– 80.

Ting, F.C.K. and Kirby, J.T. (1995) "Dynamics of surf-zone turbulence in a strong plunging breaker." *Coastal Engineering,* Vol. 24, pp. 177– 204.

Vischer, D.L. and Hager, W.H. (1998) *Dam hydraulics* (New York; John Wiley and Sons).

Watanabe, Y. and Saeki, H. (1999) "Three-dimensional large eddy simulation of breaking waves." *Coastal Engineering Journal,* Vol. 41, pp. 281-301.

Yilmaz, O., Incecik, A. and Han, J.C. (2003) "Simulation of green water flow on deck using non-linear dam breaking theory." *Ocean Engineering* Vol. 30, pp. 601-610.

Yue, W.S., Lin, C.L. and Patel, V.C. (2003) "Numerical Simulation of Unsteady Multidimensional Free Surface Motions by Level Set Method," *Int. J. Numer. Meth. Fluids*, Vol. 42, pp. 853-884.

Zalesak, S.T. (1979) "Fully Multidimensional Flux-Corrected Transport Algorithms for Fluids," *Journal of Computational Physics*, Vol. 31, pp. 335-362.

Zoppou, C. and Roberts, S. (2003) "Explicit schemes for dam-break simulations." *Journal of Hydraulic Engineering,* Vol. 129, pp. 11-34.

Appendices

Appendix A – "Use of bubble image velocimetry for measurement of plunging wave impinging on structure and associated greenwater" by Yonguk Ryu, Kuang-An Chang and Ho-Joon Lim, Department of Civil Engineering, Texas A&M University, College Station, TX 77843-3136. Meas. Sci. Technol. 16 (2005) 1945–1953.

Appendix B – "Breaking Wave Impinging and Greenwater on a Two-Dimensional Offshore Structure" by Yonguk Ryu and Kuang-An Chang, Ocean Engineering Program, Department of Civil Engineering, Texas A&M University, College Station, TX, U.S.A. ISOPE Proceedings (2005) 660-665/

Appendix C – "Simulation of Wave Runup Around Offshore Structures by a Chimera Domain Decomposition Approach" by Hamn-Ching Chen, Kai Yu and Sheng-Yi Chen, Ocean Engineering Program, Department of Civil Engineering, Texas A&M University, College Station, Texas 77843. Proceedings of Civil Engineering in the Oceans VI Conference, October 20-22, 2004, Baltimore, Maryland A3-1-A3-14.

Use of bubble image velocimetry for measurement of plunging wave impinging on structure and associated greenwater

Yonguk Ryu, Kuang-An Chang and Ho-Joon Lim

Department of Civil Engineering, Texas A&M University, College Station, TX 77843-3136, USA

Abstract

The measurement of velocity fields of a plunging wave impacting on a structure in a two-dimensional wave tank was investigated experimentally. As the wave impinged and overtopped the structure, a large highly aerated region was created in front of the structure and on top of the structure. The broken wave in front of the structure and associated greenwater on top of the structure are highly aerated containing not only a large number of bubbles but also very large sizes of bubbles. The highly aerated bubbly flow caused the traditional particle image velocimetry (PIV) technique to fail due to the uncontrollable scattering of laser light. A modified PIV method, called bubble image velocimetry (BIV), was introduced by directly using bubbles as the tracer and measuring the bubble velocity by correlating the 'texture' of the bubble images. No laser light sheet was needed while the depth of field was limited to minimize the error. Velocity measurements using BIV and fibre optic reflectometer were compared to validate the BIV technique. While the fluid velocity in the region where no or few bubbles exist can be successfully obtained using PIV, the velocity in the high void fraction region can be measured using BIV. Therefore, BIV can be seen as a complementary technique for PIV. The use of BIV is essential in the studied problem here due to the fact that in the vicinity of the structure the flow is almost entirely bubbly flow. From both the PIV and BIV measurements, it was found that the maximum fluid particle velocity as well as the bubble velocity in front of the structure during the impinging process is about 1.5 times the phase speed of the waves.

Keywords: velocity measurement, multiphase flow, wave breaking, particle image velocimetry, wave–structure interaction

1. Introduction

It is well known that extreme waves have caused significant damage to offshore structures due to the tremendous forces created by wave impingement (e.g., Buchner (1995), Hamoudi and Varyani (1998), Schoenberg and Rainey (2002)). Frequently, the impinging waves rush upward to the deck and create so-called greenwater on the deck that washes out and damages equipment and, in some cases, causes injury or death to persons working on the deck. One recent example is the greenwater damage caused by Hurricane Ivan

in the Gulf of Mexico in 2004 that damaged several offshore platforms.

The interaction of extreme waves and structures has been studied for decades. Typically large breaking waves were used to represent the extreme waves. The focus of the studies has been on the forces of the waves on structures and flow field kinematics. While many studies were carried out using numerical models, most of the models were based on the potential flow theory, therefore the multiphase highly turbulent flow in the problem was not realistically simulated. The results were therefore for the 'engineering use' for

prediction of wave forces rather than looking for physical insight of the phenomenon. On the other hand, more advanced approaches, either based on the Reynolds averaged Navier–Stokes equations (RANS) or large eddy simulation (LES), that feature turbulent models and provide much more physical insight have started to be used in the study (e.g., Lin and Liu (1998a, 1998b), Watanabe and Saeki (1999), Christensen and Deigaard (2001)). However, limited success was achieved due to the lack of comprehensive treatments on the splashing free surface and the high void fraction bubbly flow, and lack of experimental data to validate the calculations and the models.

Since very few non-intrusive quantitative velocity measurements of breaking waves impinging on structures exist, we thus review the measurement of breaking waves instead. The measurement on breaking waves itself has been of great interest to numerous researchers. Various measurement techniques, including laser Doppler velocimetry (LDV) and particle image velocimetry (PIV), have been employed for the velocity measurements of the wave breaking process in both the surf zone and deep water (e.g., Greated and Emarat (2000), Ting and Kirby (1994, 1995), Perlin *et al* (1996)). Among the efforts, PIV is a newcomer and only about ten years old. However, the technique is perhaps the most robust and state-of-the-art technique among all the methods. This is due to not only its full field nature but also its recent advances in the improvement of the spatial and temporal resolution and time resolving capability, and its still-evolving foreseeable future.

Among the recent advances in breaking wave measurement using PIV, Chang and Liu (1998) measured the maximum velocity and associated acceleration and vorticity of the overturning jet of a breaking wave. Unfortunately, as a wave breaks and entrains air bubbles, the technique is then restricted to the region outside the aerated area, in general under the trough level or away from the breaking point. Despite some success on the measurement of the breaking wave flow field and generated turbulence outside the aerated region (Chang and Liu 1999, 2000, Melville *et al* 2002), advances in the understanding of the flow structure inside the highly aerated region have rarely been reported. The few exceptions are perhaps the early work of Jansen (1986) and the very recent work of Govender *et al* (2002). Jansen measured particle trajectories in the aerated region of breaking waves using fluorescent tracers and ultraviolet light, but the measurements suffered from poor spatial resolution. More comprehensive measurements were obtained by Govender *et al* (2002), who used a technique similar to PIV based on digital image acquisition and cross-correlation algorithms with the use of a laser light sheet to illuminate the aerated region. Bubble structures in the images were used for correlation between consecutive images for velocity determination. Even though the measurements are promising, no detailed description on the technique itself was provided.

In addition to the direct measurement of bubbly flow under breaking waves, the measurement of gas–liquid flows has been investigated in various areas. Typically the bubble void fraction and the bubble size are much lower and smaller than those in a breaking wave. For such flows the scattering of laser light due to bubbles is much less and thus more controllable. The PIV technique has been successfully used

to measure bubble velocity by correlating bubbles or tracking each bubble in the recorded images that were taken by applying the 'shadowgraphy' method (Hassan *et al* 1998, Nishino *et al* 2000, Lindken and Merzkirch 2001). The method uses a light source behind the bubbles, therefore the bubbles appear in the images as their shadows. Again, the density and size of bubbles have to be within a certain limit so the shadows are separated and identifiable. Typically the methods are used in low void fraction flow with small bubbles, and may not be applicable in breaking wave measurements.

This paper presents an experimental study on the kinematics of plunging waves impinging and overtopping a structure. The velocity field in the aerated region around the structure that is the most interesting and important to the problem but difficult to measure using PIV was obtained using the bubble image velocimetry (BIV) technique. The BIV technique is similar to PIV except it directly correlates the bubble images and does not require a laser light sheet for illumination. The principle of the BIV method will be described in detail. The velocity fields measured by using both the traditional PIV technique with a laser light sheet and the new BIV method will be compared and discussed. The BIV measurement will be compared with the result using fibre optic reflectometry (FOR) (Chang *et al* 2003) for validation. The sequential velocity field in the vicinity of the structure will be demonstrated.

2. Experimental condition and setup

2.1. Experimental condition

The experiments were performed in a glass-walled wave tank located at the Department of Civil Engineering, Texas A&M University. The wave tank is 36 m long, 0.9 m wide and 1.5 m high. The water depth was kept constant at $h = 0.80$ m throughout the experiments. The wavemaker is of dry-back flap type installed at one end of the wave tank and controlled by a computer. A 1:5.5 sloping beach with a layer of horsehair is at the other end of the tank to absorb the wave energy and reduce reflection. A rectangular model structure that has a length of 0.15 m, a height of 0.31 m and a width the same as that of the tank was installed in the wave tank. The draft of the model structure is 0.20 m. The model was constructed based on a simplified tension-leg platform with a scale ratio of 1:168. The model structure was mounted on aluminium frames that were rigidly fixed to the bottom of the tank and suspended from the top of the tank. The aluminium frames were designed to minimize the vibration of the model structure induced by breaking wave impingement. The sketch of the model structure is shown in figure 1 with the coordinate system and the fields of view (FOV) used for particle image velocimetry and bubble image velocimetry measurements. Note that the origin $(x, z) = (0, 0)$ is at the intersection of the structure front wall and the stationary water level. The structure was located 21.7 m away from the wavemaker. All the control signals, including the signals controlling the wavemaker and triggering the PIV/BIV system, and measured data were synchronized.

The breaking wave tested is a plunging breaker that was generated using a wave focusing method similar to that in
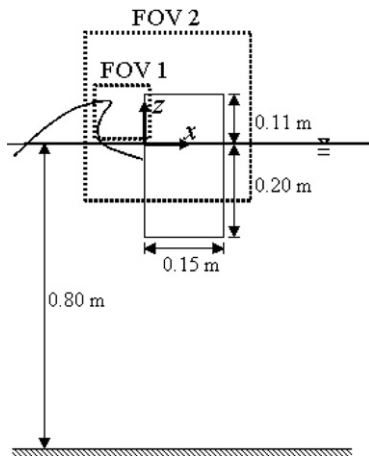
Figure 1. Sketch of the model structure, coordinate system, and fields of view used in PIV and BIV.
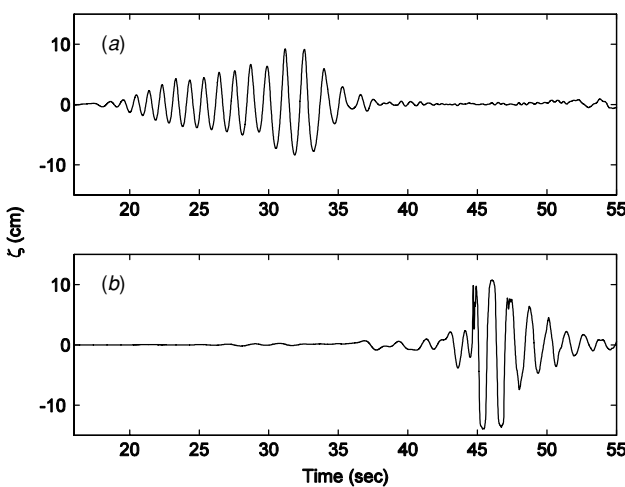
Figure 2. Wave elevations measured at (*a*) 5.1 m ($x = -16.6$ m), and (*b*) 21.7 m ($x = 0.0$ m) from the wavemaker.

Skyner *et al* (1990). The wave train consists of waves with various frequencies ranging from 0.7 Hz to 1.3 Hz. With the superposition of different wave frequencies and some trial and error, the plunging breaker broke at the desired location right in front of the structure. The free surface elevation was measured using two wave gauges located at 5.1 m and 21.7 m from the wavemaker (i.e., $x = -16.6$ m and $x = 0.0$ m in front of the structure) to measure the incoming waves and the water elevation at the front edge of the structure. The measured wave condition is shown in figure 2.

2.2. Setup of PIV system

The PIV technique in the present study was first used to measure the velocity field near the front wall of the model structure. The light source of the PIV system is a dual-head frequency-doubled Spectra-Physics Nd:YAG laser that has a 532 nm wavelength, 400 mJ maximum output energy, 6 ns pulse duration and 10 Hz repetition rate for each head. A set of optics consisting of cylindrical and spherical lenses was used to generate the light sheet. The image recording device is a CCD camera from LaVision Inc. that has an eight frames per second (fps) maximum framing rate, a resolution of 1024 ×

1280 pixels and a 12-bit dynamic range. The seeding particles, Vestosint 2157, have a mean diameter of 56 μm and a specific weight of 1.02. The FOV for the PIV measurements is from $x = -14$ cm to $x = 0.7$ cm and from $z = 1$ cm to $z = 13$ cm with $x = 0$ being the leading edge of the structure and $z = 0$ being the calm water level as shown in figure 1 (denoted as FOV1). The time interval between two successive laser pulses is 0.6 ms. The frame rate was set at 7.27 Hz during all experiments. The measurements were repeated 11 times with a small delay between each so continuous velocity fields with a time interval of 0.025 s were obtained. The interrogation area for velocity determination was 32×32 pixels with a 50% overlap. Commercial software from LaVision was used for the velocity computation.

2.3. Principle and setup of the BIV system

The BIV technique was used to obtain the velocity field in the aerated region. The technique correlates the bubble images and 'texture' in the images created by the bubbles and the air–water interfaces. No small seeding particles as used in the traditional PIV technique are needed. The idea of the BIV method came from combining the shadowgraphy technique that illuminates the fluid from behind to reveal the flow pattern, and the PIV technique that correlates the consecutive images to determine the velocity. Since the velocity is calculated through cross-correlating the images obtained by the shadowgraphy technique with the bubble structure in the images as tracers, the BIV technique requires only two light projectors to illuminate the air bubbles in the aerated region. Unlike the traditional PIV technique, no laser light sheet is needed. In this study, regular 600 W light bulbs with reflecting mounts were used to illuminate the flow. The images were captured by a Phantom high speed camera mounted with a Nikon 105 mm micro focal lens. The camera has a resolution of 512 × 512 pixels, an 8-bit dynamic range and a maximum framing rate of 1000 fps. The aperture of the camera was set with the *f*-number equal to 1.8.

The illumination of the flow is a modification of the traditional shadowgraphy method with lights being placed at both sides of the wave tank. One light placed at the back side of the tank was used to illuminate the flow from behind (the high speed camera was located on the other side). A thin sheet of translucent white plastic glass was attached to the back-side glass wall of the tank. This way the light bulb will illuminate the flow more uniformly without the use of a costly large high intensity light emitting diode (LED) plate typically used in the shadowgraphy technique. However, for the region with a high concentration of bubbles the captured images will be filled with shadows and appear to be all dark in that region. The images do not provide the needed differences in intensity to reveal the bubble structure or bubble 'texture' for later correlation. To resolve this problem, a light was placed on the other side of tank (on the same side as the high-speed camera but at an angle) in order to produce the desired intensity differences in the images. The light illuminating behind the tank was located at an angle of $0°$ (normal to the FOV) while that on the other side had an angle of about $60°$. Subsequently, images captured using the modified shadowgraphy technique were inverted so high intensity (bright) represents the bubbles.

The flow velocity was calculated by cross-correlating the flow texture from the inverted consecutive images.

Since the BIV technique does not use a light sheet to illuminate a specific plane of interest like the traditional PIV method, it is necessary to know where the measured bubbles are in the cross-tank direction (i.e. the y direction). The problem is solved by limiting the depth of field (DOF) in the experiment, achieved by carefully setting up the camera. The DOF is defined as the distance within which objects captured by the camera are well focused and appear to be sharp. The camera focal point and the DOF can be considered as the light sheet plane and light sheet thickness, respectively, in the PIV technique. This way the FOV of the captured images can be defined. Assuming that a lens focuses on a point at a distance L from the forward nodal point of the lens (which is sufficiently close to the distance between the lens front and the point), the DOF can be calculated using the formulae below. Following Ray (2002), the formulae for the nearest limit, R, and the farthest limit, S, of the DOF can be expressed as $R = Lf^2/(f^2 + NLC)$ and $S = Lf^2/(f^2 - NLC)$, in which f is the focal length of the camera focal lens, C is the value for the circle of confusion that depends on the property of the camera and N is the f-number of the camera aperture. The DOF is $D = S - R$.

Objects located in front of and behind the DOF will appear to be blurred without a clear texture in the captured image and therefore have little effect on the later correlation process for velocity determination. On the other hand, objects located within the DOF will be sharp in the image with a featured pattern due to the flow. This means that the obtained velocity from cross-correlating the captured images is indeed mainly contributed from the image of fluid within the DOF. The uncertainty on the position of the images in the cross-tank direction is therefore one-half of the thickness of the DOF from the centre of the DOF. As a result, the error due to the thickness of the DOF in the obtained velocity can be estimated approximately as $\varepsilon = D/2L$. If the depth of view D is thin and the distance between the camera and the focal plane L is long, the error can be minimized. In the present study, $L = 4.0$ m, $f = 105$ mm, $N = 1.8$ and $C = 0.03$ mm. The calculated R is about 3.92 m and S is about 4.07 m therefore the corresponding DOF in the present study is $D = 0.15$ m. The error due to the thickness of the DOF is estimated as 2%. The arrangement of the BIV system is sketched in figure 3.

The FOV for the BIV measurement is 37.8 cm × 37.8 cm and centred at $x = 5.2$ cm and $z = -5.3$ cm as shown in figure 1 (denoted as FOV2). The time interval between the recorded images was 1.75 ms, which is equal to the time separation between the consecutive frames captured by the high speed camera. The images were processed using the LaVision PIV software and the velocity field was calculated using an adaptive multi-pass algorithm with an initial interrogation window size of 32 × 32 pixels and a final window size of 16 × 16 pixels with a 50% overlap. A median filter was subsequently applied to eliminate the spurious vectors in the calculated velocity map. The mean velocity was calculated from ensemble averaging ten instantaneous velocity fields from repeated runs with the same test condition.
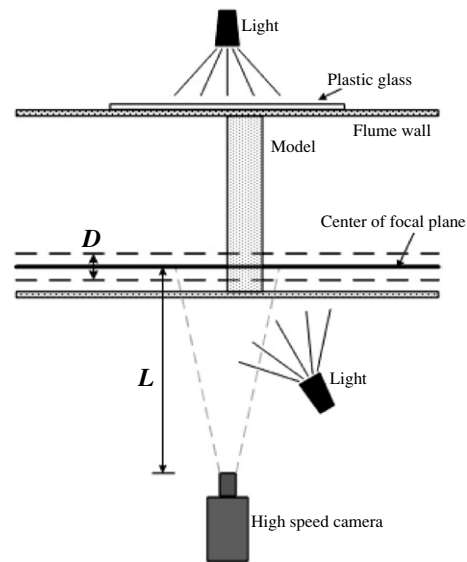
Figure 3. BIV apparatus.

3. Validation of the BIV method

The validation of BIV was performed in two ways: first to compare the velocity measured using the BIV technique with that measured using the fibre optic reflectometry technique; second to check the effect of the blurry images out of the DOF in the BIV velocity measurement. A bubble plume in a water tank was used in the validation.

A two-phase quasi-steady bubbly flow in a vertical narrow tank was measured using both the BIV technique and the FOR technique. The objective of this experiment is to validate the BIV method by comparing the results obtained from these two methods. The FOR technique is capable of measuring the velocity time history of both water (seeded with small particles) and air bubbles at a given point in a multi-phase flow. Details of FOR are given by Chang *et al* (2003).

The vertical narrow tank used in the validation has a length of 0.4 m, a width of 0.4 m and a height of 0.8 m. Water was filled to a depth of 0.7 m in the tank. An air diffuser generating air bubbles was located at the bottom of the tank. A bubble plume was formed in the tank with a diameter approximately 0.11 m at the measurement section. The BIV method was used to measure the velocity of the bubble plume with a FOV of 12.6 cm × 12.6 cm. Subsequently, the FOR technique was employed to measure the velocity at $x_b = 0$ and $z_b = 45$ cm, located in the region of the BIV FOV with $x_b = 0$ and $z_b = 0$ being the centre of the air diffuser. The void fraction is 4% with the average size of a bubble equal to 3 mm at the FOR measurement point, obtained by FOR. Figure 4 shows the measured bubble velocities using both the BIV and FOR methods at the point where the FOR probe was located. The mean velocities were obtained using 20 and 10 instantaneous velocities in the BIV and the FOR measurements, respectively. The comparison of the mean velocities shows very good agreement with a relative error about 1% (approximately 4 mm s^{-1}). The scattering of the instantaneous velocities may be due to the turbulent nature of the flow.
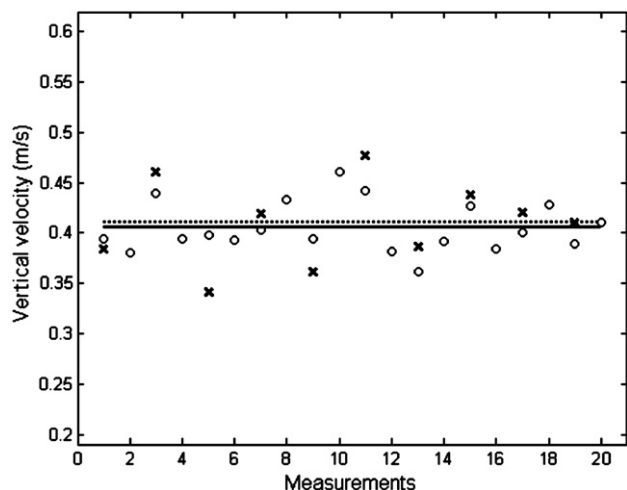
Figure 4. Comparison of velocities by BIV and FOR measurements: 'o', BIV instantaneous velocities; '×', FOR instantaneous velocities; solid line, BIV mean velocity; dotted line, FOR mean velocity.
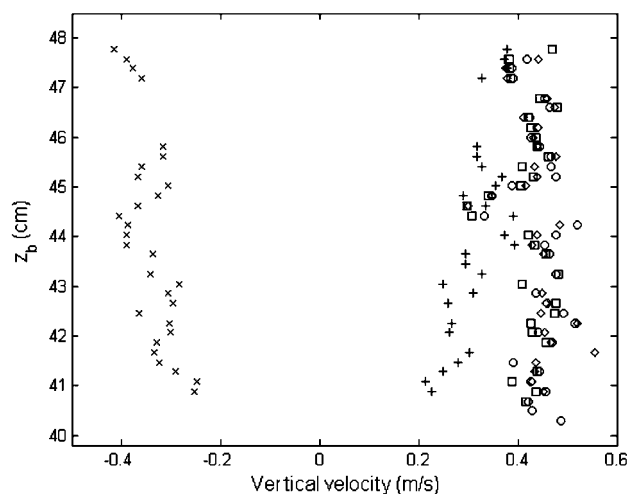
Figure 5. Velocity distribution along the centreline of the bubble plume obtained from: clear images (o), blurry images (+), upside down blurry images (×), superimposed clear and blurry images (□), superimposed clear and flipped blurry images (◇).

In theory the blurred images contributed from bubbles outside the DOF are expected to have insignificant influence in the correlation for velocity determination because the intensity of the bubbles is much weaker (and spread wider) than that of the well-focused bubbles inside the DOF. Since typical BIV measurements are performed in highly aerated bubbly flows, the captured images are indeed the sharp images inside the DOF superimposed with blurry images outside the DOF. In order to investigate the blurry image effect on the BIV accuracy, the velocity obtained from clear bubble images was compared with that obtained from artificially superimposed blurry bubble images. One set focused at the centre of the bubble plume so the bubble images are sharp and clear, while another set focused 15 cm behind the centre of the plume therefore the bubble images are blurred and out of focus. Both sets of original images were processed with velocities obtained.

Clear and blurry images were then artificially added in two ways. Firstly, the blurry images were added to the clear images directly. Secondly, the blurry images were vertically flipped and then added to the clear images. Figure 5 shows the instantaneous vertical velocity distribution obtained along the centreline of the bubble plume from the clear images, blurry images, vertically flipped blurry images, the superposition of the clear images and blurry images, and the superposition of the clear images and vertically flipped blurry images. The figure shows that both the velocities obtained from the clear–blurry superimposed images are very close to that from the clear images. Therefore, the blurry and out of focus bubble images have little effect on the accuracy of the BIV velocity measurement.

4. Results and discussion

The velocity measurement in the vicinity of the model structure was first carried out using the PIV technique. For the spilling type of breaking waves impinging on the structure, the air pocket between the wave front face and the structure is relatively small therefore the majority of the region in front of the leading edge of the structure is not highly aerated and suitable for PIV. However, even for the cases with only a small air pocket, greenwater above the structure due to overtopping is highly aerated and not ideal for PIV. If the impinging wave is of plunging type, a large air pocket in front of the structure will form and cause severe light scattering and result in saturated and not useful images for PIV correlation. The problem continues to the greenwater on top of the structure. Figure 6 shows the PIV measurement of the plunging breaking wave taken at FOV1 shown in figure 1. Clearly there exists a large region where no velocity vectors were obtained due to the large amount and size of air bubbles. A similar problem was also observed in Chang and Liu (1999, 2000). One thing we would like to point out is that the maximum magnitude of the velocity in figure 6(*a*) reached 1.5 times the phase speed of the wave. This result is consistent with that reported in Chang and Liu (1998).

The BIV technique uses the bubbles as tracers and correlates the bubble texture in the aerated region. This means that the BIV technique works in the region where the PIV technique does not work. Figure 7 shows a sample of inverted BIV images captured for the present study. The flow pattern of the bubble in front of the structure and the splashing jet above the structure are clearly identified in the image. Figure 8(*a*) shows the image and texture in the aerated region that is a close-up of figure 7 (see the marked area in the figure) without image inversion. Since the air bubbles appeared to be dark, the image was inverted, as shown in figure 8(*b*), before performing correlation for velocity determination. Figure 8(*c*) shows the obtained BIV velocity vectors through cross-correlating the inverted images. As a result, it is shown that as long as there exists a certain amount of air bubbles or air–water interfaces that form a distinct flow pattern or texture in the images, velocities can be obtained by cross-correlating the images.

Figure 9 shows the velocity field under the same experimental condition as in figure 6 but measured using the BIV technique. The field of view is shown in figure 1
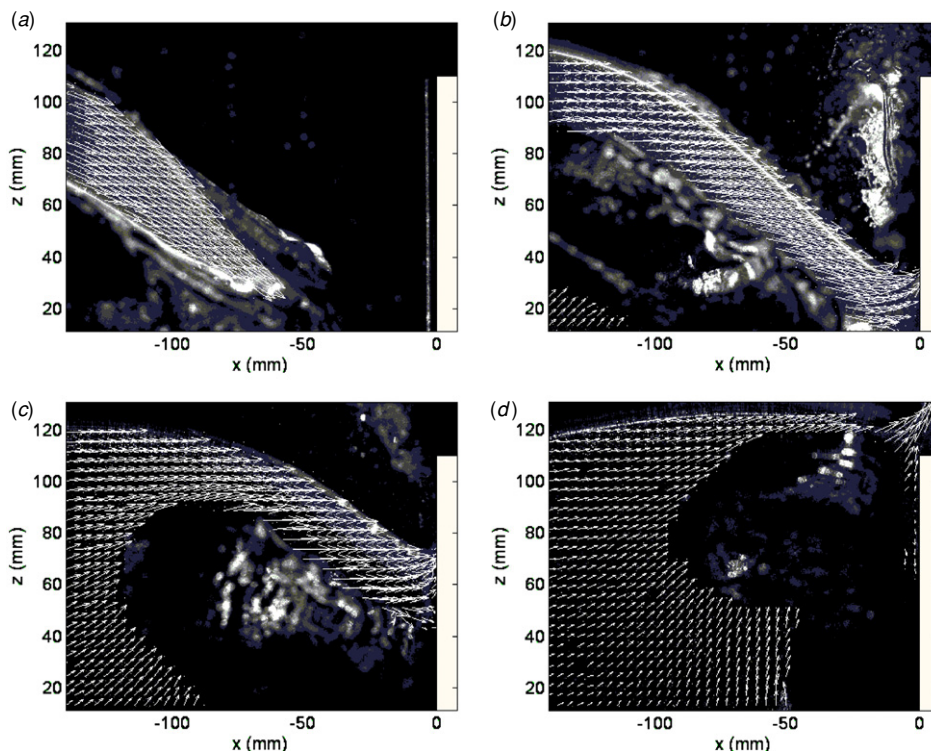
Figure 6. PIV measurement of plunging breaking wave impinging on structure. The time separation between the panels is 25 ms.
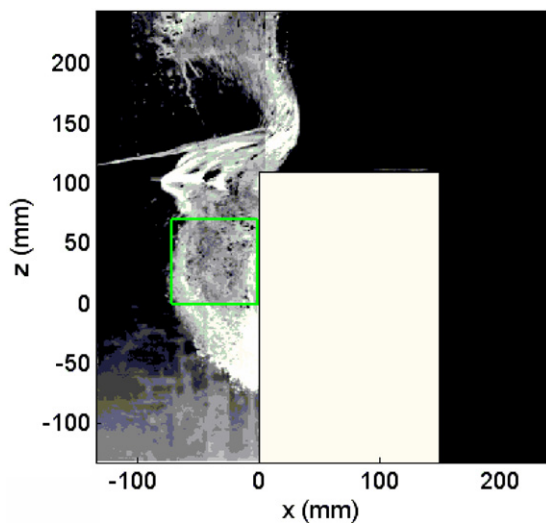
Figure 7. Sample BIV image of wave impinging on structure.

and denoted as FOV2. The entire sequence of the velocity field during the impinging and greenwater processes is demonstrated in the figure. Note that the velocity field is the mean velocity obtained from ensemble averaging ten repeated instantaneous BIV velocity measurements while the images were picked from one of the ten realizations (i.e., the images are instantaneous). Since the wave breaking process is highly turbulent, the instantaneous images do not match the mean velocities perfectly in some instants. $t = 0$ in the figure represents the instant when the overturning jet of the breaking wave touched the front water surface before impinging on the structure.

Figure 9(*a*) shows the moment right after the overturning jet touched its front water surface and before it touched the front wall of the structure. The jet velocity is moving downstream and downward. After a short duration of 35 ms in figure 9(*b*), the overturning wave impinged the structure's frontal wall and splashed upward. At this moment a large part of wave was still moving horizontally towards the structure while the splashing jet was moving vertically. The process continued to figure 9(*c*) until the wave momentum pushed the wave front to move forward onto the deck, as shown in figure 9(*d*). At the same time, when the wave momentum pushed part of the water to move upward, it also pushed part of the water to move downward and created a large vortex at around $z = 0$, starting in figure 9(*c*). The upward greenwater (i.e., water above the deck) did not touch the deck surface until the instant in figure 9(*e*). The horizontal velocity on the deck was small initially until the water started to touch the deck. In figures 9(*f*), (*g*) the greenwater lost its vertical momentum and the velocity became completely horizontal. This could create a large horizontal force exerting on any objects located on the deck due to the large horizontal momentum of water. Since the deck is not long, the greenwater on top of the deck passed the deck and moved downward back to the 'ocean' quickly at the rear edge of the deck. The velocity of the greenwater continued to move downstream but started to change to the downward direction as seen in figures 9(*h*), (*i*). After this moment the greenwater quickly receded and lost its momentum with the velocity being significantly reduced, as seen in figures 9(*j*)–(*l*).

We would like to point out that the measured velocity using BIV in figure 9 is indeed mainly the bubble velocity for the highly aerated region in front of the structure, and the
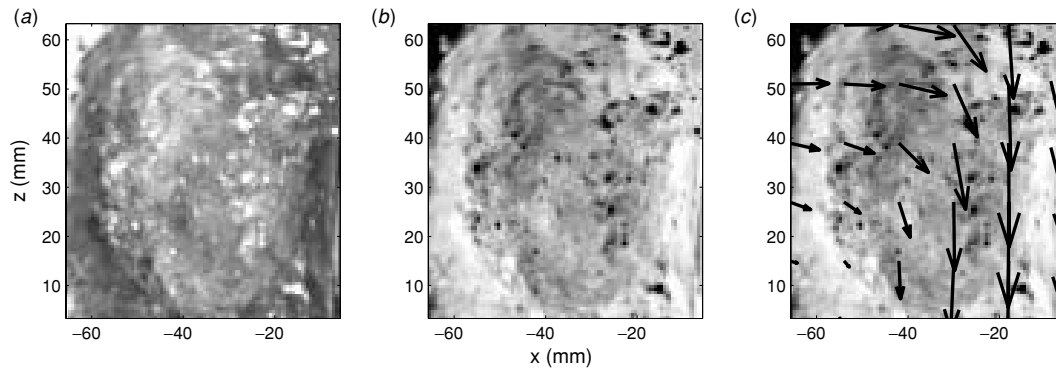
Figure 8. Close-up of the bubbly flow in figure 7 and associated velocity vectors obtained using BIV. (*a*) Raw image, (*b*) inverted image, (*c*) instantaneous velocity field.
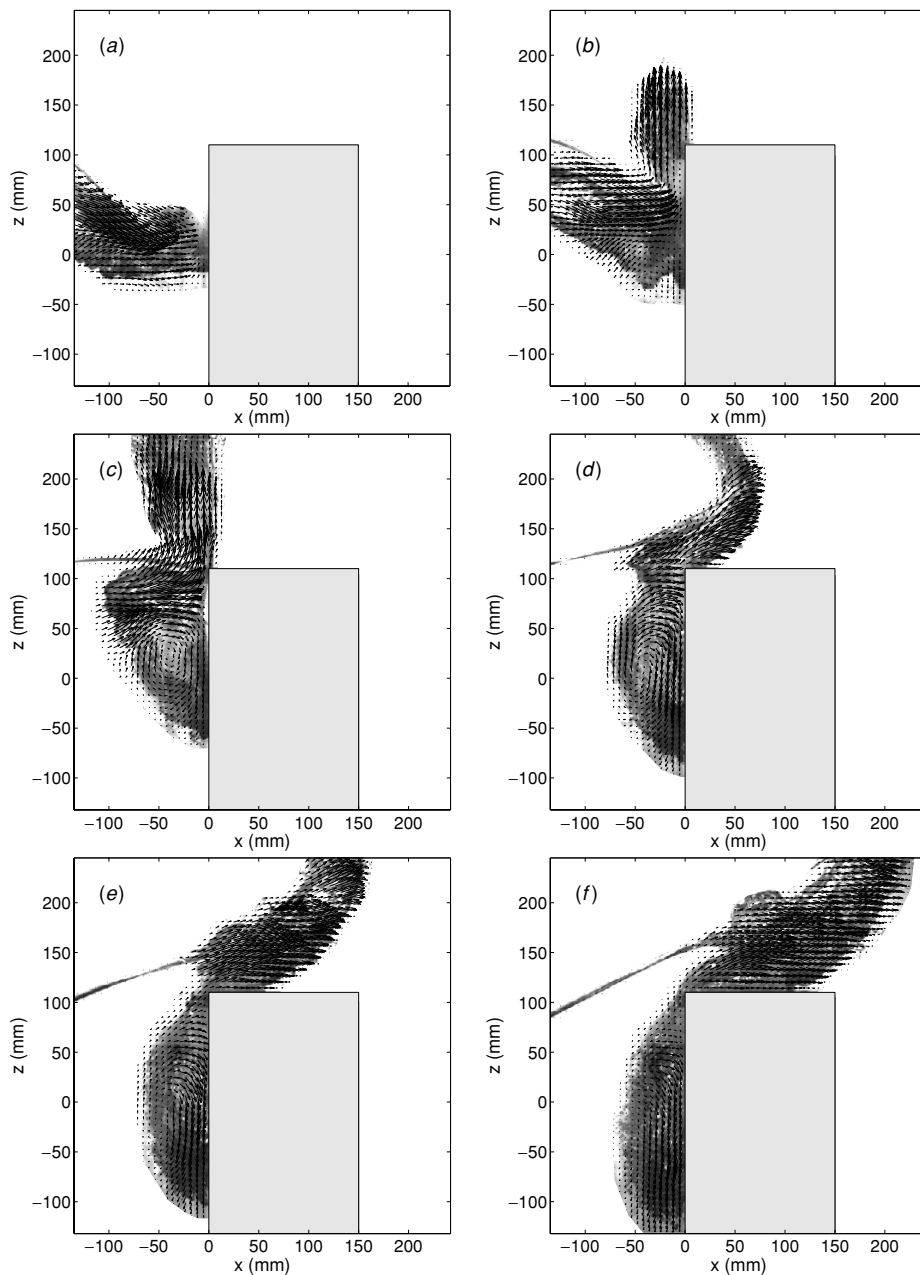
Figure 9. BIV measured mean velocity fields of plunging breaking wave impinging on structure. $t =$ (*a*) 0.022 s, (*b*) 0.057 s, (*c*) 0.092 s, (*d*) 0.127 s, (*e*) 0.162 s, (*f*) 0.197 s, (*g*) 0.232 s, (*h*) 0.267 s, (*i*) 0.302 s, (*j*) 0.337 s, (*k*) 0.372 s and (*l*) 0.507 s.
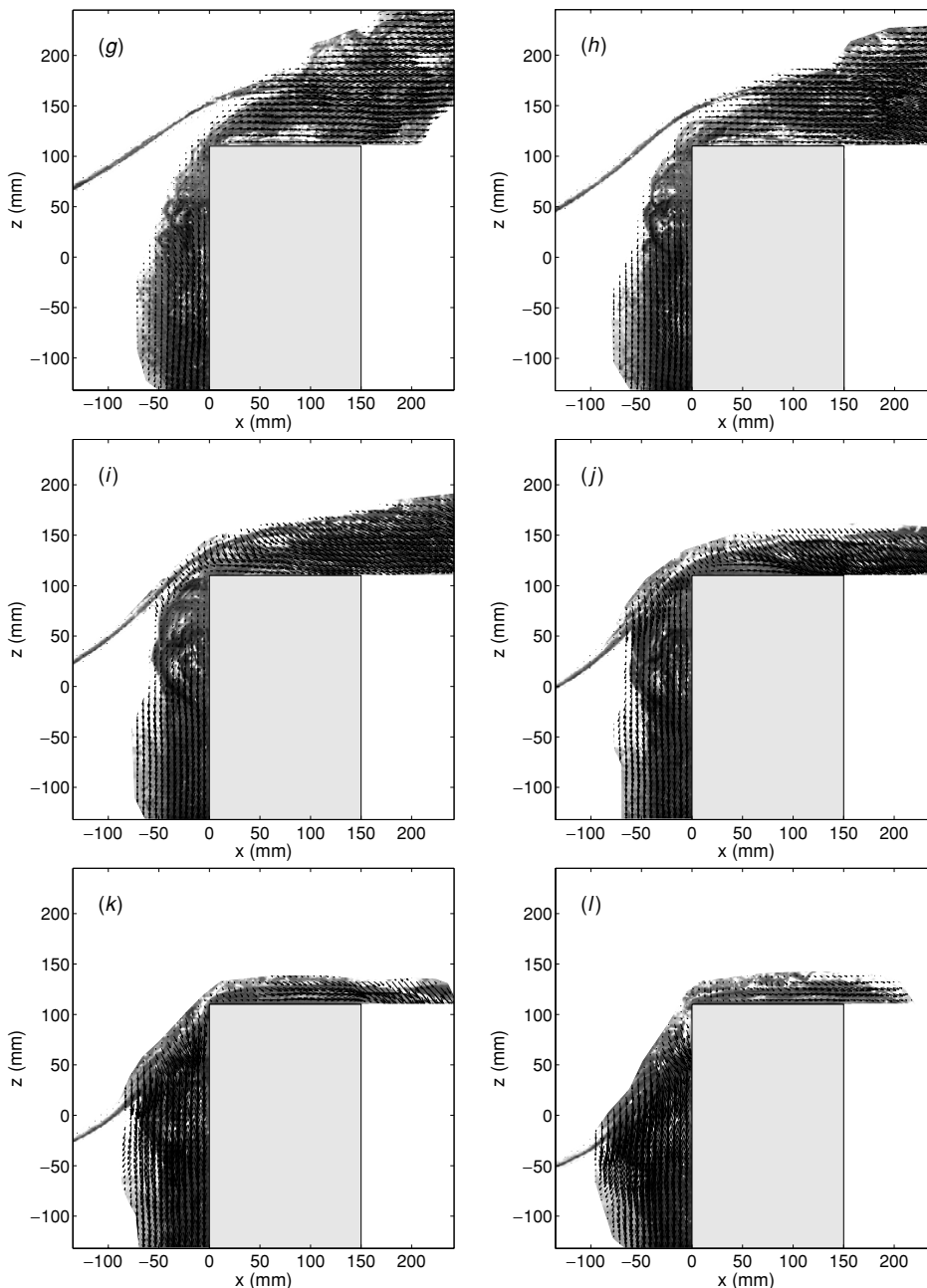
Figure 9. (Continued.)

fluid (air–water mixture) velocity above the structure deck. While we are more confident on the measured greenwater velocity above the deck due to the relatively minor effect of the buoyant force on the inertial force in that region, we are not sure whether the fluid velocity followed the air bubble velocity in the aerated region in front of the structure. The buoyant force may be significant in that region due to the relative low fluid velocity. This is especially true when large air bubbles were generated at certain phases. From the images captured by the fast speed camera, the bubble size reached nearly 5 cm in diameter during the period between figures 9(*i*) and (*j*). More studies are needed to clarify the differences between the velocity of air bubbles and that of water.

5. Summary and conclusion

The measurements of the velocity fields of a plunging breaking wave impinging on a structure and the associated greenwater above the structure using the PIV and BIV techniques were presented. While the PIV technique was only capable of obtaining the velocity field outside the aerated region in front of the structure, the BIV technique successfully measured the velocity field of the greenwater and the aerated region of the breaker. The BIV technique is indeed a modified PIV technique with images captured based on a modified shadowgraphy technique. The technique does not require the use of a laser thus has a much lower cost and is easier to set up. The BIV technique was validated by comparing the

velocity measured using the FOR method. The BIV technique measures velocity mainly in the multiphase region where the PIV technique does not work well or does not work at all. The technique therefore can be considered as a complementary technique for PIV in the study of high void fraction multiphase flows such as breaking waves.

Acknowledgments

References

Buchner B 1995 The impact of green water on FPSO design *Offshore Technology Conf. 95 OTC* 7698 pp 45–57

Chang K-A, Lim H-J and Su C B 2003 Fiber optic reflectometer for velocity and fraction ratio measurements in multiphase flows *Rev. Sci. Instrum.* **74** 3559–65

Chang K-A and Liu P L-F 1998 Velocity, acceleration and vorticity under a breaking wave. *Phys. Fluids* **10** 327–9

Chang K-A and Liu P L-F 1999 Experimental investigation of turbulence generated by breaking waves in water of intermediate depth *Phys. Fluids* **11** 3390–400

Chang K-A and Liu P L-F 2000 Pseudo turbulence in PIV breaking-wave measurements. *Exp. Fluids* **29** 331–8

Christensen E D and Deigaard R 2001 Large eddy simulation of breaking waves *Coast. Eng.* **42** 53–86

Govender K, Mocke G P and Alport M J 2002 Video-imaged surf zone wave and roller structures and flow fields *J. Geophys. Res.* **107** 3072

Greated C A and Emarat N 2000 Optical studies of wave kinematics *Advances in Coastal and Ocean Engineering* vol 6 ed P L-F Liu (Singapore: World Scientific) pp 185–223

Hamoudi B and Varyani K S 1998 Significant load and green water on deck of offshore units/vessels. *Ocean Eng.* **25** 715–31

Hassan Y A, Schmidl W D and Ortiz-Villafuerte J 1998 Investigation of three-dimensional two-phase flow structure in a bubbly pipe *Meas. Sci. Technol.* **9** 309–26

Jansen P C M 1986 Laboratory observations of the kinematics in the aerated region of breaking waves *Coast. Eng.* **9** 453–77

Lin P and Liu P-F 1998a A numerical study of breaking waves in the surf zone *J. Fluid Mech.* **359** 239–64

Lin P and Liu P-F 1998b Turbulence transport, vorticity dynamics, and solute mixing under plunging breaking waves in surf zone *J. Geophys. Res.* **103** 15677–94

Lindken R and Merzkirch W 2001 A novel PIV technique for measurements in multi-phase flows and its application to two-phase bubbly flows *4th Int. Symp. on Particle Image Velocimetry* paper A 231

Melville W K, Veron F and White C J 2002 The velocity field under breaking waves: coherent structures and turbulence *J. Fluid Mech.* **454** 203–33

Nishino K, Kato H and Torii K 2000 Stereo imaging for simultaneous measurement of size and velocity of particles in dispersed two-phase flow *Meas. Sci. Technol.* **11** 633–45

Perlin M, He J and Bernal L P 1996 An experimental study of deep water plunging breakers. *Phys. Fluids* **8** 2365–74

Ray S D 2002 *Applied Photographic Optics* (Oxford: Focal) pp 215–33

Schoenberg T and Rainey R C T 2002 A hydrodynamic model of green water incidents *Appl. Ocean Res.* **24** 299–307

Skyner D J, Gray C and Greated C A 1990 A comparison of the time-stepping numerical predictions with whole-field flow measurement in breaking waves *Water Wave Kinematics* ed A Torum and O T Gudmestad (Boston: Kluwer) pp 491–508

Ting F C K and Kirby J T 1994 Observation of undertow and turbulence in a laboratory surf zone *Coast. Eng.* **24** 51–80

Ting F C K and Kirby J T 1995 Dynamics of surf-zone turbulence in a strong plunging breaker *Coast. Eng.* **24** 177–204

Watanabe Y and Saeki H 1999 Three-dimensional large eddy simulation of breaking waves *Coast. Eng. J.* **41** 281–301

Breaking Wave Impinging and Greenwater on a Two-Dimensional Offshore Structure

Yonguk Ryu and Kuang-An Chang
Ocean Engineering Program
Department of Civil Engineering
Texas A&M University
College Station, TX, U.S.A.

ABSTRACT

The measurement of velocity fields of a plunging wave impacting on a structure in a two-dimensional wave flume was investigated experimentally. As the wave impinged and overtopped the structure, a large highly aerated region was created in front of the structure and water splashed on top of the structure. The broken wave in front of the structure and associated greenwater on top of the structure are highly aerated containing not only a large number of bubbles but also very large sizes of bubbles. A modified PIV method incorporating the traditional PIV method with the shadowgraphy technique was introduced to obtain the velocity in the highly aerated region and the splashing water on the deck by correlating the "texture" of the bubble images. It was found that the maximum fluid particle velocity in front of the structure during the impinging process is about 1.5 times the phase speed of the wave, while the maximum horizontal velocity above the deck is less than the phase speed. It was also found that the dam breaking solution does not work well in predicting the greenwater velocity.

KEY WORDS: Wave breaking; particle image velocimetry; wave-structure interaction; greenwater.

INTRODUCTION

It is well known that extreme waves have caused significant damages to offshore structures due to the tremendous forces of wave impingement (e.g., Buchner, 1995; Hamoudi and Varyani, 1998; Schoenberg and Rainey, 2002). Frequently, the impinging waves rush upward to the deck and create so-called greenwater on the deck that washes out and damages equipment and, in some cases, causes the injury or death to persons working on the deck. One recent example is the greenwater damage caused by Hurricane Ivan in the Gulf of Mexico in 2004 that damaged several offshore platforms.

The interaction of extreme waves and a structure has been studied for decades. Although some studies were carried out using numerical models, most of the models are based on the potential theory therefore the multiphase highly turbulent problem was not realistically simulated. The results were therefore for prediction of wave forces rather than looking into the physical insight of the phenomenon. On the other hand, more advanced approaches, either based on the Reynolds averaged Navier-Stokes equations (RANS) or large eddy simulation (LES), that feature turbulent models and provide much more physical insight have started to be used in the study (e.g., Lin and Liu, 1998; Watanabe and Saeki, 1999; Christenson and Deigaard, 2001). However, limited success was achieved due to the lack of comprehensive treatments on the splashing free surface and the high void fraction bubbly flow, and lack of experimental data to validate the calculations and the models.

For experimental approach, since very few non-intrusive quantitative velocity measurements for breaking wave impinging on a structure exist, we thus review the measurement for breaking waves instead. Various measurement techniques, including laser Doppler velocimetry (LDV) and the particle image velocimetry (PIV), have been employed for the measurements of flow field of the wave breaking process both in a surf zone and in deep water (e.g., Greated and Emarat, 2000; Ting and Kirby, 1994; Perlin et al., 1996). Among the efforts, PIV is a new comer and only about 10 years old. However, the technique is perhaps the most robust and state-of-the-art technique among all the methods. This is due to not only its full field nature but also its recent advances in the improvement of the spatial and temporal resolutions.

This paper presents the experimental study on the kinematics of plunging waves impinging and overtopping a structure. The velocity field in the aerated region around the structure that is the most interesting and important to the problem but difficult to measure using PIV was obtained using the bubble image velocimetry (BIV) technique. The sequential velocity field in the vicinity of the structure was demonstrated. The measured velocity was used to compare with the dam breaking solution.

EXPERIMENTAL CONDITION AND SETUP

The experiments were performed in a glass-walled wave tank that is 36 m long, 0.9 m wide and 1.5 m high. The water depth was kept constant at $h = 0.80$ m throughout the experiments. The wavemaker is of dry-back flap type installed at one end of the wave tank and controlled by a computer. A 1:5.5 sloping beach with a layer of horsehair is at the other end of the tank to absorb the wave energy and reduce reflection. A rectangular model structure with a length of 0.15 m, a height of 0.31 m and a width the same as that of the tank. The draft of the model structure is 0.20 m. The model was constructed based on a simplified two-dimensionally tension-leg platform with a scale ratio of 1:168. The model structure was mounted on aluminum frames that were rigidly fixed to the bottom and suspended from the top of the tank. The sketch of the model structure is shown in fig. 1 together with the coordinate system and the fields of view (FOV) used for particle image velocimetry (PIV) and bubble image velocimetry (BIV). The breaking wave tested is a plunging breaker that was generated using a wave focusing method. The wave train consists of waves with various frequencies ranging from 0.7 Hz to 1.3 Hz. The plunging breaker broke at a desired location right in front of the structure.
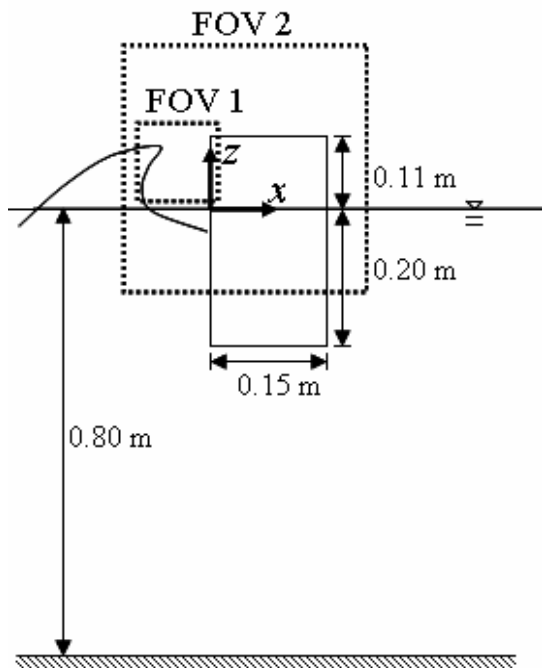
The PIV technique in the present study was first used to measure the velocity field near the front wall of the model structure. The light source of the PIV system is a dual-head frequency-doubled Nd:YAG laser that has a 532 nm wavelength, 400 mJ maximum output energy, 6 ns pulse duration, and 10 Hz repetition rate for each head. A set of optics consisting of cylindrical and spherical lenses was used to generate the light sheet. The image recording device is a CCD camera that has an 8 frames per second (fps) maximum framing rate, a resolution of 1024×1280 pixels, and a 12-bit dynamic range.

The BIV technique was used to obtain the velocity field in the aerated region and splashing greenwater. The technique uses the bubble images and the "texture" in the images created by the bubbles and the air-water interfaces instead of the small seeding particles used in the traditional PIV technique. The idea of the BIV method came from combining the shadowgraphy technique that illuminates the fluid from behind to reveal the flow pattern, and the PIV technique that correlates the consecutive images to determine the velocity. Since the velocity is calculated through cross-correlating the images obtained by the shadowgraphy technique with the bubble structure in the images as tracers, the BIV technique requires only two light projectors to illuminate the air bubbles in the aerated region. Unlike the traditional PIV technique, no laser light sheet is needed. In this study, regular 600 W light bulbs with reflecting mounts were used to illuminate the flow. The images were captured by a high speed camera mounted with a 105 mm focal lens. The camera has a resolution of 512×512 pixels, an 8-bit dynamic range, and a maximum framing rate of 1000 fps. The aperture of the camera was set with the f-number equal to 1.8.

Fig. 1: Sketch of the model structure, coordinate system, and fields of view used in PIV and BIV
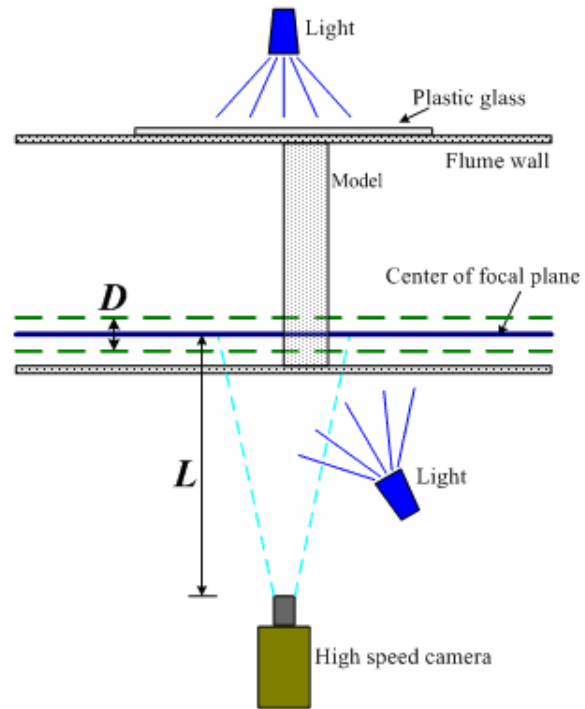

Fig. 2: BIV apparatus

Since the BIV technique does not use a light sheet to illuminate a specific plane of interest like the traditional PIV method, it is

necessary to know where the measured bubbles are in the cross-tank direction (the *y* direction). The problem is resolved by limiting the depth of field (DOF) in the experiment which is achieved by carefully setting up the camera. The DOF is defined as a distance within which objects captured by the camera is well focused and appear to be sharp. The camera focal point and the DOF can be considered as the light sheet plane and light sheet thickness, respectively, in the PIV technique.

Objects located in front of and behind the DOF will appear to be blurring without a clear texture in the captured image and therefore have little effect on the later correlation process for velocity determination. On the other hand, objects located within the DOF will be sharp in the image with a featured pattern due to the flow. This means that the obtained velocity from cross-correlating the captured images is indeed mainly contributed from the image of fluid within the DOF. The error due to the thickness of DOF in the obtained velocity can be estimated approximately as $\varepsilon = D/2L$. If the depth of view *D* is thin and the distance between the camera and the focal plane *L* is long, the error can be minimized. In the present study, the error due to the thickness of the DOF is estimated as about 2%. The arrangement of the BIV system is sketched in fig. 2. The mean velocity was calculated from ensemble averaging 10 instantaneous velocity fields from repeated runs with the same test condition.

RESULTS AND DISCUSSION

The velocity measurement in the vicinity of the structure was first carried out using the traditional PIV technique. The impinging wave was of plunging type. A large air pocket in front of the structure was formed and caused severe light scattering and resulted in saturated and not useful images for PIV correlation. The problem continued to the greenwater region on top of the structure. Fig. 3 shows the PIV measurement of the plunging breaking wave taken at FOV1 shown in fig. 1. Clearly there exist a large region where no velocity vectors were obtained due to the large amount and size of air bubbles. One thing we would like to point out is that the maximum magnitude of the velocity in fig. 3(a) reached 1.5 times the phase speed of the wave. The result is consistent with that reported in Chang and Liu (1998).

The BIV technique uses the bubbles as tracers and correlates the bubble texture in the aerated region, and the splashing water on the deck. Therefore the BIV technique works in the region where the PIV technique does not. Fig. 4 shows the velocity field under the same experimental condition as that in fig. 3 but measured using the BIV technique. The field of view is denoted as FOV 2 and shown in fig. 1. The sequence of velocity field during the impinging and greenwater processes is clearly demonstrated in the figure. Note that the velocity field is the mean velocity obtained from ensemble averaging 10 repeated instantaneous BIV velocity measurements but the images in the figure were picked from one of the 10 realizations (i.e., the images are instantaneous). Note that *t* = 0 in the figure represents the instant when the overturning jet of the breaking wave touched the front water surface before impinging on the structure.
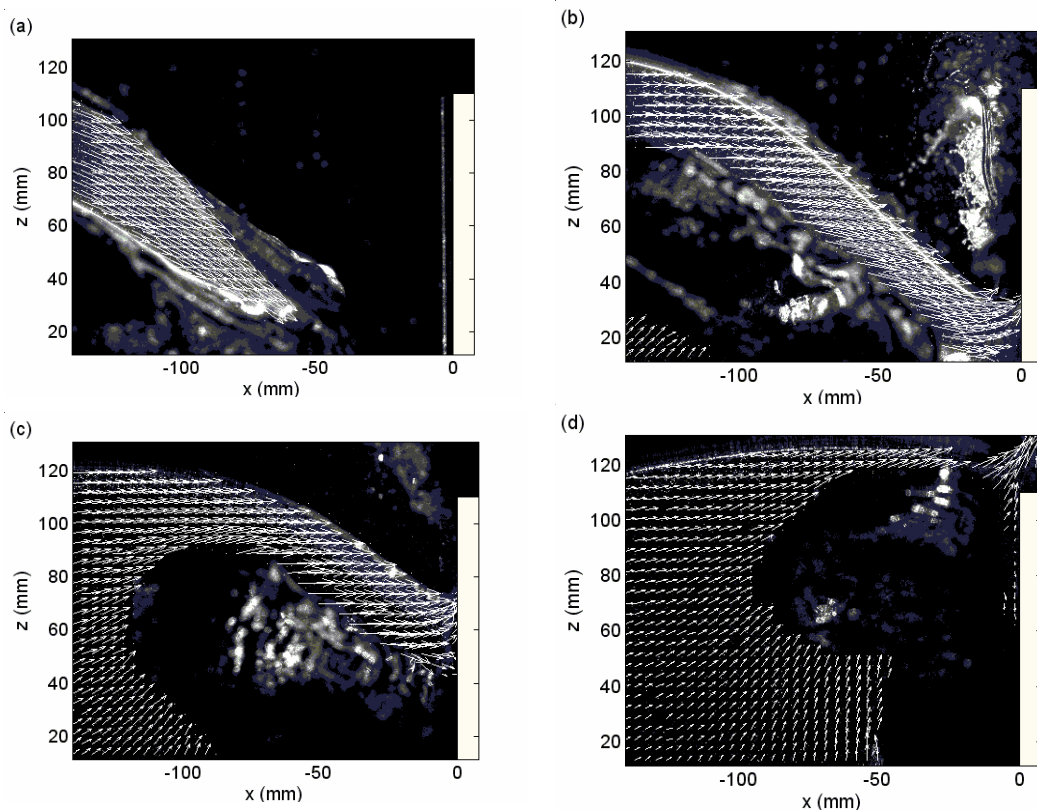
Fig. 3: PIV measurement of plunging wave impinging on the structure
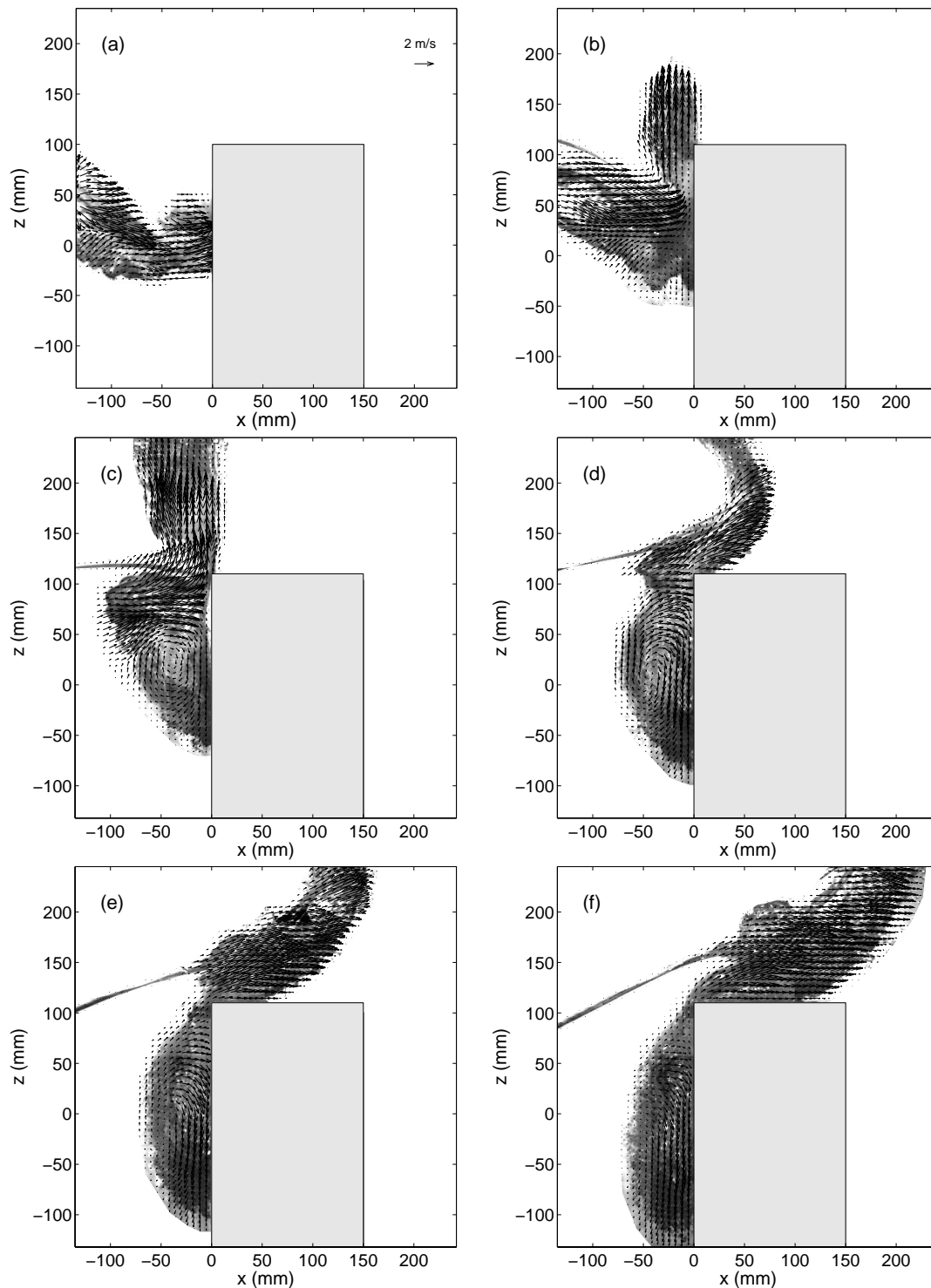
Fig. 4: BIV measured mean velocity fields of plunging breaker impinging on the structure. t = (a) 0.022 s, (b) 0.057 s, (c) 0.092 s, (d) 0.127 s, (e) 0.162 s, (f) 0.197 s.

Fig. 4(a) shows the moment right after the overturning jet touched its front water surface but before it touched the front wall of the structure. The jet velocity is moving downstream and downward. After a short duration of 35 ms in fig. 4(b), the overturning wave impinged the structure frontal wall and splashed upward. Note that the time interval between the recorded images in the BIV method using the high speed camera was 1.75 ms. The velocity fields in fig. 4 were plotted from every 20 images. At this moment a large part of wave was still moving horizontally towards the structure while the splashing jet was moving vertically. The process continued to fig. 4(c) until the wave momentum pushed the front to move forward onto the deck, shown in fig. 4(d). At the same time when the wave

momentum pushed part of the water to move upward, it also pushed part of the water to move downward and created a large vortex, started in fig. 4(c). The water did not touch the deck surface until the instant in fig. 4(e). The horizontal velocity on the deck was small initially until the water started to touch the deck. In fig. 4(f) the greenwater lost its vertical momentum and the velocity became completely horizontal. This could create a large horizontal force exerting to any objects on the deck due to the large horizontal

momentum of the water. Since the deck is not long, the greenwater on top of the deck past the deck and moved downward back to the "ocean" quickly at the rear edge of the deck. The velocity of greenwater continued to move downstream but started to change to downward direction. Later the greenwater level quickly recessed and lost its momentum with the velocity significantly reduced (not shown here).
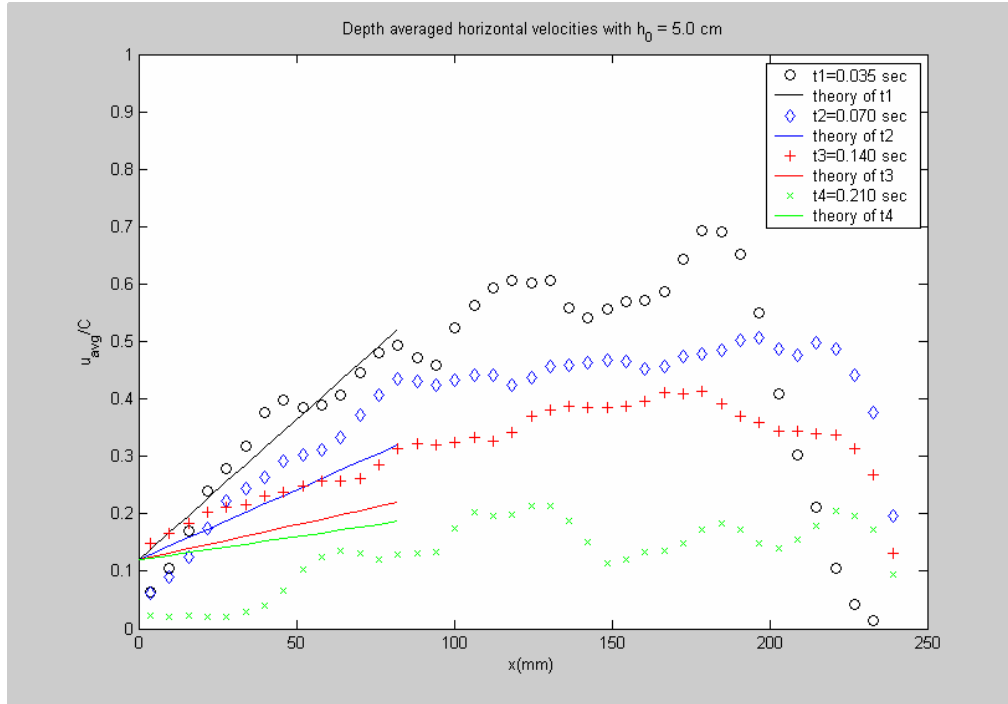

Fig. 5: Comparison between the measured horizontal velocity and the dam breaking solution

The dam breaking problem has been used to simulate the greenwater on the deck without validation. To check this, the measured horizontal velocity on the deck was compared with the analytical solution of the dam breaking problem. From the Ritter solution, the dam breaking velocity can be expressed as $u = \frac{2}{3}\left(\sqrt{gh_0} + x/t\right)$, where u is the horizontal velocity, g the gravitational acceleration, h_0 the initial water depth in the reservoir. For the greenwater flow, $h_0 = 5$ cm was used by assuming it is the water elevation measured from the top of the wave to the top of the structure when the wave started to overtop the model. The comparison is shown in fig. 5. We first matches the solution with the measurement at an instant when the greenwater velocity has just turned horizontal ($t = t_1$ in the figure). If starting from there, the comparison shows the analytical solution underpredicts the greenwater velocity. However, before $t = t_1$ the solution indeed overpredicts the velocity, though during that period, according to the measurement, the horizontal velocity component was not yet developed and splashing jet was mainly moving upward. It is obvious the comparison is not good. By simply looking at fig. 4, it is hard to believe the velocity field is of any close to that of a breaking dam.

SUMMARY AND CONCLUSION

The measurements of velocity field of a plunging breaking wave impinging on a structure and associated greenwater on top of the structure using the PIV and BIV techniques were presented. While the PIV technique was only capable of obtaining the velocity field outside the aerated region in front of the structure, the BIV method successfully measured the velocity field of the greenwater and the aerated region of the breaker. The maximum velocity reached 1.5C before the breaking jet hitting the structure. For greenwater, the simple dam breaking solution seems to overpredict the greenwater velocity field at the initial stage when greenwater just occurred, and underpredict the velocity field after the initial stage.

ACKNOWLEDGEMENTS

REFERENCES

Buchner, B (1995) "The impact of green water on FPSO design." *In: Offshore Technology Conference 95*, OTC, Vol 7698, pp 45–57.

Chang, K-A, and Liu, PL-F (1998) "Velocity, acceleration and vorticity under a breaking wave." *Physics of Fluids,* Vol 10, pp 327-329.

Christensen, ED, and Deigaard, R (2001) "Large eddy simulation of breaking waves." *Coastal Engineering,* Vol 42, pp 53-86.

Greated, CA, and Emarat, N (2000) "Optical studies of wave kinematics." *Advances in Coastal and Ocean Engineering vol. 6* ed P L -F Liu (Singapore; World Scientific), pp 185-223.

Hamoudi, B, and Varyani, KS (1998) "Significant load and green water on deck of offshore units/vessels." *Ocean Engineering,* Vol 25, pp 715–731.

Lin, P, and Liu, P-F (1998) "A numerical study of breaking waves in the surf zone." *Journal of Fluid Mechanics,* Vol 359, pp 239-264.

Perlin, M, He, J, and Bernal, LP (1996) "An experimental study of deep water plunging breakers." *Physics of Fluids,* Vol 8, pp 2365-2374.

Schoenberg, T, and Rainey, RCT (2004) "A hydrodynamic model of Green Water incidents." *Applied Ocean Research,* Vol 24, pp 299–307.

Ting, FCK, and Kirby, JT (1994) "Observation of undertow and turbulence in a laboratory surf zone." *Coastal Engineering,* Vol 24, pp 51– 80.

Watanabe, Y, and Saeki, H (1999) "Three-dimensional large eddy simulation of breaking waves." *Coastal Engineering Journal,* Vol 41, pp 281-301.

Simulation of Wave Runup Around Offshore Structures by a Chimera Domain Decomposition Approach

Hamn-Ching Chen[1], Kai Yu[1] and Sheng-Yi Chen[1]

[1]Ocean Engineering Program, Department of Civil Engineering, Texas A&M University, College Station, Texas 77843; email: hcchen@civil.tamu.edu

Abstract

A Reynolds-Averaged Navier-Stokes (RANS) numerical method has been employed in conjunction with a chimera domain decomposition approach for time-domain simulation of wave runup around offshore structures. Simulations were performed first for a simplified two-dimensional TLP configuration under two different incident wave conditions. The results are in very good agreement with the available data obtained from the particle image velocimetry (PIV) measurements. The method was then extended for the simulation of wave runup around single and multiple vertical cylinders. The simulation results clearly demonstrated the capability of the chimera RANS method for time-domain simulation of wave runup including both the viscous and fully nonlinear wave effects.

Introduction

The interaction between the extreme waves and floating structures is of primary concern in the design of offshore structures. Most of the earlier work employed potential flow theory without considering the viscous effects. In the past several years, however, the viscous-flow methods have been used by, among others, Ananthakrishnan (1998), Dong and Huang (1999), Park et al. (2001), and Chen et al. (2001, 2002) for the study of fully nonlinear free surface flow around coastal and offshore structures. In order to provide accurate resolution of viscous, nonlinear free surface flow around offshore structures, it is necessary to employ more sophisticated numerical methods and turbulence models which are capable of dealing with complex three-dimensional flow separation and fully nonlinear free surface waves.

In the time-domain simulation of nonlinear waves around offshore structures, it is convenient to use separate body-fitted numerical grids for the structures and the ambient wave field. In the present chimera domain decomposition approach, the numerical grids around the offshore structures remain fixed while the free surface grids are adjusted every

time step to conform to the exact free surface. Since the submerged portion of the structures change continuously at different time instants, the interpolation between different chimera grid blocks were updated every time step to enforce conservation of mass and momentum across block boundaries over the entire simulation. In addition, an effective damping beach approach was implemented on the wavemaker boundary to prevent the reflected waves from reaching the wavemaker boundary. This enables us to perform long-duration simulations without significantly increase the size of the computational domain. In the present study, the chimera RANS method of Chen et al. (2001, 2002) has been generalized for time-domain simulation of fully nonlinear wave runup around two- and three-dimensional offshore structures.

Governing equations and solution approach

The present study is concerned with the prediction of wave runnp around offshore structures. Calculations have been performed using the chimera RANS method of Chen et al. (2001, 2002) for accurate resolution of the viscous and nonlinear wave effects. The method solves the nondimensional Reynolds-Averaged Navier-Stokes equations for incompressible flow in orthogonal curvilinear coordinates (x^i, t):

$$U^i_{,i} = 0 \tag{1}$$

$$\frac{\partial U^i}{\partial t} + U^j U^i_{,j} + \overline{u^i u^j}_{,j} + g^{ij} p_{,j} - \frac{1}{\text{Re}} g^{jk} U^i_{,jk} = 0 \tag{2}$$

where U^i and u^i represent the mean and fluctuating velocity components, and g^{ij} is the conjugate metric tensor. t is time p is pressure, and $\text{Re} = U_o L/\nu$ is the Reynolds number based on a characteristic length L, a reference velocity U_o, and the kinematic viscosity ν. The equations are written in tensor notation with the subscripts, $_{,j}$ and $_{,jk}$, represent the covariant derivatives. In the present study, the two-layer turbulence model of Chen and Patel (1988) is employed to provide closure for the Reynolds stress tensor $\overline{u^i u^j}$.

The RANS equations have been employed in conjunction with a chimera domain decomposition technique for accurate and efficient resolution of body boundary layer and flow separation around offshore structures. For present wave runup simulations, the kinematic free surface boundary condition is solved to determine the exact free surface:

$$\eta_t + U\eta_x + V\eta_y - W = 0 \quad \text{on} \quad z = \eta \tag{3}$$

where η is the wave elevation and (U, V, W) are the mean velocity components on the free surface. The dynamic free surface conditions are also enforced on the exact free surface to provide accurate prediction of the fully nonlinear waves. A more detailed description of the chimera RANS/free-surface method was given in Chen et al. (2001, 2002).

In the far field, a radiation condition or absorbing beach must be employed to avoid wave reflections from the downstream boundary. Open boundaries enclosing the fluid domain are artificial and essentially arbitrary. In the present study, an absorbing

beach proposed by Clement (1996) was implemented by adding a viscous term in the dynamic free surface boundary condition. For long-duration simulations, it is also necessary to prevent the reflected and diffracted waves from reaching the wavemaker boundary. In the present study, the wavemaker absorbing beach proposed by Chen and Huang (2004) for linear potential flow problems was generalized to absorb the reflected and diffracted waves before they reach the wavemaker boundary.
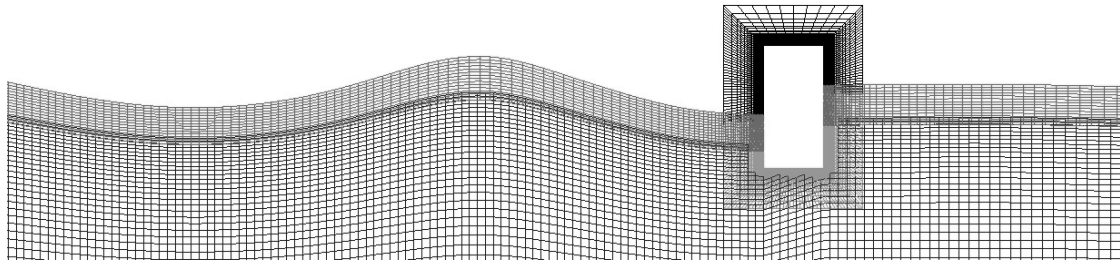
Results and Discussion

Recently, Ryu and Chang (2004) performed detailed velocity measurements in a laboratory flume at Texas A&M University for wave runup on a two-dimensional fixed rectangular structure based on the dimensions of a typical tension leg platform (TLP). The length and height of the model platform are 0.15 m and 0.30 m, respectively. The still water level is 0.105 m below the platform deck. Velocity fields in the vicinity of the structure were measured using the particle image velocimetry (PIV) technique for 8 phases per each wave period. Both instantaneous and phase-averaged quantities were obtained and analyzed. These PIV data provide an excellent database for the validation of the present numerical method.
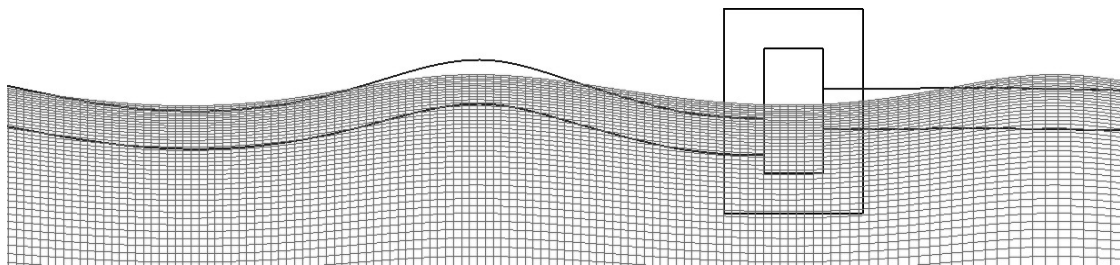
In the present chimera domain decomposition approach for platform wave runup simulation, the solution domain is divided into several computational blocks as shown in Figure 1 to provide appropriate resolution of the platform boundary layers, wakes, as well as the nonlinear free surface waves. Figures 1(a) and 1(c) shows the chimera grid block structures around the platform at $t/T = 20.375$ and 20.875, respectively. For completeness, the wave tank grids at the same time instants are also shown in Figures 1(b) and 1(d). These wave tank grids are not linked to the other grid blocks and are used solely for the implementation of absorbing beach in front of the wavemaker. For long-duration simulations over many wave periods, it is well known that the wave reflected by the platform will propagate back to the wavemaker boundary and interfere with the incident wave field. In the present study, a new absorbing beach approach developed recently by Chen and Huang (2004) has been implemented to prevent the reflected wave from returning to the wavemaker. In this absorbing beach approach, the wave tank grids shown in Figures 1(b) and 1(d) were used to allow concurrent computation of the incident wave field without the presence of the offshore structure. This enables us to determine the exact pattern of the reflected wave since both wave fields with and without the structure were computed simultaneously at every time step. A damping function was then used to absorb the reflected waves so that the time-domain simulation can be continued for many wave periods without unphysical wave reflection from the wavemaker.

In the present wave runup simulations, the incident wave field was generated using the higher order nonlinear wave theory of Cokelet (1977). The free surface grid blocks are updated at every time step to follow the instantaneous free surface wave elevation. Furthermore, nonlinear dynamic free surface boundary condition is imposed on the exact free surface for accurate prediction of the fully nonlinear wave field. It
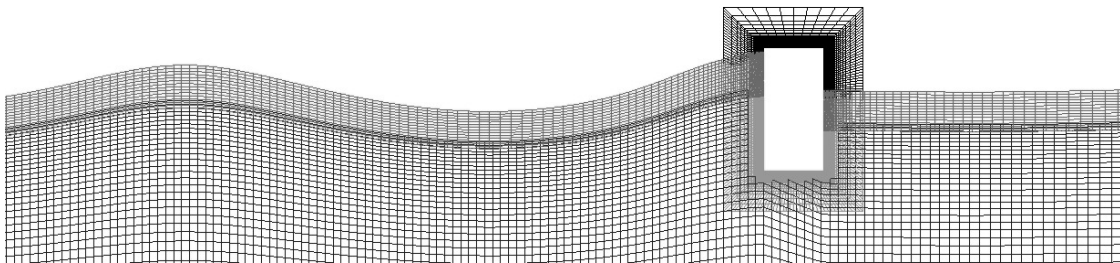
should also be noted that the platform grid covers the entire platform surface including the dry deck area. Moreover, the platform grid remains fixed during the entire simulation even though the submerged section changes with instantaneous wave elevation. This not only simplifies the grid-generation process, but also eliminates undesirable grid distortion which typically occurs in the simulation of large amplitude wave motions.
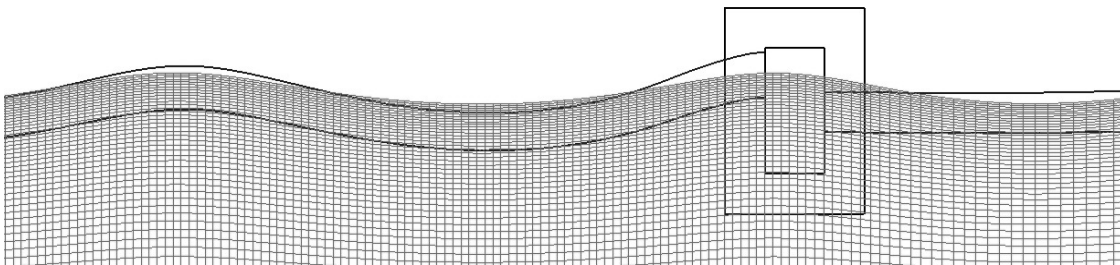

(a) Chimera grid with structure; t/T = 20.375

(b) Wave tank grid without the structure; t/T = 20.375

(c) Chimera grid with structure; t/T = 20.875

(d) Wave tank grid without the structure; t/T = 20.875

Figure 1. Chimera grid structure for wave runup simulation

Simulations were performed for wave runup on the two-dimensional platform used in the experimental study of Ryu and Chang (2004) with two different incident wave heights of $H = 0.0575$ m and 0.0875 m, respectively. Figure 2 shows the computed free surface wave elevation and pressure contours at t/T = 20.375, 20.625, and 20.875, respectively, for the $H = 0.0575$ m case. The superposition and cancellation of the incident and reflected waves at different time instants can be clearly seen from this figure. The present simulation results also clearly demonstrated the effectiveness of the new absorbing beach approach as the simulation was continued for more than 20 wave periods without any distortion in incident wave field.
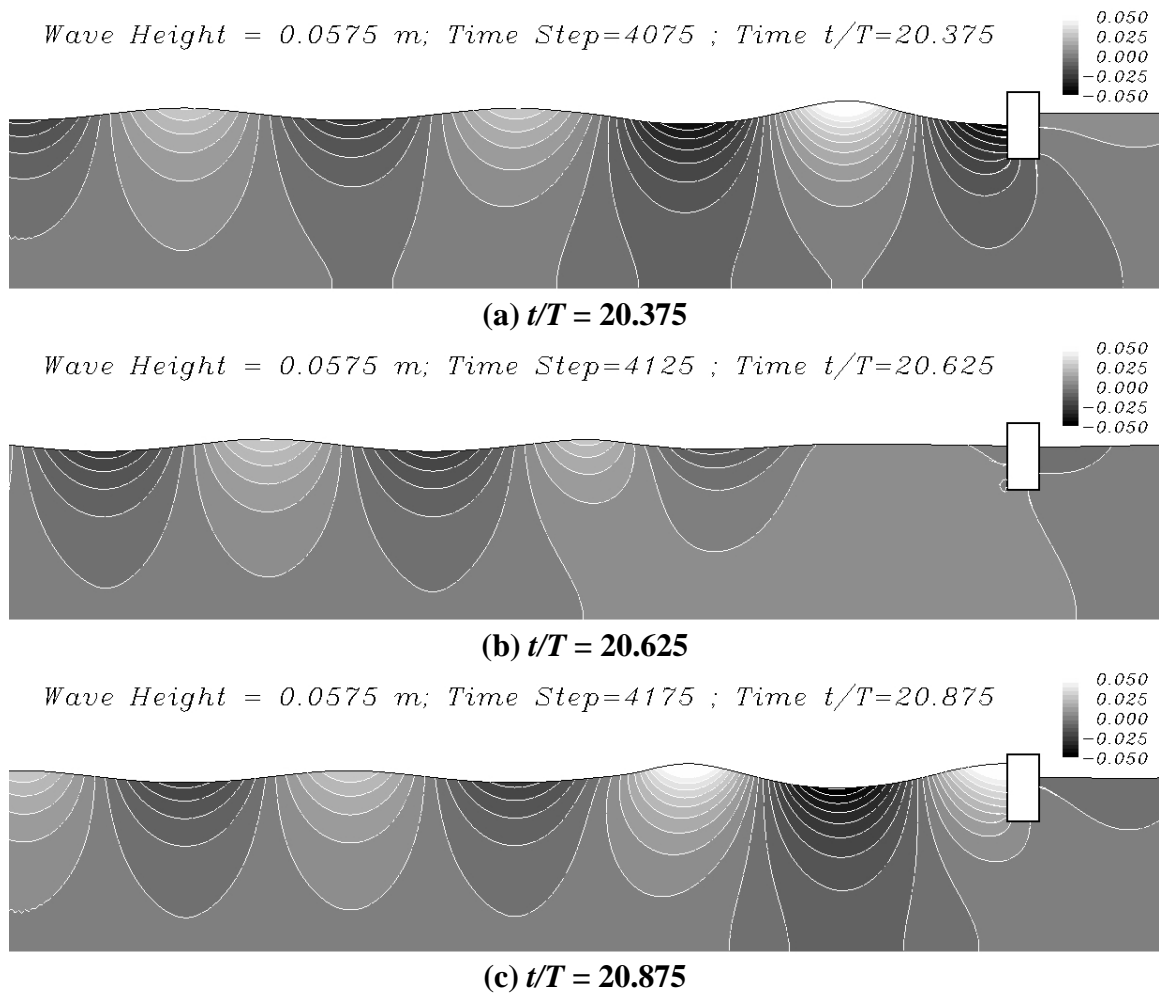

(a) *t/T* = 20.375

(b) *t/T* = 20.625

(c) *t/T* = 20.875

Figure 2. Wave elevation and pressure contours; incident wave height $H = 0.0575$m

Figure 3 shows the time history of the wave elevation in front of the structure. It is seen that the first wave reaches the structure after three wave periods since the wavemaker is located about three wavelengths upstream of the model TLP. Note that the relatively large waves occurred around the 12th-13th wave periods followed by a transition period with significant fluctuation in wave height. The flow attained a nearly periodic pattern after about 20 wave periods. It is quite clear that the absorbing beach in front of the wavemaker successfully absorbed all the waves reflected from the structure so that the same incident wave can be maintained for long duration simulation with a rather small solution domain.
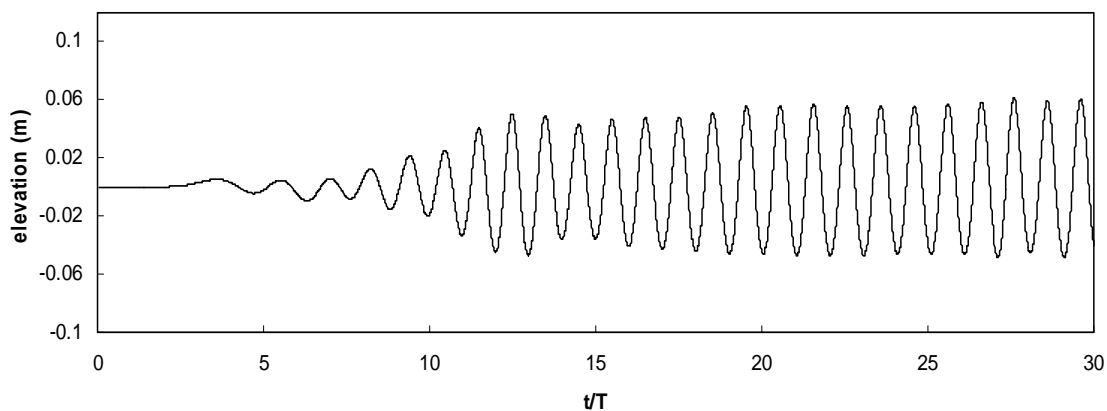

Figure 3. Time history of wave elevation in front of the model TLP; $H = 0.0575$m

Figure 4 shows the predicted velocity vectors and the corresponding vorticity contours at $t/T = 20.125$, 20.375, 20.625 and 20.875, respectively. At $t/T = 20.125$, the wave-induced current is moving downward and produces a strong counterclockwise vortex on the platform bottom surface adjacent to the weather side corner. Another weaker counterclockwise vortex was also observed on the lee side. The wave reaches its lowest elevation and begins to move upward around $t/T = 20.375$. At $t/T = 20.625$, the upward current velocity reaches a maximum value and a pair of clockwise vortices were induced around the sharp platform corners. The wave in front of the platform continue to move upward until the maximum runup is reached at $t/T = 20.875$. It is also worthwhile to note that the water elevation on the lee side of the platform changes only slightly since the platform draft is relatively deep with negligible wave transmission. The predicted velocity vector plots are in very good agreement with the corresponding PIV measurement of Ryu and Chang (2004) at the same phases.

(a) *t/T* = 20.125

(b) *t/T* = 20.375

(c) *t/T* = 20.625
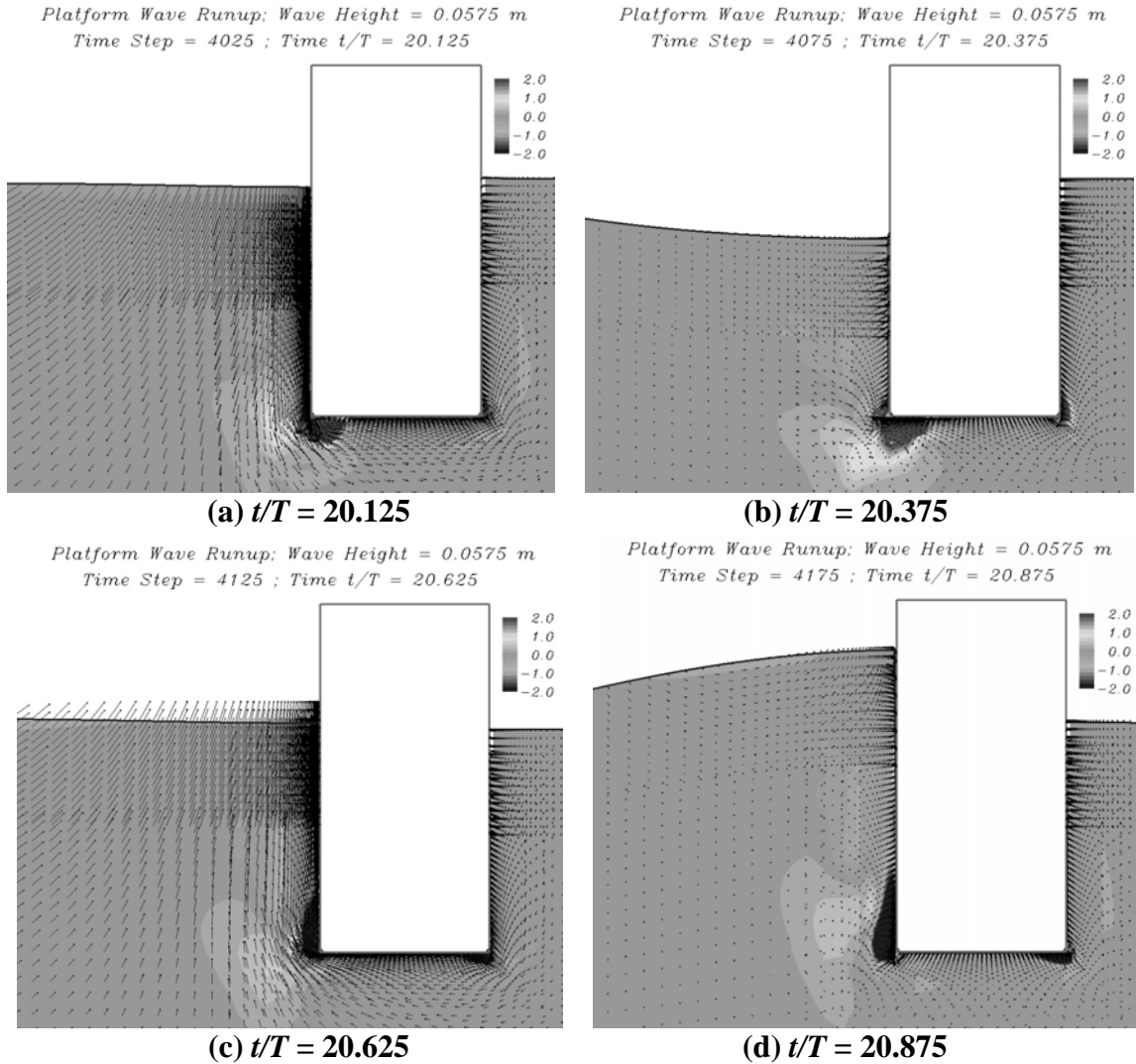
(d) *t/T* = 20.875

Figure 4. Velocity vectors and vorticity contours around the platform; $H = 0.0575$ m

Calculations were also performed for the higher wave case with an incident wave height $H = 0.0875$ m for a more critical evaluation on the capability of the chimera RANS method for large amplitude wave runup. In this simulation, the wavemaker is located at about five wavelengths in front of the structure. An absorbing beach is again implemented in front of the wavemaker to prevent the waves reflected by the model TLP from returning the wavemaker. Figure 5 shows the predicted free surface elevation and pressure contours for the higher incident wave case at $t/T = 21.27$, 21.52, and 21.77, respectively. At $t/T = 21.27$, the wave runup is very close to the platform deck. However, no greenwater was observed either in the experiment or in the simulation. At $t/T = 21.52$, there is a nearly complete cancellation of the incident and reflected waves in front the structure. It is further noted that the reflected waves are completely absorbed in the wavemaker absorbing beach region and the incident waves are not affected by the presence of the structure. For completeness, the detailed velocity vectors and vorticity

contours are also shown in Figure 6 at eight (8) different time phases where detailed PIV measurement was made. The predicted velocity vector plots are again in close agreement with the corresponding PIV data of Ryu and Chang (2004).
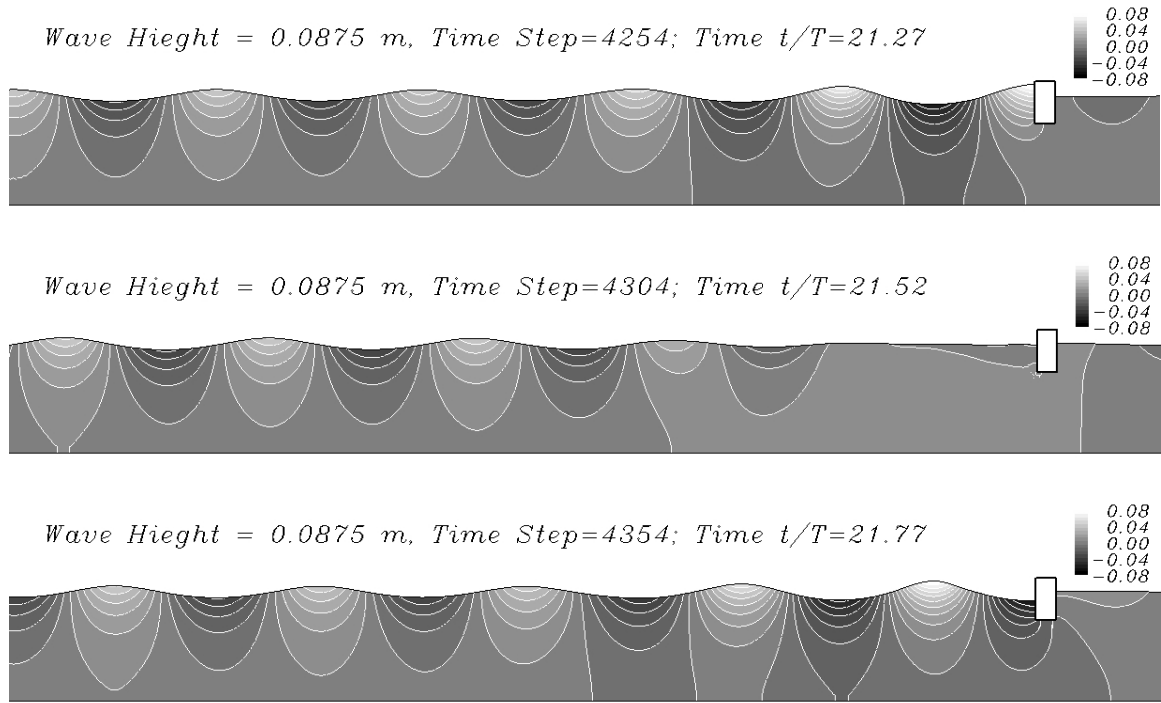

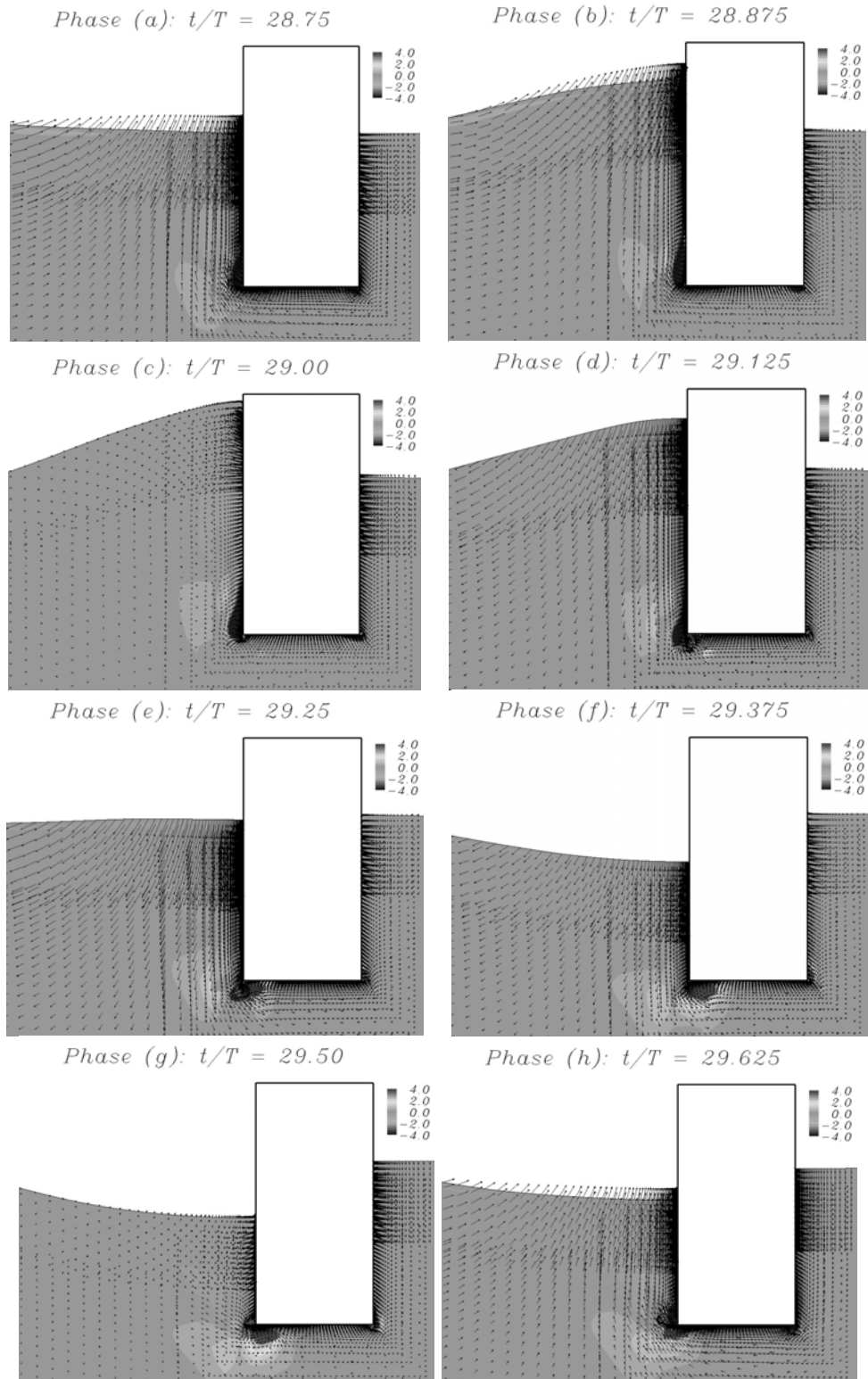Figure 5. Wave elevation and pressure contours; incident wave height $H = 0.0875$m

Figure 6: Vorticity contours and velocity vectors at eight different phases; *H* = 0.0875m.

After successful validations of the chimera RANS method for two-dimensional platform configurations, the method was further generalized for time-domain simulation of wave runup around single and multiple vertical cylinders which are common structural elements of TLP and other types of offshore structures. Figure 7 shows the numerical grids around three vertical cylinders. In the chimera domain decomposition approach, it is convenient to use overset grid system with body-fitted cylindrical grids embedded in the background rectangular grids. For the fully nonlinear waves considered here, the numerical grids are updated every time step to conform with the exact free surface.
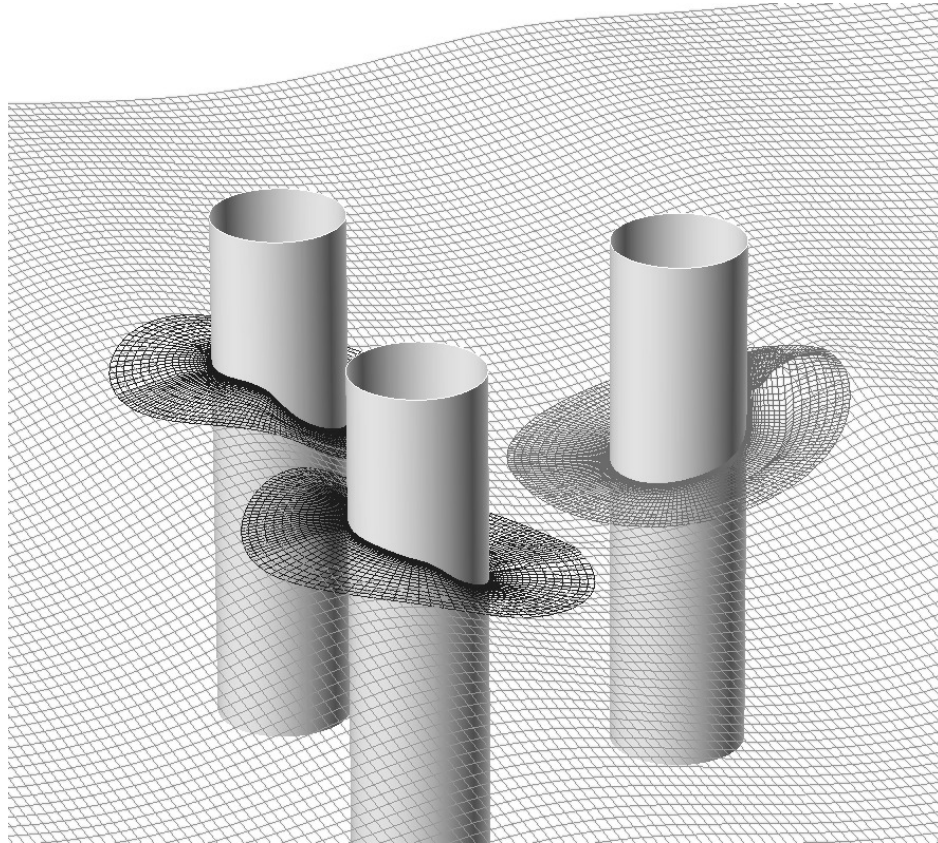

Figure 7. Chimera grids around vertical cylinders

Figure 8 shows the computed wave elevation and pressure contours around a single vertical cylinder. The incident wave height is $H/D = 0.1$ and the incident wavelength is $\lambda/D = 6.28$, where D is the diameter of the cylinder. The absorbing beaches were placed on all outgoing flow boundaries including the downstream boundary and the side walls. In addition, the wavemaker absorbing beach described earlier was used in front of the wavemaker boundary to absorb the reflected and deflected waves. The maximum wave height is nearly two times of the incident wave height as seen at $t/T = 0.45$. It is clearly seen that interaction of incident and diffracted waves produces a distinct ring wave diffraction pattern similar to those observed in Chen and Huang (2004) for wave diffraction around breakwaters and other coastal structures.

(a) *t/T* = **2.0**   **(b)** *t/T* = **3.0**

(c) *t/T* = **3.75**   **(d)** *t/T* = **4.0**

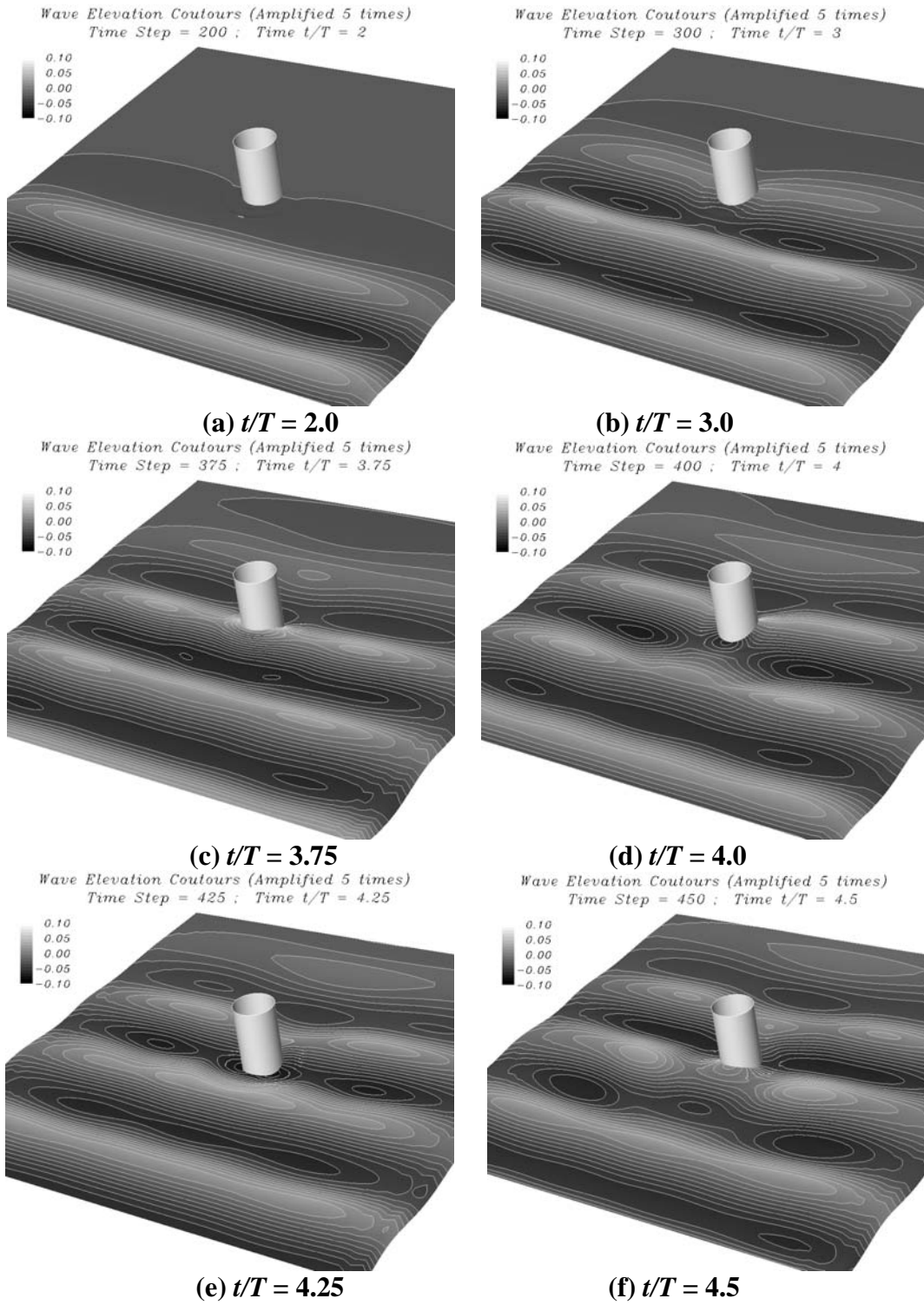**(e)** *t/T* = **4.25**   **(f)** *t/T* = **4.5**

Figure 8: Free surface pressure contours around a single vertical cylinder

Time-domain simulations were also performed for wave diffraction around three vertical cylinders. The center-to-center spacing between the two front cylinders is 2.96 D, where D is the diameter of the cylinder. The third cylinder is placed at 2.56 D (center-to-center) downstream of the two front cylinders. Figure 9 shows the predicted wave patterns at $t/T = 0.55, 0.60, 0.64, 0.66, 0.68$ and 0.70. The incident wavelength specified in the present simulation is $\lambda/D = 5.62$ and the incident wave height is $H/D = 0.30$. The simulation results clearly indicated the presence of strong interactions between the two front cylinders in side-by-side arrangement. It is also seen that the wave runup on the downstream cylinder is almost completely out-of-phase in comparison with the front cylinders since the wavelength is about twice of the cylinder spacing. Moreover, the wave diffraction pattern on the downstream cylinder is significantly different from that of the single cylinder case. This is clearly due to the strong interactions among the three vertical cylinders.

Conclusions

Time-domain simulations of wave runup around offshore structures were performed using a Reynolds-Averaged Navier-Stokes (RANS) numerical method in conjunction with a chimera domain decomposition approach. The simulation results for a two-dimensional TLP configuration are in close agreement with the corresponding PIV measurements. Calculations were then performed for single and multiple vertical cylinders which are common structural elements of TLP and other offshore structures. The numerical results clearly demonstrated the capability of the chimera RANS method for accurate resolution of the wave runup problems including both the viscous and nonlinear wave effects.

Acknowledgements

(a) *t/T* = **5.5**

(b) *t/T* = **6.0**

(c) *t/T* = **6.4**

(d) *t/T* = **6.6**
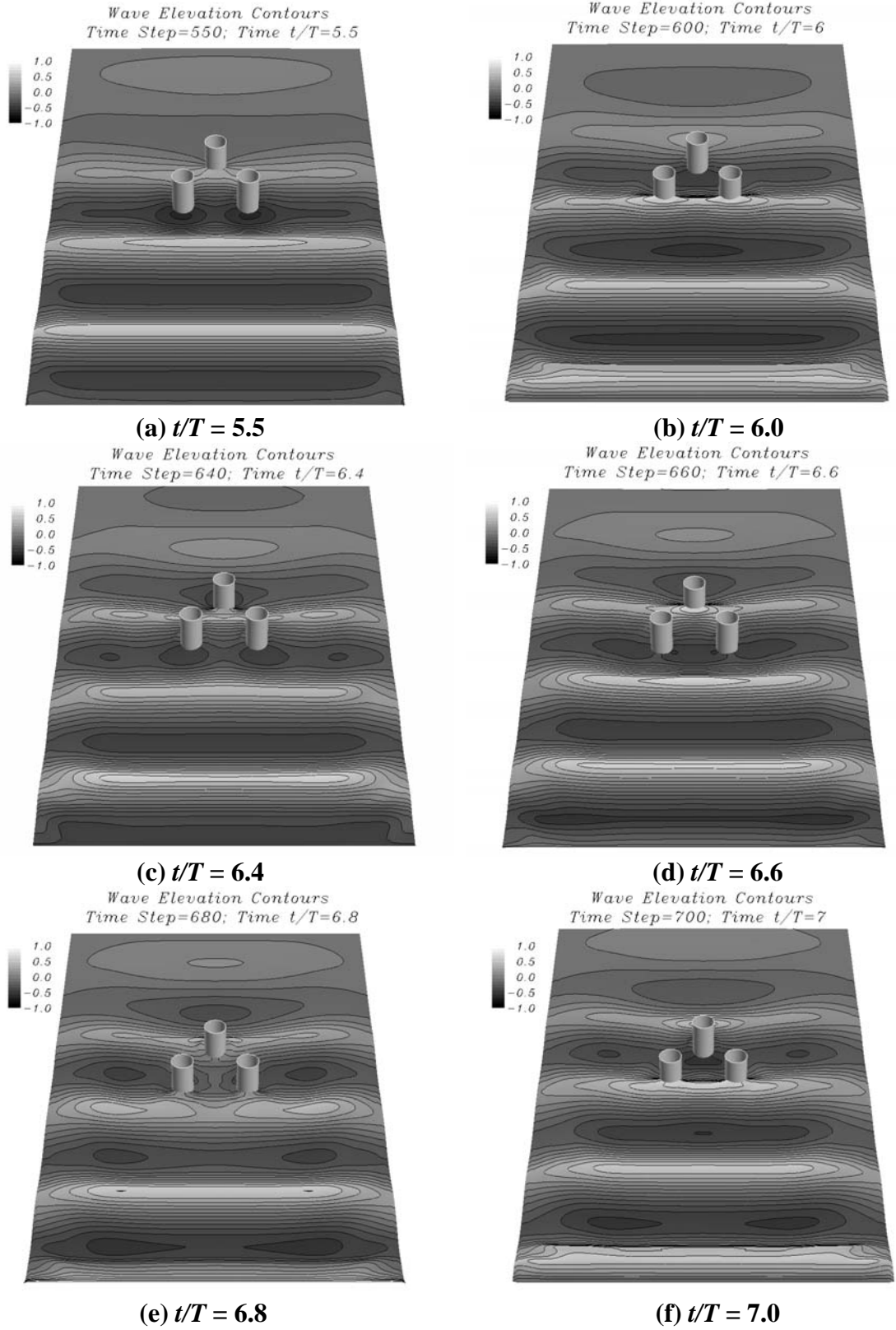
(e) *t/T* = **6.8**

(f) *t/T* = **7.0**

Figure 9: Free surface pressure contours around three vertical cylinders

References

Ananthakrishnan, P. (1998), "Nonlinear Diffraction of Waves Over a Submerged Body in a Real Fluid," *Proceedings*, *8th International Offshore and Polar Engineering Conference*, Vol. III, pp. 288-293, Montreal, Canada.

Chen, H.C. and Huang, E.T. (2004), "Time-Domain Simulation of Floating Pier/Ship Interactions and Harbor Resonance," Vol. III, pp. 772-779, *Proceedings of 14th International Offshore and Polar Engineering Conference*, Toulon, France.

Chen, H.C., Liu, T., and Huang, E.T. (2001), "Time-Domain Simulation of Large Amplitude Ship Roll Motions by a Chimera RANS Method," *11th International Offshore and Polar Engineering Conference*, Vol. III, pp. 299-306, Stavanger, Norway.

Chen, H.C., Liu, T., Chang, K.A., and Huang, E.T. (2002), "Time-Domain Simulation of Barge Capsizing by a Chimera Domain Decomposition Approach," *12th International Offshore and Polar Engineering Conference*, Vol. III, pp. 494-501, KitaKyushu, Japan.

Chen, H.C. and Patel, V.C. (1988), "Near-Wall Turbulence Models for Complex Flows Including Separation," *AIAA Journal*, Vol. 26, No. 6, pp. 641-648.

Clement, A. (1996), "Coupling of Two Absorbing Boundary Conditions for 2D Time-Simulations of Free Surface Gravity Waves," *Journal of Computational Physics*, Vol. 126, pp. 139-151.

Cokelet, E.D. (1977), "Steep Gravity Waves in Water of Arbitrary Uniform Depth," *Philosophical Transactions of Royal Society of London*, Vol, 286, pp. 183-230.

Dong, C.M. and Huang, C.J. (1999), "Vortex Generation in Water Waves Propagating Over a Submerged Rectangular Dike," *Proceedings, 9th International Offshore and Polar Engineering Conference*, Vol. III, pp. 388-395, Brest, France.

Park, J.C., Uno, Y., Matsuo, H., Sato, T. and Miyata, H. (2001), "Reproduction of Fully-Nonlinear Multi-Directional Waves by a 3D Viscous Numerical Wave Tank," *Proceedings, 11th International Offshore and Polar Engineering Conference*, Vol. III, pp. 140-147, Stavanger, Norway.

Conversion Factors for Different Units of Measurements			
Quantity	**SI Unit**	**Other Unit**	**Inverse Factor**
Length	1m	3.281 feet (ft)	0.3048 m
	1 km	0.540 nautical miles	1.852 km
	1 km	0.6213712 mile	1.609344 km
Area	1 m^2	10.764 ft^2	0.0929m^2
Volume	1 m^3	35.315 ft^3	0.0283 m^3
	1 m^3	264.2 gallon (US)	0.00379 m^3
	1 m^3	220.0 gallon (UK)	0.00455 m^3
	1 m^3	6.29 barrel (US Petroleum)	0.1589 m^3
Velocity	1 m/s	3.281 ft/s	0.305 m/s
	1 m/s	1.943 knot	0.515 m/s
	1 m/s	2.2369 mph	0.44704 m/s
	1 km/hr	0.62137 mph	1.6093 km/hr
Mass	1 kg	2.205 pound	0.454 kg
	1 Mg	0.984 ton (long)	1.016 Mg
	1 Mg	1 tonne (metric)	1 Mg
Force	1 N	0.225 pound force	4.448 N
	1 MN	100.4 ton force	9964 N
	1 MN	224.81 kip	4448 N
Pressure	1 N/m^2	0.000145 psi	6895 N/m^2
	1 MN/m^2	20.885 kip/ft^2	47880 N/m^2
Energy	1 J	0.738 foot pounds	1.356 J
Power	1 W	0.00134 horsepower	745.7 W
Temperature	0^0 Celsius	32^0 Fahrenheit	-17.78^0 Celsius
Frequency	1 cycle/s	1 hertz	1 cycle/second
Flow Rates	1 m^3/day	6.289 barrel/day	0.1589 m^3/day
	1 m^3/day	35.3146 ft^3/day	0.0283 m^3/day
Density	1 g/cm^3	0.578 oz./$inch^3$	1.73 g/cm^3